Growth, Structural and Electrical Characterization of Topological Dirac Materials

Angadjit Singh

Queens College

Department of Physics

University of Cambridge

A thesis submitted for the degree of

Doctor of Philosophy

June 2018

Growth, Structural and Electrical Characterization of Topological Dirac Materials by Angadjit Singh

Abstract

We are living in an era of digital electronics. The number of robots have already exceeded the human population of the entire earth. An article in the Guardian newspaper dated 30th March 2018 suggests that 10 million UK workers will be jobless within 15 years as they will be replaced by robots[1]. These astonishing facts shed light on the importance of knowledge and how important it is to use it wisely for our benefit without ultimately destroying us. Knowledge in all forms is accessible without going to a library or buying a newspaper. Furthermore to access information, we often use sleek devices such as smart phones, using highly developed multimedia platforms which consume large amounts of power. In 2016, IBM found that humans create 2.5 quintillion bytes of data daily[2]. Since high computing usage is related to large power consumption, the basic building block of electronics *i.e.* the transistor is required to be more power efficient. This is now possible through spintronics, where the spin of an electron is exploited instead of the charge.

A new class of exotic materials called topological insulators are predicted to exhibit efficient spintronic applications. These materials can conduct spin polarised current on their surface while remaining completely insulting from the inside. Moreover, doping topological insulators with magnetic impurities unlocks new avenues for spin memory devices in the form of a single spin polarized dissipationless conduction channel. In topological insulators, there is always a contribution from the inside (bulk) in addition to surface conduction, thereby yielding charge transport rather than spin transport. On this basis, the aim of my PhD was to explore techniques to grow, characterize, fabricate and measure devices on topological Dirac materials, with the hope to experimentally distinguish the bulk from the surface states and also exploit their exotic properties arising from opening of the bulk band gap by intentional magnetic doping.

Samples consisted of thin films of Bi_2Se_3, Sb_2Te_3, Cr doped Sb_2Te_3, bilayers of Dy doped Bi_2Te_3/Cr doped Sb_2Te_3 and Cd_3As_2 nanowires. It was found that a seed layer of an undoped topological insulator was a crucial first step to ensure high quality growth

by molecular beam epitaxy, followed by the desired stoichiometry. By physically doping Sb_2Te_3 with Cr, a successful control of the magnetic and electrical properties such as coercivity, anomalous Hall resistance R^A_{xy}, Curie temperature T_c, carrier density and mobility were achieved. A substitutional Cr doping ranging from 7.5% to 38% was attained revealing a T_c reaching up to 186 K. Gated electrical measurements displayed a change in R^A_{xy} and carrier density by ~ 50% on applicating of just -3 V gate bias in a sample with 29% doping. A comparison between electrical transport, Magneto-optical Kerr effect and terahertz time domain spectroscopy measurements revealed that the mechanism of magnetization was RKKY mediated. Furthermore, the bilayer structure displays a clear exchange bias coupling arising from the proximity of the antiferromagnetic Dy doped Bi_2Te_3 layer with the ferromagnetic Cr doped Sb_2Te_3 layer. Electrical transport measurements on Bi_2Se_3 Hall bars fabricated using Ar^+ milling and wet chemical etching were compared. The results showed a more bulk type response in the chemical etched sample even though Ar^+ milling was responsible for creating more disorder in the system leading to a higher carrier density and lower mobility. A thickness dependent study on Sb_2Te_3 thin films revealed a single conducting channel associated with a coupled surface and bulk state for a 12 nm sample, compared to, two conducting channels associated with the top and bottom surfaces for the 25 nm sample. Electrical transport on Dirac semimetal Cd_3As_2 nanowires reveal an ultra-high mobility of 56884 $cm^2V^{-1}s^{-1}$ at 1.8 K from analysis of Shubnikov-de Haas oscillations. By studying various Dirac materials, new avenues for practical device applications can be explored.

Dedication

This Dissertation is Dedicated to Krishna

Declaration

The work presented in this dissertation was carried out at the Department of Physics, University of Cambridge in United Kingdom, between October 2013 and June 2018 under the supervision of Prof. Crispin Barnes.

I hereby declare that, except for where specific reference is made to the work of other authors or specifically indicated in the text, the contents of this dissertation are my own work, and include nothing done in collaboration, except where specifically indicated in the text. This dissertation has not been previously submitted in part, or in whole, to any other university for a degree, diploma or other qualification.

In accordance with the Department of Physics and the degree committee guidelines, the dissertation does not exceed the prescribed word limit.

Signed:_____

Date:_____

Angadjit Singh

Cambridge, UK

Acknowledgement

There are a number of people who have contributed to the completion of this work. I am extremely thankful for all contributions, however small they may be. I would like to express my gratitude to the following people in no particular order. First I thank my supervisor Prof. Crispin Barnes for selecting me for my persistence while motivating me through all the rocky moments with his positive attitude. Weekly meetings with him have always been scientifically fruitful and at the same time jovial. I would like to express my heartfelt gratitude to Prof. Thorsten Hesjedal at the University of Oxford without whom my PhD would not have been completed. He has guided me through every step by opening new avenues, offering new projects. His openness to share knowledge and hands on experience has taught me to be humble. At this point, I would also like to thank the team at Oxford consisting of Dr Liam-Collins-Mcintyre, Liam Duffy and Dr Piet Schönherr who have taught me various scientific skills helping me upgrade my knowledge. This work could not have been possible without the help of my main proofreader Dr Adrian Ionescu. My journey at Cambridge began with him. He has taught me the life-long skill to write scientifically and shared his vast knowledge on magnetism with me. Many thanks to Dr Justin Llandro for providing clean room training and teaching me the importance of perfection. Many thanks to Dr Vijay Narayan who helped me setup the cryostat lab while Dr Stuart Holmes from Toshiba who taught me how to carry out electrical measurements on a cryostat. Gratitude to Dr Deepyanti Taneja and Prof. Chris Ford for teaching me to use the software required to carry out transport measurements and to Thuy-Anh Nguyen for all the support with technical discussions. My heartfelt gratitude also goes out to Dr Thierry Ferrus from Hitachi who has been more like a friend and excellent research collaborator. The Proofreaders of this thesis were Dr Adrian Ionescu, Dr Peter Newton and Dr Harvey Beere, thank you all. Many thanks also to Dr Jon J. Rickard from the microscopy suite for all his help and patience while imaging samples. I am indebted to all the funding agencies: The Cambridge Commonwealth Trust, SGPC, The Philosophical Society, Queens college, Professors Crispin Barnes and David Ritchie for supporting me financially leading me to having a comfortable life during my PhD.

I thank my family for their constant support and daily encouragement and for the many enjoyable summers spent in Cambridge with them. I am extremely grateful for their

unconditional financial and emotional support. Thank you Sarah Partridge for all the love and care. Last but not the least I would like to thank all my friends from Cambridge, York and Amity. Many thanks to Varun, Jieye, Razan, Amandeep, Satya, Aakriti, Gayatri, Somesh, Arjun and Gaurav who have made my life cheerful. I am grateful to be a part of the Queens college badminton team. We finally won the league, after four years of dedicated team work. A special appreciation to Krishna who's will I surrender to.

List of Publications

The results of this thesis have been partially presented and published in:

1. **Singh, A**.; Kamboj, V. S.; Liu, J.; Llandro, J.; Duffy, L. B.; Senanayak, S. P.; Beere, H. E.; Ionescu, A.; Ritchie, D. A.; Hesjedal, T.; Barnes, C. H. W.; Systematic Study of Ferromagnetism in $Cr_xSb_{2-x}Te_3$ Topological Insulator Thin Films using Electrical and Optical Techniques. *Sci. Rep.* **2018,** under consideration with reviewers.
2. Kamboj, V. S.; **Singh, A**.; Ferrus, T.; Beere, H. E.; Duffy, L. B.; Hesjedal, T.; Barnes, C. H. W.; Ritchie, D. A.; ThZ carrier dynamics and magnetotransport study of topological surface states in thin film Bi_2Se_3. *Proc. SPIE - Int. Soc. Opt. Eng.* **10531,** 105310I–1 (2018).
3. Kamboj, V. S.; **Singh, A**.; Ferrus, T.; Beere, H. E.; Duffy, L. B.; Hesjedal, T.; Barnes, C.H.W.; Ritchie, D. A.; Probing the topological surface state in Bi_2Se_3 thin films using temperature-dependent terahertz spectroscopy. *ACS Photonics* (2017). doi:10.1021/acsphotonics.7b00492
4. Kamboj, V. S.; **Singh, A.;** Beere, H. E.; Hesjedal, T.; Barnes, C. H. W.; Ritchie, D. A.; Temperature evolution of topological surface states in Bi_2Se_3 thin films studied using terahertz spectroscopy. *Proc. SPIE - Int. Soc. Opt. Eng.* **10103,** 101030D (2017).
5. Collins-McIntyre, L. J.; Duffy, L. B.; **Singh, A.;** Steinke, N.-J.; Kinane, C. J.; Charlton, T. R.; Pushp, A.; Kellock, A. J.; Parkin, S. S. P.; Holmes, S. N.; Barnes, C. H. W.; Van Der Laan, G.; Langridge, S.; Hesjedal, T.; Structural , electronic , and magnetic investigation of magnetic ordering in MBE-grown $Cr_xSb_{2-x}Te_3$ thin films. *Eur. Lett.* **115,** 27006 (2016).
6. Nguyen, T.; Backes, D.; **Singh, A**.; Mansell, R.; Barnes, C. H. W.; Ritchie, D.; Mussler, G.; Lanius, M.; Grützmacher, D.; Narayan; Topological states and phase transitions in Sb_2Te_3-GeTe multilayers. *Sci. Rep.* **6,** 27716 (2016).
7. Kamboj, V. S.; Braeuninger-Weimer, P.; Kidambi, P. R.; Jessop, D. S.; **Singh, A**.; Sibik, J.; Ren, Y.; Hofmann, S.; Zeitler, J. A.; Beere, H. E.; Ritchie, D. A; Low-bias gate tunable terahertz plasmonic signatures in chemical vapour deposited graphene of varying grain size. *Proc. SPIE - Int. Soc. Opt. Eng.* **9747,** 974707–1 (2016).

Table of Contents

List of Figures

List of Tables

LIST OF ACRONYMS

ARPES	Angle resolved photoemission spectroscopy
AMR	Anisotropic magnetoresistance
AHE	Anomalous Hall effect
ALD	Atomic layer deposition
BE	Binding energy
CVD	Chemical vapor deposition
DUT	Device under test
DS	Dirac semi-metal
DP	Dirac point
DOS	Density of states
DMS	Dilute magnetic semiconductor
EB	Exchange bias
F, AF	Ferromagnetic/Anti-ferromagnetic
FET	Field effect transistor
HLN	Hikami-Larkin-Nagaoka
IC	Integrated circuit
KE	Kinetic energy
K-F	Kouvel-Fisher
K cell	Knudsen cell
LCC	Leadless chip carrier
MOKE	Magneto-optical Kerr effect
MRAM	Magnetic random access memory
MTI	Magnetic topological insulator
MI	Magnetic insulator
MR	Magneto-resistance
MBE	Molecular beam epitaxy
PID	Proportionality Integral Differentiation
QL	Quintuple layer
QAHE	Quantum anomalous Hall effect
RBS	Rudderford back-scattering
RMS	Root mean square

RHEED	Reflection high-energy electron diffraction
RGA	Residual gas analyser
RPM	Rotations per minute
RKKY	Ruderman-Kittel-Kasuya-Yosida
SOC	Spin orbit coupling
SQUID	Superconducting quantum interference device
SdH	Shubnikov-de Haas
TI	Topological insulator
TM	Transition metal
TRS	Time reversal symmetry
TSM	Topological surface mode
THz-TDS	Terahertz time domain spectroscopy
UHV	Ultra-high vacuum
UV	Ultraviolet
WAL/WL	Weak-antilocalization/weak localization
XRD/XRR	X-ray diffraction/Reflectometry
XPS	X-ray photoemission spectroscopy

LIST OF SYMBOLS

a	Lattice parameter in XRD, number of topological channels in transport
B	Magnetic field
B_F	SdH Oscillation frequency
c	Lattice parameter in XRD
d	Lattice spacing in XRD, thickness of film in XRR
E	Electric field
E_a	Activation energy
E_F	Fermi energy
e	Charge of electron
ξ	Localization length
F	Lorentz force
h,k,l	Miller indices in XRD
H_c	Coercive field
$\hbar$	Planck constant

j	Charge density
K_F	Fermi wave vector
l, l_e	Mean-free path
L	Sample size, length of channel
l_φ, L_φ	Phase coherence length or dephasing length
M	Magnetic moment/magnetization
m^*	Effective mass
m_{cyc}	cyclotron mass
n, N	Landau level index, order of reflection in XRD
N_A	Avogadro number
n_s , n_{2D}	Sheet/2D carrier density (n-type)
p, p^{2D}	Carrier/2D density (p-type)
R	Rydberg constant
R_{OHE}, ρ_{OHE}	Ordinary Hall resistance/resistivity
R_{AHE}, ρ_{AHE}	Anomalous Hall resistance/resistivity
ρ_{xx}, ρ_{xy}	Longitudinal and transverse resistivity
$\sigma^T{}_{xy}$	Total Hall conductivity
$\sigma^O{}_{xy}$	Ordinary Hall conductivity
$\sigma^A{}_{xy}$	Anomalous Hall conductivity
σ_{xx}	Longitudinal conductivity
$\Delta\sigma_{xx}^{2D}$	2D sheet conductivity
S_F	Fermi surface
τ_e, τ	mean free time
τ_φ	Dephasing time
T_c,T_N	Curie/Neel temperature
μ_B	Bohr magneton
μ_t,μ,μ_{FET}	Transport/FET mobility
v_d	Drift velocity
v_F, V_F	Fermi velocity
λ_F	Fermi wavelength
ω_c	angular frequency
γ	Berry phase

1. Chapter 1

Dissertation Outline

This thesis comprises of a comprehensive study with regards to growth, fabrication and electrical transport in topological Dirac materials such as topological insulators, magnetically doped topological insulators and topological Dirac semimetals.

The thesis is divided into an introduction and experimental techniques chapter followed by four experimental chapters and future work. Each chapter describes a literature review, motivation and conclusion independently.

Chapter one gives a brief introduction and theoretical background to topological insulators along with the scientific knowledge required to understand the rest of the chapters.

Chapter two sheds light on all the experimental techniques used for the completion of the work.

Chapter three describes in detail the high-quality growth of magnetically doped topological insulators using molecular beam epitaxy and their structural characterization.

Chapter four describes electrical transport related to magnetically doped topological insulators and magnetically doped heterostructures while the device fabrication was described in detail in the next chapter.

Chapter five describes fabrication and device processing of topological insulators followed by electrical transport in first generation topological insulators: Bi_2Se_3 and Sb_2Te_3.

Chapter six describes fabrication and electrical transport on nanowires: Cd_3As_2 topological Dirac semi-metal.

Finally chapter seven describes future work followed by a conclusion.

1.1 Introduction

In 1947, the transistor was first invented at Bell Labs and for its deep effects on our world, it has been considered the most important invention of the 20th century[3]. It has allowed both scientists and engineers to create complex systems and develop new electronic applications. Following that, in 1959, 'Fair child semiconductors' invented the first Integrated Circuit (IC) which marked the birth of a revolution: The invention of the microprocessor. It began in 1968, when three scientists Gordan Moore, Robert Noyce and Andrew Grove resigned from 'Fair child semiconductors' and started their own company: 'Integrated Electronics' now commonly known from its abbreviation: 'Intel'. In 1971, they invented the first microprocessor which ran at a clock speed of 108 kHz[4]. Now more than forty years later, we are still using the systems based on more or less the same "system on a chip" design. The road map in semiconductor fabrication which started with a 10 μm channel length on a transistor in 1971 is till date an astonishing 10 nm length with 4.3 billion transistors on a 87.66 mm^2 die in Apple's new A11 chip[5]. The reduction in size of a transistor is governed by Moore's law and it is predicted that the growth trend will come to a standstill latest by 2022-25 reaching the limit for a single electron transistor[6]. The question then arises whether there is a superior strategy to fabricate nano-transistors with a different architecture?

In most semiconductor devices, electrical currents are needed to transport "information". The charge of the electron carries this information. For example, in a field effect transistor (FET) the capacitors plates can be charged or discharged resulting in an ON or OFF state. In reality, this charging is affected by electrons scattering by static defects or phonons therefore making the transport dissipative. Hence, researchers have spent much of their time growing good quality crystals for semiconductor devices to reduce defects. It is possible to use the spin of the electron rather than the charge, which can be related to the magnetic moment of a single electron. The field of spintronics promises many advantages such as that, no external current is needed to manipulate the spin information (up or down) and typical spin relaxation times are much higher than the lifetime of a charge state, which can be destroyed by defect scattering[7].

1.1.1 Topological Insulators

Topological insulators (TIs) as a new class of condensed matter physics, have taken a major leap forward in spintronic research. These exotic materials conduct electrical current on their surface and behave as insulators inside. The origin of the surface channel is a quantum mechanical effect which is highly robust against surface defects and modifications. They form a so called Dirac cone *i.e.* the energy of the surface carriers depends linearly on their momentum. Figure 1(a) and 1(b) show a schematic and experimental angle-resolved photoemission spectroscopy (ARPES) of a Dirac cone in Bi_2Se_3. Figure 1(c) highlights the spin momentum locking of surface channels, an electron in the +k direction is propagating in the y direction (blue) and *vice versa* (red). From a theoretical point of view spin polarization of more than 50% is possible because of its unique properties[8]. Pan *et al.* provided evidence of weak electron-phonon coupling on the surface which shows promising applications for room temperature spintronics[9]. In addition, helicity of surface state could give rise to physical phenomena such as magnetic monopole[12] and Majorana fermions[13].

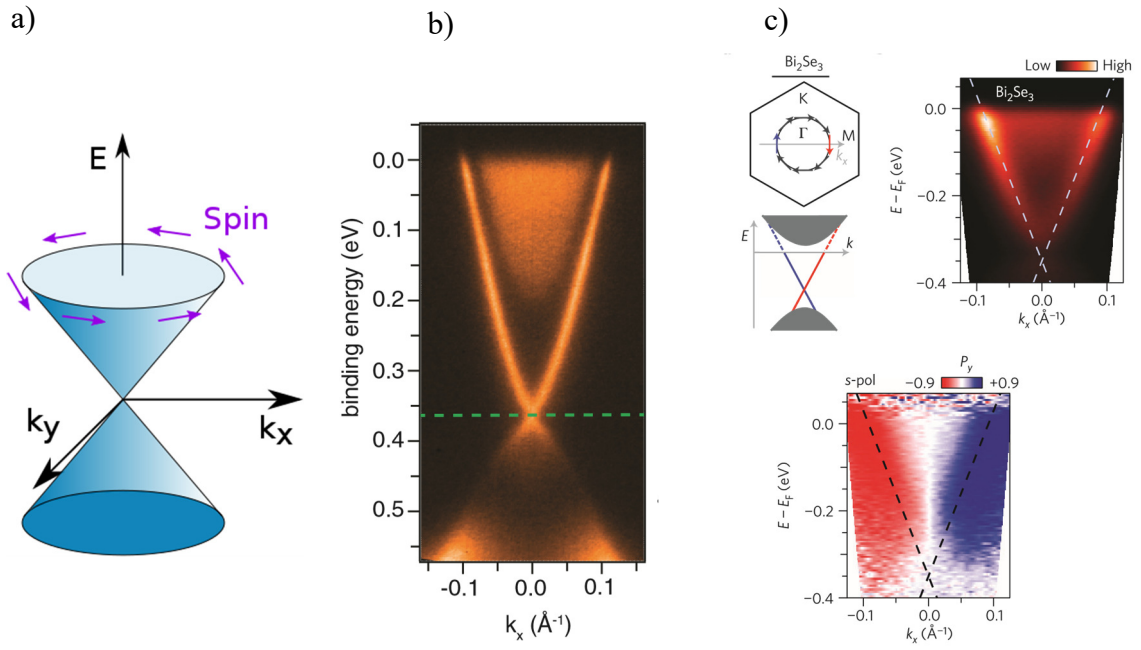

Figure 1.1 The exotic band structure of TIs. (a) Sketch of the spin– polarized Dirac cone associated with the surface of a TI. (b) ARPES spectrum of the 3D TI Bi_2Se_3[10]. The linear surface bands are clearly observable (c) Detailed ARPES spectrum of Bi_2Se_3 (top) and the corresponding spin–polarized spectrum showing the helicity of the surface states (color denotes the spin–polarization in y–direction)[11]. Figure adopted from ref. 11 without permission.

All the above mentioned properties seem hopeful however their existence has been a challenge to verify by transport studies. One of the obvious reasons is due to the conductivity originating from the unwanted bulk contribution. In typical chalcogenides such as Bi_2Se_3, Bi_2Te_3 (*n*-doped) and Sb_2Te_3 (*p*-doped) the origin of the bulk conductivity is reported in literature. Firstly during growth of TIs, point defects (vacancies) can result in doping leading to extra charge carriers[14–16], and secondly a surface oxide might form when exposed to ambient conditions, charging the surface[17,18]. Hence transport measurements are dominated by the low resistive bulk. There are several solutions to the problem mentioned in literature. One of them is to counter-dope the bulk[19,20] or make alloys from different TIs[21,22]. The above solutions often lead to low carrier mobilities and therefore prevent the observation of quantum oscillations which give information regarding the surface state[23]. Therefore another approach is to improve the synthesis of the crystal quality by Molecular Beam Epitaxy (MBE). The major advantage of MBE is that it allows the user to grow ultra-thin films which will increase the surface to bulk ratio. In fact transport measurements on MBE grown samples led to the observation of the quantum Anomalous Hall effect in magnetically doped TI thin films for the first time in 2013[24].

1.1.2 Understanding the Band Structure

Definition:

A topological insulator is a material which has gapless electronic states on the sample boundary with a bulk electronic excitation gap generated by spin-orbit interaction which is topologically distinct from an ordinary insulator. This distinction is characterized by a Z2 topological invariant, robustness and helicity of the surface state[25].

In principle a TI is nothing but an electrical conductor on its surface and an insulator in its interior. Electrical conduction on the surface is spin polarized which means that the orientation of the spin is coupled to the direction of motion. An electron moving from left to right thus has an opposite spin orientation as compared to an electron propagating from right to left. If an electron collides with a non-magnetic impurity it will not backscatter unless the spin flips. As a consequence the surface conduction is dissipationless.

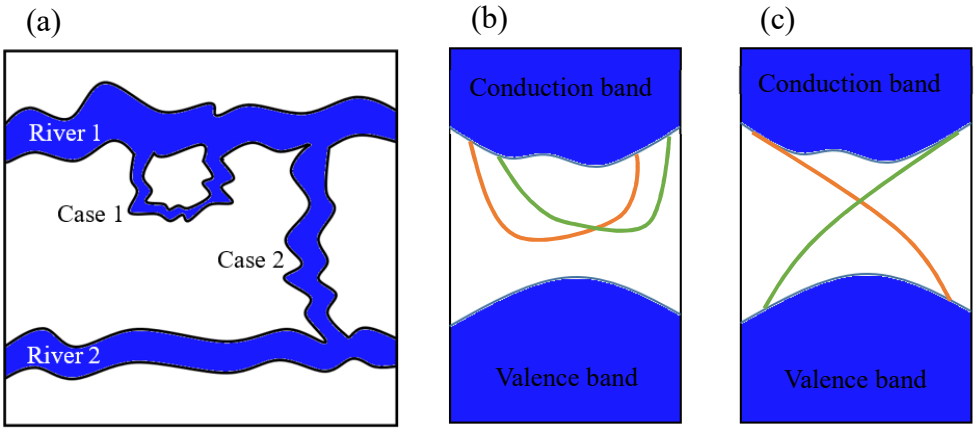

Figure 1.2 Types of surface states (a) Two types of rivulets may be formed case 1: one that starts and ends in the same river and case 2: which ends in another river. (b) A trivial insulator, spin splitting which start and end in the conduction band. c) A non-trivial TI surface state, the surface states connect the valence and conduction bands. These are robust against any change in the energy topography[28]. Figure adopted from ref. 28 without permission.

The origin of this surface conduction/surface state lies in breaking of the translation symmetry on the surface. Insulators or semiconductors have an energy gap which separates the conduction band from the valence band and these surface states can be dispersed in such a way that either they start and end in the same bulk bands or the surface states start in one and end up in the other band. This can be explained by imagining two rivers flowing parallel to each other acting as the bulk bands as shown in Figure 1.2 (a). There are two different ways in which a rivulet can be constructed; case 1: which starts from river 1 and ends in the same river, and case 2: which starts at river 1 and ends inside river 2. Now, from time to time if the topography of the landscape changes, then the course of the rivulet can be affected. In case 1, due to the disturbance, the rivulet can completely vanish into river 1; however this can never happen in case 2. Hence case 2 is robust against topographical effects. While applying the same principle to TIs two extra concepts are added, time reversal symmetry (TRS) and spin-orbit interaction. In TRS, we just need to reverse the arrow of the time by rewinding the system and see the changes in the materials physical properties. For example, if electrons are moving in the $+k$ direction, after applying TRS, the electrons should now move in the $-k$ direction. In addition TRS will also reverse the direction of the spin of electrons. Hence a system which is time reversal symmetric can be described by: $E(+k,\downarrow) = E(-k,\uparrow)$. For a normal material, TRS has little effect since every state is two times degenerate. However in heavy atom materials, electrons orbit with a high speed so that their

orbital angular momentum starts to influence the spin orientation. This interaction between the orbital momentum and the spin leads to the breaking of the degeneracy of spin up and spin down electrons. As a consequence, according to TRS, for every electron with spin up moving in the $+k$ direction, there must be a single state with spin down in the $-k$ direction. As explained by the concept of two rivers, there will still be only two possible ways to arrange bands that start and end in the bulk bands. These are shown in Figure 1.2(b,c). The first is two states with opposite spins starting and ending in the same band *i.e.* a trivial insulator and the second is two states with opposite spins starting and ending in different bands *i.e.* a non-trivial insulator. From this a conclusion can be made that the topology of the band structure defines if the material is a normal insulator or topological insulator. Topology is a branch of mathematics which describes how certain properties of geometric objects remain preserved even after continuous deformations such as stretching and bending. Topology simply counts the number of holes in an object. For example, a sphere can be pressed into a wine glass making them topologically compatible, but a donut and sphere are not, since a donut has a hole in it (Figure 1.3).

The same concept can be applied to the electronic band structure of materials. TIs exhibit a so-called inverted band structure, *i.e.* the order of the two bands is switched which results in a "negative band gap". The bands will now have a different symmetry which is topologically distinct from a normal insulator.

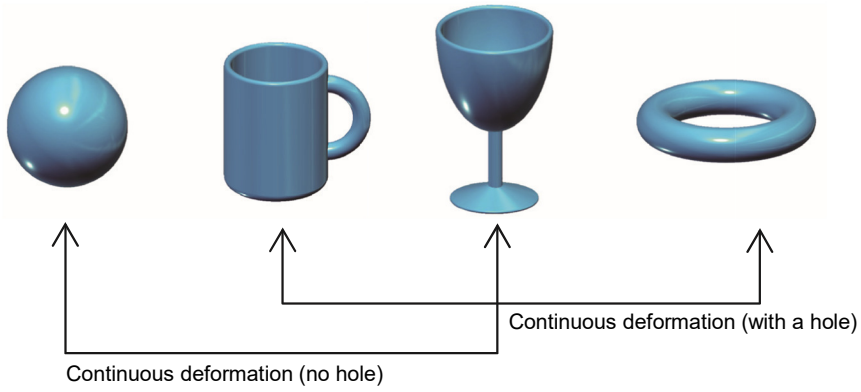

Figure 1.3 The Topology defined by preservation of the object by continuous deformation. A sphere can deform into a wine glass but not into a donut[26].

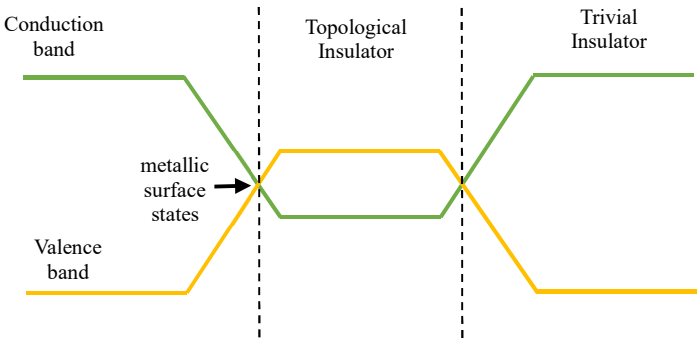

Figure 1.4 Difference in topology for a normal insulator and a topological insulator. At the interface, the band closes and then reopens inverting the bands. The crossing over of the bands leads to a metallic surface state, the so called Dirac cone[28]. Figure adopted from ref. 28.

Figure 1.4 shows a TI and a normal insulator linked to each other. The topology changes at the interface. The band gap is open in a normal insulator and in order to go into the TI regime, the band gap has to close first and then re-open. This process inverts the gap and makes it nontrivial thus creating a metallic state on the surface.

Another important concept to understand the basics of topology is the Berry phase that TIs possess. The Berry phase is the change in the phase acquired by a system over the course of a cycle when the system is subjected to cyclic adiabatic processes. This can be simplified by looking at the experiment Berry proposed in 1988, also found in his lecture notes at the University of Bristol[27]. He placed a pencil at one of the poles of the earth with the pencil tip pointing towards one of the longitudes as shown in Figure 1.5. The pencil was then moved along the same longitude (from 1-3) until it intersected the equator. At this point the pencil made a left turn and moved along the latitude (from 3-5) until it intersected another longitude. Here, another left turn led the pencil back to the point from where it began its journey (at 7). It was observed that the pencil was now pointing in a different direction. The shift in the angle was α *i.e.* the berry phase. The Berry phase here is equal to the solid angle subtended over the area enclosed by the path the pencil took. Similarly in quantum mechanics, the Berry phase can describe the phase shift in the electrons wavefunctions. For example there might be a phase shift when a system in a certain eigenstate is adiabatically transferred to the same initial eigenstate enclosed in a closed path in the parameter space. This can be executed by applying a magnetic field, which would rotate the direction of the spin of the electron. Now, the magnetic field is changed in such a way that the electron follows a closed

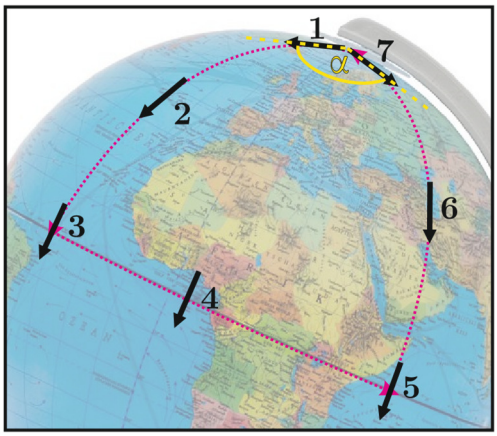

Figure 1.5 A pencil moved on the surface of the earth along the path 1-7, after reaching the same point, its angle changed by an angle α which is the Berry phase[28]. Figure reproduced from ref. 28 without permission.

loop. Thus even though the electron has reached back to its original position its phase has changed. The Berry phase in this case is given by the product of the spin quantum number and the solid angle of the area enclosed by the path the electron takes.

1.2 3D Topological Insulators

The best way to search for a 3D TI is to consider a material with an inverted band structure at certain points in their Brillouin zone having a strong spin orbit interaction. Fu and Kane first theoretically predicted strong TI behaviour in $Bi_{1-x}Sb_x$ bulk structures[29]. This was later experimentally proved using ARPES by Hseih et al[30]. Pure Bi is a semimetal with the conduction band minima separated from the valence band maxima by a small bandgap of ~ 10 meV at three equivalent L points while overlapping with a valence band maximum at the T point. When Sb and Bi are alloyed together, at the certain concentration of $x = 0.04$, the small band gap at the L point closes and then reopens again in an inverted fashion. At higher concentrations of $x = 0.09$, the T band falls down below the valence band and the system becomes an inverted semiconductor. Although ARPES was enough to show that $Bi_{1-x}Sb_x$ was a strong TI, electrical transport measurements have been challenging. Firstly an extremely good control of x was required, since the TI phase only exists between the range $0.07 < x < 0.22$ and secondly alloys tend to form impurity bands which can show an extra conduction

channel during electrical measurements. Also with ARPES, the electronic band structure showed five surface states crossing the Fermi level which was very complicated to decode. Thus the search for simpler structures began and, not long after, new TIs were experimentally discovered with a single Dirac cone crossing the Fermi level: Bi_2Se_3, Bi_2Te_3 and Sb_2Te_3[31].

The chalcogenides Bi_2Se_3, Bi_2Te_3 and Sb_2Te_3 have a rhombohedral crystal structure as shown in Figure 1.6 (a,b) (space group $R\bar{3}m$) consisting of hexagonally close packed atomic layers of five atoms forming one quintuple layer (1QL = 0.97 nm). They are weakly bonded together through van der Waals forces. In the case of Bi_2Se_3, the stacking order is $Se^{(1)}$-Bi-$Se^{(2)}$-Bi-$Se^{(1)}$. Figure 1.6 (c) shows the calculated band structure of Bi_2Se_3; the non-trivial character is quite apparent. When spin orbit coupling is strong, a pronounced anti-crossing feature is observed at the Γ point. This camel back like feature in the valence band indicates the inversion of the two bands suggesting that Bi_2Se_3 is a non-trivial insulator. The results show that there was only a single Dirac cone formed at the Γ point[31]. This was also confirmed experimentally by Xia *et al*. later that year using ARPES[14]. Bi_2Te_3 and Sb_2Te_3 also exhibit similar band structures with only a single Dirac cone at the Γ point, rendering these materials ideal systems to investigate further.

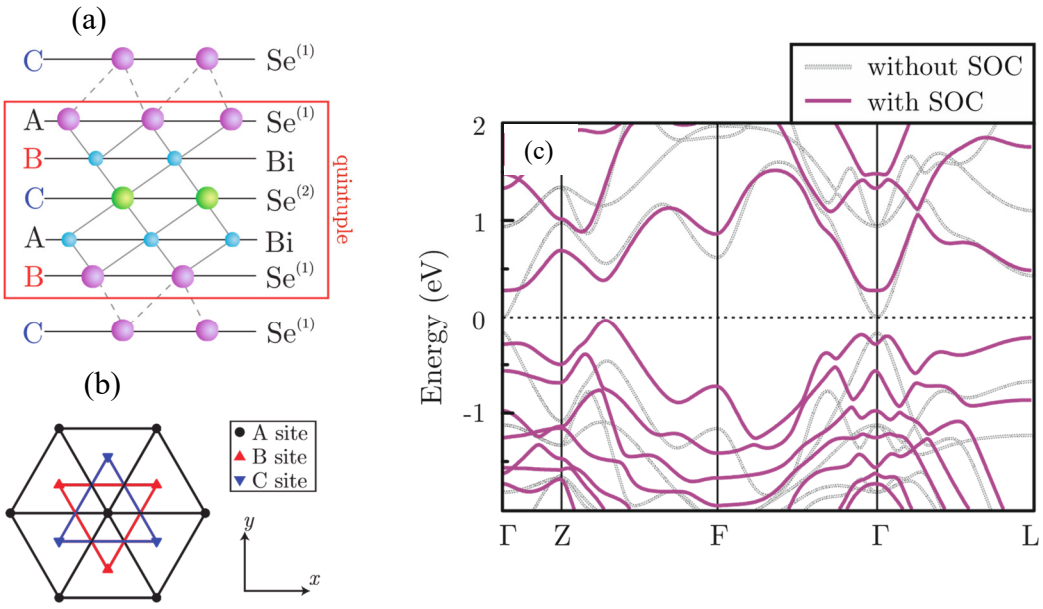

Figure 1.6 a,b) Crystal structure for chalcogenides. c) The theoretically calculated band structure of Bi_2Se_3 with and without spin-orbit coupling[31]. Figure reproduced from ref. 31 without permission.

1.3 Magnetic Doping in Topological Insulators

After understanding the band structure of TIs, it is also important to understand the role of magnetic impurity doping in TIs. Introducing magnetism into a TI structure is known to break TRS which opens up a gap to the helical Dirac surface states and the study of this is of central importance from both fundamental aspects[12,32–34] and as well device applications[34–37]. A more thorough understanding of its applications and a literature background has been covered in the beginning of each experimental chapter based on magnetic topological insulators (MTIs). Briefly speaking, there are two main methods to open a gap at the Dirac point. These are by magnetic proximity effects and by magnetic doping, shown in Figure 1.7 (a) and (b) respectively. In the magnetic proximity effect, a magnetic insulator (MI) is epitaxially grown on top or below an undoped TI. The magnetic properties then may incorporate in the TI layer via exchange coupling. In the magnetically doped system, transitional metal ions are incorporated inside the TI itself (doping levels ranging from 1% to 40%), which forms a magnetic order and the TI turns into a diluted magnetic semiconductor (DMS). The proximity effect can be further divided into two systems. The first type deals with a magnetic insulator, for instance magnetite (Fe_3O_4) or EuS. In these materials direct coupling between magnetic ions leads to ferromagnetism. The second type deals with a magnetic metal, for example Fe or Co where an uneven number of spin up and down electrons leads to magnetism. These two systems are shown in Figure 1.8 (a) and (b). Transitional metal doping into TIs also involves two mechanisms. These are the RKKY mechanism and the Van Vleck magnetism shown in Figure 1.8 (c) and (d). In case of the RKKY mechanism, neighboring magnetic ions communicate with each other indirectly via free electrons which carry the magnetic information to the next magnetic ion. Hence RKKY magnetism has a direct correlation with the carrier density of the system. The Van Vleck magnetism on the other hand is purely a quantum mechanical second-order perturbation effect which is independent of carrier density or movement of free electrons. Overall, both proximity coupling or transitional metal doping open a bulk gap at the Dirac point. However, ideally speaking the controllability of the electronic states and preservation of the TI crystal structure with the doping method is greatly superior to the proximity effect, leading to the realization of the Quantum anomalous Hall effect in MTIs[24]. The differences between the two systems are summarized in table 1.

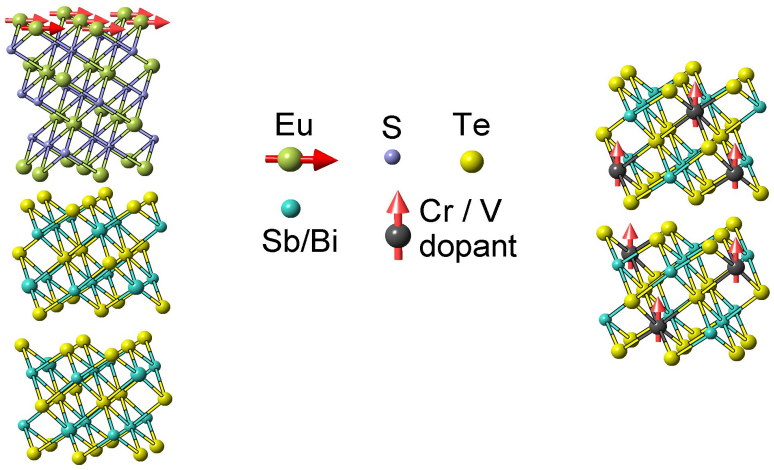

Figure 1.7 (a,b) Two ways to induce magnetism in TIs. (a) the magnetic proximity effect (b) transition metal doping in TIs[38]. Figure adopted from ref. 38 without permission.

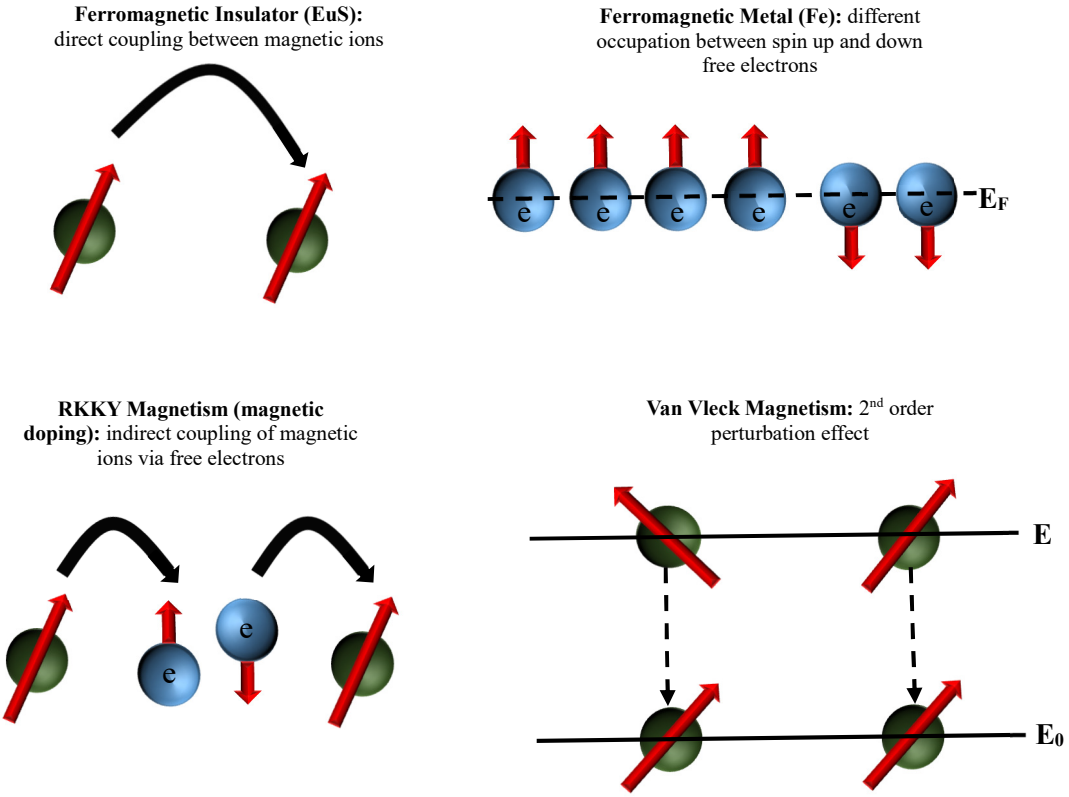

Figure 1.8 Two ways to create an MTI: the magnetic proximity effect and transitional metal doping. (a) in the proximity effect, one magnetic insulator layer (EuS) is in proximity with an undoped TI (b) The using of a ferromagnetic metal (Fe) which has uncompensated spins leading to magnetism. (c) In the transitional method doping, RKKY mechanism can lead to magnetism where magnetic ions couple indirectly via free electrons or (c) the Van Vleck magnetism where magnetism is independent of the carrier density[209]. Figure adopted from ref. 209 without permission.

Table 1.1 shows a comparison between proximity effect coupled TIs and magnetically doped TIs[209].

	Proximity effect	MTI
Curie Temperature T_c	Very Low (20 K)	High (above 200 K)
QAHE realization	Not yet	At 30 mK
Magnetization	Only at the interface	Whole sample
Uniformity	Good	Depends on the doping concentration
Coupling	Exchange-coupling with outermost shell electrons (f electrons)	RKKY/Van Vleck mechanism

Now that a basic overview of TIs is covered, the next section covers some concepts which are very important to understand with regards to magnetotransport phenomena.

1.4 Magnetotransport

Magnetotransport measurements form the key to understanding a materials electrical properties which would eventually lead to a commercialized device such as a transistor. There are various regimes of electrical transport which depend on the sample size L which relates to some special characteristic lengths. One of them is the carrier mean free path l_e. In a disordered classical system, electrons are scattered by impurities or phonons on a typical time scale τ_e, and hence the mean free path defines the distance an electron can propagate between scattering events given by $l_e = v_F \tau_e$ where v_F is the Fermi velocity. Whereas in a quantum mechanical system, an electron may be described as a wave with a Fermi wavelength λ_F, having a phase φ which changes with time τ_φ due to various interactions. Then the resulting phase coherence length $l_\varphi = v_F \tau_\varphi$ is crucial to understand the crossover between quantum mechanical and classical systems, since after a length l_φ any information related to its interference phenomena will be lost. In a strongly disordered classical system, scattering is so strong that the carriers become localized on a certain length scale defined by the localization length ξ. Comparing these length scales to the system size L allows us to classify electrical transport phenomena into various types. These are :

a) **Diffusive classical transport:** When a system undergoes pronounced scattering, the

individual electrons paths can be considered as random walks and hence the charge transport can be described by the Drude model. Here $L, \xi >> l_e \geqslant l_\phi >> \lambda_F$.

b) **Weak localization regime:** The electrons still undergo scattering and are described by a semiclassical picture *i.e.* quantum diffusion. Since the system is semiclassical, the electrons still follow random walks as in the earlier case, but carry an extra phase information which allows for interference. Interference can further lead to back scattering and thus to localization. Here $L, \xi >> l_\varphi \geqslant l_e > \lambda_F$.

c) **Quantum regime for strong localization**: When electrons undergo many scattering events they can get localized around an impurity. The transport in this case can be described by hopping of electrons between localized regions. Here $l_\varphi > \xi \approx l_e \approx \lambda_F$.

d) **Ballistic transport:** When the electrons mean free path becomes larger than the sample size, the system can be described as a waveguide for individual electrons waves with a group velocity v_g. Here $l_e > L$.

e) **Mesoscopic regime:** When the electrons phase coherence length becomes larger than the width of a 2D sample, the system can be treated as a 1D mesoscopic system. Here $l_\varphi > L$. Also comparing the length with the mean free path allows us to define a diffusive ($l_e < L$) and ballistic ($l_e > L$) 1D system.

1.4.1 Diffusive Electrical Transport

The simplest model to describe diffusive electrical transport in metallic systems is the Drude model. It considers an electron moving in the presence of an electric field E, which gets accelerated in the direction of the field with an average drift velocity v_d which can be simply derived from Newtons 2nd law, given by $v_d = \frac{Ee\tau_e}{m^*}$, where τ_e is the mean time between momentum relaxing collision events. Now the current density j which can be derived easily from Ohm's law is given by : $j = n_s e v_d = \sigma E$. Placing the value of v_d in this equation leads to $j = \frac{n_s e^2 \tau_e E}{m^*}$, therefore in the absence of a magnetic field the Drude conductivity becomes: $\sigma_D = \frac{j}{E} = \frac{n_s e^2 \tau_e}{m^*}$. At zero temperature the electron states are filled up to the Fermi energy E_F . All electrons acquire the same drift velocity induced by the applied electric field and the Fermi circle shifts in k-space in the direction of the field. The drift velocity is then defined as $v_d = \mu E$ and so the transport mobility μ_t is given by $\mu_t = \frac{e\tau_t}{m^*}$. These equations form the basics of all the analysis performed on TI samples in the experimental chapters on

electrical transport where $\rho_{xx} = \frac{E_x}{j_x} = \frac{1}{n_s e\mu}$ is used to calculate the mobility of samples.

To further understand diffusive electrical transport, the behaviour of electrons in an external magnetic field needs to be covered. An external magnetic field imports a Lorentz force on the electrons and as the direction of this force is always perpendicular to the direction of propagation of electrons, they are forced into circular orbits between two scattering events with angular frequency ω_c known as the cyclotron frequency given by $\omega_c = \frac{eB}{m^*}$. This leads to the following classical equation of motion: $F = e(\boldsymbol{E} + \boldsymbol{v}_d \times \boldsymbol{B})$. By considering the relaxation caused by scattering as a decay term, the equation for force can be rewritten as: $m^*\dot{\boldsymbol{v}} = -e(\boldsymbol{E} + \boldsymbol{v}_d \times \boldsymbol{B}) - m^*\frac{\boldsymbol{v}_d}{\tau}$. When acceleration is zero *i.e.* taking the stationary case $\dot{\boldsymbol{v}} = 0$, the solution yields: $v_x = -\mu_t E_x - \frac{eB}{m^*}\tau_e v_y$, $v_y = -\mu_t E_y - \frac{eB}{m^*}\tau_e v_x$ and $v_z = -\mu_t E_z$. In a 2 dimensional system, the electrons are confined to a plane and so E_z , the electric field component perpendicular to the plane is zero. Also for a sample in the shape of a Hall bar, the current cannot flow in the *y* direction so v_y is zero. Therefore solving the above equations yields: $\rho_{xx} = \frac{E_x}{j_x} = \frac{1}{n_s e\mu}$ and $\rho_{xy} = \frac{E_y}{j_x} = \frac{B}{n_s e}$. In the *x* direction this is the same equation as obtained from the equation of motion in an electric field. In the *y* direction the presence of magnetic field has caused a voltage to be built across the edge of the sample known as the Hall effect. Using this Hall effect voltage, the carrier density of samples have been calculated in the experimental chapters.

1.4.2 The Shubnikov-de Haas Effect

In the presence of a strong magnetic field and low disorder, the semi-classical description doesn't hold and a quantum mechanical solution is required. As mentioned already, a magnetic field curves the trajectories of electrons. As a consequence, they take circular orbits with a cyclotron frequency $\omega_c = \frac{eB}{m^*}$. If $\omega_c > \frac{1}{\tau_e}$, an electron can complete an orbit before experiencing any scattering. Thus, it can interfere with itself forming a standing wave. This leads to the quantization of energy for different orbits described by a quantum number n_l, where n_l is the Landau quantization. The result is a modified version of the Schrödinger equation taking the magnetic field into account given by: $E = E_z + (n_l + \frac{1}{2})\hbar\omega_c$, where E_z is the energy due to confinement in the *z*-direction. Thus, the energy spectrum of the system consists of discrete Landau levels whose energy is determined by the strength of the external

magnetic field *B* and so the number of states in each Landau level increases as the applied magnetic field increases. At a critical field, the electrons can all be housed in the lower Landau levels and so the Fermi energy drops into the lower Landau level. As the magnetic field is increased the Fermi energy oscillates. From the Einstein Conductivity equation it can be seen that oscillations in the Fermi energy will give rise to oscillations in the conductivity of the device and these oscillations are known as Shubnikov-de Haas oscillations. The standing waves discussed above become discrete and the density of states (DOS) can be described by delta functions located at every *E*. In real samples, carrier scattering events occur, and therefore this discrete density of states broadens showing a Lorentzian-shaped DOS at every E. As mentioned above, to observe oscillations there are two main requirements. Firstly the disorder of the system must be small which will allow completion of the cyclotron orbit without scattering taking place and secondly the temperature must be sufficiently low so that the electrons near the Fermi surface do not cause partial population of the Landau levels.

1.4.3 Magnetoresistance

Magnetoresistance (*MR*) is the change of a material's resistivity with the application of a magnetic field. This is a well-known phenomenon and in 1988, Baibich *et al*. for first time, reported an *MR* of up to 50% at low temperatures in multilayer structures[39]. Magnetic read heads using the *MR* effect have now been successfully fabricated and marketed. There are a few types of *MR* effects which can occur in material systems and these are ordinary, anisotropic, giant and colossal *MR* effects. The ordinary *MR* effects usually occurs in all metallic systems. Classically, the *MR* effect depends on both the strength of the magnetic field and the relative direction of the magnetic field with respect to the current applied at the source and drain of the material. For non-magnetic metals, the *MR* effects at low fields are expected to be very small, and the effect can be very big for high fields. The effect of a weak field $\omega_c\tau \ll 1$ is described according to the Kohler's rule as: $MR \approx (\mu B)^2$. Whereas at high fields, provided that there are open orbits, transport will result in a non-saturating magnetoresistance. According to a model proposed by Parish and Littlewood[40], they calculated the magnetoresistance for semi-conductors and found the $MR \propto \mu B$, thus proving a linear relationship with *MR* and B even at low fields. Nevertheless, the change in resistivity $\Delta\rho$, is positive for both magnetic field parallel and normal to the current direction. Now depending on the structure of the electron orbitals at the Fermi surface, there are two

distinct cases for the ordinary *MR*:

a. When the Fermi surface is closed in metals, the electrons are constrained to their orbits in k space, and an application of the magnetic field in either direction increases the cyclotron frequency of the electrons in their closed orbits. In this case, the resistance saturates at high fields.
b. If the orbits are open at the Fermi surface in metals, a large unsaturated *MR* is observed.

In the case when metals or alloys are doped with ferromagnets, instead of the ordinary *MR* effect, the anisotropic magnetoresistance effect (AMR) is observed. The effect is anisotropic in a way that the resistance increases when the field increases and then decreases with field. The physical origin of the AMR effect lies in spin orbit coupling. Most samples grown and measured in this thesis were magnetically doped and it was important to understand the AMR effect.

As the conduction electrons are passing through the lattice, they experience scattering events which result from the slight deformation of the electron cloud about each nucleus as the direction of the magnetization rotates. In other words, the closed orbit orientation rotates when the direction of the magnetization rotates. If the external field and magnetization of the sample are oriented parallel to the current direction, then the electronic orbits are perpendicular to the current and the cross-section for scattering increases giving a high resistance state, whereas if the field and magnetization are oriented perpendicular to the current direction, then the electron orbits are in the plane of the current leading of lesser scattering events and a low resistance state. This is shown in the Figure 1.9 (a and b).

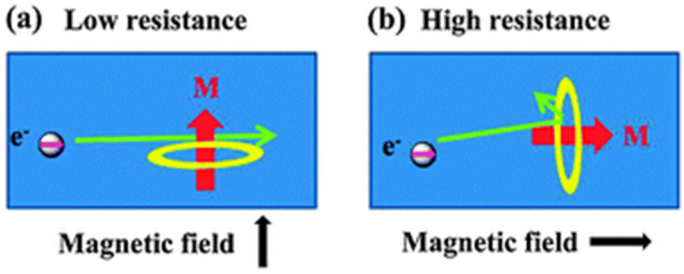

Figure 1.9 The AMR effect and its physical origin. (a) when the field is perpendicular to the direction of the current and (b) when the external field is parallel to the current direction[41]. Figure reproduced from ref. 41 without permission.

1.4.4 Diffusive Quantum Transport

In a diffusive system, the mean free path l_e of an electron is small compared to the size of the system L. Thus, scattering events dominate the electrons motion, equivalent to a random walk. In the previous section, electrons were treated as classical particles which only interact by scattering. If, by contrast, the phase coherence length l_φ of the electrons becomes adequately long, they will keep their quantum phase information over many scattering events. This can lead to interesting interference phenomena such as localization effects. In the case of weak localization, imagine an electron that is scattered such that it follows a closed path after covering many short paths between scattering centres. This is possible if the scattering events originate from impurities and are elastic, which conserves the phase of the electron after each scatter event. However, interference may occur if the electrons travelling around the loop clockwise are equal to those travelling anticlockwise (the paths are time reversed). This interaction of clockwise and anticlockwise electrons in a closed loop causes constructive interference leading to an additional resistance compared to the classical case. This increase in resistance in the presence of zero magnetic field is known as weak localization. Now, if a magnetic field is applied, the closed loop also encloses a magnetic flux and there is a phase difference between the two paths. The clockwise path electrons therefore have a different phase relative to the anticlockwise electrons which leads to breaking of symmetry and the interference is reduced. This manifests itself as a decrease in the resistance with increasing magnetic field.

In materials with strong spin-orbit coupling (SOC), upon getting scattered along a closed path, the spin of the electron will be slightly rotated between every scattering event. If the spin-orbit time of the system, *i.e.* the typical time required to randomize the spin orientation due to SOC, is very small the spin of the electron will be completely randomized after performing the closed loop. By comparison, the spin of the electron taking the time-reversed path has experienced the opposite rotation. This leads to destructive interference between time-reversed paths and a decrease in the resistance is observed at zero field. Like for weak localization, this effect is destroyed on application of an external magnetic field[42]. An analytical expression to describe localization in 2D diffusive systems has been derived by Hikami, Larkin and Nagaoka (HLN) given by[43]:

$$\Delta\sigma_{xx}^{2D} \equiv \sigma_{xx}^{2D}(B) - \sigma_{xx}^{2D}(0) = \alpha \frac{e^2}{2\pi^2 \hbar}\left[ln\left(\frac{\hbar}{4eBL_{\varphi}^2}\right) - \Psi\left(\frac{1}{2} + \frac{\hbar}{4eBL_{\varphi}^2}\right)\right]$$

Where where $\Delta\sigma_{xx}^{2D}$ indicates the normalized 2D sheet conductivity, B is the magnetic field perpendicular to the plane of the film, e is the electronic charge, $\hbar$ is the reduced Planck constant, Ψ is the digamma function, α is the number of topological surface modes (TSM) and L_{φ} is the phase coherence length. This formula has been used in experimental chapter 5 to determine the phase coherence length in TI samples.

1.5 Anomalous Hall Effect

The anomalous hall effect phenomenon was experimentally discovered in 1881 by E.H. Hall; it took over 100 years to understand the microscopic mechanism of the origin of this effect. During the beginning it was found that the AHE was a special general effect that depended on the spin-orbit interaction of a material. The effect was later known as the spin Hall effect. While the spin Hall and the anomalous Hall effects were known for many years, the interest to study these further in TIs has only increased in the last decade. Before the AHE is discussed in detail, the table below shows a timeline of all the Hall effects discovered to date. This gives an idea of the timescales on which the field of condensed matter physics has progressed. As can be noticed from the table, it has taken over 130 years to progress from the AHE to the QAHE.

Table 1.2 showing the timeline of the discovery of Hall effects.

Hall Effect (1879)	Spin Hall Effect (1889)	Anomalous Hall Effect (1881)
Quantum Hall Effect (1980)	Quantum Spin Hall Effect (2006)	Quantum Anomalous Hall Effect (2013)

In a conductive ferromagnetic material, the spin orbit effects give rise to the AHE. A ferromagnet contains an unequal number of spin up and spin down electrons. Now when a

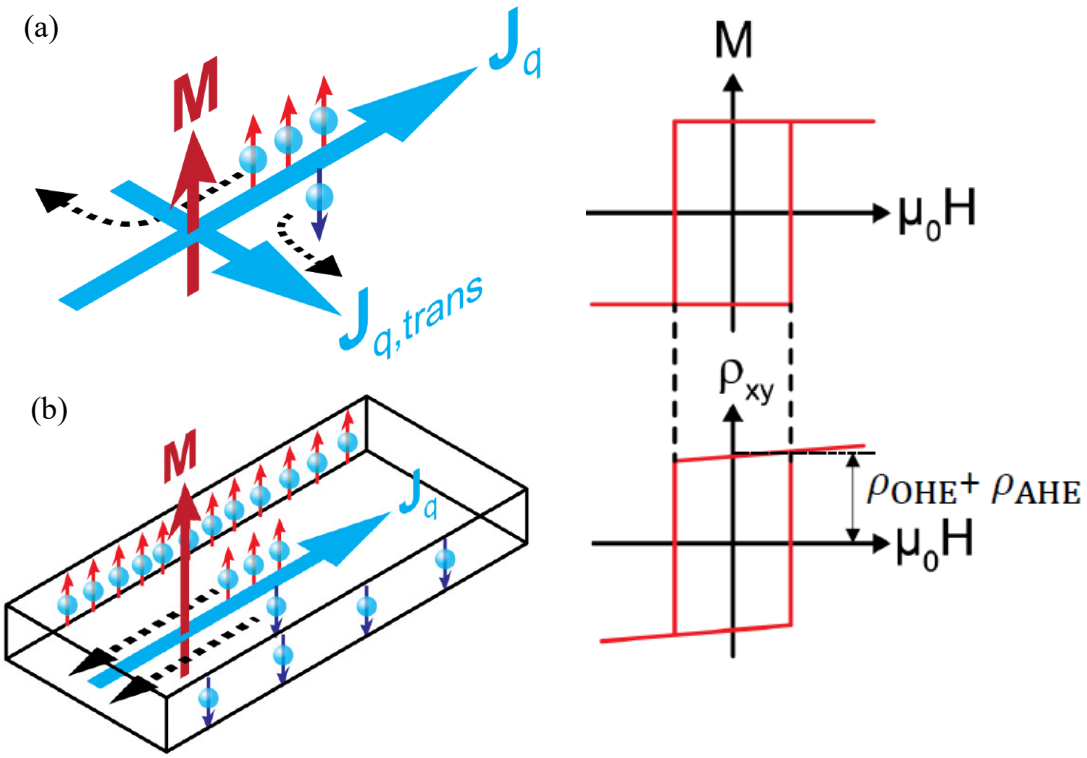

Figure 1.10 Anomalous Hall effect in a conductive ferromagnet. (a) spin dependent scattering and an even number of spin-up and spin-down electrons leads to a transverse charge current flow. (b) a charge and spin accumulation forms at the transverse side of the sample[44]. Figure reproduced from ref. 44 without permission.

perpendicular external magnetic field is applied, due to unequal number of spin up and spin down electrons there will not only be a charge current as expected in the ordinary Hall effect, but also a spin current generated in the transverse direction as illustrated in Figure 1.10 (a). A typical experimental geometry for measuring the AHE is shown in Figure 1.10 (b). A charge current density j_q is applied to a rectangular shaped ferromagnetic sample, while an external magnetic field is applied in the perpendicular direction producing a magnetization M in the sample also pointing perpendicular to j_q. Now depending on the boundary conditions imposed on the sample, the AHE can manifest itself as a contribution to the longitudinal conductivity (resistivity). An electric field along y will be generated (measured as a voltage difference between the sample edges) if open circuit boundary conditions are imposed along y, leading to a charge and spin accumulation at the boundaries in the y direction. The resistivity in the y direction can then be defined as a combination of the ordinary Hall effect (which depends on the external field) as well as an anomalous Hall resistivity term (which depends on the Magnetization of the sample) given by: $\rho_{xy} =$

$R_{OHE}\mu_0 H + R_{AHE}\mu_0 M = \rho_{OHE} + \rho_{AHE}$. As discussed in the beginning of this section, the origin of the AHE lies in spin orbit interaction and can be further divided into three distinct mechanisms. These mechanisms can be classified into intrinsic effects, that happen in between scattering events, and extrinsic effects, that occur during scattering events[44]. In the case of extrinsic effects, one further distinguishes between skew scattering and side-jump scattering. The basic idea of spin skew scattering is illustrated in Figure 1.11(a). Due to strong spin-orbit coupling, an electric field gradient is generated in the scattering plane. This gradient can cause a force on the spin orientation towards or away from a scattering center which leads to a spin dependent trajectory of the atom beams. The anomalous Hall conductivity σ_{xy}^{A} is independent of impurities and scales linearly with the longitudinal conductivity σ_{xx} of the material. The side jump mechanism is shown in Figure 1.11 (b). Due to a spin-dependent acceleration and deceleration during a scattering event, an effective displacement of the electron occurs. Side-jump scattering can mostly be neglected compared to skew scattering and intrinsic effects. In this case the anomalous Hall conductivity σ_{xy}^{A} is independent of the longitudinal conductivity σ_{xx} of the material. The intrinsic mechanism arises from the spin-orbit coupling effect [Figure 1.11 (c)] and depends on the band structure and is independent of scattering. These three mechanisms lead to the AHE.

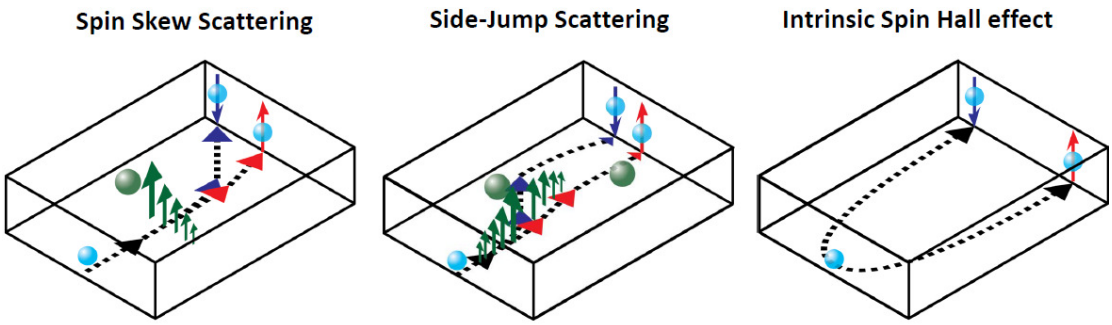

Figure 1.11 Showing the different mechanisms contributing to transverse spin-dependent velocity. (a) spin skew scattering (b) side jump scattering (c) intrinsic spin hall effect[44]. Figure reproduced from ref. 44 without permission.

2. Chapter 2

Experimental Techniques

A few techniques have been used during the duration of the research work presented in this dissertation. The focus of the work centers mainly on thin film growth of TIs using MBE followed by device fabrication and electrical cryogenic transport measurements. The samples used to complete the thesis work were characterized using a variety of lab based analysis tools such as x-ray diffraction/reflectivity (XRD/XRR), x-ray photoelectron spectroscopy (XPS) and superconducting quantum interference device magnetometry (SQUID). Various facilities were used in Oxford and Cambridge to characterize and grow all the samples. In this chapter, a brief overview of the practical knowledge of the experimental techniques used will be provided.

2.1 Molecular Beam Epitaxy

MBE has been a central technique for growth of high quality TIs since they were experimentally discovered in 2008. MBE portrays its dominance over other growth techniques by its very fine control of elemental source temperatures along with precision in controlling the substrate conditions and therefore the beam fluxes. It establishes itself as a non-equilibrium growth technique uniquely different from other methods allowing the growth of single crystal thin films at low substrate temperatures. The cells in the system which contain the elemental sources are heated independently producing molecular beams which are considered non-interacting in the gas phase. This ensures the thin film growth only occurs on the substrate where the surface reactions can take place. So by controlling the substrate temperature, fine control over the deposition conditions and surface reactions are allowed. Another major advantage of using MBE is to incorporate dopants of high concentration by exploiting its non-interacting nature which prevents the formation of secondary phases. These facts form the main justification for the use of MBE as a growth tool for the investigation of transition metal doped TIs.

2.1.1 An MBE System

MBE is an ultra-high vacuum (UHV) technique. UHV conditions are generally accepted when the base pressure in the system is in the range of 8×10^{-8} - 8×10^{-13} Torr. From a thermodynamic point of view, UHV conditions can be demonstrated by the mean free path of a single molecule in an ideal gas which is given by: $\lambda = \frac{RT}{\sqrt{2}\pi d^2 N_A P}$, where R is the Rydberg gas constant, *T* is the temperature, *d* is the diameter of the gas molecule, N_A is the Avogadro number and *P* the gas pressure. The MBE system which was used by me at the University of Oxford had a base pressure ~ 1×10^{-10} Torr, which for a diatomic nitrogen molecule at room temperature gives a mean free path of $\lambda = 690$ km. This number is many orders of magnitude higher than the dimensions of any chamber, therefore we can assume that any given molecule of gas may travel inside the chamber as if it was a perfect vacuum. This also suggests that the molecular beams themselves lack gas phase reactions, hence permitting the epitaxial deposition of the correct material in a pure environment, though this does not guarantee secondary phase formation. Atomic layers grown by MBE may have a typical deposition rate of ~1 nm/min.

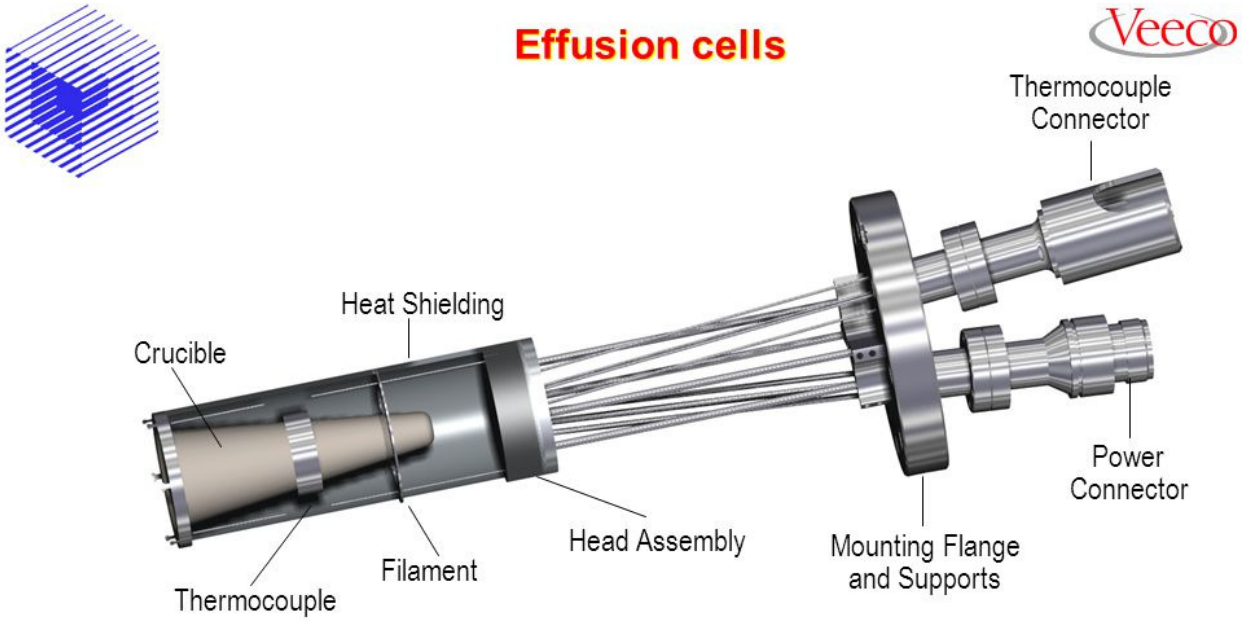

Figure 2.1 A picture of a standard effusion cell. The cell consists of a crucible, heating wires, a thermocouple and heat shields. NOTE: thermocouple and filament not shown in figure. The diagram was taken from Veeco Instruments Inc[45]. Figure reproduced from ref. 45 without permission.

A very slow rate is chosen so that the least amount of impurities are incorporated in the thin film while growing. In this thesis, pure elemental source materials (purity 5N and 6N grade) in the form of pellets, grindings and tiny pieces were used inside standard effusion (Knudsen) cells. An effusion cell consists of source material placed inside a conical shaped non-reactive crucible (usually made out of boron nitride or alumina), with a wound filament used for the purpose of heat shielding made from refractory metal (W or Ta) as shown in Figure 2.1. A thermocouple is placed surrounding the crucible material and is connected to a Eurotherm temperature controller which can vary the power applied across the cell. Ta metal is usually used as a heat shield which surrounds the cell to avoid any losses in the form of heat and from neighboring hot cells. Most conventional MBE systems have their effusion cells cooled with a closed water loop system for thermal stability, though the cells in the Oxford chamber used by me were only cooled with a continuous liquid Nitrogen flow through the cryo-shield. Effusion cells involve heating a source material placed inside the crucible by a wire surrounding the crucible which is very resistive. This causes the source to evaporate or sublimate into a gas phase with some kinetic energy outwards away from the cell. It is assumed that within the crucible, the vapor phase and the solid/liquid phase are in equilibrium. The behaviour of the delivered flux of material can then be well understood as, being dependent mainly on the temperature of the cell and also two other characteristic temperatures. These two temperatures are characteristic of two different thermodynamic processes. The evaporation of the elemental source into the gas phase and the temperature at which the departure of the gas phase takes place at the aperture of the cell. The crucible, for this reason, is wide at the top, hence the flux is dominated only by the evaporation of the material.

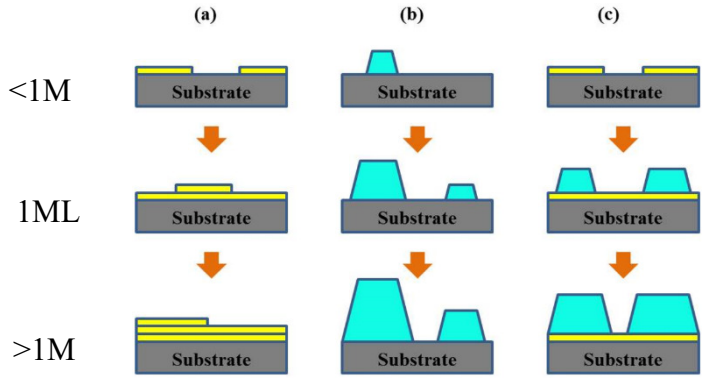

Figure 2.2 Growth modes of thin films as a function of layer thickness. (a)Frank van der Merwe, layer-by-layer growth. (b) Volmer-Weber growth, 3D islands and (c) Stranski-Krastanov, a wetting layer followed by island growth[46]. Figure reproduced from ref. 46.

The calibration of each cell with their linear fittings are shown in section 3.3. Epitaxial growth may occur in various forms where a monolayer which sticks at the substrate may set differently. In a perfect MBE growth, one full monolayer is deposited first onto the substrate material followed by the growth of the next layer on top of the first, fully covering the first such as the one described by Frank-van der Merwe growth mode. Usually, this is not always the case. Some other type of growth modes are shown in the Figure 2.2. The different types of growth modes can be found in this reference book[46]. In simple terms, the mode in which a film grows depends upon the chemical potential of the deposited film and it is possible to distinguish between the modes using reflection high-energy electron diffraction (RHEED) during the growth process discussed in section 2.1.2.

The MBE system used by me in this thesis work was the machine in Thorsten Hesjedal's Group at the University of Oxford. The MBE system consists of three chambers: the load lock system, the preparation chamber and the main growth chamber. The load lock as the name suggests is used for loading of substrate materials and removal of the already grown samples. It could hold up-to four samples of 2 inches in diameters on their sample holders at one time. The samples were clipped onto Riber style sample holders which were 1/4 of a 2 inch circle wafer holder, as shown in Figure 2.3.

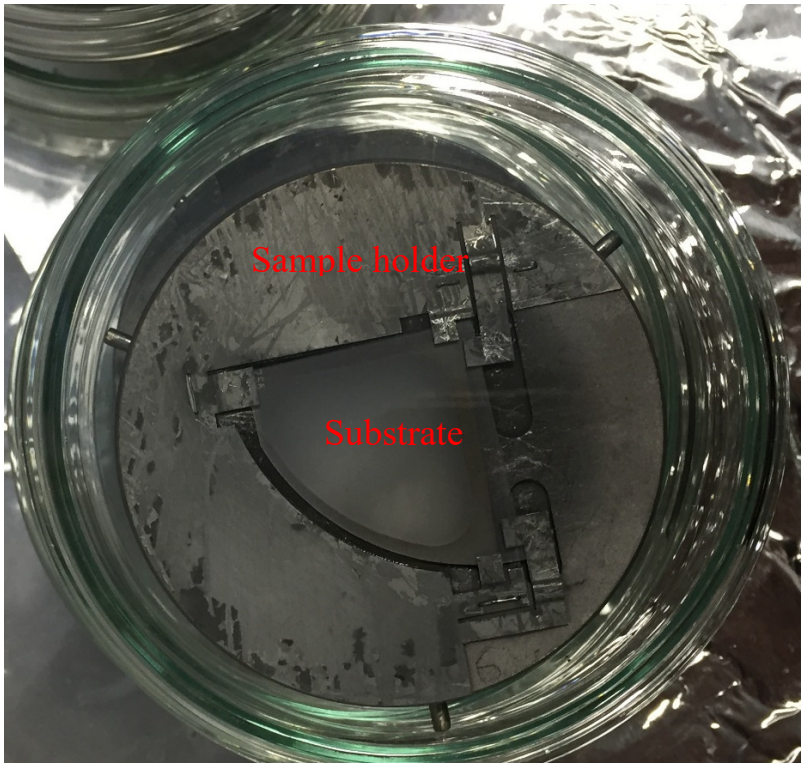

Figure 2.3 Riber type sample holder of size ¼ of 2 inch wafer. The ¼ inch sapphire substrate placed in the center held with clamps.

The load lock was pumped by an Edwards nEXT 400D turbomolecular pump backed by a scroll pump. After loading four substrates into the load lock, the load lock was pumped to UHV conditions. The typical pressure of 3×10^{-9} Torr may be achieved. The Load lock chamber contains a 1 kW heating lamp which was used to bake the chamber from inside under UHV conditions. This procedure helps to remove any residue water vapor left on the substrates during ex-situ substrate cleaning, the procedure of which is described in more detail in Section 3.3. The substrates were usually baked for about 8 hours before they were transferred into the Preparation chamber using an in-situ arm through a manual gate valve. The preparation chamber also had a capacity of holding four samples. It was pumped using an ion pump and reached a typical base pressure of $\sim 8 \times 10^{-11}$ Torr.

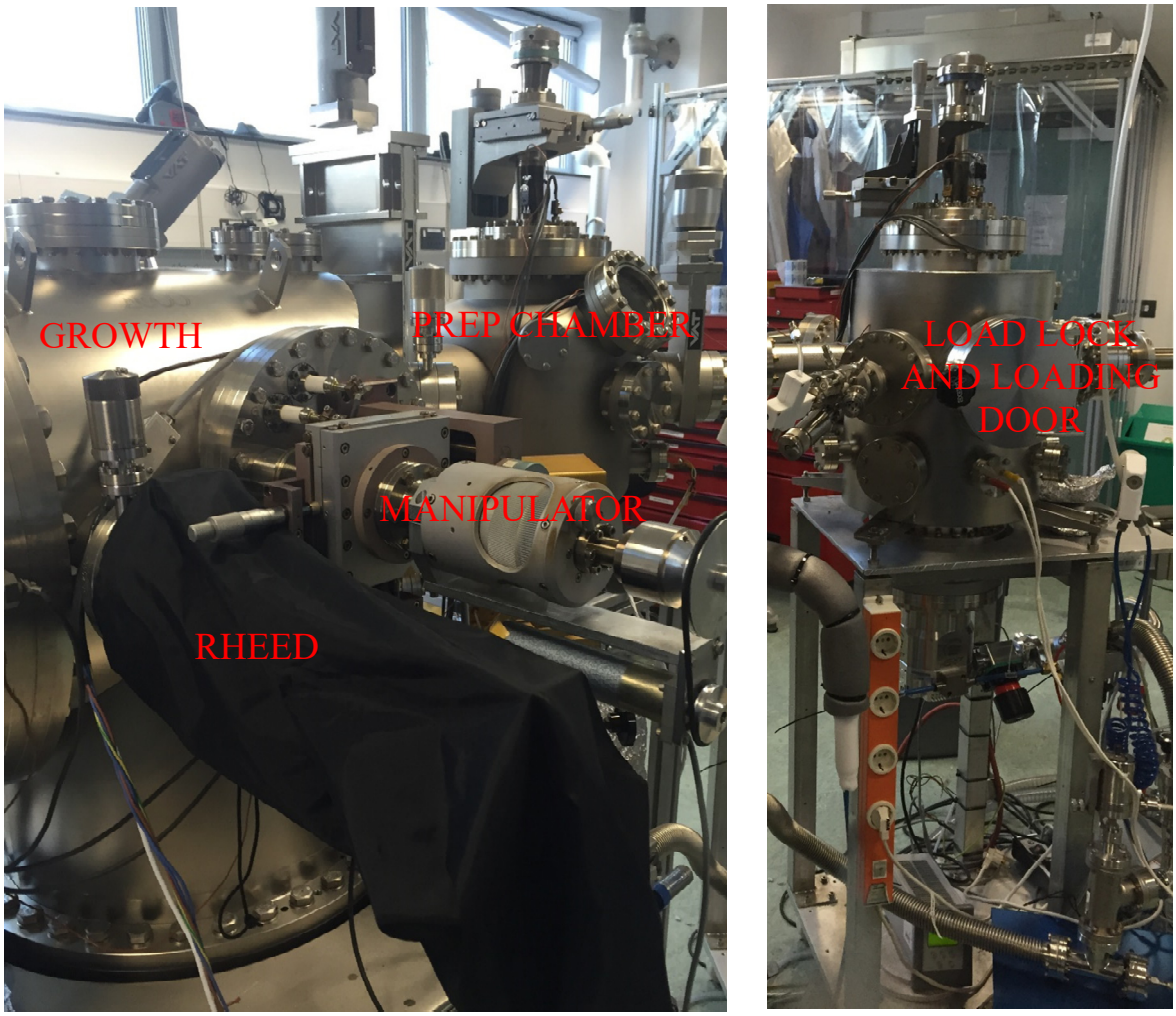

Figure 2.4 A picture of the Oxford MBE system used to grow films with different parts labelled.

Presently the preparation chamber was only used as a buffer chamber between the load lock and the main growth system. This is so that a pure environment is maintained inside the growth chamber. One sample at a time could be moved into the growth chamber onto the manipulator arm which could hold one sample inside the main chamber. The growth chamber was pumped through various mechanisms to account for the high vapor pressures produced from elemental sources. A Leybold magnetic levitation turbomolecular pump was used which had a documented pumping rate of 1500 l/s for nitrogen gas. A small Pfeiffer mechanical turbo and a scroll pump were used as backing pumps for the big turbo. The chamber was also concurrently pumped by a gamma Vacuum ion pump. To help the pumping further, during growth, when the effusion cells are hot, a cryo-pumping effect is achieved by pouring liquid nitrogen in the cryo-shroud. This cryo-shroud helps both in pumping and thermal stability of the cells. For example it was possible to have an Effusion cell at 1100°C in close vicinity to a cell at 100°C with very good thermal isolation. Another pumping method available was a titanium sublimation pump. In this method, a titanium filament was used to coat the walls of the pump with Ti.

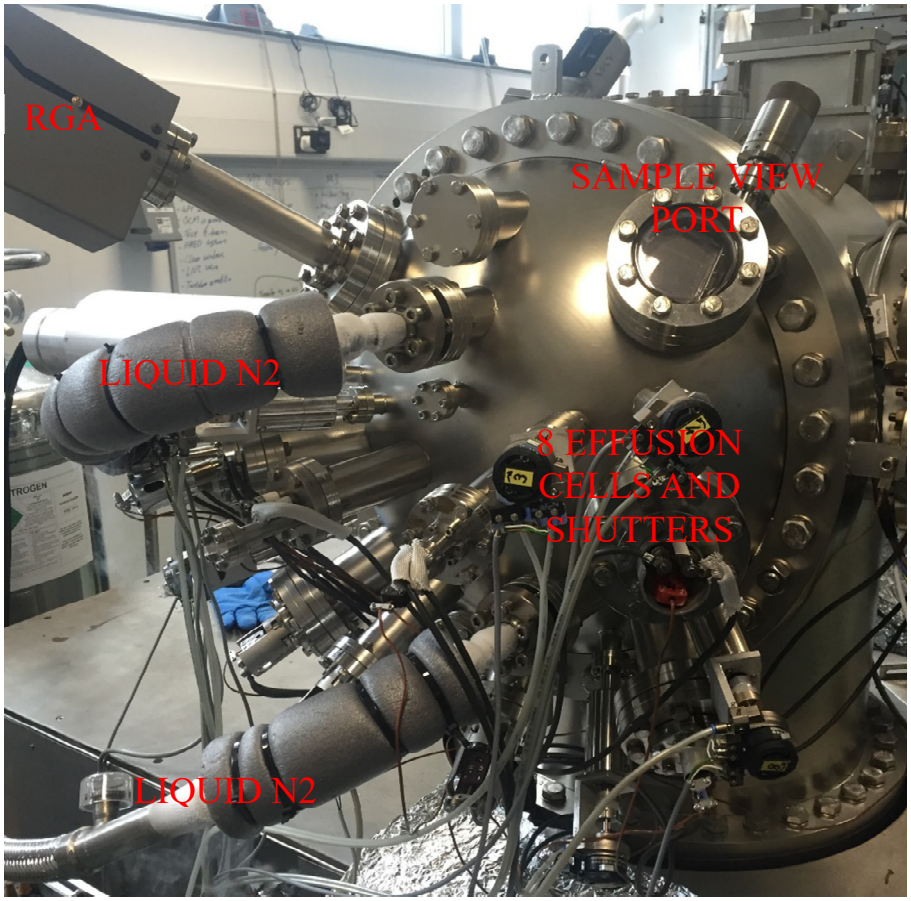

Figure 2.5 Picture of the front view of the main chamber showing the different parts labelled.

Since Ti reacts very easily with oxygen, most contaminants mainly water can easily be removed. Usually the pump was only used when the effusion cells were degassed or used for the first time with a new source material. The chamber included 8 effusion cells. The times when I was in Oxford, the cells consisted of four base elements of the chalcogenide TIs which were Sb, Bi, Se, Te and two transition metals Cr and V. The cells for Cr and V were not standard effusion cells but high temperature cells. All the source elements were heated in their respective cells one at a time usually at the start of the day and the corresponding beam- fluxes were measured using a beam flux monitor placed on the manipulator. The manipulator also consisted of a rotating stage on which the substrate could be placed and a filament heater underneath to heat the substrate during growth up to 850°C. A detailed account of the calibration of cells and substrate preparation is described in the MBE experiment chapter. The growth procedure could also be monitored using a real time RHEED system. A mass spectrometer (SRS RGA 300) was also attached to the chamber to measure the rest gas of the system. This was used to identify sources of possible contaminations inside the chamber.

2.1.2 In-Situ Probes

There were three main *in-situ* probes attached on the MBE main chamber. There were a beam flux monitor attached on the manipulator, a RHEED gun and a residual gas analyzer (RGA). Here a basic description of the RHEED is explained. It is an electron diffraction technique employed to gain qualitative and quantitative data about the surface of the substrate and the growing film on top in real time. From the images obtained, one may acquire knowledge related to surface reconstruction, surface cleanliness, in-plane lattice constants, smoothness/roughness and growth modes[47]. A filament is heated which leads to a thermal emission of electrons. These electrons are accelerated up to an energy of 10-30 keV by an acceleration field focused by a magnetic lens. The high energy electrons then bombard the sample at a very shallow angle (~1-5°) after which the diffracted electrons hit a phosphorous screen. These electrons form a pattern which can be recorded with a camera. A schematic of the geometry used for RHEED is shown in Figure 2.7. The use of grazing incidence angles bombarding the sample and the highly interacting nature of electrons as a diffraction probe means that the incident electrons only penetrate the first few nanometers of the film surface. So from the perspective of diffracting electrons the film surface represents a two-dimensional grating since the lattice spacing in the direction of the surface

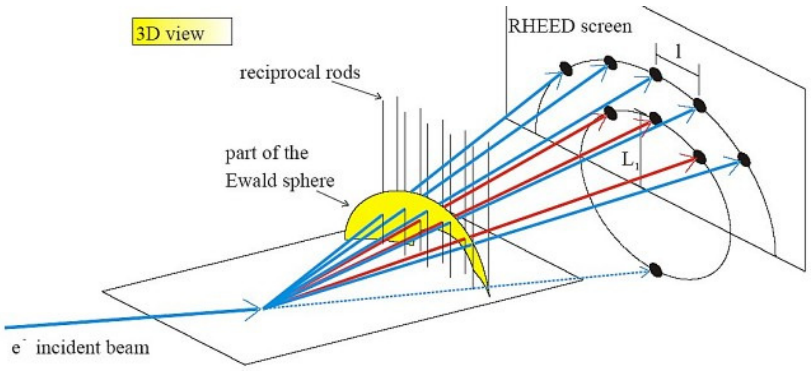

Figure 2.6 Schematic of the RHEED setup used inside the MBE chamber. An incident beam of electrons bombards the sample and then diffracts onto a phosphorus screen. The diffraction occurs at points where the Ewald sphere intersects with the reciprocal lattice[48]. Figure reproduced from ref. 48 without permission.

normal is effectively zero. The diffraction pattern by RHEED on the screen can be understood by using a Ewald sphere[49]. A periodic 2D surface is assumed to be a series of lattice rods in momentum space as shown in Figure 2.6. The diffraction will only take place wherever the Ewald sphere intersects with the reciprocal lattice rods. In real space, spots are observed at the places where the Ewald sphere intersects the rods. Qualitatively, knowledge related to the film morphology can be acquired from studying the RHEED pattern, making it a highly valuable tool for quick understanding of the growth process in real time. For instance RHEED streaks give in-plane lattice spacings with significant error bar (in absolute values). The different possible RHEED patterns are shown in Figure 2.7. In brief, for a perfect 2D single crystal, stripes are seen. If the surface is dominated by 3D islands (if they are small enough), transmission spots are seen, *i.e.* reciprocal lattice vectors are defined in all 3 directions. If the films were growing in a polycrystalline way then the lattice rods get smeared out across the screen and instead rings are seen (not shown here). This is because the non-perfect crystallinity cause the reciprocal lattice rods to have a finite width which results in broadening of the RHEED streaks. Quantitative information about the film structure may also be obtained from studying the RHEED pattern. For example the spacing of the RHEED streaks D can be linked to the lattice spacing d using the following formula: $D = \frac{\lambda L}{d}$, where λ is the wavelength of incoming electrons and L is the distance from the sample to the screen. In practice, the same information can also be obtained from x-ray diffraction which was the method used in this thesis to calculate the spacing. More useful information about the film can also be gained by recording the intensity of the reflection from RHEED as a function of time.

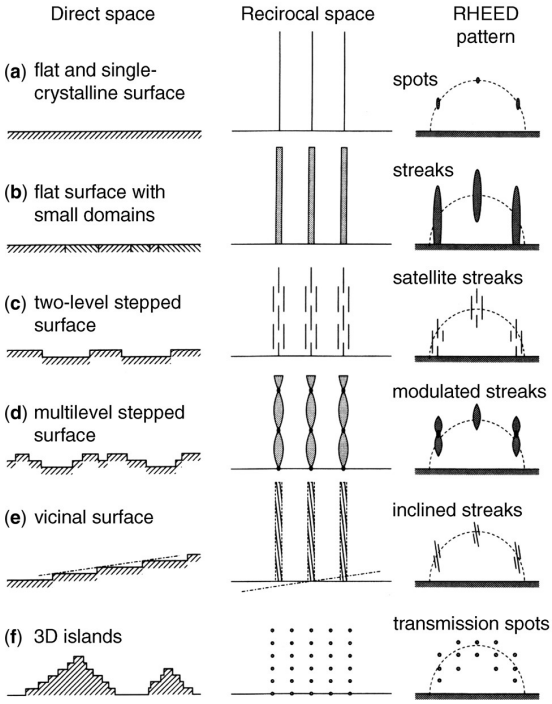

Figure 2.7 The commonly observed RHEED patterns showing (a) an ideal smooth surface intersecting the Ewald sphere. (b) A real smooth surface intersecting along a finite length. (c,d,e) a flat, stepped, multilevel and vicinal growth (f) Diffraction through 3D clusters[47]. Figure reproduced from ref. 47 without permission.

As a film is growing, the intensity of the RHEED pattern oscillates with time. These oscillations occur as a function of the filling factor of the surface layer as shown in Figure 2.8. It is usually considered that a maximum in reflection occurs for a smooth surface having a fully filled layer while a minimum occurs for a completely rough surface. By measuring these oscillations as a function of time, a picture in terms of monolayers (or quintuple layers here) grown per unit time may be obtained. If information about the lattice constants and film orientation is already known then this may be easily converted to a growth rate in nm/min.

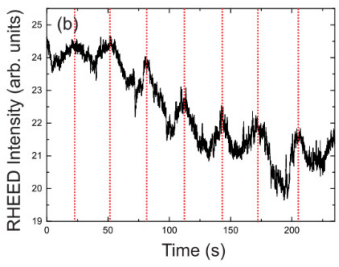

Figure 2.8 Measured RHEED oscillations for a thin film of Bi_2Te_3 showing a growth rate of ~2QL per minute. The red lines show the completion of each QL[50]. Figure reproduced from ref. 50 without permission.

An example of RHEED oscillations obtained using the MBE is shown in Fig. 2.8. The distance between each of the red dash lines shows the completion of one quintuple layer growth. From this the growth rate can be estimated. Experiments on TIs have shown that real time exposure of RHEED has a significantly harmful effect on the structural development of the grown film, seen visibly as a dark patch (‘burnt) on the sample surface. This is the reason why RHEED oscillations are generally not used on TIs to determine its thickness and growth rate instead this information is obtained ex-situ by x-ray reflectivity.
Another in-situ system fitted on the MBE system was an RGA. Measurement of the residual gas by mass spectrometry gives useful information about the rest gas of the system and is predominantly used to identify sources of contamination though it was not used by me in the thesis.

2.2 Structural Characterization

The first step for any thin film which was grown in the MBE machine was to get characterized. The results from the characterizations formed the bases for the next growth recipe *i.e.* the results were used as a qualitative feedback to know what to grow next. X-ray diffraction and reflectivity, used as characterization tools, form a fast feedback to improve the quality of the films before they can be used for other detailed studies, for example electrical transport devices.

2.2.1 X-Ray Studies

XRD and XRR were the main methods employed to characterize the quality of the thin films. XRD is a powerful tool which can give information about the crystal phase, stoichiometry and lattice constants. The principle of the setup is based on Braggs law, the theory of which can be found in many undergraduate physic text books[51]. If the incident x-rays of wavelength λ strikes a crystal, where all atoms are placed in a regular periodic array with interplanar spacing d, diffraction beams of sufficient intensity are detected only when the “Bragg condition” or “Bragg law” is satisfied (shown in Figure 2.10) given by $2d\ sin\theta = n\lambda$. Here, n the order of reflection and is equal to the number of wavelengths(λ = 1.54 Å) in the path difference between diffracted x-rays from adjacent crystal planes and θ is the angle at which diffraction occurs. XRD measurements are a must for crystallography and condensed matter physics, also providing clear information regarding the crystallographic properties of the probed matter for instance the out-of-plane lattice spacing to five significant figures.

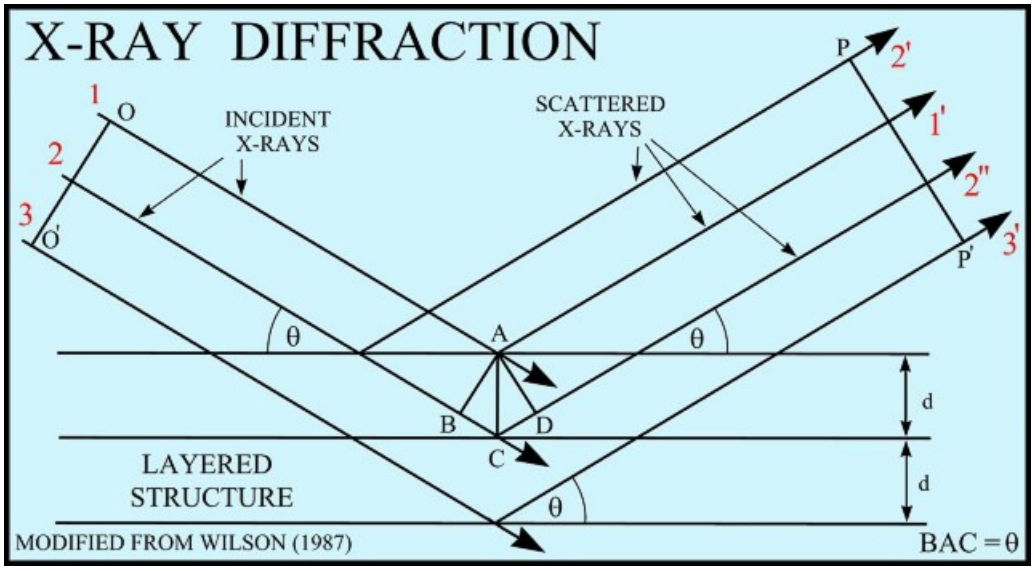

Figure 2.9 Schematic diagram of diffraction of x-rays by a crystal (Bragg condition)[52]. Figure reproduced from ref. 52 without permission.

TIs have a rhombohedral space group where the *d* lattice spacing is related to the lattice parameters by[51]: $\frac{1}{d^2} = \frac{4}{3}\left(\frac{h^2+hk+k^2}{a^2} + \frac{l^2}{c^2}\right)$, where *h*, *k* and *l* are the Miller indices of the relevant reflection while *a* and *c* are the crystal axis lattice parameters. XRD of thin films in this work were measured for a purely out of place diffraction geometry meaning the measurements were taken along the 00*l* set of lattice planes. It was possible to extract the desired *c* lattice constant by gaussian fits of the XRD peaks shown in the experimental MBE chapter 3.

XRR measurements are recorded as a result of reflections at the surface and interfaces due to different scattering length densities of the layers. Well defined layer structures typically produce an oscillatory response in XRR if the SLD differences are large enough. These oscillations provide information regarding inhomogeneities perpendicular to the sample surface for example densities of each layer and thicknesses of each layer in a multilayer stack. The measurements are fed into a software which builds an appropriate model of the system using iterative regression techniques to match a simulated pattern to the measured pattern. Figure 2.10 shows an example XRR scan and the physical properties which can be extracted by looking at the measurements. The most important feature to look at is the period of oscillation which depends on the thickness *d* of the film. Then the critical angle and oscillation amplitude provide information about the densities of the substrate/film and the surface/interface roughness respectively[53].

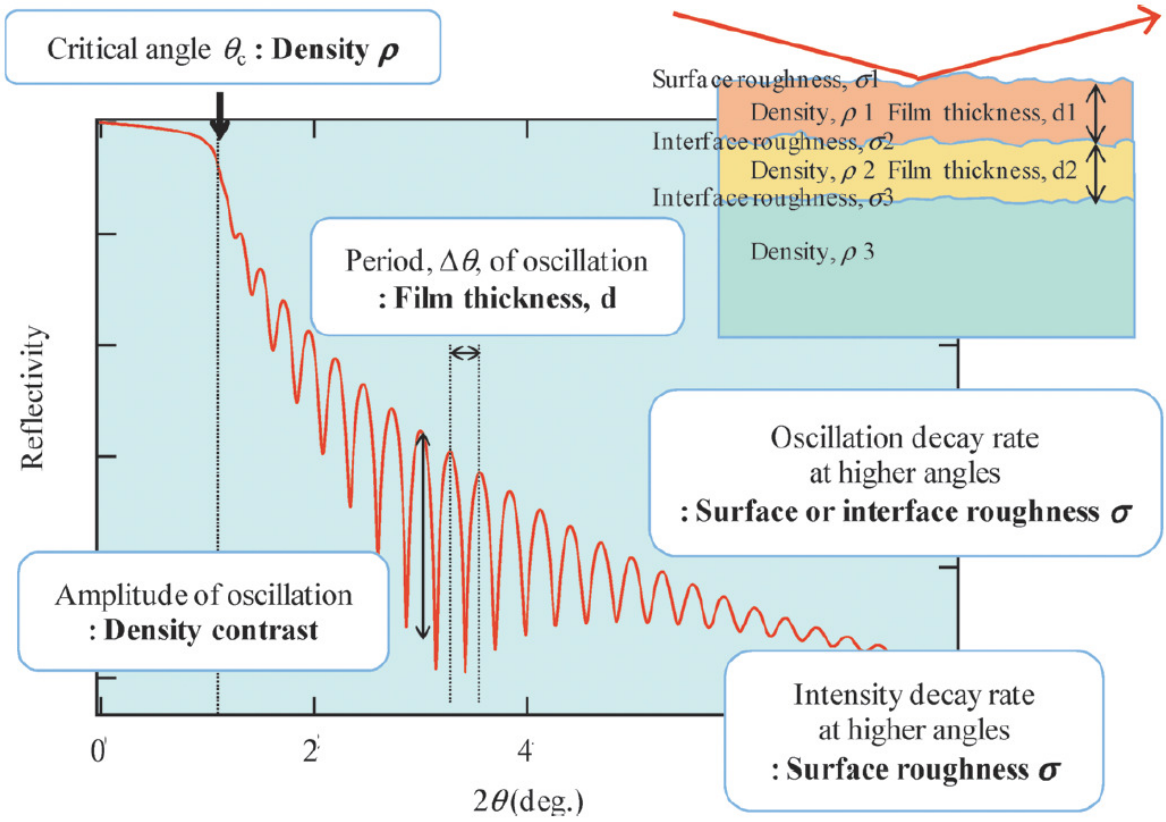

Figure 2.10 Information provided by an XRR profile[53]. Figure reproduced from ref. 53 without permission.

2.2.2 Doping Concentration Studies

Although XRD is an great technique to determine the crystal phase, stoichiometry and quality, it provides limited information regarding the doping levels/concentrations of individual elements in an alloy, specially magnetic dopants where the concentrations are very low. The determination method used for the films in this thesis, unless specified otherwise, was XPS. A much simpler method to determine doping concentration is to use the beam flux monitor, this method makes some assumptions. For example to determine the nominal doping concentration of a transition metal (TM) doped TI, a simple approximation would say that, for substitutional doping on the group V site, the doping concentration *x*, (in $TM_xSb_{2-x}Te_3$) scales proportionally with the TM: Sb flux ratio measured by the beam flux monitor. Substitution of a TM onto a Sb site may not always be the case, hence it is best to determine the concentrations using XPS. XPS is a simple analysis tool which uses x-rays in a UHV condition to determine the composition and chemical state of compounds. It is based on two simple processes that result from the interaction between x-rays and core electrons of the elements.

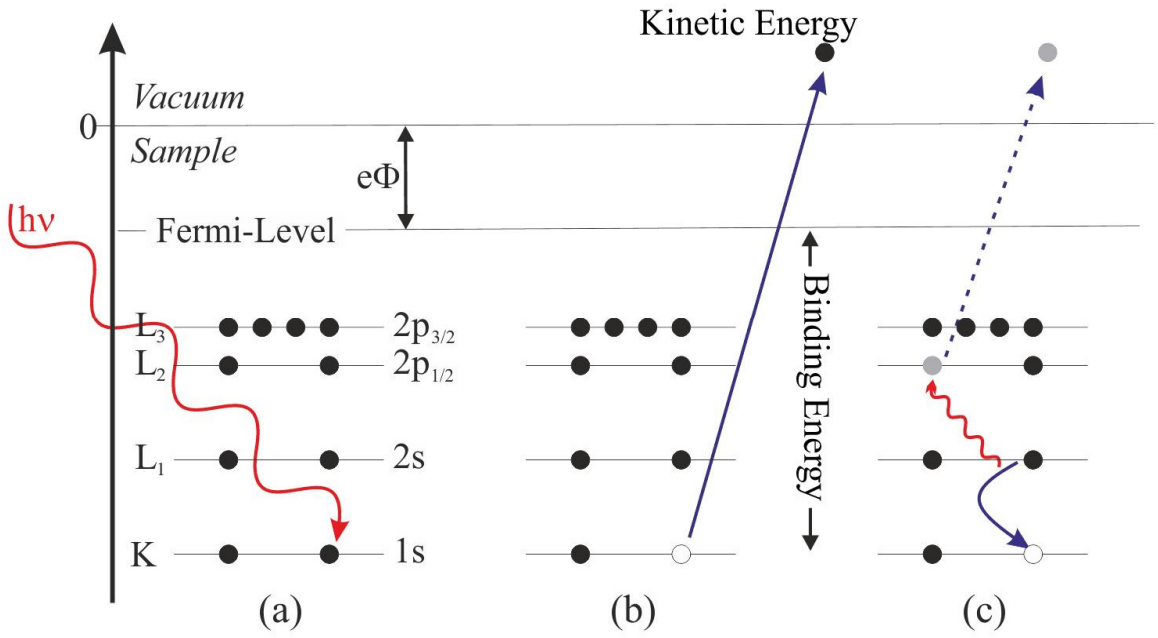

Figure 2.11 Principle of photoelectron emission and the Auger relaxation effect.[54] Figure reproduced from ref. 54 without permission.

Figure 2.11(a) displays an incident x-ray (in red) colliding with a core electron which causes the core electron to be ejected from the innermost electronic shell. The electron which is released [Figure 2.11(b)] has a certain kinetic energy (KE) which is directly related to the binding energy (BE) of the electron of the atom. The ejection of the core electron leads to another second process. A hole is left behind which is unstable. So an electron from the valence shell falls down to fill the hole. This causes an Auger electron [Figure 2.11(c) in red] to be emitted from the valence shell to conserve energy. Again, the KE of the emitted electron is directly related to the BE of the electron to the atom. These two processes are used to identify the elements of the compound since the BE of the electrons are unique to each element. A detector is used to collect the intensity of the electrons released (KE) and hence the BE can be calculated if the wavelength of the incident x-rays is known given by[55]: $BE = h\nu - KE - \varphi_{spec} + \psi$, where ν is the frequency of the x-ray and φ_{spec} is a correction factor that is unique to the spectrometer and ψ is the work function of the sample. The XPS system used in this thesis was in the optoelectronics group and was measured using a Kα (Thermo Fisher Scientific) x-ray photoelectron spectrometer, equipped with a monochromatic Al Kα source (1486 eV) having an energy resolution of 0.1 eV. All XPS spectra were fitted by Gaussian/Lorentzian convolution functions with simultaneous optimization of the background parameters. The background was modelled using a combination of a Shirley and a Tougaard background[210].

2.3 Magnetic Properties

The main technique employed to study the magnetic properties of transition metal doped TIs was SQUID which stands for superconducting quantum interference device magnetometry. The aim was to dope TIs with chromium to induce long-range ferromagnetic ordering in the film, therefore opening a surface band gap.

2.3.1 SQUID Magnetometry

SQUID magnetometers can probe very small magnetic moments, hence making it a powerful tool to study the effect of doping. A loop of superconducting material is designed with a deliberate 'weak-link' which forms a Josephson junction. The ring then works as a very sensitive interferometer where a current is generated which is proportional to any magnetic moment threaded through the loop[56]. The SQUID used by me was in Oxford and is a Quantum design MPMS XL system. The instrument was capable of reaching a maximum field of 7 T with the lowest temperature at 1.5 K. Thin films were typically cleaved in 5mm × 5mm squares and wedged into a cut in a drinking straw. The direction of the sample could be adjusted in-plane or out-of-plane. All samples were grown on a sapphire substrate which had a very large diamagnetic contribution. This background contribution was removed by a linear fit to the high field data. The instrument measured the data in 'emu' magnetic units and, for comparison with literature, emu was converted into μ_B/ion. To carry out this conversion, a few parameters need to be known from beforehand. For example, the magnetic doping concentration x, the film thickness t, density of the film ρ and its volume V. These were already known using other techniques already discussed, except for the volume. The samples mass m was measured using a precision weighing scale balance with the assumption that the complete mass was of the substrate. The first step was to calculate the cross-sectional area of the sample given by: $A = \frac{m}{\rho_{sapphire} t}$, where t was the thickness of the substrate and the density of the sapphire substrate was known. Combining A with the thickness measured from XRR gave the film volume. Then a normalization formula can be used to convert emu to μ_B/ion described as[50]: $M\left(\frac{\mu_B}{ion}\right) = M(emu)\frac{m_{rel}}{N_A \mu_B \rho V x}$, where M is the magnetic moment (in different units), m_{rel} is the relative molecular mass of the film, x is the atomic % dopant concentration, N_A is the Avogadro's number, μ_B the Bohr magneton (in emu), ρ the film

density and V the film volume. SQUID can then be used to produce two main graphs, Magnetization vs. applied field and Magnetization vs. temperature. Both of these measurements can be performed in-plane and out-of-plane to provide information about anisotropy of the sample as well as the Curie temperature T_c.

2.4 Clean Room Techniques

After the samples are grown using MBE, small pieces can be cleaved and a series of processing stages are required to produce suitable devices for measurement. All these devices in this thesis were processed by me in the Semiconductor Physics Group cleanroom facility (class 10000) at the Cavendish Laboratory.

2.4.1 Photolithography

Photolithography is a process used in fabrication to selectively remove parts of a thin film or the bulk of a substrate. It uses light to transfer a geometric pattern from a photomask to a light-sensitive chemical photoresist, on a substrate. It includes five basic steps: wafer preparation, photo resist coating, exposure, development, and etching**.** The process is sensitive to natural light and is therefore undertaken in yellow light. Figure 2.12 shows an optical lithography process. Photoresist is drop casted on the sample and then spun at a certain angular velocity to evenly spread the resist over it. The sample is then baked for a few seconds to harden/set the resist. A photo mask is then carefully aligned flat on top of the sample and UV light is exposed onto it. If the mask is not aligned carefully the UV light will not evenly expose the sample which can cause light to diffract through the edges and eventually have a defective device. There are two types of photo resist processes which can be followed thereafter. Negative photoresist and positive photoresist is decided in the development stage using chemicals. After the development, the sample is etched carefully either chemically or dry etching, leaving a permanent pattern on the sample. The remaining resist can then be removed with acetone known as the lift off process. A more detailed description of the process specific to TIs is described later in experimental chapter 5.

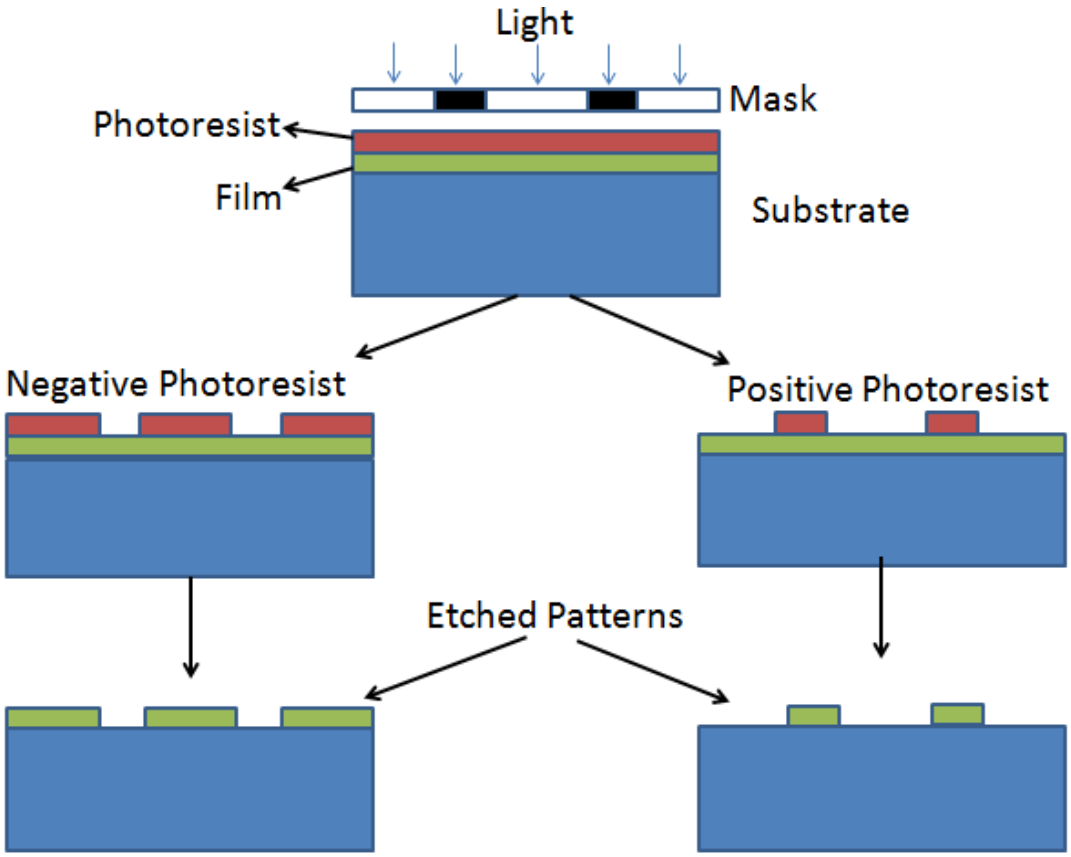

Figure 2.12 Procedure for Photo-lithography showing a Positive and negative resist developing process.

2.4.2 Thermal Evaporation

Thermal evaporation is one of the most commonly used methods of deposition of a metallic thin film. The source material is heated in a vacuum chamber up-to its sublimation temperature. At this stage, the metal sublimes to form metallic vapor's that condenses directly on the sample substrate exposed to it. Since this process is carried out under high vacuum, it is a quick method of depositing pure thin layers of a desired metal on a suitable film/substrate. Figure 2.13 shows the working and internal structure of a thermal evaporator. The substrate is placed at the top of the jar and the metal to be evaporated is placed in tungsten boats below it. The entire system is then pumped down to achieve a suitable vacuum. The boat is subsequently heated to the extent that the metal placed in them sublimes and a desired deposition rate is achieved which can be measured with a quartz crystal monitor.

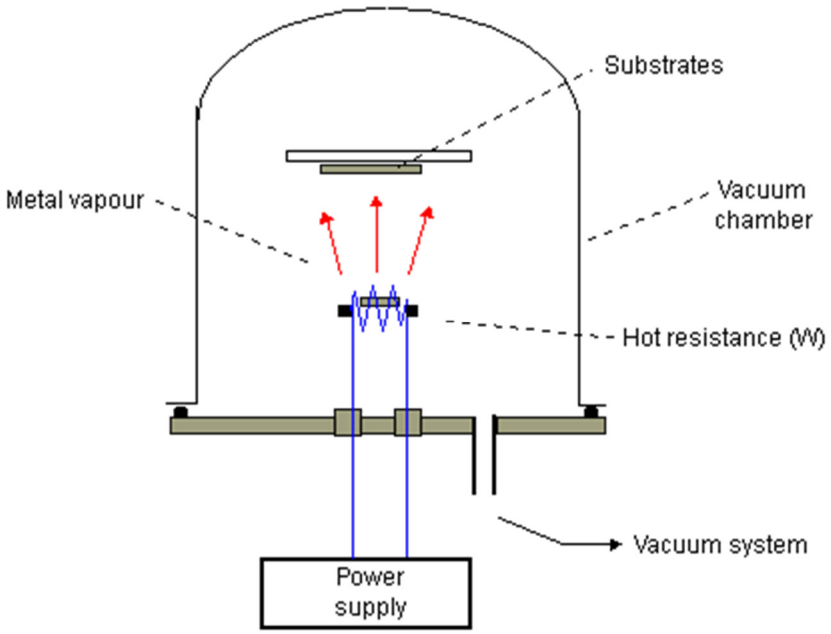

Figure 2.13 Bell jar set-up for thermal evaporation.

2.5 Cryogenic Measurements

2.5.1 Continuous Flow Cryostat

Most electrical measurements on topological materials were performed inside a cryostat. As the name suggests cryo means cold and stat being the short form of static. The purpose of measuring inside a cryostat is to achieve cold static temperatures which can be very precisely controlled. A schematic of the cryostat used by me is shown in Figure 2.14 (a). The design of the cryostat consists of an outer nitrogen jacket which surrounds another chamber containing liquid helium, hence this design is also referred to as double walled. The two layers/walls consisting of the liquid nitrogen jacket and helium jacket are separated via a vacuum space. It is extremely important to maintain a vacuum of less than 1×10^{-7} mbar between the walls whilst setting up the cryostat to work for the first time or after warming the system entirely during yearly maintenance checks. This ensures that the He jacket never comes in direct contact with air or the outside world. At all times during the working of the cryostat, liquid nitrogen and helium are stored in the cryostat to ensure that the system is always cold. There is also an innermost chamber which can be pumped down to below □ 5 mbar. A sample placed on a probe can be lowered into this inner most chamber after which liquid helium can be slowly introduced into the sample space via a needle valve while the sample cools.

a)

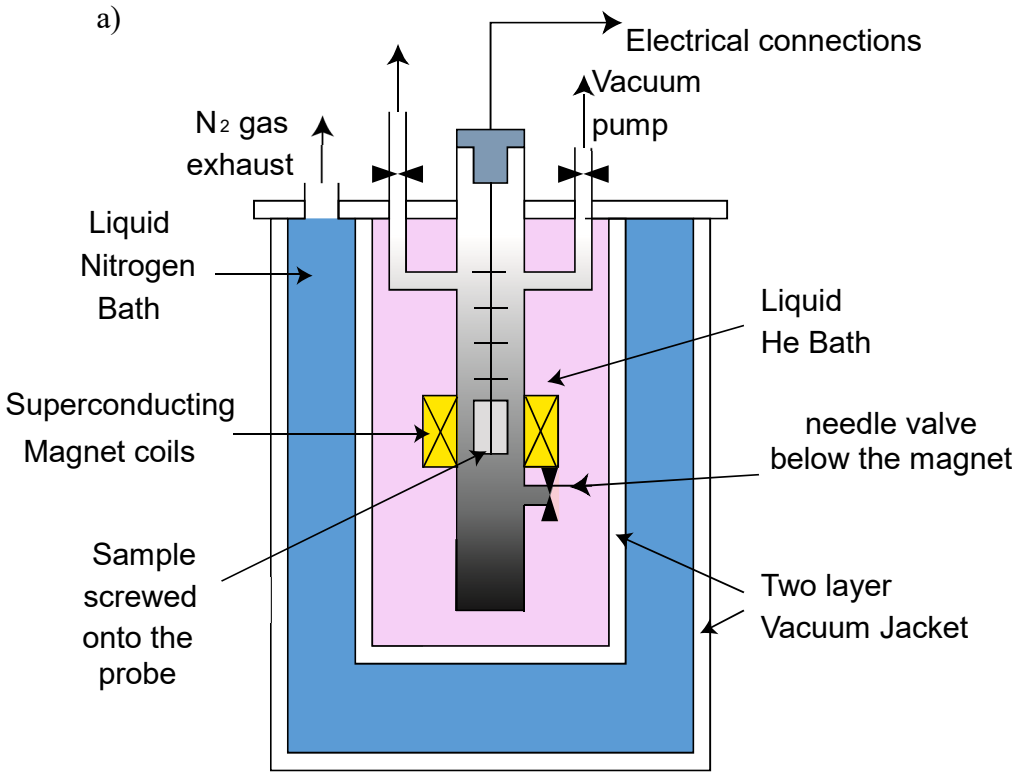

b)

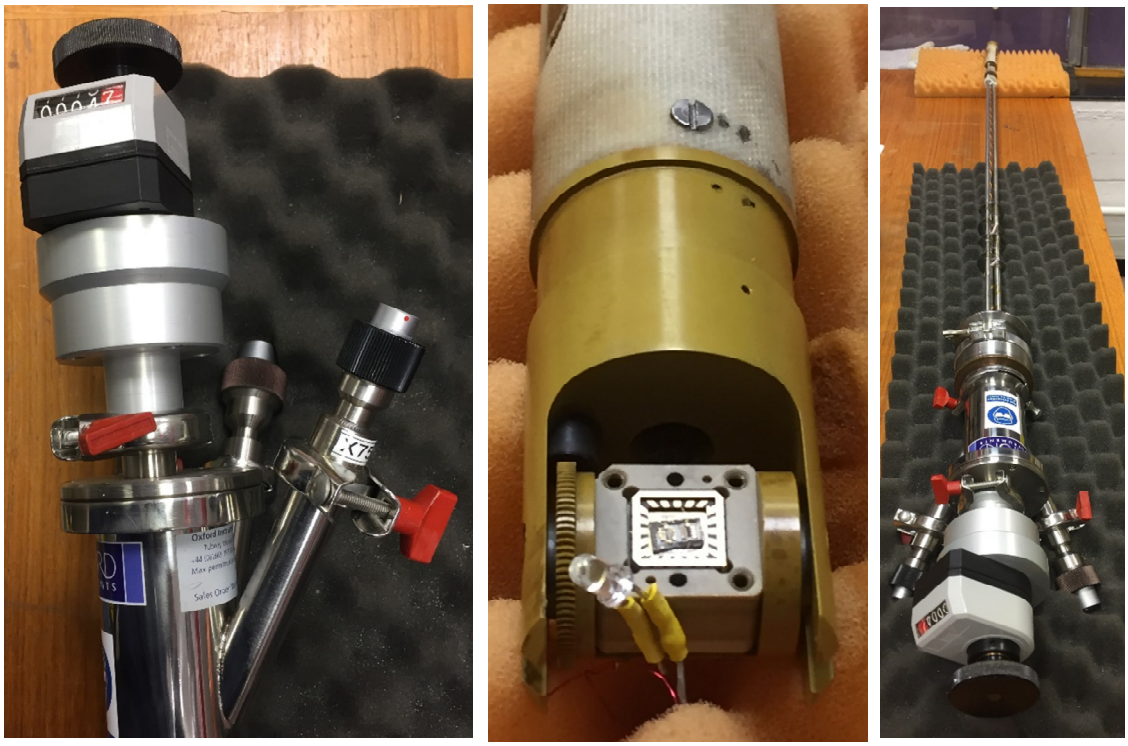

Figure 2.14 (a) Schematic of a 1.5 K cryostat system. (b) The probe itself, with the sample placed on a rotatable cylindrical arm which can be manually adjusted.

It usually took two hours to cool a sample to base temperature in the TFM groups cryostat while the sample space was being pumped by a rotatory pump. Pumping constantly on helium lowers the boiling point to around 1.5 K and by controlling the speed of pumping and the rate of flow of He it is possible to achieve a stable temperature for a long period of time. A standard probe which is inserted inside the cryostat is shown in Figure 2.14 (b). The probe contains a 20 pin leadless chip carrier (LCC) holder along with a twenty wire loom made from copper or Constantine connected to the back of the twenty pins on the holder. The probe also contains a thermometer in the form of a four-terminal resistor made from carbon glass which is mounted very close to the twenty pin sample holder. In addition, a heater rod is also positioned close to the sample to be able to heat the end of the probe while performing a temperature dependent measurement. All parameters can be recorded with the help of an Oxford Instruments ITC4 temperature controller which carries out the measurement and then using a calibration curve for that particular thermometer, displays the temperature directly. Inside the cryostat a superconducting magnet is present which can be swept up to 9 T, also present is another carbon glass thermometer close to the helium inlet. But clearly the probe mounted thermometer is preferable as it is in closer vicinity with the sample. The system is well designed to conduct measurements on several devices quickly. Once a device is ready to be measured, an AC or DC measurement is made possible using source measure units of lock-in amplifiers. Whilst DC measurements to study the electrical properties may seem attractive due to its simplicity, the main drawback is its susceptibility to noise. On the other hand, AC measurements can be carried out with respect to a reference frequency. The lock-in would only measure signals which are at the set lock-in frequency and therefore even large background noise signals can be excluded. All electrical measurements were carried out using the *Cryomeasure* software (an add-on to *Labview*) written by Prof. C. J. B. Ford of the Semiconductor Physics Group. This software communicates with the measurement setup and decodes the output plotting the results on the computer screen in real time. Data files in text format can be outputted for analysis in *Origin* plotting software. The main advantage of Cryomeasure over packages such as *LabView* lies in its simple scripting language. Cryomeasure is a user friendly software and more importantly, quick, allowing changes in the experiment to be made without unnecessary difficulties.

2.5.2 Magneto Optical Kerr Effect Measurements.

The magneto-optical Kerr effect occurs in magnetic materials due to optical anisotropy. This anisotropy arises when the magnetization of the sample within the surface domains is influenced by an external magnetic field. When a linear polarized light in incident on the magnetic material in the presence of a varying external magnetic field, the magnetization of the sample couples with the electric field of light. This causes the optical anisotropy to alter the state of the linearly polarized light which is reflected from the magnetic material. The change in the state of the linearly polarized incident light after being reflected off the magnetic sample is known as the Kerr effect and it is directly proportional to the magnetization of the sample. This makes it very useful to study the surface magnetism from which hysteresis loops can be plotted. The optical path of the polar MOKE experiment used in this thesis is illustrated in Figure 2.15. The sample was mounted on a piezoelectric XYZ stage with a 10 nm step size, in the same cryostat as used for the transport measurements.

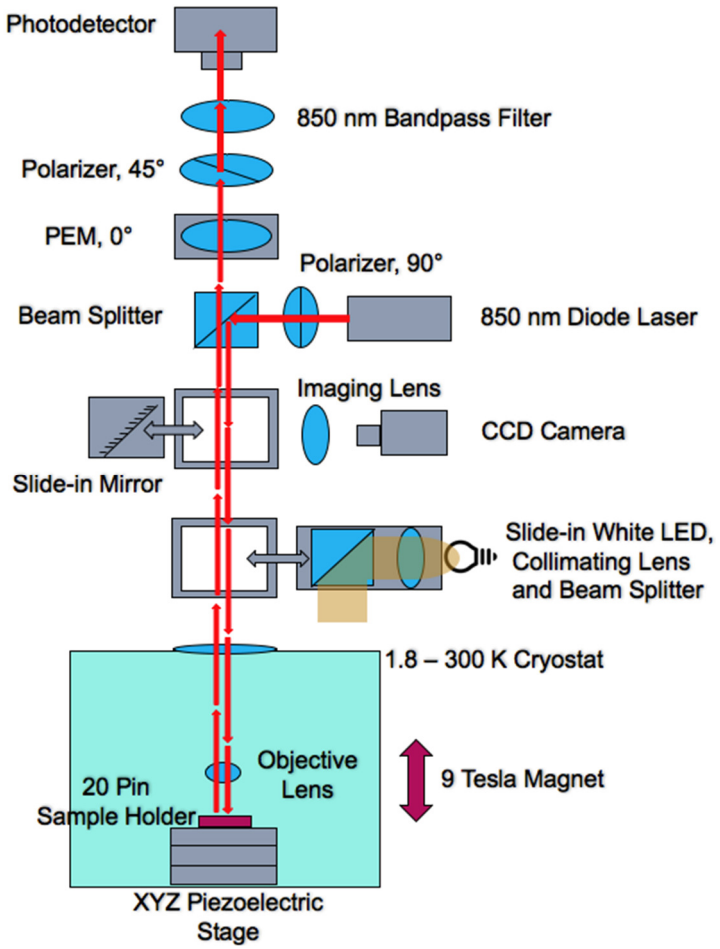

Figure 2.15 Schematics of the polar MOKE setup inside the cryostat designed by Jieye Liu.

The light coming from an 850 nm diode laser was polarized by a Glan-Taylor polarizer and reflected by a beam splitter into the vertical main optical path on the MOKE probe. After passing through the cryostat window, the linearly polarized light was focused down to a 3 μm spot size onto the sample via an objective lens. The light after reflecting from the sample passed through a photoelastic modulator, a second Glan-Taylor polarizer, and an 850 nm bandpass filter before reaching the detector. The detected light in the form of a photovoltage can then be converted into the Kerr rotation angle and plotted with respect to an external magnetic field displaying a hysteresis loop.

3. Chapter 3

Epitaxial Thin Film Growth and Structural Characterization of Magnetically-Doped Topological Insulators

3.1 Introduction and Motivation

The breaking of TRS in three dimensional TIs has been shown to be of central importance from both a fundamental aspect and for device applications. Transition metal doping in TIs is predicted to break the TRS which opens a surface gap at the Dirac point[33,57]. This has led to the recent experimental observations of the topological magnetoelectric effect[58], induction of a magnetic monopole[12] and the quantum anomalous Hall effect (QAHE)[59]. For instance in the topological magnetoelectric effect, an electric-field spin transistor device is used where opening a surface band gap is a prerequisite to reach the "OFF" state, otherwise the gapless surface states would lead to a leakage current and a very low "ON/OFF" ratio. On the other hand, in the QAHE, gapped surface states are accompanied with backscattering-protected dissipationless edge transport channels without the application of an external magnetic field. Hence a wide range of industrial applications have found their way in literature such as magnetic sensing[60], information storage[60], phase change memories[61] and various spin injectors[62]. More importantly it opens up the possibility for next generation low-dissipation electronic devices.

This experimental chapter covers a brief literature review followed by the MBE growth, structural and magnetic characterization of transition metal-doped tetradymite-type semiconductor– Cr doped Sb_2Te_3 thin films undertaken at the University of Oxford. By adjusting the flux of the high temperature Cr Knudsen cell a series of samples with different Cr content were prepared with the expectation to explore the robust ferromagnetism and tune the surface band gap.

All the experimental findings carried out in this chapter was completed at the Rutherford Appleton laboratory, in Professor Thorsten Hesjedal's laboratory under the supervision, guidance and collaboration of Dr. Liam Collins McIntyre. Numerous visits were made by me at a stretch of three weeks to learn, grow and characterize the samples hence leading to the completion of this work.

Before the discussion of our experimental findings, it is worth spending some time

explaining the work carried out by other scientists around the world in the growth of TIs and acknowledge their credibility.

3.2 Literature Review

Three-dimensional (3D) TIs covering Bi_2Se_3, Bi_2Te_3, Sb_2Te_3 and their alloys, such as $(Bi_xSb_{1-x})_2Te_3$, $(Bi_xSb_{1-x})_2Se_3$ and $Bi_2(Sb_xTe_{1-x})_3$ have long been recognized to have a high figure of merit with regards to thermoelectric materials. Recently, they have attracted intense interest because of their salient features linked with their unique robust surface states[14,31,63,64]. Electronically detecting a signal solely from the surface states has been hindered, mostly due to the overwhelming bulk contribution. The cause of this is very evidently because of imperfect materials. The search for fabricating the perfect TI is still ongoing and many techniques have been suggested to distinguish the surface state from the bulk such as applying an electric field to deplete the bulk conduction[65], by counter-doping to lower the bulk carrier density[66] and most recently by MBE growth of thin films to eliminate the bulk carriers[67]. At the current stage, experimental realizations of TIs are mainly by chemical vapor deposition (CVD)[68], bulk Bridgman growth[69], wet chemical synthesis[70] and now by MBE. Among these techniques MBE has flowered into the most superior one due to the following reasons:

a. Convenient physical deposition without complex chemistry involved in CVD
b. Accurately controlling the film thickness down to a single atomic quintuple layer (QL)
c. Excellent doping control and integration of heterostructures for realistic devices

In general, during MBE, individual atomic and molecular elements are generated and deposited onto a substrate on which the desired compound is formed. As discussed in the introduction chapter explaining the structure of TIs, they grow in the form of QLs held together by Van der Waal bonds, hence their growth mechanism is different from conventional MBE growth for covalent or ionic bond structures. For example, the lattice-matching conditions are slightly relaxed in the case of Van der Waals epitaxy[71] and so TIs can grow relatively well on a variety of substrates despite a large lattice mismatch between the films and the substrates. Some examples of lattice mismatch percentages are described in the Table 3.1. An excellent review is given in Ref. [72].

Substrate	Bi_2Se_3	Bi_2Te_3	Sb_2Te_3
Al_2O_3	14.9 %	8.7 %	12.0 %
Si	–7.3 %	–12.3 %	–9.7 %
GaAs	–3.4 %	–5.9 %	–8.7 %
SiO_2	18.6 %	12.1 %	15.5 %

Table 3.1 Lattice mismatch for different TI binary compounds on various substrates[72]

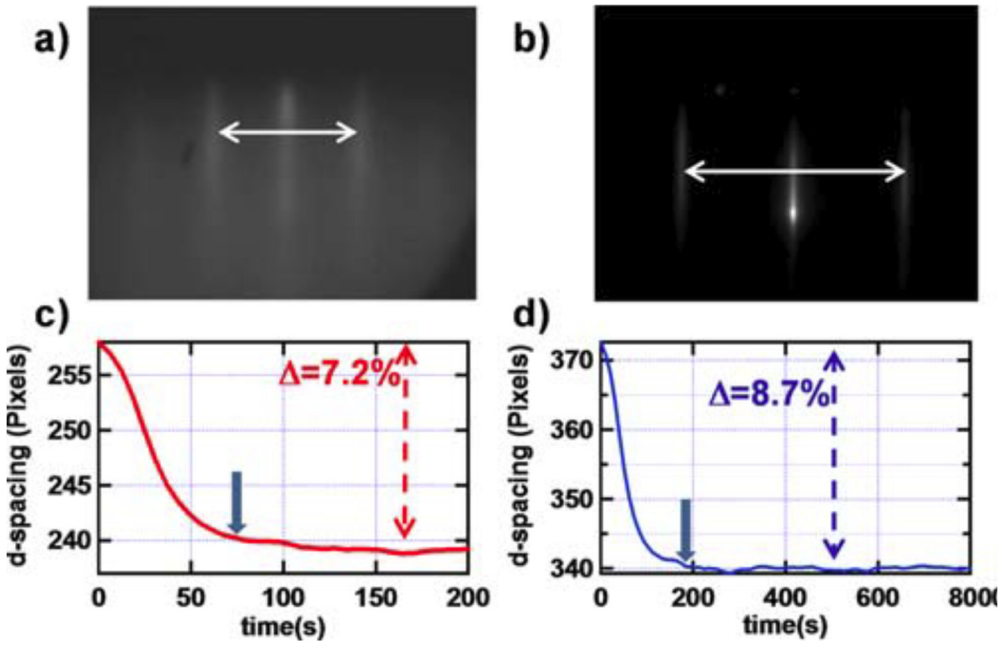

Figure 3.1(a) and (b) Typical RHEED images of a Bi_2Se_3 film on Si (111) and a Bi_2Te_3 thin film grown on GaAs (111) B terminated respectively. The arrow between the two stripes represent the *d*-spacing, which is inversely proportional to the lattice constant. (c, d) Shows the evolution of the *d*-spacing as a function of time. The value reaches a constant after a certain growth time marked with a blue arrow suggesting that the lattice is almost fully relaxed.[72] Figure reproduced from ref. 72 without permission.

RHEED is usually used to monitor the growth process and it is good practice to observe the pattern while growing at all stages until the recipe of the growth is optimized. Some examples of RHEED patterns of as-grown Bi_2Se_3 film on Si (111) and a Bi_2Te_3 thin film on GaAs (111) B terminated are shown in figure 3.1 (a) and (b) respectively. The white arrow marked in between the two first-order stripes represent the *d*-spacing, which is inversely proportional to the lattice constant. The evolution of the *d*-spacing with growth time is illustrated in figures 3 (c) and (d) for Bi_2Se_3 film on Si (111) and a Bi_2Te_3 thin film on GaAs (111) B terminated respectively. After a certain growth time, the *d*-spacing stabilizes and reaches a constant value marked by a blue arrow. This suggests that the lattice is relaxed. It also points out the importance of Van der Waals growth in which despite having a huge lattice mismatch there is no strain which is transferred onto the film.

Although RHEED is a great technique to qualitatively study the surface in-situ, the morphology of the surface has also been demonstrated in literature using Atomic force microscopy (AFM). It is observed that TI thin films grow characteristically in steps forming triangular-shaped terraces. Figure 3.2 reflects the structure inside the (0001) plane with the height of each step ~ 1 nm which is approximately equal to 1 QL (1 QL = 0.97 nm). The surface morphology of TIs varies to some extent, namely the size of the terraces and the width between adjacent layers.

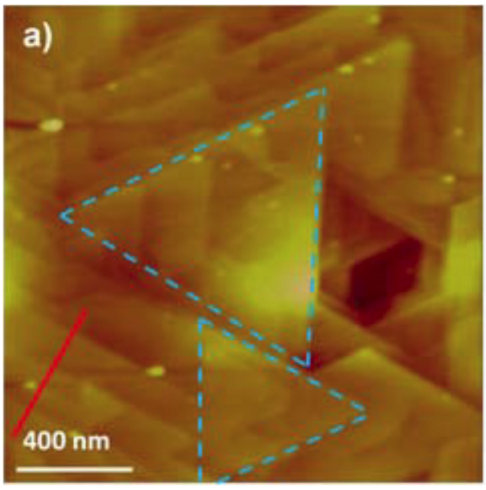

Figure 3.2 An AFM image describing the surface morphology of a 30 QL Bi_2Se_3 film grown on Si(111). Triangular shaped terraces are observed with a typical size of 400 nm. The blue dashed lines reflect twining defects.[72] Figure reproduced from ref. 72 without permission.

The overall size of the terraces ranges from 100 nm to 1 μm with a width of 10 nm to 100 nm between adjacent layers. It is fairly obvious that larger terraces are desired and interestingly these numbers depend on the growth rate and the substrate temperature hence it is worth examining more closely the growth recipes which lead to larger terraces. The substrate temperature can be controlled during MBE growth and as suggested decides the reaction rate of different materials, their kinetic energy and hence overall the composition and quality of the resulting film. It has been experimentally observed that the window for the optimal substrate temperature T_{sub} is very narrow for TIs (<50°C) and normally if T_{sub} is too low, atoms will not have enough energy to sit at the lowest potential energy site or diffuse adequately hence resulting in an amorphous or polycrystalline film[73]. On the other hand, if the T_{sub} is too high, a large number of 3D islands grow because the sticking coefficient of the elements is too low[73]. An example is demonstrated below where a systematic study was performed on 30 nm Bi_2Se_3 thin films grown on Si(111) at various substrate temperatures T_{sub}. The size of the terraces exhibit a sharp peak of 400 nm at an optimal T_{sub} = 250°C. Keeping the substrate at a lower temperature 200°C or a higher temperature 300°C leads to smaller terraces as shown in Figure 3.3(a) and (c). Interestingly the RHEED patterns for all the films demonstrates similar streaky patterns suggesting a 2D growth, consistent with good quality epitaxial films (not shown here)[74].

Along with substrate temperature, other factors need to be considered before deciding to grow TIs, for example the termination of the substrate. Growing Bi_2Se_3 directly on Si (111) is not recommended as unsaturated bonds on the substrate surface can react with Se to form $SiSe_2$. This initial growth layer forms a complex surface reconstruction at the interface[74].

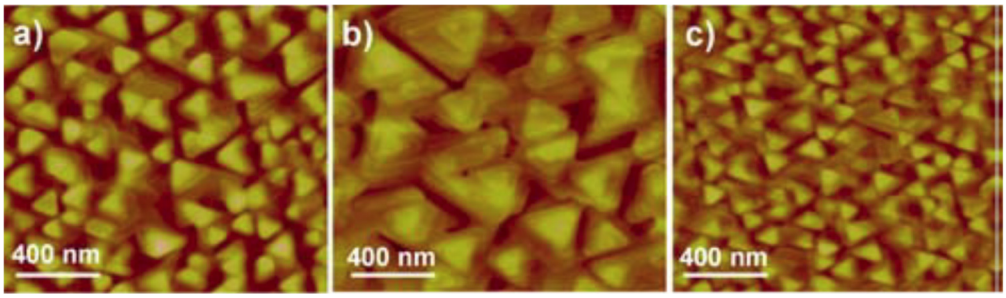

Figure 3.3 A 30 nm thin film of Bi_2Se_3 grown at different substrate temperatures on a Si (111) substrate. (a) lower temperature 200°C leads to islands roughly 200 nm in size (b) optimal temperature of 250°C leads to islands of roughly 400 nm (c) high temperature of 300°C leads of countless number of smaller islands 100 nm in size.[72] Figure adopted from ref. 72 without permission.

To prevent this from happening, the unsaturated bonds of Si need to be passivated. This is performed by dipping the Si in hydrofluoric acid after cleaning[75]. A layer of hydrogen gets absorbed on the surface leading to significant improvements in the surface terrace size[76]. Another way is to adopt a passivation layer is by creating a Se-atom-terminated Si(111)[77]. If Si(111) is first treated with a monolayer of Se keeping T_{sub} = 100°C before the growth of Bi_2Se_3, very sharp interfaces corresponding to clear 2D lines in RHEED images have been observed. The substrate temperature is the most critical component as temperatures above 200°C or below 70°C again form $SiSe_2$ or an amorphous Se layer accumulated on the Si substrate respectively[74,78].

Similar work has been demonstrated with Se- terminated GaAs (111) B where a GaSe was used to terminate dangling bonds from the GaAs substrate[79]. Here the growth of Bi_2Te_3 was performed with a monolayer of GaSe. The substrate was first heated to 580°C for 10 minutes to remove the surface oxide and then cooled in a Se environment. Figures 3.4 (a) and (b) show the RHEED patterns of the GaAs (111) B substrate before and after the growth of a 10-QL Bi_2Te_3 thin film. It begins with a conventional 2D surface with the pattern eventually becoming brighter and sharper. The evolution of the *d*-spacing can also be seen. Figure 3.4 (c) shows a cross-sectional TEM image of the as-grown film. Each QL can clearly be resolved by looking at the 5 atom layer structure. The blue lines indicate the position of the Van der Waals gaps between two QLs. A single layer of GaSe can also be seen at the interface. Colored space-resolved EDX analysis describe the Se atom concentrated region in red at the interface. The presence of a GaSe monolayer and the observation of the gap between 2 QLs is consistent with Van der Waals epitaxial growth.

Another crucial factor to achieve high-quality epitaxial growth is to accurately control the atomic flux ratio of the V (Bi and Sb) and VI (Se and Te) species. The growth is similar to the conventional III-V's such as GaAs where the As/Ga ratio is kept above the stoichiometric ratio as only one species controls the growth rate. In TIs the ratio of Bi or Sb to Se or Te has been widely adopted to be 4:5. But many groups have tried to re-engineer their cells to lower this flux ratio. For example Zhang *et al*. used a radio frequency cracker cell to grow Bi_2Se_3 while achieving a flux ratio of 1:2 for Bi:Se[80].

Although many approaches have been used to grow ultra-high quality TI films achieving the first generation MBE grown, the presence of imperfections in the crystals still stays an unresolved concern. These defects lead to a high bulk carrier density and as a result, bulk conduction still dominates the conduction above the surface states.

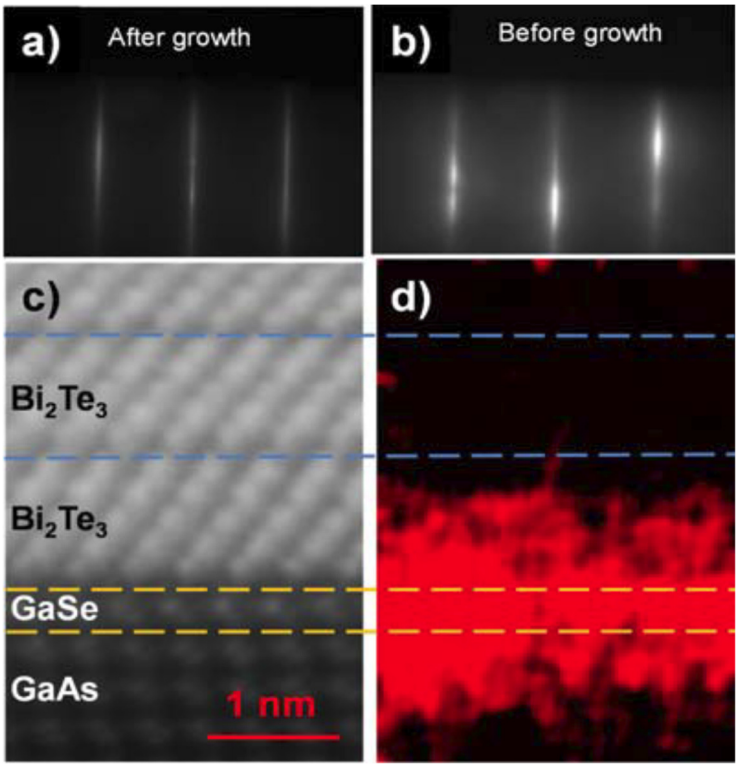

Figure 3.4 (a, b) RHEED images before and after the growth of a 10-QL Bi_2Te_3 (c) TEM image showing a monolayer of GaSe at the interface between the substrate and the Bi_2Te_3 film. (d) A color resolved EDX analysis indicating the Se atoms in red concentrated at the interface.[72] Figure adopted from ref. 72 without permission.

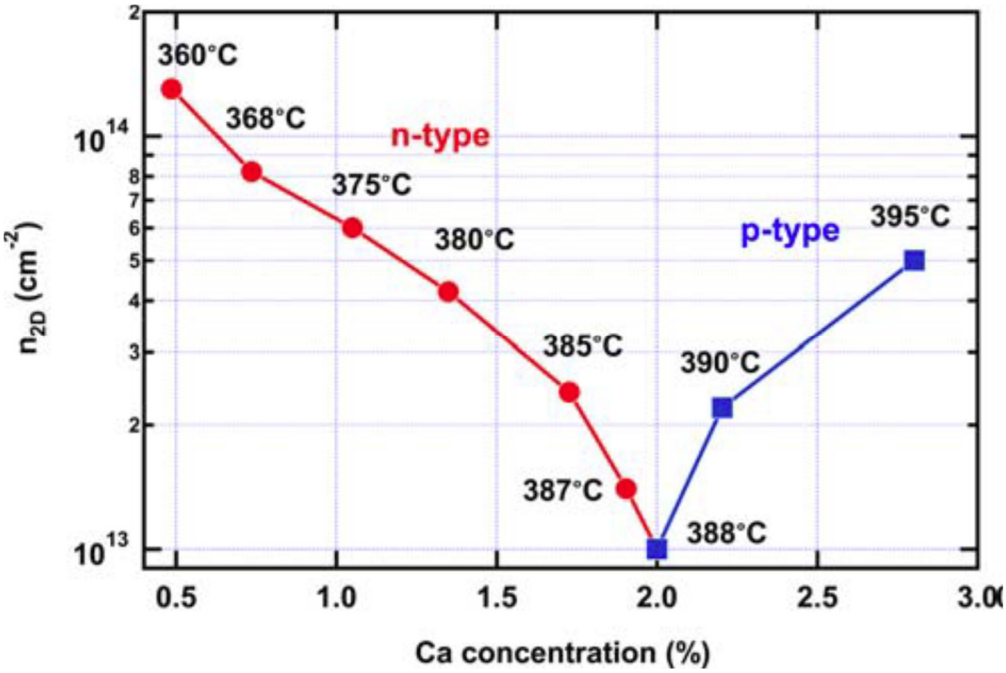

Figure 3.5 Carrier density vs. Ca concentration demonstrating a systematic change of carrier density from *n*-type to *p*-type in Ca-doped Bi_2Se_3.[72] Figure adopted from ref. 72 without permission.

During the last few years many research groups have started to explore means and ways to produce a perfect TI which truly has an insulating bulk behavior. This has led to the second generation of TIs where doping and counter-doping techniques have been used to control the Fermi level, all of which is only possible through MBE techniques. A few example growths are worth mentioning. He *et al.*[72] showed that Ca-doped Bi_2Se_3 can be grown epitaxially. By tuning the cell temperature of the Ca cell, the bulk carrier density was changed as shown in Figure 3.5 from *n*-type to *p*-type. The cell temperature of 388°C gave a carrier density of 10 times lower for than that grown at 360°C.

Another possible technique was producing alloys of Bi, Sb and Te. Bi_2Te_3 tends to be *n*-type while Sb_2Te_3 tends to be *p*-type. So by combining them and making an alloy of Bi_2Te_3 and Sb_2Te_3 a successful reduction in the bulk carrier concentration is possible. This was first demonstrated by Kong *et al.*[21] using CVD. By adjusting the composition *x* in $(Bi_xSb_{1-x})_2Te_3$ the overall band structure could change and the position of the Fermi level adjusted to be in the bulk conduction band, valence band or in the gap demonstrating an ambipolar behavior. This was the first measurement demonstrating a clear dominant surface conduction. However the major problem with this published result was that this technique could only synthesize layers of μm sizes at most and was not practical for thin film applications.

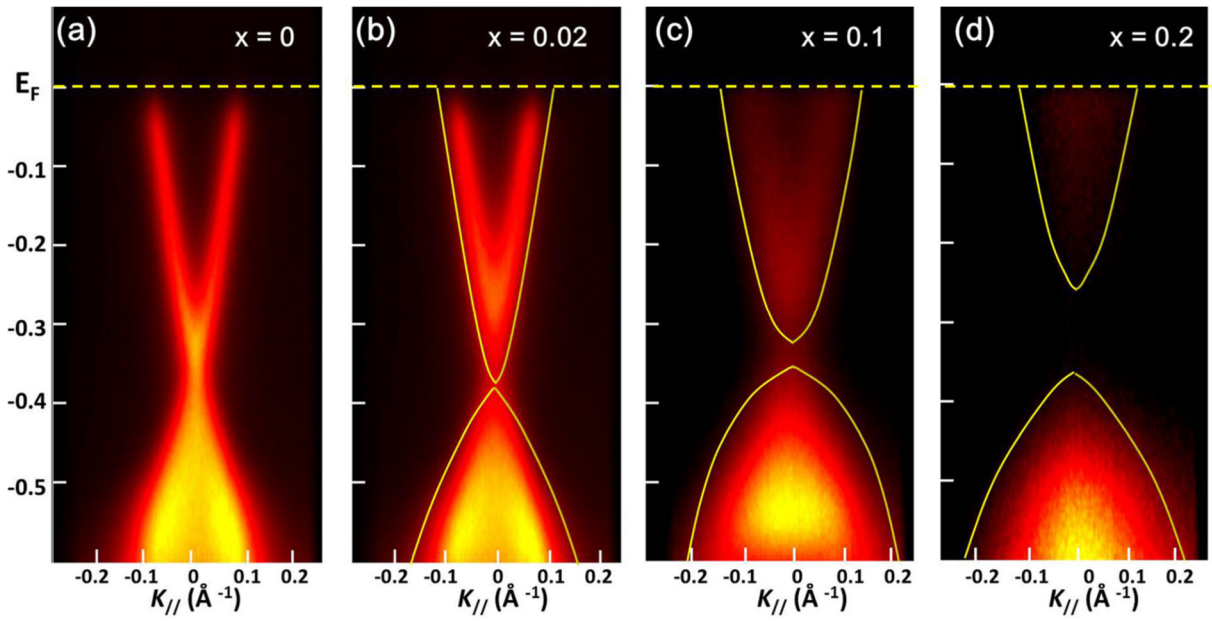

Figure 3.6 ARPES results from a 50-QL $Cr_xBi_{2-x}Se_3$ thin film[81] with (a) $x = 0$, (b) $x = 0.02$, (c) $x = 0.1$ and (d) $x = 0.2$. As *x* increased, the surface state changed from a linear massless Dirac fermion state to a massive state with the opening of a gap. The gap broadened with increasing *x*.[81] Figure adopted from ref. 81 without permission.

In 2012-13, experimentalists realized that transition-metal doping in TIs for ferromagnetic applications are suitable for magnetic sensing[60], information storage[60], phase change memories[61] and spin injectors[62]. More importantly it opens the possibility for next generation low-dissipation electronic devices. Much of this work is inspired by the idea of doping semiconductors producing DMS where transitions metals have been used to dope Ge[82], GaAs[83], ZnO[84] etc. One of the key features of TIs is the protection of the surface states by time reversal symmetry which exhibit a linear E-*k* relationship possessing Dirac fermions[64]. Theoretical calculations made by Liu *et al*.[33] claimed that if magnetic impurities were introduced in the TI lattice, a surface band opens up a gap, breaking TRS thus the massless Dirac fermion surface state turn into a massive region[85]. Experimentally this was first observed by Chen *et al*. in Fe- and Mn- doped Bi_2Se_3 bulk samples, grown by a Bridgman growth method[85]. Another example using MBE was studied in Cr doped Bi_2Se_3 sample[81] shown in figure 3.6. Epitaxial 50-QL $Cr_xBi_{2-x}Se_3$ with x varying between 0 and 0.2 were grown on top of a Si(111) substrate. With increasing Cr concentration, the Dirac cone shown in 3.6 (a) deviated from a linear massless surface state to a gap opening state (Fig. 3.6 (d)) the size of which increased with increasing x.

Although a lot of progress has been made in the field of growth, I have tried to make a humble contribution to the field of MBE growth in the process increasing my knowledge and learn from my development. The next section will cover the work carried out by me in collaboration with Dr Liam-Collins Mcintyre at the Rutherford Appleton laboratories in Professor Thorsten Hesjedal's MBE system.

3.3 Sample Preparation and Growth Parameters

Perhaps the most important step of the MBE procedure of thin films is the preparation work that goes in before the actual growth starts. Incorrect preparation of the substrate may lead to no worthwhile film growth. It is therefore important to cover the basic technical details of the preparation of the substrate material and the chamber itself. The preparation of the chamber is explained in more detail in the experimental section 2.1.1.

Various considerations affect the choice of substrate material and high quality growth has been successfully established on a wide variety of substrate materials. All the thin films in this chapter were grown on Sapphire (0001) substrates where it is also possible to grow high quality TIs as presented below. Sapphire is relatively low on cost, easy to prepare, readily available and provides an excellent surface for growth, moreover its heavy use in the semiconductor industry makes it an ideal choice to grow TIs on. These substrates were commercially purchased as pre-cut epi-ready 2" diameter circular wafers from a company called MTI crystals. These were further cleaved in ¼ pieces of the 2" wafer. In theory these substrates are delivered and ready to be grown on. However in practice a wet chemical process was first used to make sure the substrates are free from organic contaminants introduced during manufacturing, handling and shipping. Any contaminants which may be present were removed by following the steps outlined below:

a. Substrates were first dipped in acetone for 3 minutes which was placed on a hot plate at 80°C.
b. Then in trichloroethylene for 3 minutes
c. Followed by a cold dip in isopropanol
d. Then boiled in isopropanol for 3 minutes kept at 80°C
e. Followed by a cold dip in methanol
f. Then boiled in methanol for 3 minutes at 80°C
g. Finally rinsed with de-ionized water and blow dried with nitrogen gas

Often mistakes were made while handling substrates with tweezers, and it is important to mention that the tweezers used should very clean and free from contaminants. All the solvents used were of the highest purity and labeled "semiconductor grade". After the cleaning of the substrates, they were transferred into the load–lock of the MBE system, followed by a transfer into the preparation chamber. Here they were baked under a heat lamp

overnight (8-10 hours at ≈150°C) in UHV conditions. This ensured removal of any water vapors present during the rinsing process. The sapphire was then transferred into the MBE chamber onto a manipulator before the start of the source material calibrations. During the source material calibration process, the substrate was heated to 450° C and rotated to further purify it uniformly and also to prevent any deposition of material during the calibration procedure. Throughout the calibration procedure the substrate position was pointed away from the site of the effusion cells to ensure no direct incident flux, instead a beam flux monitor in the form of a nude ion gauge attached onto the manipulator placed itself in direct vision of the cells. Standard effusion cells were used for Sb and Te along with a high temperature cell for Cr. Before ramping the three cells to their standby temperatures, liquid nitrogen was introduced into the MBE cryo-shield. Liquid nitrogen helps to ensure thermal stability of the cells and also acts as a cryo-pump (by removing kinetic energy from free gas molecules present on the walls of the chamber). The flow of liquid was controlled directly from the nitrogen Dewar to obtain an optimum and economical consumption. All cells used were controlled by a Eurotherm process controller. A typical controller uses a PID (proportionality, integral and differentiation) control loop in which the applied current is regulated from the power supply in order to maintain a constant temperature with very high accuracy (usually ±1°C). Each Eurotherm's PID controller was manually tuned to match the specific design of the cell and material being evaporated. For example the high temperature cell for Cr uses very different parameters compared to the low temperature sources. After the cells reached their standby temperature each of them was calibrated independently and manually. The cells are always maintained (during an idle state) at their respective standby temperatures to avoid degassing and to ensure a uniform flux. Starting with the Sb source, the cell was ramped from its standby temperature of 125°C to 275°C. The calibration was then performed by ramping the temperature of the cell in steps of 10 degrees up to 400°C whilst opening and closing the shutter at each step until a stable pressure reading was taken on the beam flux monitor. These pressure readings were subtracted from the overall background pressure reading in the chamber to obtain the partial pressure which is directly related to the incident flux for the Sb cell. A plot of partial pressure vs. Sb cell temperature can then be plotted as shown in the figure 3.7 (a). The Te and Cr cells were calibrated in a similar procedure as discussed above, the partial pressures of which are shown in Figure 3.7 (b) and (c). The pressures were recorded repeatedly over a period of days or even months before the beginning of each growth, displayed in different colors on the graphs.

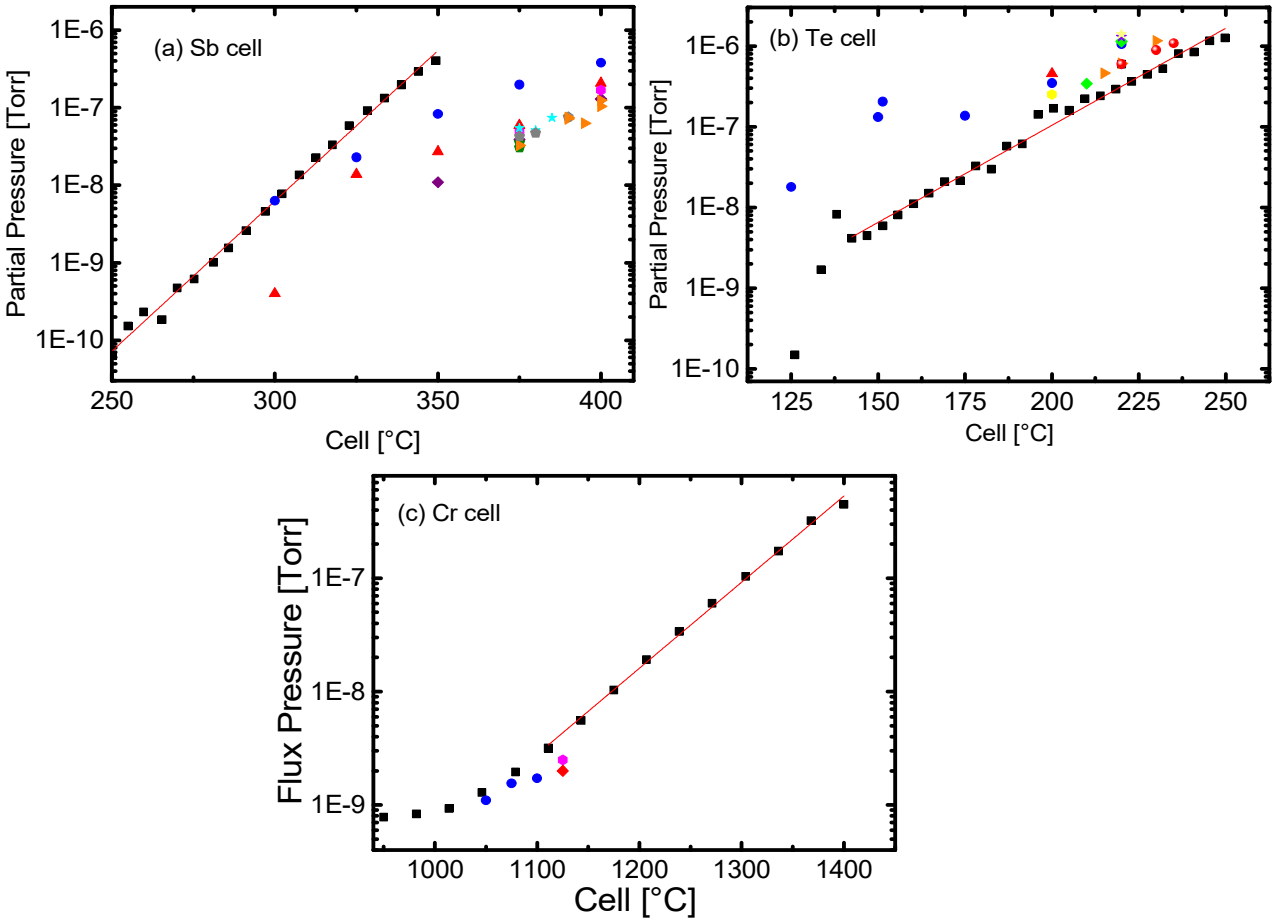

Figure 3.7 Calibration curves for the effusion cells for Sb, Te and Cr showing partial pressures at different temperatures measured by a beam flux monitor.

3.4 Thin Film Growth and Structural Characterization of Sb_2Te_3

Before the growth of Cr doped Sb_2Te_3 was established, MBE growth of un-doped Sb_2Te_3 was carried out. Based on many previous publications[74,86–89] and local experience from Liam who has grown Bi_2Se_3 and Bi_2Te_3 before, the Sb:Te flux ratio was fixed at ~1:10 for all growth samples. This flux ratio has shown to reduce the formation of Te vacancies and anti-site defects which are commonly observed in this material system[90]. An overpressure of Te also ensures the correct phase of the compound is formed leading to a desired 2:3 stoichiometry[91]. The growth rate was typically limited by the incident Sb flux and any excess Te not incorporated into the crystal would desorb from the surface. Typically a Sb flux was set to ~ 7×10^{-8} Torr. After the source calibrations were completed and the desired fluxes were obtained, the substrate's RHEED pattern was recorded by rotating the manipulator to the "RHEED position". Typical energy of the RHEED gun was 30 KeV which was slowly

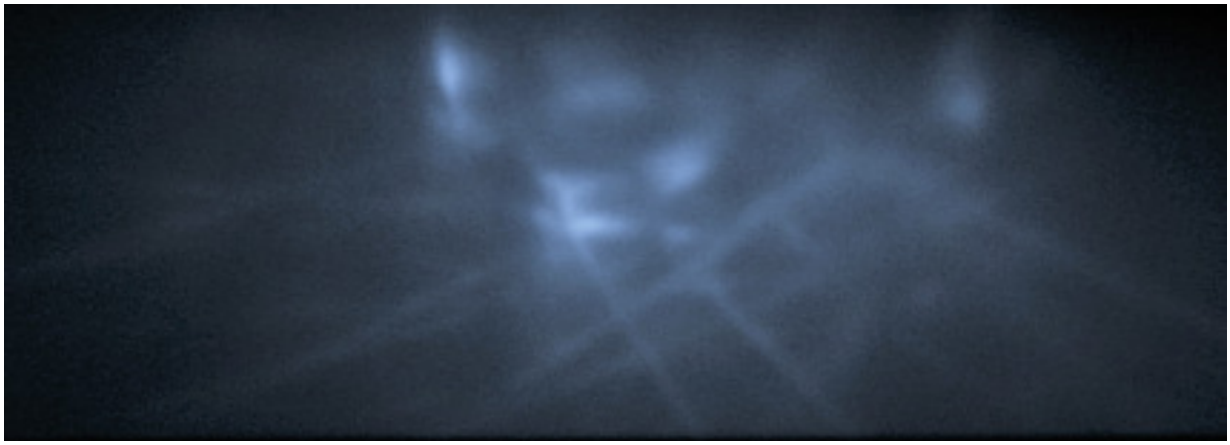

Figure 3.8 RHEED pattern for a sapphire substrate kept at 300°C on the manipulator before the start of the MBE growth of thin film Sb_2Te_3. The pattern was obtained along the $[10\bar{1}0]$ azimuth of $Al_2O_3(0001)$.

increased to account for degassing of the filament in the gun. Figure 3.8 shows the full RHEED pattern for a sapphire substrate uniformly heated to 300°C. The picture demonstrates Kikuchi lines which indicate a high quality surface. Kikuchi lines pair up to form bands in an electronic diffraction pattern and show up in the pattern by diffusely scattered electrons for example as a result of thermal atom vibrations. In principle, some incident electrons penetrate into the sample and fulfil the Bragg condition in the out-of-plane direction which causes the Ewald spheres to connect up forming Kikuchi arcs. This ensures a clean surface to begin the growth of Sb_2Te_3 on Sapphire.

A few recipes of growth were tried and tested and the results below are for all grown samples which were successful as well as unsuccessful as shown in the table 3.2 below :

Sample name	Structure grown	Thickness calculated from XRR ~ (nm)
1. M2-0560	Sb_2Te_3	30
2. M2-0561	Cr doped Sb_2Te_3	Not performed
3. M2-0562	Cr doped Sb_2Te_3	Not performed
4. M2-0566	Cr doped Sb_2Te_3	Not performed
5. M2-0563	$Cr_{0.42}Sb_{1.58}Te_3$	60
6. M2-0564	$Cr_{0.26}Sb_{1.74}Te_3$	56
7. M2-0565	$Cr_{0.15}Sb_{1.85}Te_3$	60
8. M2-0567	$Cr_{0.71}Sb_{1.29}Te_3$	60
9. M2-0574	$Cr_{0.15}Sb_{1.85}Te_3$	20

10. M2-0575	$Cr_{0.41}Sb_{1.59}Te_3$	19
11. M2-0576	$Cr_{0.58}Sb_{1.42}Te_3$	20
12. M2-0577	$Cr_{0.76}Sb_{1.22}Te_3$	20

Table 3.2 All the sample names grown with their structures and thicknesses.

Recipes for each growth differed slightly. Starting with an un-doped sample the procedure is described below for sample name M2-0560 for pure Sb_2Te_3 of thickness ~30 nm.

Growth of sample M2-0560, undoped Sb_2Te_3

Sb_2Te_3 thin films were deposited by first growing a lower temperature seed layer at T_{sub} = 200°C. This was done by keeping the Sb cell beam flux reading at ~ 7.5×10^{-8} Torr achieved at 380°C and keeping the Te cell beam flux pressure reading at ~ 1×10^{-6} Torr at 205°C. The flux ratios of Sb : Te was approximately 1:13 close to the ideal 1:10. The substrate was first moved to the "growth position" manually by rotating the manipulator after which the Sb cell along with the Te cell shutters were opened. The shutter opening and closing mechanism as well as the Eurotherm controllers were software controlled using a pre written script. After 20 minutes the Sb shutter was closed, while the Te cell shutter was left open. This yielded a thickness of approximately 5 nm. A RHEED image was taken at this point shown in figure 3.9 by manually rotating the manipulator to the "RHEED" position.

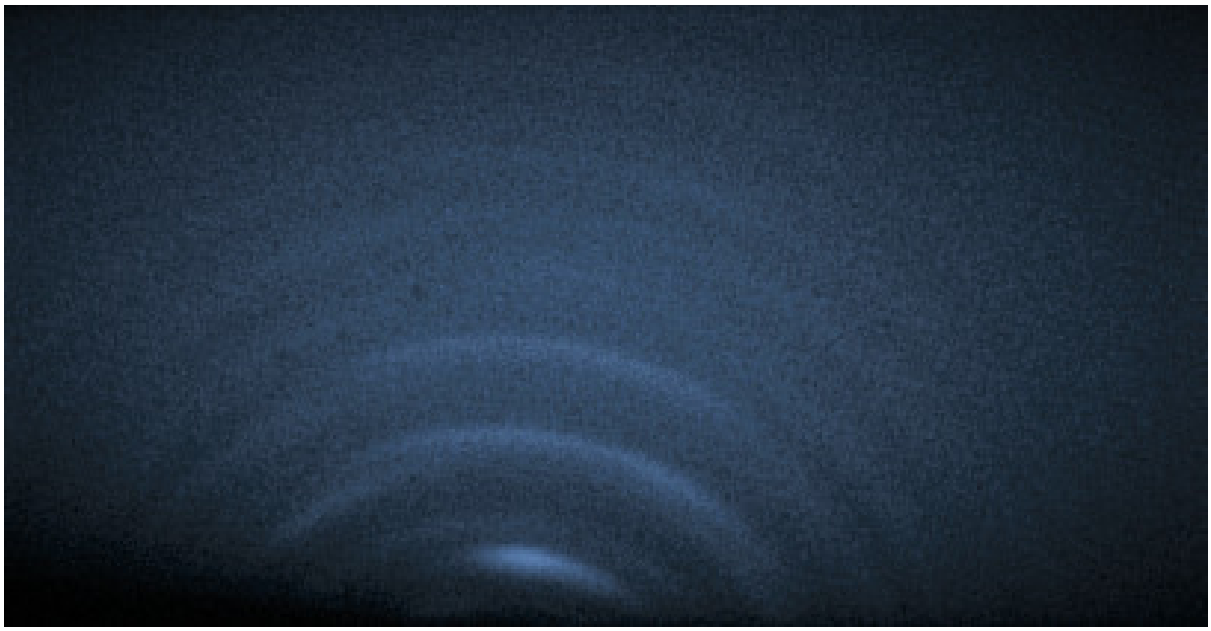

Figure 3.9 RHEED image taken after the first seed layer of Sb_2Te_3 was grown on T_{sub} = 200°C.

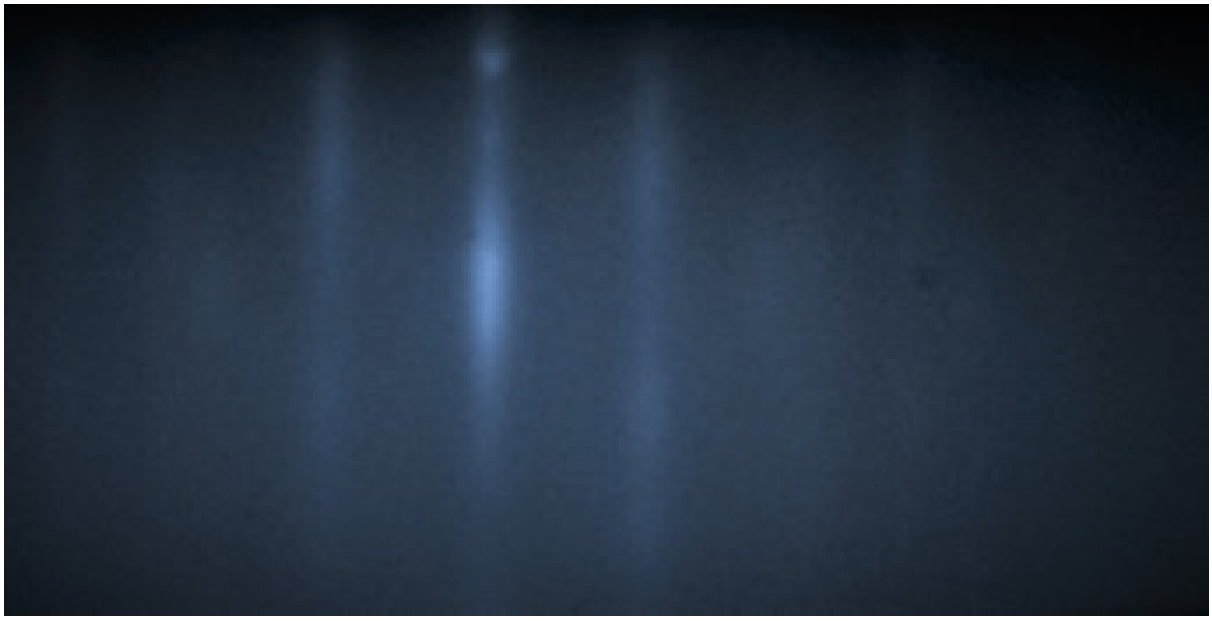

Figure 3.10 RHEED image taken after the annealing of the seed layer at T_{sub} = 250°C in a Te rich atmosphere. The pattern was obtained along the $[10\bar{1}0]$ azimuth of Sb_2Te_3.

The deposition of the seed layer was followed by ramping the substrate to T_{sub} = 250°C keeping only the Te cell shutter still open. It was found that this is a key step to ensure the highest quality film was yielded and to establish the correct crystalline phase. Another RHEED image at this point was taken and shown in figure 3.10.

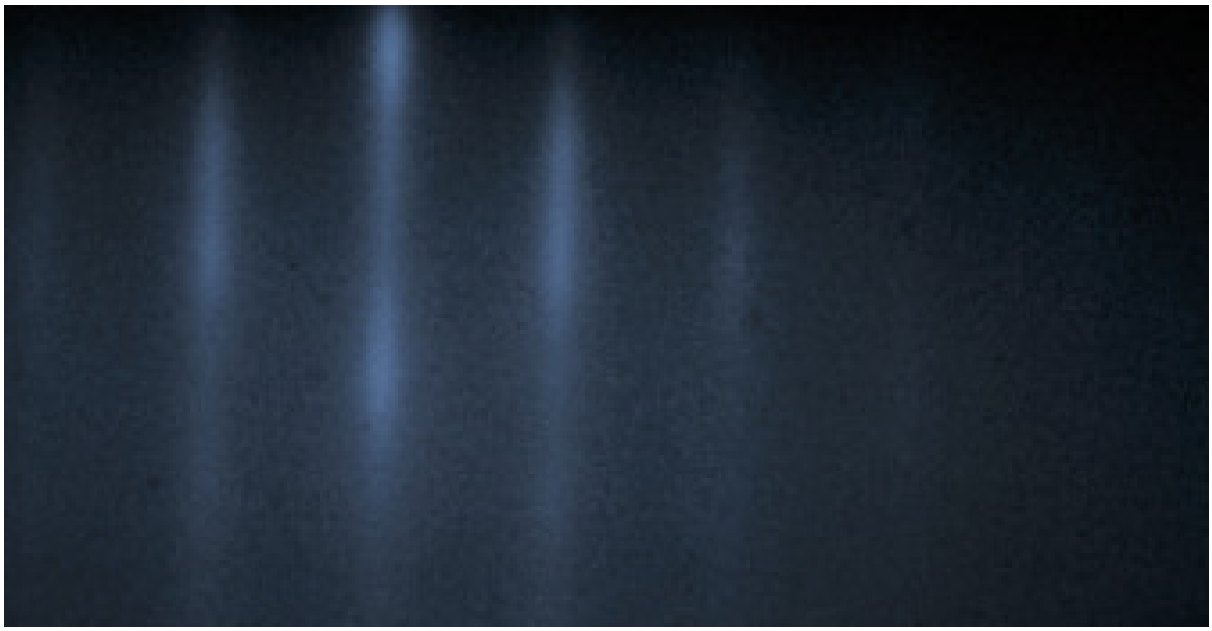

Figure 3.11 RHEED image taken at the end of the growth of a Sb_2Te_3 sample when the cells and the substrate were ramped down to their standby temperatures. The pattern was obtained along the $[10\bar{1}0]$ azimuth of Sb_2Te_3.

After 30 minutes of annealing under a Te rich atmosphere, the Sb cell shutter was re-opened to grow Sb_2Te_3 for a total of 60 minutes. After the growth was finished both the shutters were closed and the cells along with the substrate were ramped down to their respective standby temperatures. Another RHEED image was taken to confirm the sharp two-dimensional like pattern shown in figure 3.11.

The reflection high-energy electron diffraction pattern in Figure 3.11 indicates that the films grow with their *c*-axis perpendicular to the plane of the substrate and streak-like diffraction corresponds to a near two-dimensional mode of the film grown. Figure 3.9 illustrates a RHEED pattern after the first seed layer of Sb_2Te_3 is grown. The pattern shows semi-circular like rings which indicate a polycrystalline growth characterized by the smearing of the lattice due to the more isotropic diffraction. After annealing the spotty ring patterns gradually disappear while a streak like pattern becomes more clearer. After the final growth is complete, the evolution of the RHEED pattern continues to show streaky lines this time more pronounced, indicative of a two dimensional single crystal growth. A rapid lattice relaxation takes place within a few atomic layers as the Sb_2Te_3 strata evolves from a highly strained layer to essentially a bulk-like layer. The RHEED pattern is also meant to repeat itself at every step of 60 degree rotation of the film indicating that the films grow with their basal plane parallel to the substrates surface and the *c*-axis (trigonal axis) perpendicular to the substrate (not shown here).

XRD was carried out after the sample was taken out of the chamber and before cutting to confirm their tetradymite-type crystal structure. Figure 3.12 (a) shows the X-ray diffraction pattern of the bulk-crystal sample number M2-0560 prepared by MBE. Only the (0 0 *l*) peaks in the hexagonal unit cell are present, confirming that the films grow along the *c*-axis direction. After comparing possible X-ray characteristic diffraction peaks from pure Sb, Te and their other compounds such as SbTe, $SbTe_2$ and Sb_2Te_5, no traces of any secondary phase formation was found in the XRD scan. All the peaks along with the substrate peak is indicated in the XRD pattern shown in figure 3.12.

XRR studies were carried out and modelled using GenX software in collaboration with Liam as shown in Figure 3.12 (b). The best fit to the experimental data is obtained by using a 2-layer structure for the Sb_2Te_3 film that will allow the film thickness and density to independently vary towards the substrate and surface interfaces. This approach permits the

incorporation of strain and relaxation effects present in the film into the fitted model. The model indicates a full film thickness of (27.92 ± 1) nm with a surface roughness of (3.3 ± 0.1) nm close to the expected 30 nm desired film thickness.

In summary, high quality crystalline Sb_2Te_3 was grown successfully by following the crucial steps summarized in table 3.3:

Sample	First step : Buffer layer growth for 20 mins	Annealing time in Te over-pressure	Growth Temperature at second step for 60 mins	Finishing steps
Sb_2Te_3	**5 nm at T_{sub} = 200°C**	**30 minutes**	**T_{sub} = 250°C**	**take substrate and cells to standby temperatures**

Table 3.3 Growth recipe for sample M2-0560, ~30 nm undoped Sb_2Te_3

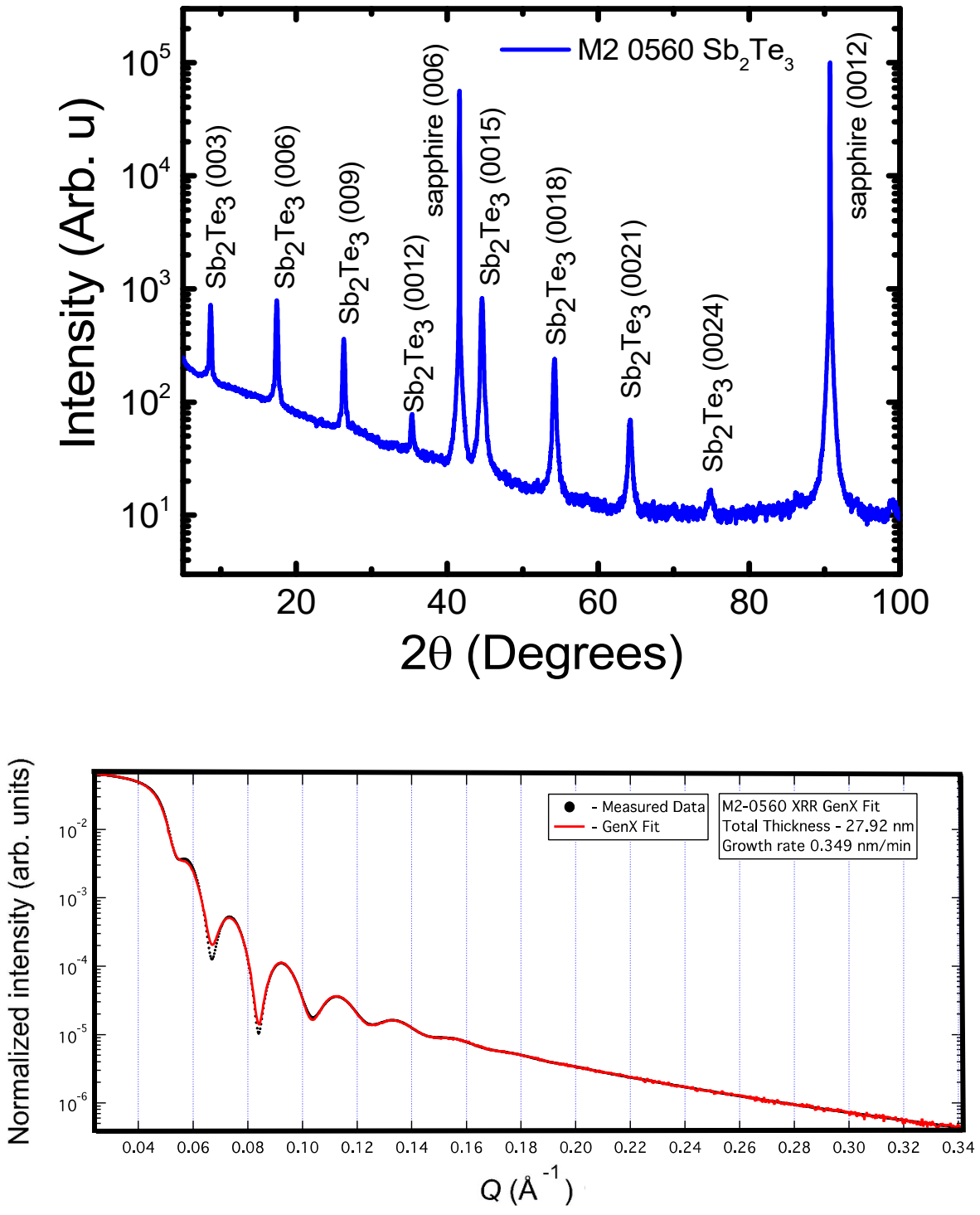

Figure 3.12 (a) X-ray diffraction diffractogram (2θ) of an undoped Sb_2Te_3 film on Al_2O_3 (0001). The (0 0 l) film peaks ($l = 3, 6, \ldots$) are labeled. (b) X-ray reflectivity of the measured film (black) and fitted model in GenX (red) performed by Dr. Liam-Collins Mcintyre.

3.5 Thin Film Growth, Structural and Magnetic Characterization of Cr Doped Sb_2Te_3

The aim of this growth run was to induce a ferromagnetic ground state in the material through doping with 3*d* transition metals into the bulk of the chalcogenide TI. Although previous work has already been carried out on Cr doped Sb_2Te_3[92] details such as film thickness were not given and the work was carried out before TIs were discovered, this work forms a much greater understanding of the nature of the doping with regards to higher Cr doping concentrations and for instance whether the doping is substitutional or interstitial and finally the impact the doping has on the magnetic properties of the TI material. A variety of techniques have been employed to investigate structural and magnetic properties of doped TIs. Here, XRD, XPS and SQUID were the main characterization methods to determine MBE growth quality.

Growth of sample number M2 - 0561: First growth run #1

Similar preliminary steps were followed to prepare the chamber and calibration of cells as discussed in the previous growth of pure Sb_2Te_3.

We started with the two step growth process involving a buffer layer of Cr-doped Sb_2Te_3 keeping the substrate temperature T_{sub} = 200°C. This was done by keeping the Sb cell again at ~ 385°C which presented a beam flux reading of ~ 8.2×10^{-8} Torr and keeping the Te cell again at 215°C which gave a beam flux pressure reading of ~ 7.8×10^{-7} Torr. In addition, we also had the Cr cell at 1100°C which gave a flux of 3×10^{-9} Torr. The flux ratios of Sb: Te was approximately 1:9.5 close to the ideal 1:10 ratio. The substrate was first moved to the "growth position" manually by rotating the manipulator after which the Sb cell along with the Te and Cr cell shutters were opened. After 20 minutes the Sb and Cr shutter were closed. The deposition of the seed layer was followed by ramping the substrate again to T_{sub} = 250°C keeping the Te cell shutter still open. After 30 minutes of annealing under a Te rich atmosphere, the Sb and Cr cell shutters were re-opened to grow Cr-doped Sb_2Te_3 for a total of 60 minutes. After the growth was finished both the shutters were closed and the cells along with the substrate were ramped down to their respective standby temperatures.

A final RHEED image was taken at the end of the final step of the growth as displayed in Figure 3.13.

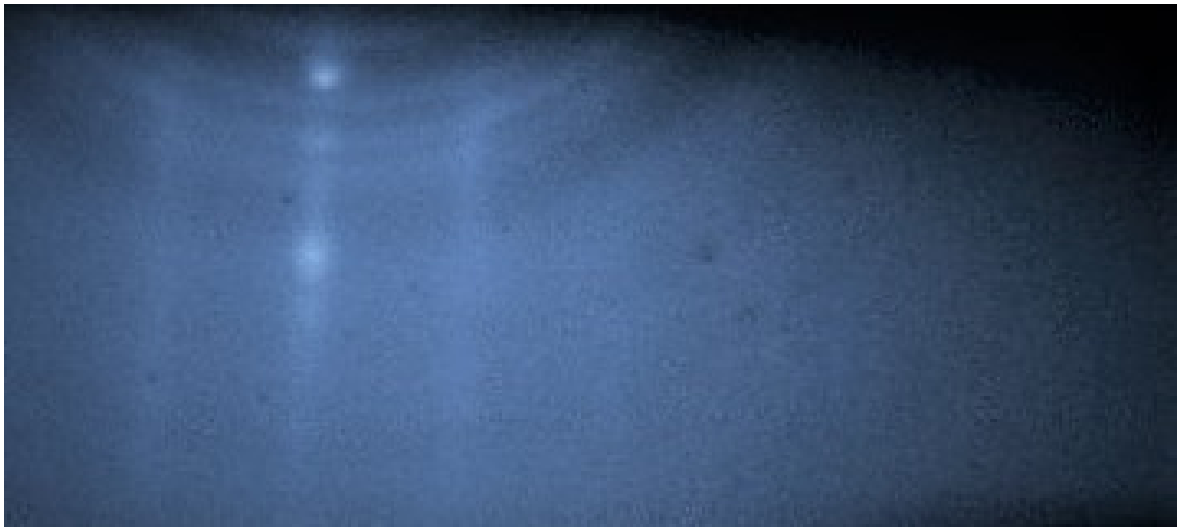

Figure 3.13 RHEED image of sample M2-0561 sample grown with a buffer layer of Cr-doped Sb_2Te_3 after the growth was completed.

By looking at the RHEED image of the growth we observed a mixture of polycrystalline behavior confirmed by the concentric ring patterns as well as some parts of epitaxial growth confirmed by a streaky like pattern. It was also noticed that the film was visually not very shiny and appeared to have some sort of a milky texture. A picture of the sample is displayed in Figure 3.14.

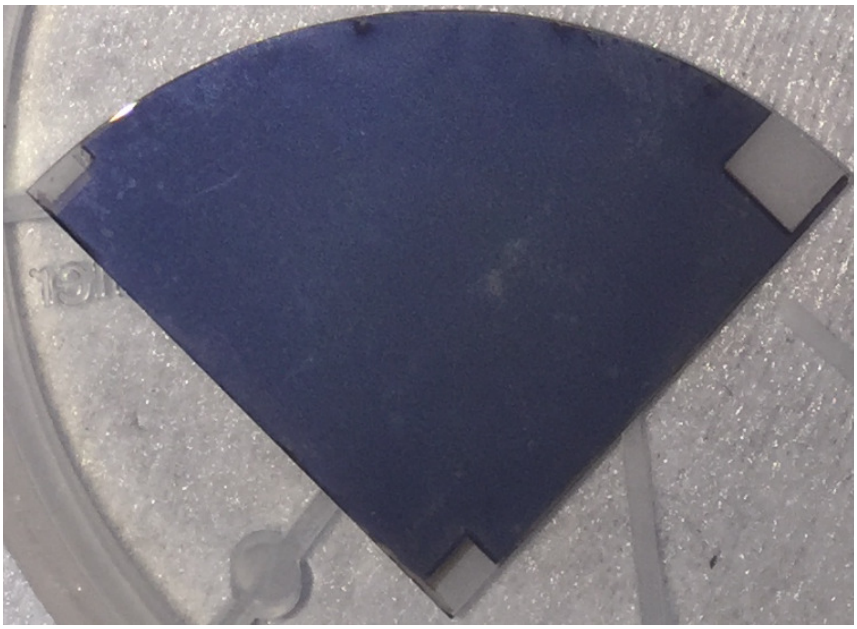

Figure 3.14 An image taken after the sample was removed from the MBE chamber, showing a milky like texture confirming a polycrystalline growth.

In summary the growth of Cr doped Sb_2Te_3 was attempted following the recipe shown in table 3.4.

Sample	Buffer layer grown for 20 mins	Annealing time in Te overpressure	Growth Temperature	Cr cell temperature	Finishing steps
M2 - 0561 Cr doped Sb_2Te_3	**5 nm of Cr doped Sb_2Te_3 at T_{sub} = 200°C**	**30 minutes**	**T_{sub} = 250°C**	**1100°C**	**take substrate and cells to standby temperatures**

Table 3.4 Growth recipe for sample M2-0561, Cr doped Sb_2Te_3

To further investigate the film, a structural analysis was carried out using x-ray diffraction to confirm their tetradymite-type crystal structure. Figure 3.15 shows the x-ray diffraction pattern of the thin film- sample number M2-0561. Along with the (0 0 *l*) peaks of Sb_2Te_3 in the hexagonal unit cell a lot of extra parasitic peaks were also visible marked in red. Although Sb_2Te_3 can be confirmed to grow along the *c*-axis direction, after comparing possible x-ray characteristic diffraction peaks from pure Sb, Te and their other compounds such as SbTe, $SbTe_2$, Sb_2Te_2 and Sb_2Te_5, traces of secondary phase formation were found from the XRD scan. All the peaks along with the substrate peak are indicated in the XRD pattern shown in figure 3.15.

The following peaks were identified and marked in red. Sb_2Te_2 (104), Cr_2Te_3 (114), Sb_2Te_2 (208), Sb_2Te (1113) and CrTe (300).

The growth highlights a number of elements that may have been non-optimal which are discussed in the points below:

a. On studying the RHEED image it is clear that the polycrystalline phase exists which may suggest the buffer layer may be too thin.
b. It could also suggest the annealing time was not sufficiently long for the sample to thermally settle post the buffer layer.
c. The Cr cell may have a very high flux even though it was calibrated, hence forming unwanted phases of Cr and Te.
d. The substrate temperature while growing may be too hot due to being in close vicinity to an extremely hot Cr cell. This is because the thermocouples attached to the substrate was below it, leading to non-uniformity in the measurement.

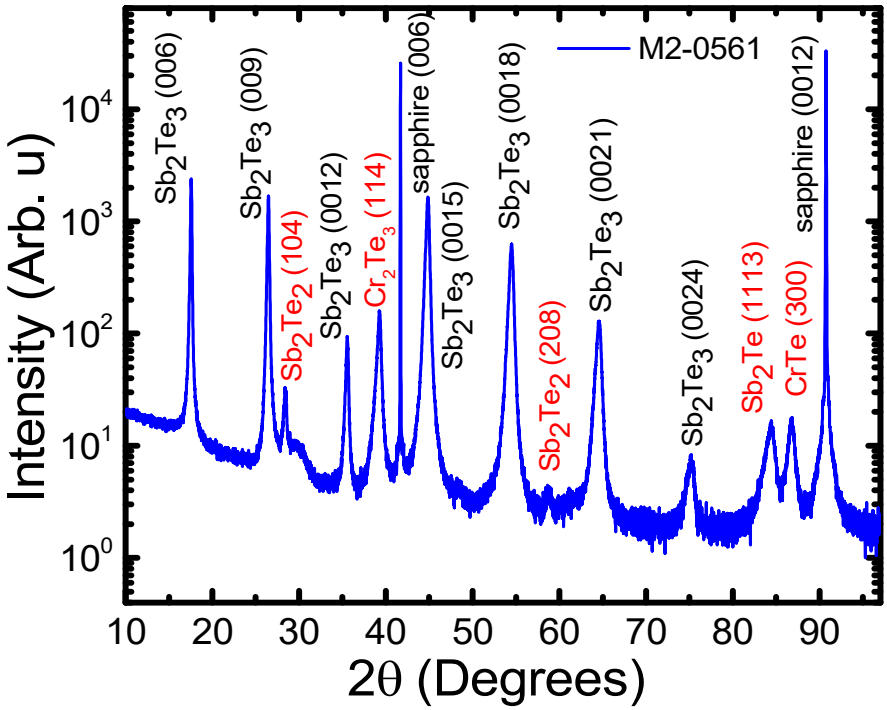

Figure 3.15 X-ray diffraction spectra (2θ) of a Cr doped Sb_2Te_3 film on Al_2O_3 (0001). The (0 0 l) film peaks (l = 3, 6, …) are labeled along with extra parasitic peaks labelled in red. The recipe followed was a two-step growth process with a 5 nm buffer layer of Cr-doped Sb_2Te_3.

Growth of sample number M2- 0562: #2

The growth of M2-0562 was the same as followed for M2-0561 but with a longer annealing time (45 minutes) and a thicker buffer (10 nm), described in brief in table 3.5.

Sample	Buffer layer grown for 20 mins	Annealing time in Te over-pressure	Growth Temperature	Cr cell temperature	Finishing steps
M2- 0562 Cr doped Sb_2Te_3	**10 nm of Cr-doped Sb_2Te_3 at T_{sub} = 250°C**	**45 minutes**	**T_{sub} = 300°C**	**1100°C**	**take substrate and cells to standby temperatures**

Table 3.5 Growth recipe for sample M2-0562, Cr doped Sb_2Te_3(thicker buffer and longer annealing)

This recipe did not seem to make much of a difference to how the sample looked on visual inspection when it was taken out of the chamber. It still had a similar non-shiny appearance as illustrated in Fig. 3.14 and also the XRD data in Figure 3.16 shows parasitic peaks again marked in red. The extra peaks identified were Sb_2Te_2 (104), Sb_2Te_2 (115), Sb_2Te_2 (208), CrTe (208) and CrTe (300) and Te (100). It was clear that increasing the buffer layer thickness to 10 nm and increasing the annealing time to 45 minutes did very little change to how the XRD looked and we continued to observe parasitic peaks.

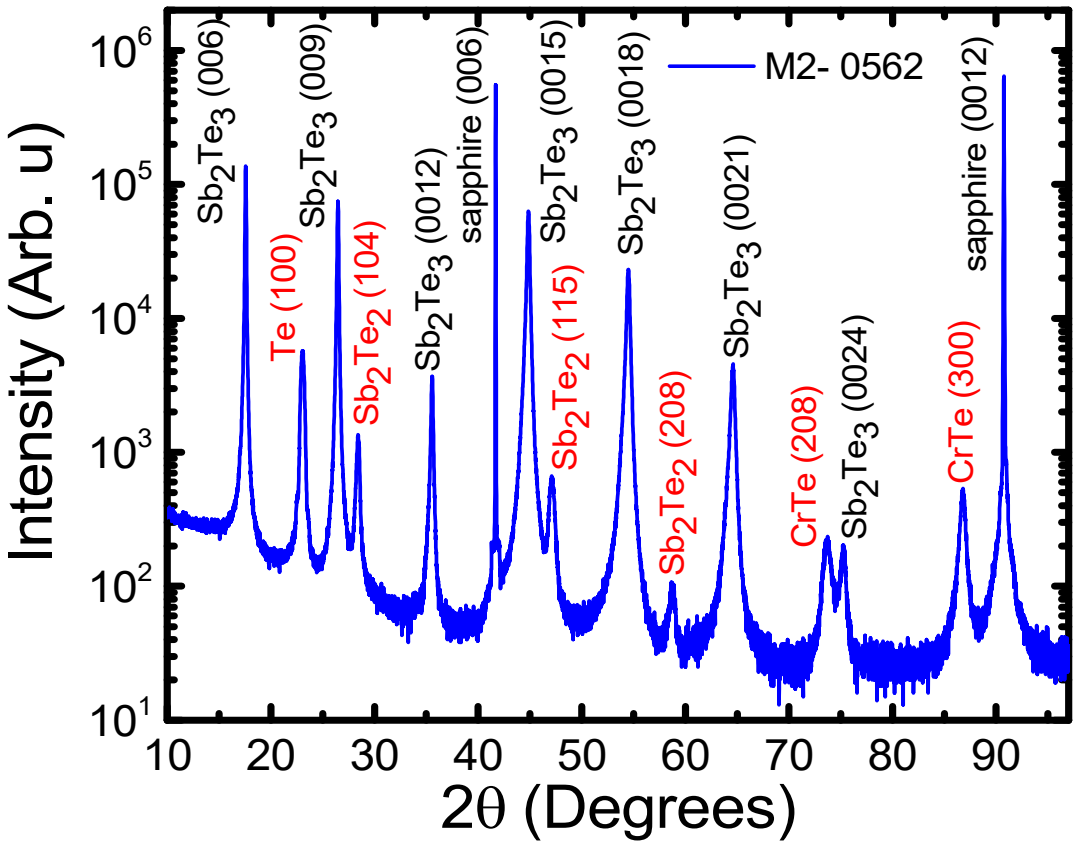

Figure 3.16 X-ray diffraction spectra (2θ) of a Cr doped Sb_2Te_3 film sample number M2 – 0562 on Al_2O_3 (0001). The (0 0 l) film peaks (l = 3, 6, …) are labeled along with extra parasitic peaks labelled in red. The recipe followed was a two-step growth process with a 10 nm buffer layer and annealing time of 45 minutes.

A few conclusions were made:

a. Here we see an extra very sharp peak from pure Te in the 100 direction at 23.04 degrees. This suggests that the increase in the annealing time in a Te overpressure to 45 minutes in this sample may have been too long.
b. The Cr flux might be too high which leads to extra phases of Cr and Te.
c. Growing a thicker buffer layer did not make any difference, we still see extra phases related to Sb and Te compounds.
d. The substrate temperature while growing may be too hot due to being in close vicinity to an extremely hot Cr cell.

It was at this point we decided to go back to think about the successful growth of un-doped Sb_2Te_3 and try a buffer layer of 5 nm of pure Sb_2Te_3 as established in sample M2-0560 and then have an extra layer of Cr doped Sb_2Te_3 in the second step.

Growth of sample number M2 – 0566 : #3

The growth of M2-0566 was the same as followed for M2-0560 but during the second growth step after the buffer layer, the Cr cell was opened.

We started with a 5-nm-thick undoped Sb_2Te_3 seed layer . The Sb cell flux was ~ 8.3×10^{-8} Torr , the Te flux pressure reading was ~ 8×10^{-7} Torr and the Cr cell again at 1100° C with a flux of 3.6×10^{-9} Torr. The flux ratio of Te per Sb was again kept at ~10:1. The seed layer was followed by an annealing step with the substrate temperature T_{sub} raised to 200°C keeping the Te cell open whilst closing the Sb cell shutter like before. The Te overpressure ensures reduction in vacancies commonly observed in this material system[90]. This was followed by the growth of the next 30 nm of Cr doped Sb_2Te_3 whilst opening the Cr and Sb cell. The summary of the growth is written in table 3.6:

Sample	Buffer layer thickness	Annealing time in Te over-pressure	Growth Temperature	Cr cell temperature	Finishing steps
M2 – 0566 Cr doped Sb_2Te_3	**5 nm pure Sb_2Te_3 at T_{sub} = 200°C**	**30 minutes**	**T_{sub} = 250°C**	**1100°C**	**take substrate and cells to standby T**

Table 3.6 Growth recipe for sample M2-0566, Cr doped Sb_2Te_3(old buffer and old annealing time)

A RHEED image was taken for this sample as shown in Figure 3.17.

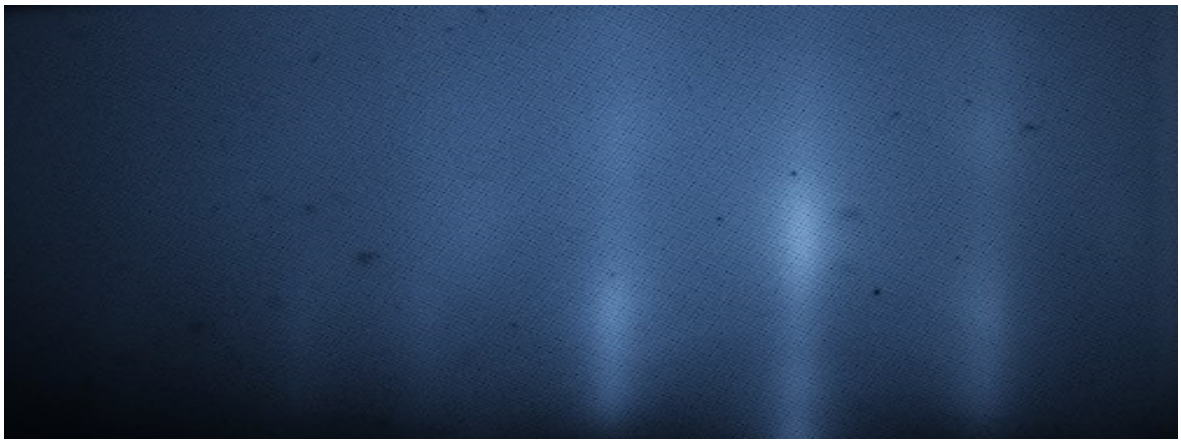

Figure 3.17 RHEED image of the sample grown with a buffer layer of undoped Sb_2Te_3 followed by Cr-doped Sb_2Te_3 after the growth was completed. The pattern was obtained along the $[10\bar{1}0]$ azimuth of Sb_2Te_3.

The RHEED pattern shows a streaky like pattern indicative of epitaxial growth. The stripes were not very sharp or bright.
Again XRD was employed to check quality of the film. The result is displayed in Figure 3.18 and shows a significant improvement. The parasitic peaks have reduced in number with only the Sb_2Te_2 phase along with a CrTe (300) peak observed marked in red.

The following conclusions were made:

a. A buffer layer of un-doped Sb_2Te_3 has improved the film quality instead of using a buffer of Cr doped Sb_2Te_3.
b. Cr flux maybe too high as CrTe (300) peak was still visible or the heat from the Cr cell is affecting the substrate temperature.

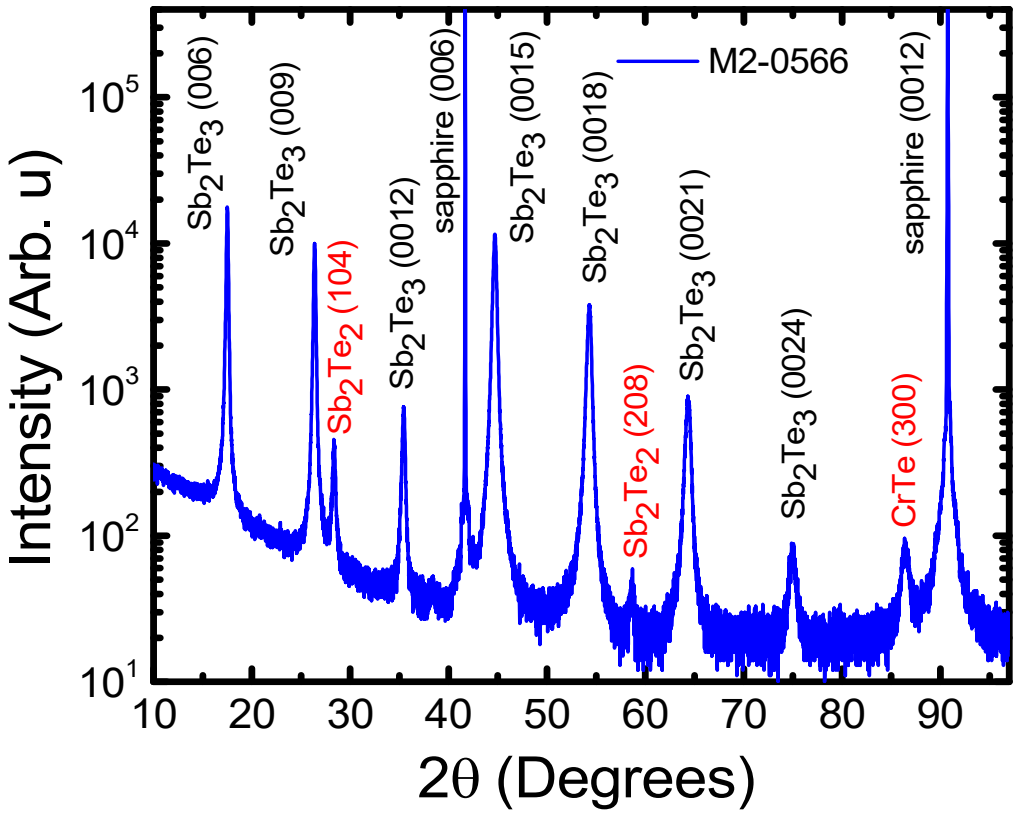

Figure 3.18 X-ray diffraction spectra (*2θ*) of a Cr doped Sb_2Te_3 film sample number M2 – 0566 on Al_2O_3 (0001). The (0 0 *l*) film peaks (*l* = 3, 6, …) are labeled along with extra parasitic peaks labelled in red. The recipe followed was a two-step growth process with a 5 nm buffer layer of un-doped Sb_2Te_3 and annealing time of 30 minutes followed by the Cr doped Sb_2Te_3 with the Cr cell 1100°C.

Table 3.7 summarizes all the imperfect growths and their recipes:

Sample ID	structure	Buffer layer And thickness	Annealing Time and T_{sub}	Cr cell temperature	RHEED	XRD
M2 -0561	Cr-doped Sb_2Te_3	Cr-Sb_2Te_3 5 nm	30 mins and T_{sub} = 250°C	1100°C	Light streaks and rings	Additional parasitic peaks visible
M2 -0562	Cr-doped Sb_2Te_3	Cr-Sb_2Te_3 10 nm	45 mins and T_{sub} = 250°C	1100°C	Light streaks and rings	Additional parasitic peaks visible
M2 -0566	Cr-doped Sb_2Te_3	Sb_2Te_3 5 nm	30 mins and T_{sub} = 250°C	1100°C	Light streaks	Very few additional peaks visible

Table 3.7 Recipe for imperfect growth on sample numbers M2-0561,0562,0566 for Cr-doped Sb_2Te_3.

Growth of sample numbers M2 – 0563, M2 – 0564, M2 – 0565 and M2 - 0567: The second growth run

The second growth run consisted of 60 nm thick Cr doped Sb_2Te_3 samples. A series of successful samples with different Cr concentrations were performed. This was done by adjusting the Cr cell temperature. The recipe is described below:

Thin film samples of nominal stoichiometry $Cr_xSb_{2-x}Te_3$ were prepared on *c*-plane sapphire substrates in a doping range of $x = 0.15$ up to $x = 0.71$. The substrates were solvent cleaned and baked for 8 hours in ultra-high vacuum to remove residual water similar to all sample preparations as before. The typical base pressure of the chamber was 1×10^{-10} Torr. The samples were grown with an overpressure of Te at a typical flux ratio of (Cr + Sb) : Te = 1 : 10, as measured by the in situ beam-flux monitor. The films were grown via a two-step deposition method, where a ~5 nm Sb_2Te_3 nucleation layer was first deposited at a lower substrate temperature (T_{sub} = 200 °C), which was then annealed under a Te flux after which the temperature was raised to (T_{sub} = 250 °C) whilst opening the Cr and Sb cells for the growth of the $Cr_xSb_{2-x}Te_3$ layer. For each sample, the Cr flux was different, controlled by the Cr cell temperature. An example of a sample is shown in the Figure 3.19 which visually looks like a shiny piece with a greyish bluish appearance.

Figure 3.19 An image taken after the sample M2-0563 was taken out of the MBE chamber, showing a shiny like texture hinting towards a good quality growth. A sharp reflection can be observed on looking at the sample.

Table 3.8 summarizes the successful samples and their recipes.

Sample ID	structure	Cr cell temperature	Annealing Time and T_{sub}	RHEED	Buffer layer And thickness	XRD
M2 -0563	$Cr_{0.42}Sb_{1.58}Te_3$	1060°C	30 mins and T_{sub} = 250°C	Light streaks	Sb_2Te_3 5 nm	Clean
M2 -0564	$Cr_{0.26}Sb_{1.74}Te_3$	1050°C	30 mins and T_{sub} = 250°C	Light streaks	Sb_2Te_3 5 nm	Clean
M2 -0565	$Cr_{0.15}Sb_{1.85}Te_3$	1040°C	30 mins and T_{sub} = 250°C	Light streaks	Sb_2Te_3 5 nm	Clean
M2 -0567	$Cr_{0.71}Sb_{1.58}Te_3$	1070°C	30 mins and T_{sub} = 250°C	Light streaks	Sb_2Te_3 5 nm	Clean, one extra peak and shoulders

Table 3.8 Summary of the recipes for ~ 60 nm thick successfully grown samples of Cr-doped Sb_2Te_3 with different Cr concentrations. “Clean” refers to an absence of intensity from secondary phases.

The doping concentrations mentioned in the table above were determined using Rutherford backscattering spectrometry (RBS). It is found that the Cr dopant incorporated in the crystal follows the expectation based on the in situ measurement of beam fluxes. These measurements were performed by Aakash Pushp at the IBM research center in USA the details of which are described in reference[91].

RHEED images for all the samples taken at the end of each growth are summarized Figure 3.20(a-f) indicating that the films grow with their *c*-axis perpendicular to the plane of the substrate and streak-like diffraction corresponding to a near 2D mode of growth. If the sample were rotated by 180°, the RHEED pattern repeated itself 3 times indicative of a 3-fold symmetry while a twinning effect may be seen in some cases as shown in Figure 3.20 (c and f).

(a) M2 -0563

(b) M2 -0564

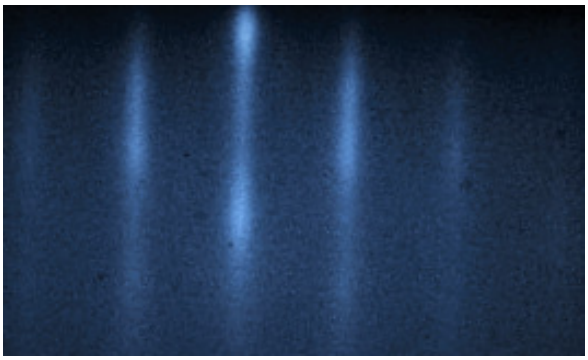

(c) M2 -0564 rotated by 60°

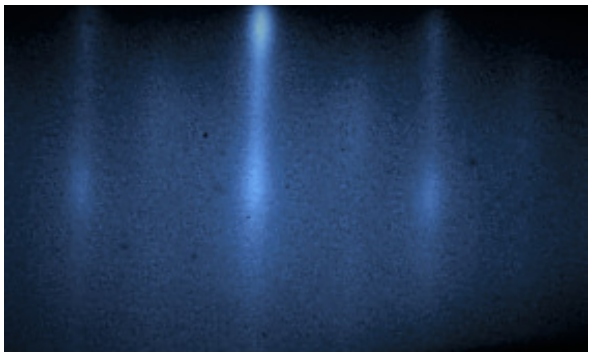

(d) M2 -0565

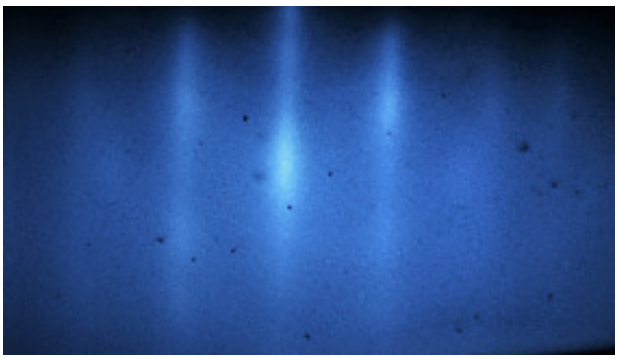

(e) M2 -0567

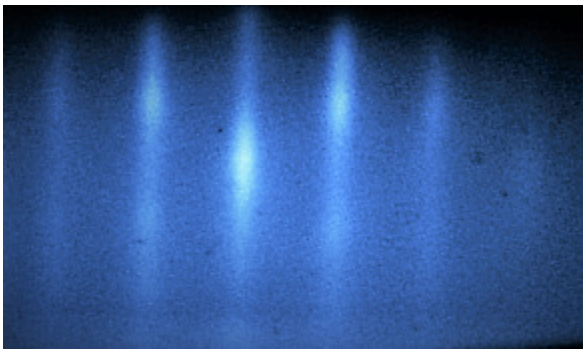

(f) M2 -0567 rotated by 60°

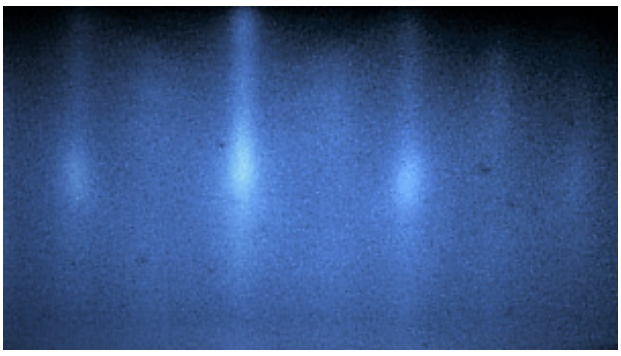

Figure 3.20 RHEED image of the sample grown with a buffer layer of undoped Sb_2Te_3 followed by Cr-doped Sb_2Te_3 after the growth was completed. Images (a),(b),(d) and (e) were obtained along the $[10\bar{1}0]$ azimuth of Sb_2Te_3 while images (c) and (f) were obtained along the $[11\bar{2}0]$ azimuth of Sb_2Te_3.

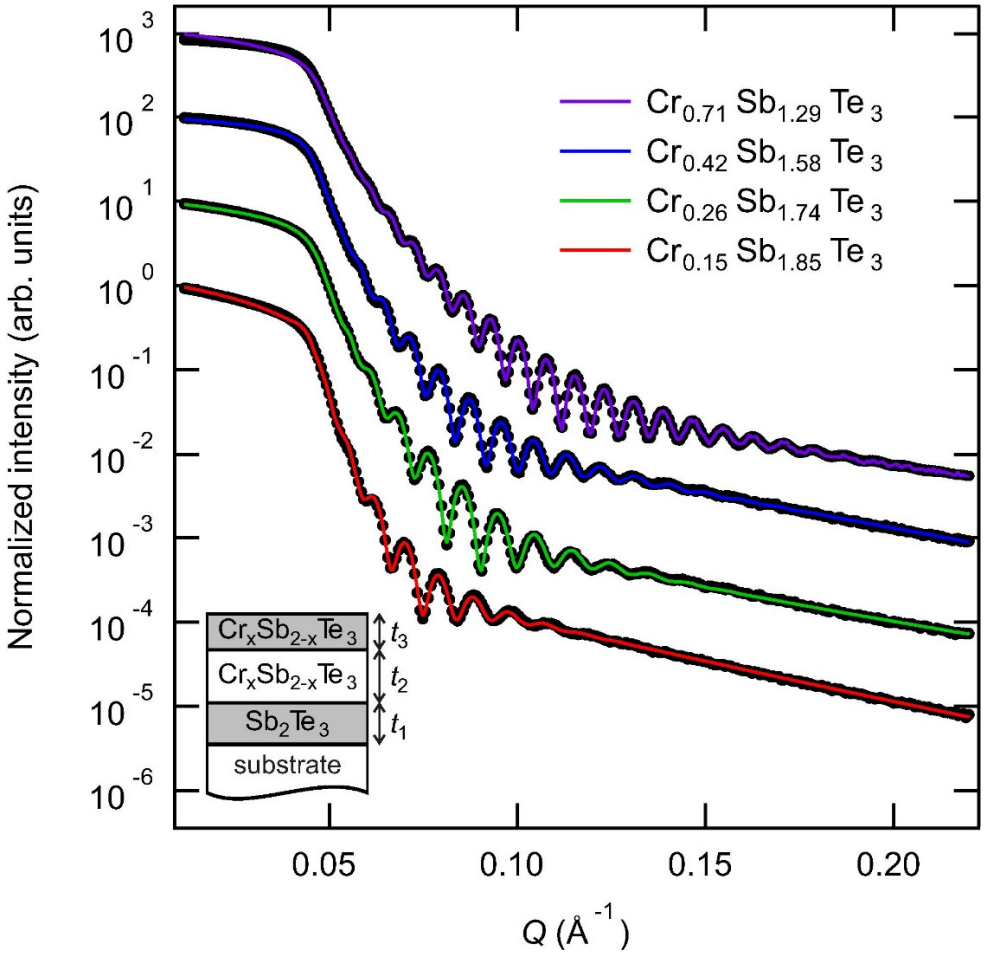

Figure 3.21 XRR plots showing the measured data (colored dots) and fitted film structure (colored lines) for films with a Cr concentration of x = 0.15, 0.26, 0.42 and 0.71. The intensities have been normalized to the maximum intensity, and offset in increments of 10 for clarity. The inset shows a diagram of the three-layer model used for the fit.

XRR and XRD was carried out on all the samples and the results displayed in the Figure 3.21 and 3.22. XRR data were fitted using a three-layer model in the GenX package[93] to account for the grown nucleation layer as shown in the inset of Figure 3.21. The thicknesses used for the three layers may be considered correct only in their total thickness, but have a greater degree of uncertainty in their individual thicknesses. This is due to the density parameter fluctuating only slightly between each layer to accommodate the Cr dopant. Due to this, it makes little sense to quote in detail the interfacial mixing between each layer. Instead, the calculated roughness parameters are stated as a total interfacial roughness (RMS of all interfacial values) plus the surface roughness[91]. The key parameters from the model fitted to the measured XRR data are shown in table 3.9.

Cr concentration *x* from RBS	Layer thickness (Å)			Roughness (Å)	
	t_1 (Sb_2Te_3)	t_2 ($Cr_xSb_{2-x}Te_3$)	t_3 ($Cr_xSb_{2-x}Te_3$)	Interfacial	Surface
0.15	50.0	600.550	37.575	18.96	75.0
0.26	54.7	557.47	31.06	13.73	50.00
0.42	85.37	603.19	8.261	13.33	24.65
0.71	51.1	716.20	22.86	13.17	16.75

Table 3.9 XRR fitting thicknesses of each layer for Cr-doped Sb_2Te_3 samples with different Cr concentrations *x*.

It can be seen from the values in the table above, that there is a small difference in the total film thickness as a function of Cr doping. Equally the interfacial roughness shows no significant systematic variation. However, the surface roughness of the film shows a clear trend toward smoother films at higher doping concentrations. It is reasonable to assume that this reduction in the surface roughness at higher Cr concentrations comes from a disruption of the growth mode of the film. Sb_2Te_3 will generally grow in triangular formations with well-defined terraces which have a naturally high surface roughness due to the island-like formations. If this growth mode is disrupted and smaller islands form at higher doping levels, this would lead to an overall smoother film from an x-ray perspective. It is also possible that an oxidation layer may lead to a smoother surface as XRR does not distinguish between roughness caused by Cr doping or oxidation roughness.

XRD data shows that the films are well ordered with their *c*-axis parallel to the surface normal of the sample. For increasing Cr doping concentration a clear shift in the peak positions towards higher angles was observed. The shift of this peak was studied in detail. In particular the 0015 peak was magnified precisely to determine the shift in the peaks with regards to increasing Cr concentration as shown in Figure 3.23. All peaks were fitted using Gausians and the *c*-lattice parameters were extracted using the following relationship:

$$\frac{1}{d_{hkl}^2} = \frac{4}{3}\frac{h^2 + hk + k^2}{a^2} + \frac{l^2}{c^2}$$

where d_{hkl} is the distance between (*h,k,l*) planes. The (00.3), (00.6), (00.9), (00.12), (00.15), (00.18) and (00.21) peaks in the X-ray diffraction pattern give the values of $d_{00.l}$ (l=3, 6, 9, 12, 15, 18 and 21) which can be used for calculating the lattice constant *c*.

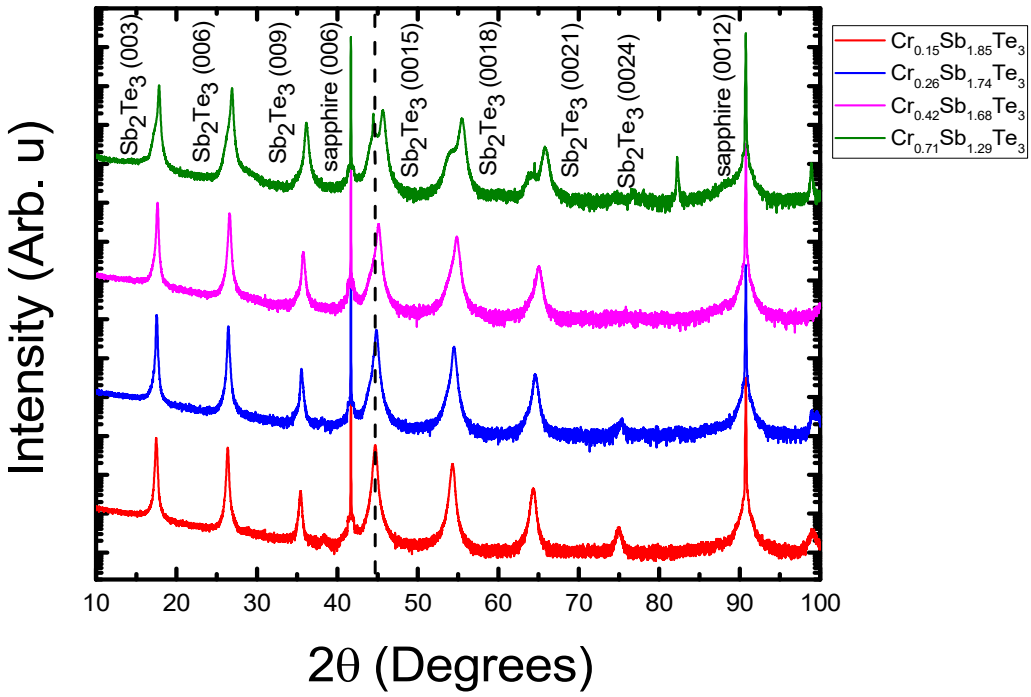

Figure 3.22 X-ray diffraction of varying Cr doping concentrations of $Cr_xSb_{2-x}Te_3$. There is a clear shift of the peak positions towards higher angles (smaller *c*-axis lattice constant) as a function of increasing Cr doping marked with a black dashed line. At the highest measured Cr doping ($x = 0.71$) the (0015) peak is split (curves offset for clarity).

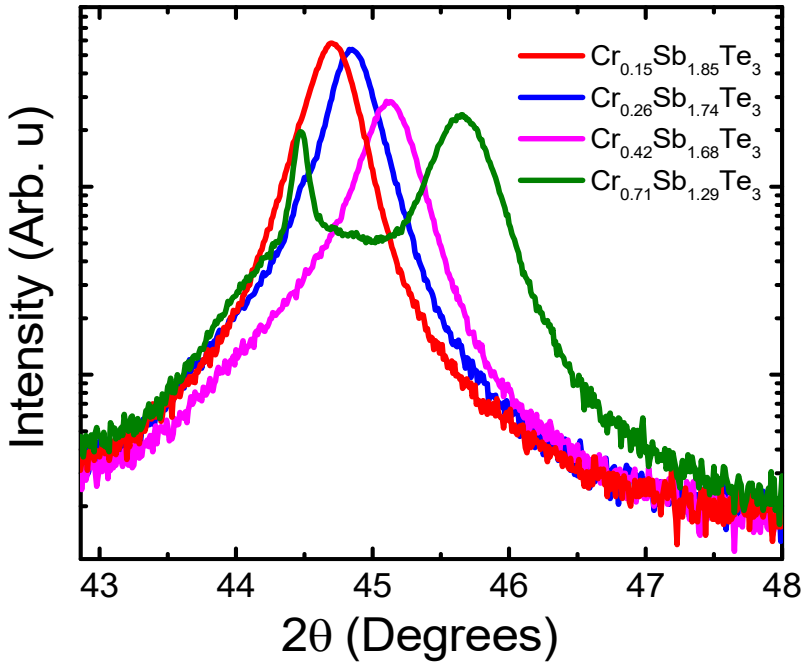

Figure 3.23 X-ray diffraction looking at the 0015 peaks with varying Cr doping concentrations of $Cr_xSb_{2-x}Te_3$.

For increasing Cr doping concentration a reduction in the *c*-axis lattice parameter from 30.458˚A for undoped Sb_2Te_3 to 30.395 Å (x = 0.15), 30.308 Å (x = 0.26), 30.127 Å (x = 0.42) and 29.816 Å (x = 0.71) for the doped samples were observed, consistent with the idea of substitutional doping with an element with a smaller ionic radius. At the highest doping level a peak splitting is observed, most obviously at the (0015) reflection. It is challenging to match this to a specific parasitic phase, given the strain present within the host crystal. However, it may be consistent with the formation of the Cr_2Te_3 phase, which in the unstrained bulk has a (110) reflection at 46.323° at this wavelength[94]. This reduction of the lattice parameter was similarly observed for the analogue system $Cr_xBi_{2-x}Se_3$[95,96], where it was ascribed to a contraction of the Cr-Se bond length compared with the Bi-Se bond length when substituting on the Bi site.

The magnetic properties of the grown films were investigated using SQUID magnetometry. All measurements were carried out at the Rutherford Appleton Laboratory in collaboration with Liam Collins Mcintyre. We were granted access to use the SQUID at Diamond Light Source.

SQUID measurements were made of the field dependence, *M(H)*, and temperature dependence, *M(T)*, for all the $Cr_xSb_{2-x}Te_3$ samples with varying Cr doping levels. All samples showed ferromagnetic behavior at low temperature, with their easy axis of magnetization parallel to the *c*-axis (out-of-plane). The *M(H)* data curves were processed by removing the linear diamagnetic background contribution of the Sapphire substrate at high fields. The data shown in Figure. 3.24 (a) is of the film with the substrate contribution removed. The units of the y-axis were scaled using the sample volume measured using a weighing scale, the Cr concentrations given to us from RBS measurements and the density from the XRR data.

The full set of measurements obtained from SQUID magnetometry [Figures. 3.24 (a) and (b)] shows temperature-dependent *M(H)* loops for the $Cr_{0.26}Sb_{1.74}Te_3$ sample with the field applied parallel and normal to the *c*-axis, respectively. For the in-plane measurements, the sample achieves a total saturation magnetization of (2.6 ± 0.2) μ_B /Cr, and out-of-plane of (2.2 ± 0.2) μ_B /Cr, respectively at 5 K. The error bars in measurement is mainly the statistical error in the determination of film volume, which is calculated based on the densities estimated in the XRR fits combined with the cross-sectional area of the substrate material. There was also a statistical contribution from uncertainty in the determination of doping concentration from RBS results. This value is less than the expected value of 3 μ_B/Cr.

However, it has been observed for Cr-doped Bi_2Se_3 that hybridization between the Cr-*d* and Se-*p* orbitals can cause some covalency, effectively reducing the oxidation state of the Cr dopant[95], and a similar effect may be anticipated in this system. Figures 3.24 (c) and (d) show the measured *M(H)* for a range of Cr-doped samples at T = 5 K for in-plane and out-of-plane applied fields respectively. All samples show ferromagnetic behavior. The magnitude of saturation magnetization was independent of doping concentration for all but the highest doping level, where clusters of Cr or parasitic (e.g., Cr_2 Te_3) phases may contribute to the magnetic order. *M(T)* measurements were taken whilst cooling in a 2 mT field applied parallel to the ab-plane, as shown in Figures 3.24 (e) and (f). The diamagnetic contribution to the signal was removed. All samples show a clear paramagnetic to ferromagnetic transition, with the Curie temperature T_c varying strongly with doping concentration. The T_c was identified from the smoothed first derivative of each curve [Fig. 3.24 (f)] and varied between 28 K for the lowest doping concentration, up to 186 K for the highest doping concentration.

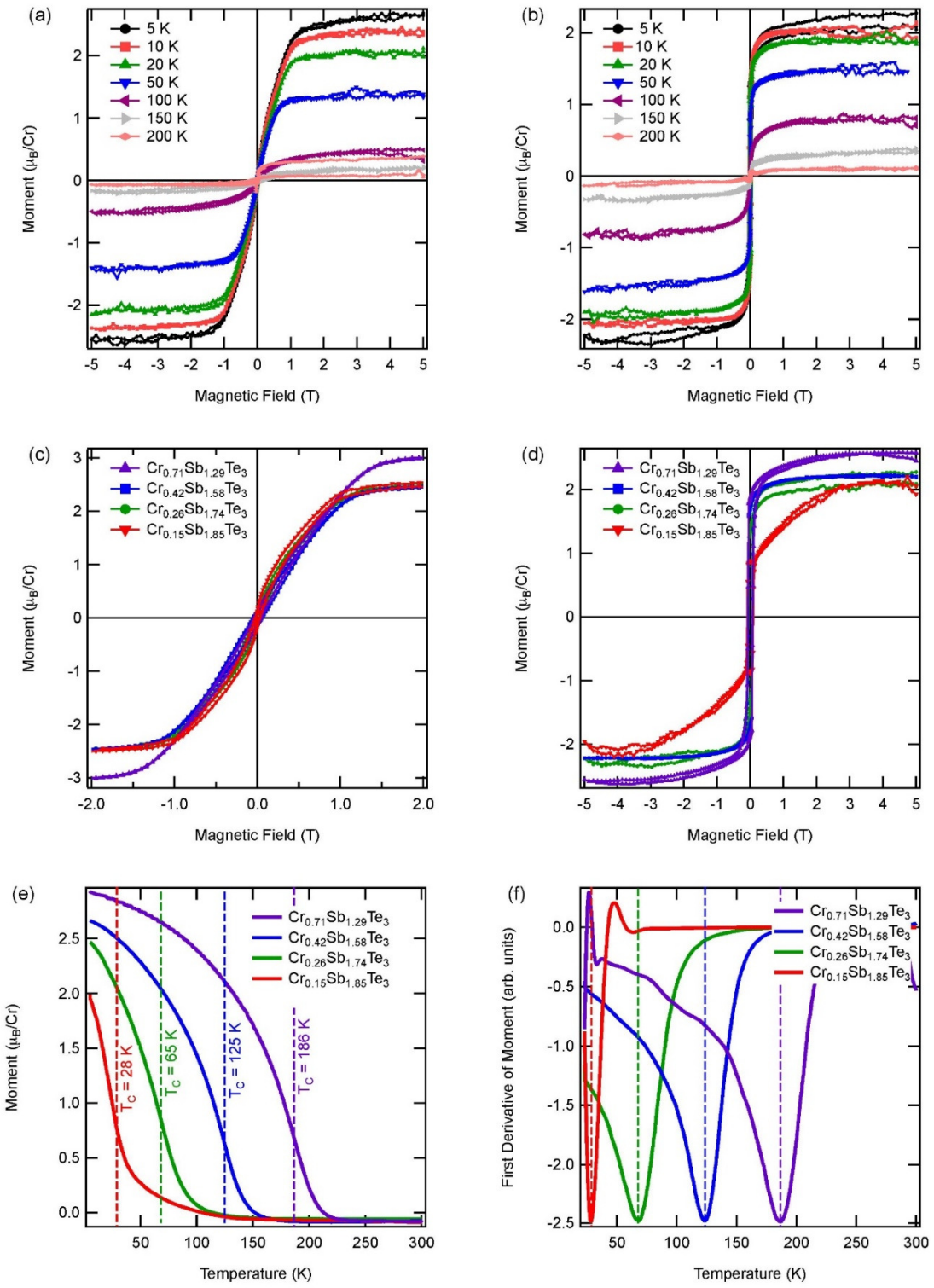

Figure 3.24 (a,b) Magnetization curve, *M(H)*, of $Cr_{0.26}Sb_{1.74}Te_3$ film measured at varying temperatures with the field in-plane and out-of-plane. (c,d) Magnetization curve of multiple samples of varying doping levels at 5 K with the field applied in-plane and out-of-plane. (e) Temperature dependence of magnetization *M(T)* of samples of varying Cr doping measured whilst cooling in a 20 mT applied out-of-plane field. The observed transition temperatures are marked. (f) First derivative of *M(T)*, used to extract T_c.

After thicker samples of Cr-doped Sb_2Te_3 were grown successfully and characterized using XRD, XRR and SQUID, to perform electrical transport measurements it would be more suitable for the films to be thinner, which would reduce any bulk conduction/contribution from the film and concentrate more on the surface states to probe the topological properties. The main motivation behind this was to observe the quantum anomalous Hall effect which had not been seen in this material system and was predicted theoretically[59,97–99]. Electrical transport is performed in great detail in the next chapter.

Growth of Samples M2 - 0574 , M2 - 0575, M2 - 0576 and M2 – 0577

The MBE growth of these samples followed a similar two-step growth recipe as followed before with an exception of the final growth step for a shorter time period (40 mins in total) to account for the thinner thickness, described briefly in table 3.10. To account for electrical transport measurements for the purpose of protection of the surface, we also grew a ~ 1 nm capping layer of Te keeping the substrate at room temperature.

Sample ID	structure	Buffer layer And thickness	Annealing time and T_{sub}	Cr cell temperature	XRD
M2 -0574	$Cr_{0.15}Sb_{1.85}Te_3$	Sb_2Te_3 5 nm	30 mins and T_{sub} = 250°C	1030°C	Clean
M2 -0575	$Cr_{0.41}Sb_{1.59}Te_3$	Sb_2Te_3 5 nm	30 mins and T_{sub} = 250°C	1040°C	Clean
M2 -0576	$Cr_{0.58}Sb_{1.42}Te_3$	Sb_2Te_3 5 nm	30 mins and T_{sub} = 250°C	1060°C	Clean
M2 -0577	$Cr_{0.76}Sb_{1.24}Te_3$	Sb_2Te_3 5 nm	30 mins and T_{sub} = 250°C	1070°C	Clean

Table 3.10 Summary of the recipes for ~ 20 nm thick successfully grown samples of Cr-doped Sb_2Te_3 with different Cr concentrations.

These samples were transported to Cambridge to conduct electrical transport measurements on them, where also doping concentration studies along with structural analysis were performed.

XPS measurements were performed in the optoelectronic group in the Physics department with the help and collaboration of Satya Prasad Senanayak. The measurements were performed to explore the effect of Cr doping on the bonding properties of the topological insulator Sb_2Te_3. XPS was measured using a Kα (Thermo Fisher Scientific) X-ray photoelectron spectrometer, equipped with a monochromatic Al Kα source. All XPS spectra were fitted by Gaussian functions with simultaneous optimization of the background parameters. Figure 3.25 shows the entire XPS scan with all labelled peaks. Upon fitting the peaks we observe that it is possible to change the doping levels in $Cr_xSb_{2-x}Te_3$ sample from $x = 0.15$ to $x = 0.76$. The lowest doped sample shows contaminants identified as Ag and Cl which were not present in any of the other films. Since $x = 0.15$ was the first sample to be measured by XPS, we assumed these may be contaminants from an earlier sample measured on the XPS system.

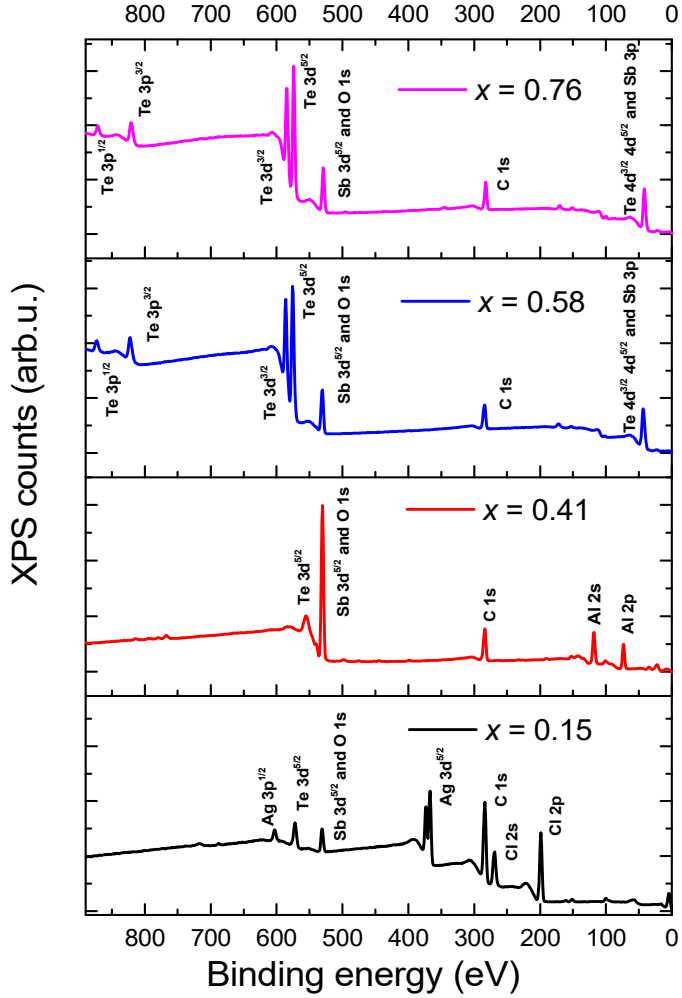

Figure 3.25 XPS spectra for all the $Cr_xSb_{2-x}Te_3$ samples with x varying from 0.15 to 0.76. All peaks are labelled with their corresponding binding energy.

Figure 3.26 (a) shows the shift in the spectra of the Sb 3*d* peaks upon the introduction of the Cr dopant. In pristine sample of Sb_2Te_3 the Sb 3*d* peak is expected at 528-529 eV. A small shift to 530.5 eV in the present case for sample with the lowest doping (x = 0.15) can be attributed to surface oxidation (labeled with arrows). Upon increasing the Cr concentration, the peaks shift close to un-oxidized pristine value of 528 eV, thus indicating the doping of Cr in Sb_2Te_3 samples prevents further oxidation of the sample which is consistent with earlier reports[61,100]. In other words, Cr atoms are more prone to oxidation compared to the Sb atoms and upon substitution the degree of surface oxidation of the sample is minimized. This conceivably demonstrates that the Cr atoms are substituting the Sb atoms in the structure. A negligible shift in the XPS pattern of Te 3*d* peaks [Figure 3.26 (b)] is observed upon increasing the dopant concentration for the peaks at 573, 583 eV (Te 3d), and 575 ,586 eV (Te-O). Moreover, it is difficult to ascertain the substitution of the Cr at Te sites due to the fact that the peaks corresponding to the Te (3*d*) and Cr (2*p*) binding energies closely resembles each other. Nevertheless, we have demonstrated in our thicker samples that the Cr atoms substitute with an ion of a smaller ionic radius, *i.e.* Sb[91].

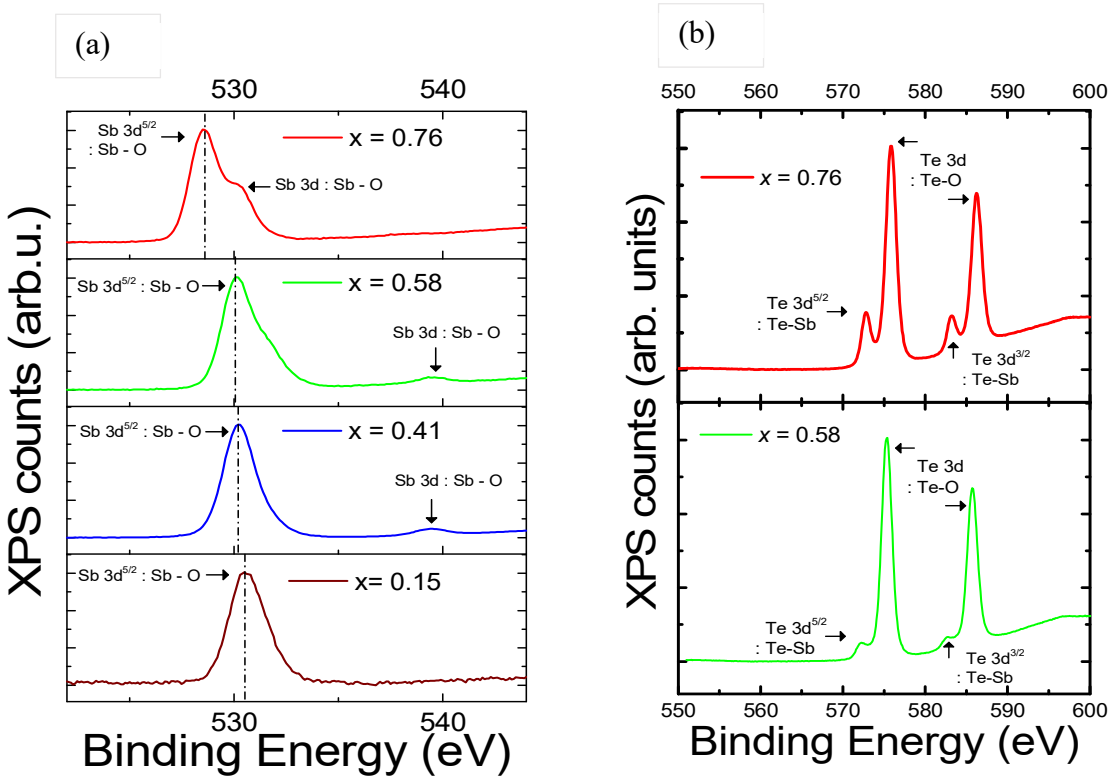

Figure 3.26 (a) XPS spectra obtained from the 3*d* Sb shell. Upon increasing the Cr concentration x, the peaks shift towards lower energy indicating the doping of Cr into Sb sites. (b) XPS spectra in the Te 3*d* region as a function of Cr concentration x, showing a very small shift in the peaks.

XRD was also carried out to confirm their tetradymite-type crystal structure shown in the Fig. 3.27 (a). All samples display the (0 0 *l*) peaks, confirming that the films grow along the *c*-axis direction. After comparing possible x-ray characteristic diffraction peaks from pure Sb, Te and their other compounds such as SbTe, $SbTe_2$ and Sb_2Te_5, no traces of any secondary phase formation were found from the scans for all samples. Also ruling out any secondary phases to Cr and Te compounds even for the highest doped samples with $x = 0.76$. For increasing Cr doping concentration a reduction in the *c*-axis lattice parameter from 30.393 Å in a sample with $x = 0.15$ to 30.177 Å ($x = 0.41$), 30.057 Å ($x = 0.58$) and 29.834 Å ($x = 0.76$) for the highest doped samples is observed marked by a shift in the (0 0 *l*) peaks (dotted line), consistent with the idea of substitutional doping. It is interesting to note that $x = 0.71$ for a thicker $Cr_xSb_{2-x}Te_3$ has an impurity phase whereas a thinner sample with $x = 0.76$ seems not to have any impurity phases in it, the only difference being the thickness.

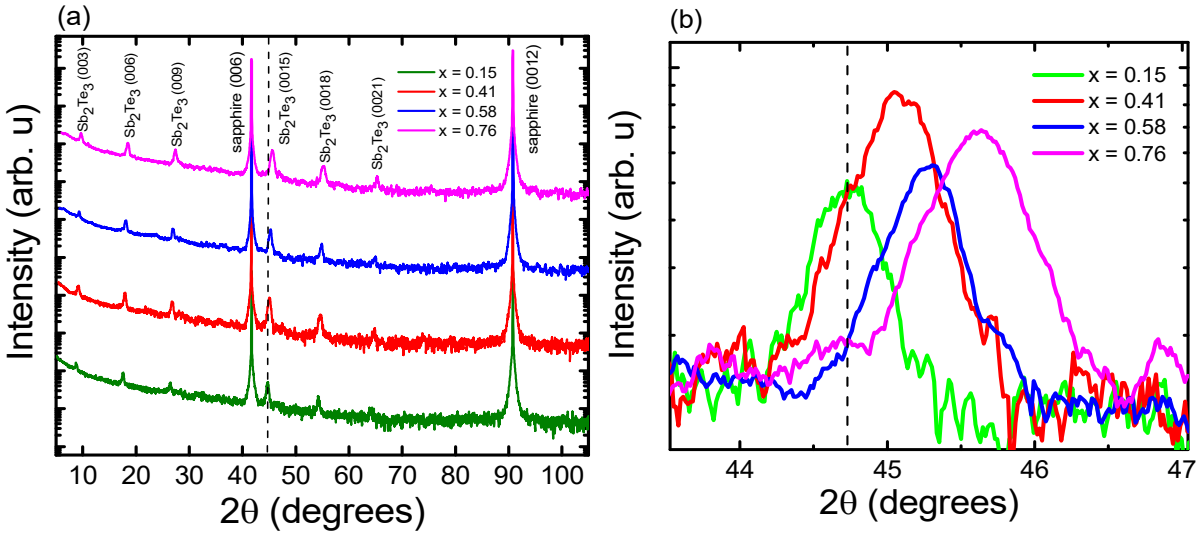

Figure 3.27 (a) X-ray diffraction spectra (2θ) of the Cr-doped Sb_2Te_3 film on Al_2O_3 (0001) as a function of Cr concentration *x*. The (0 0 *l*) film peaks (*l* = 3, 6, …) are labeled. The dashed vertical line indicates the position of the peak for the lowest doping concentration, and a shift of the peak position to larger angles (smaller *c*-axis lattice constants) is found with increasing doping concentration (Curves offset for clarity). (b) X-ray diffraction looking at the 00<u>15</u> peaks with varying Cr doping concentrations of $Cr_xSb_{2-x}Te_3$.

XRR data were fitted using a three-layer model in the leptos software[93] with the help of Razan Aboljadeyal. The total thickness may be considered accurate compared to individual layer thicknesses as before. Here we have added a TeO_2 layer on top to account for a capping layer. The key parameters from the model fitted to the measured XRR data are shown in table 3.11.

Cr concentration *x* from XPS	Layer thickness (nm)			Roughness (nm)	
	t_1 (Sb_2Te_3)	t_2 ($Cr_xSb_{2-x}Te_3$)	t_3 (TeO_2)	Interfacial	Surface
0.15	6.2294	11.5292	1.62157	5.83113	1.869
0.41	4.1791	13.0090	1.64514	2.5799	1.5313
0.58	6.8025	11.3132	1.91192	6.7185	1.1111
0.76	4.1782	14.4641	1.81256	2.7716	1.7428

Table 3.11 XRR fitting thicknesses of each layer for Cr-doped Sb_2Te_3 samples with different Cr concentrations *x*.

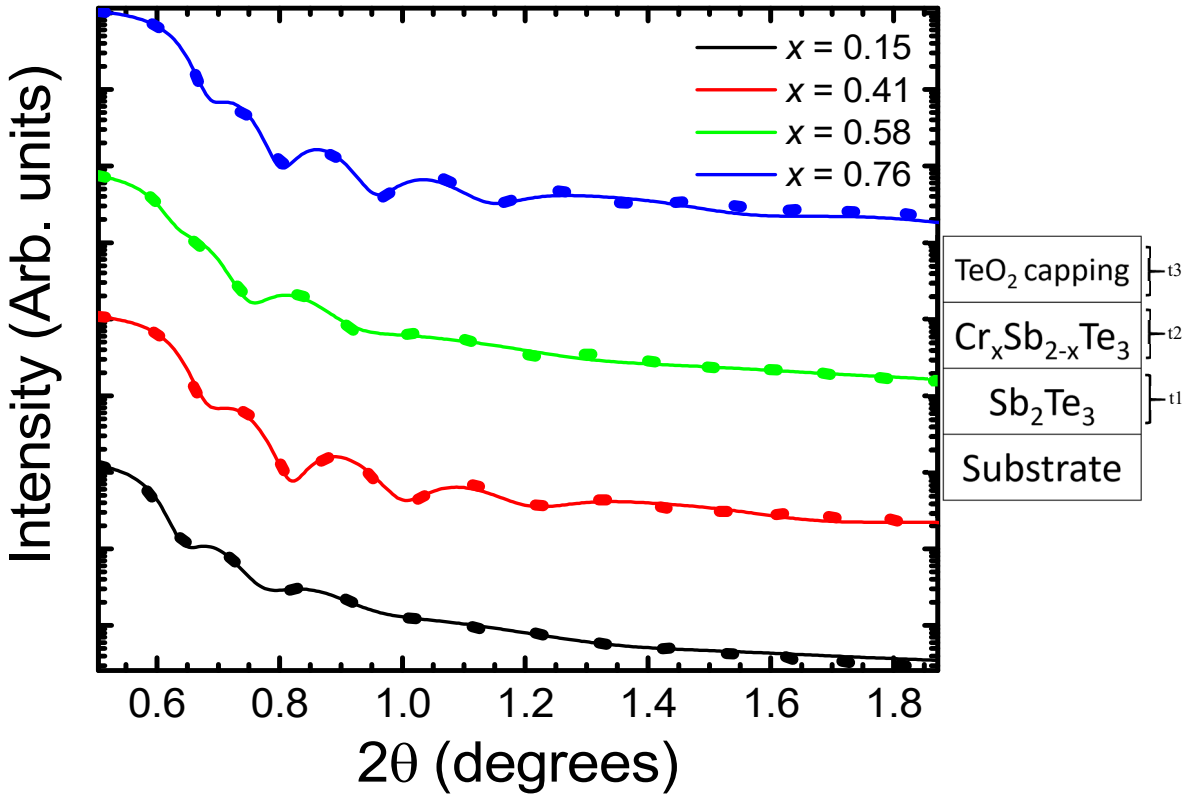

Figure 3.28 XRR plots showing the measured data (in black) and fitted film structure (colored lines) for films with a Cr concentration of x = 0.15, 0.41,0.58 and 0.76. The intensities have been normalized to the maximum intensity, and offset in equal increments for clarity. The inset shows a diagram of the three-layer model used for the fit (curves offset for clarity).

3.6 Conclusion

In summary, we have successfully prepared several thicknesses of $Cr_xSb_{2-x}Te_3$ thin films with *x* varying from 0 to 0.76 by MBE following a two-step growth recipe. Ferromagnetism that extends to temperatures of at least 186 K was found and confirmed by SQUID magnetization, the highest reported in literature in this material system. Although higher chromium doping obviously gives a higher Curie temperature, some issues are made clear such as the role the chromium impurity in the Sb_2Te_3 matrix using XRD. A clear shift in the intensity of the peaks with increasing Cr doping suggests substitutional doping *i.e.* Cr replaces Sb sites in all the samples. According to the SQUID results, Cr with 2+ valence states is very likely involved rather than the expected Cr 3+. Detailed studies of the electronic structure are needed in order to shed light on actual valence state and bonding of Cr in the Sb_2Te_3 matrix, such as ARPES, XMCD and XAS. In the following chapter, a systematical study will be devoted to Cr-doped Sb_2Te_3 thin film samples regarding electrical transport, Magneto-optical Kerr measurements and Terahertz time domain spectroscopy measurements. Additional information will be collected and more detailed properties of tetradymite-type DMS are expected to be revealed.

4. Chapter 4

Electrical Transport on Magnetically-Doped Topological Insulator Thin Films and Heterostructures

4.1 Introduction and Motivation

The term "topological insulator" was first introduced in 2007 to generalize the two-dimensional quantum spin Hall state to three dimensions[63,64]. The key reasons were the presence of TRS and spin-momentum locking[35,101]. Since then researchers have been in search of exotic quantum phenomena which can potentially revolutionize the field of condensed matter physics. Transition metal doping in TIs is predicted to break the TRS which opens a surface gap at the Dirac point[33,57]. Recently the QAHE[59] was experimentally observed in Cr doped $Bi_xSb_yTe_3$ thin films after being initially theoretically predicted in topological material systems[98,102]. This QAHE in the form of a dissipationless transport edge state may facilitate the development of low-power consumption devices using electron spins, opening there-by new avenues for spintronics. Generating a spin polarized current, manipulating the spin state, while preserving the spin polarization, and sensing the polarization are basic building blocks for the realization of spin-technologies. The easiest way to achieve this was to simply pass a current through a ferromagnetic material. In the 60s ferromagnetic transition metals were considered to do just this, as their Curie temperatures were above room temperature. This had now to be integrated into semi-conductor devices in order to enhance their functionality by exploiting the spin-degree of freedom in addition to the charge of the electrons. However, the efficiency of spin injection into semi-conductors was found to be close to only 1%[103]. The reason was fairly obvious, while taking measurements, a Schottky barrier formed at the interface between the metal–semiconductor material due to a conductivity mismatch. A few years later, advances were made to develop ferromagnetic semiconductors such as $Ga_{1-x}Mn_xAs$ which were believed to have a higher spin injection efficiency. Doping with magnetic impurities was found to be a suitable approach to induce long range ferromagnetic order in a semiconductor or insulator, if the exchange coupling between the magnetic impurities was indirect and the impurities were far from each other. Although ferromagnetism in semiconductors had been previously observed

in some materials such as Eu chalcogenides[104] as early as in the 1960s, due to fabrication difficulties the low Curie temperature and lack of reliable doping control, mainstream use of industrial materials such as GaAs and silicon are yet to be replaced with ferromagnetic semiconductors. Transition metals and rare earth materials play an important role as magnetic impurities since they have partially filled *d*- and *f*- states. These partially filled states have unpaired electrons which can give rise to magnetic behaviour in semiconductors/ TIs. The motivation behind this work was to electrically characterize magnetically doped TI materials and to study the induced magnetism by controlling the anomalous Hall voltage signal on magnetically doped TIs.

This experimental chapter covers a brief literature review study followed by the electrical transport of the transition metal-doped tetradymite-type semiconductor – Cr doped Sb_2Te_3 thin films which were grown at the University of Oxford as described in the earlier MBE Chapter 3. Identical Hall bars were fabricated on various samples with varying Cr concentrations in $Cr_xSb_{2-x}Te_3$ on 20 nm thin films with x ranging from 0.15 to 0.76. In addition, the study on the electrical and magnetic properties of this material was extended to include terahertz time domain spectroscopy (THz-TDS) and magneto-optical Kerr effect (MOKE) measurements. MOKE measurements were performed along with Jieyi Liu in the TFM group, while the THz measurements were performed in collaboration with Varun Kamboj from the SP group.

4.2 Literature Review

The idea of doping TIs with magnetic impurities has gained much interest recently, even though DMSs have been studied for over two decades[99]. Combining the properties of semiconductors with those of ferromagnets has evolved into an important field of material science. Mn-doped GaAs, InAs and InP dilute magnetic semiconductors were one of the first magnetically doped materials which were studied as these semiconductors were already established industrial materials in their undoped form[99]. However, the solubility of Mn was not very high as the Mn impurities had a tendency to form secondary phases and to segregate. Munekata *et al.*[105] used low-temperature MBE to achieve epitaxial InMnAs to suppress secondary phases which in turn led to the discovery of ferromagnetism in InMnAs at low temperatures[106]. After an intense study on DMS for over two decades, the highest Curie temperature reported has been 184 K for 12% Mn doping with the onset of in-plane

ferromagnetism[107]. Dietl *et al.*[108] theoretically predicted that wider band gap materials should have a higher Curie temperature and hence new materials showed up in literature such as Mn doped ZnO[84] and Mn doped GaN[109]. These two materials were experimentally shown to exhibit ferromagnetism above room temperature. Although many fascinating results have been published on DMS systems, the phase segregation is still a problem which needs to be addressed, furthermore many oxide based DMS systems have shown a rather high conduction[84]. A vast pool of opportunities has opened up to explore new quantum effects by combining ferromagnetic properties with TIs. The best known achievement is the observation of the quantum anomalous Hall effect[24]. The tetradymite type material, Sb_2Te_3 has been theoretically proposed and experimentally proven to be a 3D TI with a single Dirac cone which lies well inside the bulk band gap of 260 meV[31,110,111]. Combining ferromagnetism with this material system has not been studied so far in great detail. We recently reported studies on Cr doped Sb_2Te_3 using XRD and found that Cr sits on the Sb sites[91]. Other researchers have worked on similar material systems such as Cr doped $Bi_xSb_yTe_3$[24,112–116] but not much on Cr doped Sb_2Te_3 has been reported with a few exceptions[92,117–119].

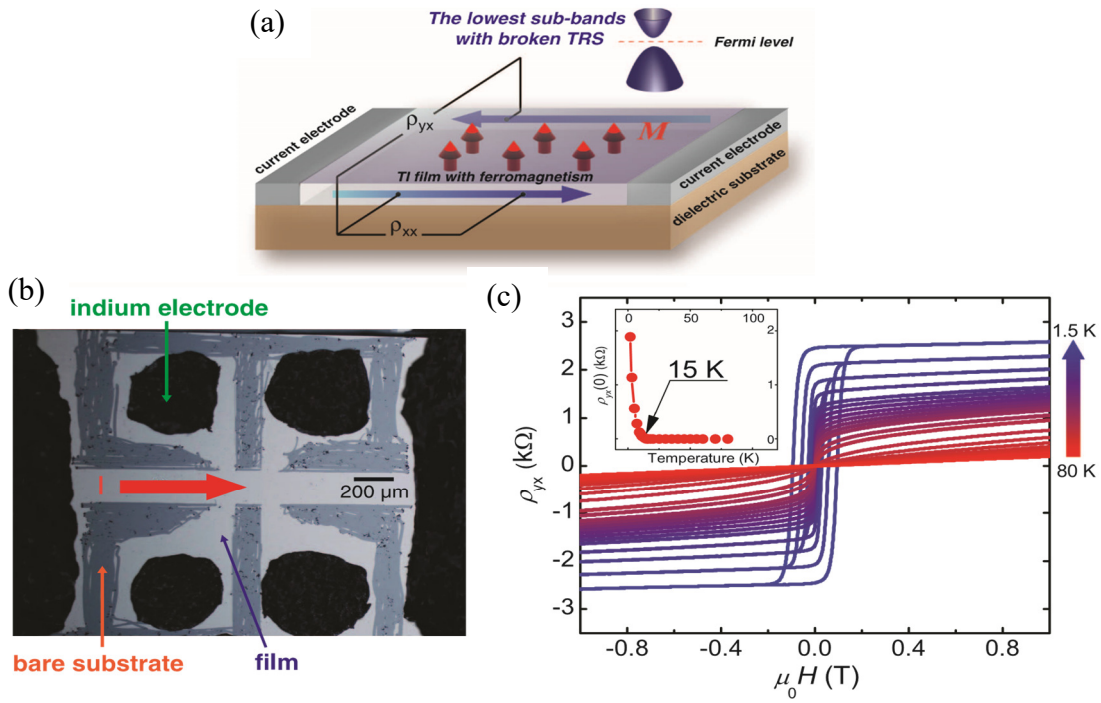

Figure 4.1 (a) A schematic drawing depicting the principle of the QAH effect in a ferromagnetic TI thin film. (b) An optical image of the scratched Hall bar device of $Cr_{0.15}(Bi_{0.1}Sb_{0.9})_{1.85}Te_3$ with the current direction shown in red. (c) Magnetic field dependence of ρ_{xy} as a function of temperature down to 1.5 K. The inset describes the dependence of ρ_{xy} with temperature[24]. Figure reproduced from ref. 24 without permission.

It is worth discussing next some of the highlights in the field. Cui-Zu Chang at Tsinghua University, China, experimentally observed a QAHE in 2013 after being theoretically predicted almost ten years earlier[98]. This was a huge breakthrough in the field of condensed matter physics. A schematic picture is shown in Figure 4.1 (a) illustrating the principle of the QAHE as described by Chang *et al*. The magnetization direction *M* is indicated by red arrows, while the dissipationless channel on the edge of the material depicts the quantized Hall resistivity ρ_{xy}. The $Cr_{0.15}(Bi_{0.1}Sb_{0.9})_{1.85}Te_3$ films with 5 QL thickness were grown on dielectric $SrTiO_3(111)$ substrates by MBE. They were then manually scratched into a Hall bar configuration [Figure. 1(b)] for transport measurements with Indium blobs as contact pads. The stoichiometry was chosen to ensure that the films were nearly charge neutral so that the chemical potential could be fine-tuned to the electron-hole regimes by applying a positive or negative back gate voltage. Figure 1(c) displays the temperature dependent Hall resistivity ρ_{xy} as a function of the magnetic field *B*. At high temperatures, ρ_{xy} shows a linear slope from which they obtained a mobility of ~760 cm^2/Vs. As they reduced the temperature, ρ_{xy} exhibited the AHE in the form of hysteresis loops. Their films displayed large-square shaped loops with a long range out-of-plane magnetic anisotropy. They also estimated T_c to be 15 K as confirmed by the ρ_{xy} vs temperature plot shown in the inset of Figure 1 (c). They performed even lower temperature dependent gated transport measurements at 30 mK. Their gate dependence ρ_{xx} and ρ_{xy} measurements at 30 mK are plotted in Figure 4.2 (a) and (c). They observed that the shape of the hysteresis loop did not vary much on applying different back-gate voltages V_g, showing a robust ferromagnetic ordering. On the other hand, the height of the hysteresis loop, *i.e.* the anomalous Hall resistance changed dramatically with V_g, with a maximum value of ~ h/e^2 at -1.5 V. The ρ_{xx} value on the contrary exhibited two sharp symmetrical peaks corresponding to the coercive field as expected from a ferromagnetic material. This measurement was the first of its kind showing a quantized value of h/e^2 for the Hall resistivity. But more important was their next measurement, which showed their V_g dependence of ρ_{xx} and ρ_{xy} at zero magnetic field as shown in Figure 4.2 (b). The zero field Hall resistivity ρ_{xy} displayed a distinct plateau with a quantized value of h/e^2 with the gate voltage V_g = -1.5 V. This observation constituted the observation of a dissipationless channel in the absence of a magnetic field *i.e.* the QAHE.

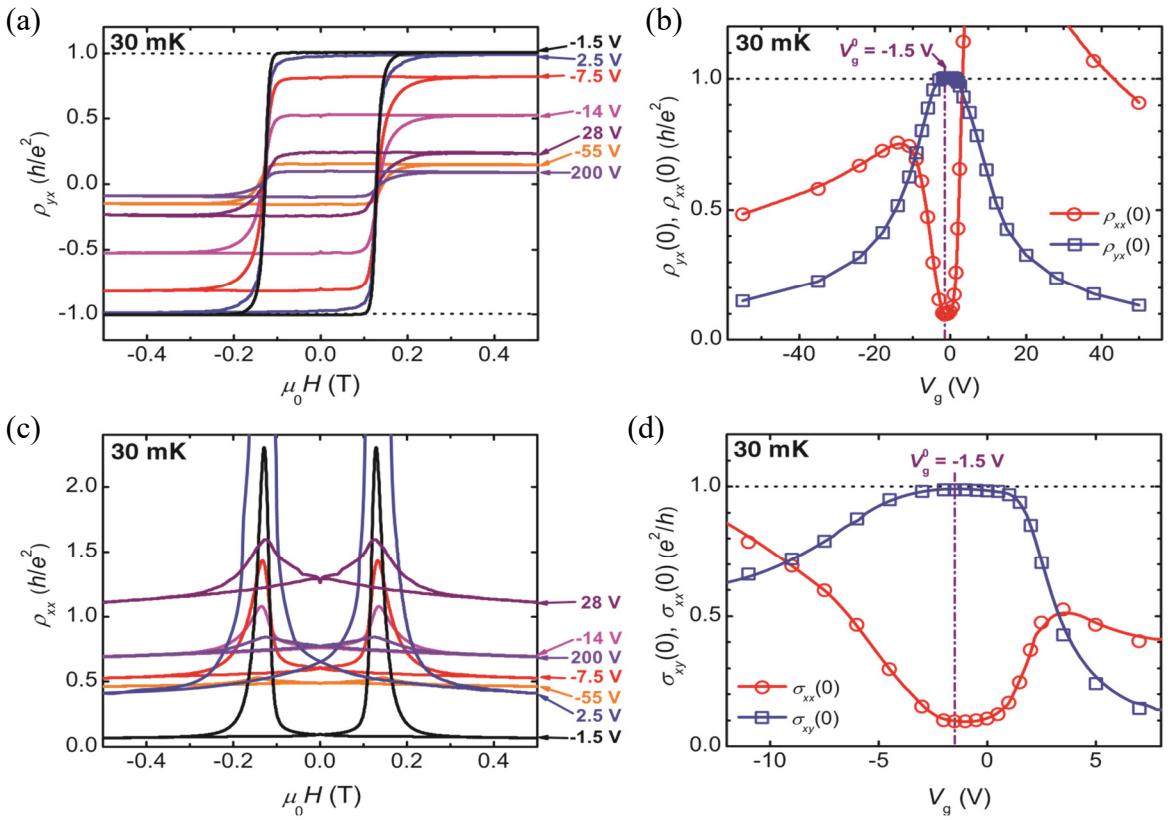

Figure 4.2 (a,c) The magnetic field dependence of ρ_{xy} and ρ_{xx} at different gate voltages V_g. (c,d) Zero-field dependence of resistivities ρ_{xy}, ρ_{xx} and conductivities σ_{xx}, σ_{xy} on the gate voltage V_g at 30mK[24]. Figure reproduced from ref. 24 without permission.

Along with this quantization, the longitudinal resistivity showed a sharp decrease down to 0.098 h/e^2. They observed a similar behavior when they converted their resistivities into conductivities and observed notable plateaus at 0.987 e^2/h in σ_{xy} and a dip down to 0.096 e^2/h in σ_{xx} as shown in Figure 4.2 (d). Their overall results paved the way for researchers to think further on ways to push the QAHE regime to room temperature with a higher T_c. Feng *et al.* conducted a thickness dependent study (4 QL – 15 QL) on the same film composition, *i.e.* $Cr_{0.15}(Bi_{0.1}Sb_{0.9})_{1.85}Te_3$ and found that the quantized value at zero field is only seen perfectly in the sample with a 5 QL thickness and no other[115]. They pinned the explanation for this as the interplay between the band gap E_g, chemical potential and the ferromagnetic exchange energy E_{ex} in their samples. If the thickness was below 4 QL [lower limit - Figure 4.3 (a)] , the film was thin enough for a significant hybridization of the top and bottom surface states to take place opening a hybridization gap E_g. Also the gap size increased with decreasing thickness while E_{ex} and T_c decreased with decreasing thickness[120,121].

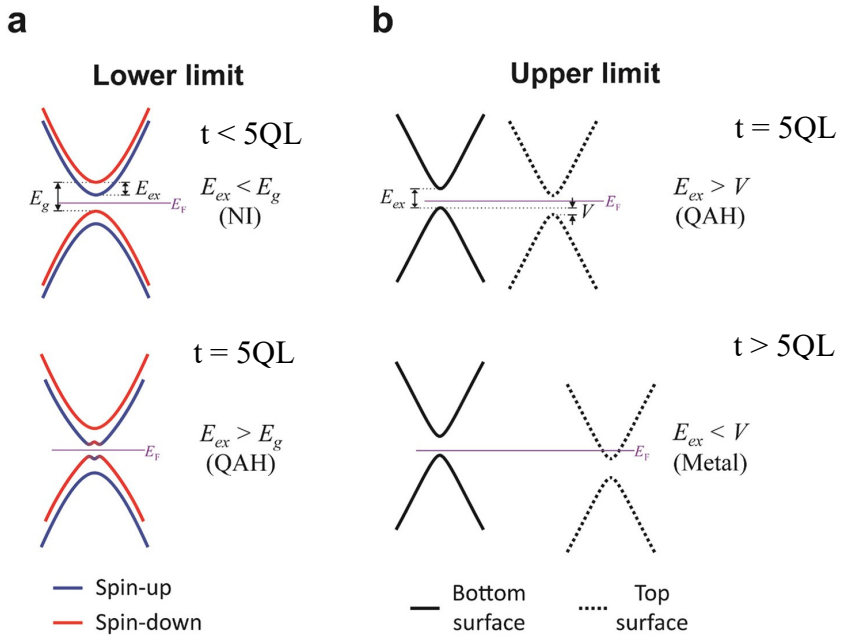

Figure 4.3 A thickness dependent explanation of the QAHE (a) A schematic band diagram for a thickness *t* less than 5 QL, samples of which behave as a trivial insulator (top) and a perfect sample 5 QL showing the QAHE. (b) A schematic band diagram for top and bottom surfaces for thicknesses more than 5 QL (bottom), showing a metal phase, while the top ~ 5 QL sample shows the QAHE[115]. Figure reproduced from ref. 115 without permission.

So to maintain the QAHE phase, the magnetic exchange energy E_{ex} should be greater than the band gap size E_g so that the exchange splitting can overcome E_g and lead to a band inversion [bottom image of Figure 4.3 (a)]. At thicknesses below 5 QL, this criteria is not fulfilled, hence the QAH phase does not exist. In the case of thicker samples, hybridization of the top and bottom surfaces do not take place hence E_g is negligible. The QAHE phase in this occasion will only exist if the contribution to the conduction channel is exclusively from the chiral edge state and not from the bulk of the film. When thicknesses exceed 5 QL [upper limit- Figure 4.3 (b)], band bending may occur. The band bending energy V of the top surface will be larger than the bottom surface in thicker films and could lead to an energy offset[120]. Now if $V < E_{ex}$ the Fermi level may well be easily gate-tuned into the magnetic gap and hence the QAHE phase could exist, but when $V > E_{ex}$, the Fermi energy cannot be tuned into the gap, and the films would be metallic in this case *i.e.* in thicker samples. In other words, the quantization cannot be obtained even if there is an edge state. When thicknesses are even higher *i.e.* above 15 QL, the film was so thick that the QAH phase is well below the Fermi level and no change in transport properties will be observed.

Zhou *et al.*[92] were the first to look into Cr doped Sb_2Te_3 MBE grown samples in 2006, but

during that time, TI were not heard off. The paper did not mention the thickness of their films but they conducted a study on increasing Cr doping concentration in MBE grown samples on Sapphire (0001) substrates. They started with a structural characterization using X-ray diffraction with increasing the Cr doping. Figure 4.4 (a) shows the (00*l*) family of diffraction peaks in the hexagonal unit cell of Sb_2Te_3. No other secondary phase was visible which proved the crystals were of high quality and grew parallel to the *c*-axis direction. They also showed that the *c*-lattice parameter changes only slightly although decreases with increasing Cr doping concentration as shown in Figure 4.4 (b). The decrease in the *c*-lattice constant meant that the hexagonal unit cell was overall decreasing in size with increasing Cr concentration.

They went on the perform SQUID and resistivity measurements on all of their doped samples with progressively increasing Cr concentrations. They took out-of-plane field cooled measurements and recorded the magnetization from 300 K to 2 K. When the temperature was reduced below 200 K, the nearly constant magnetization underwent a sharp transition corresponding to the onset of long range ferromagnetic ordering in the film *i.e.* the Curie temperature T_c of the material.

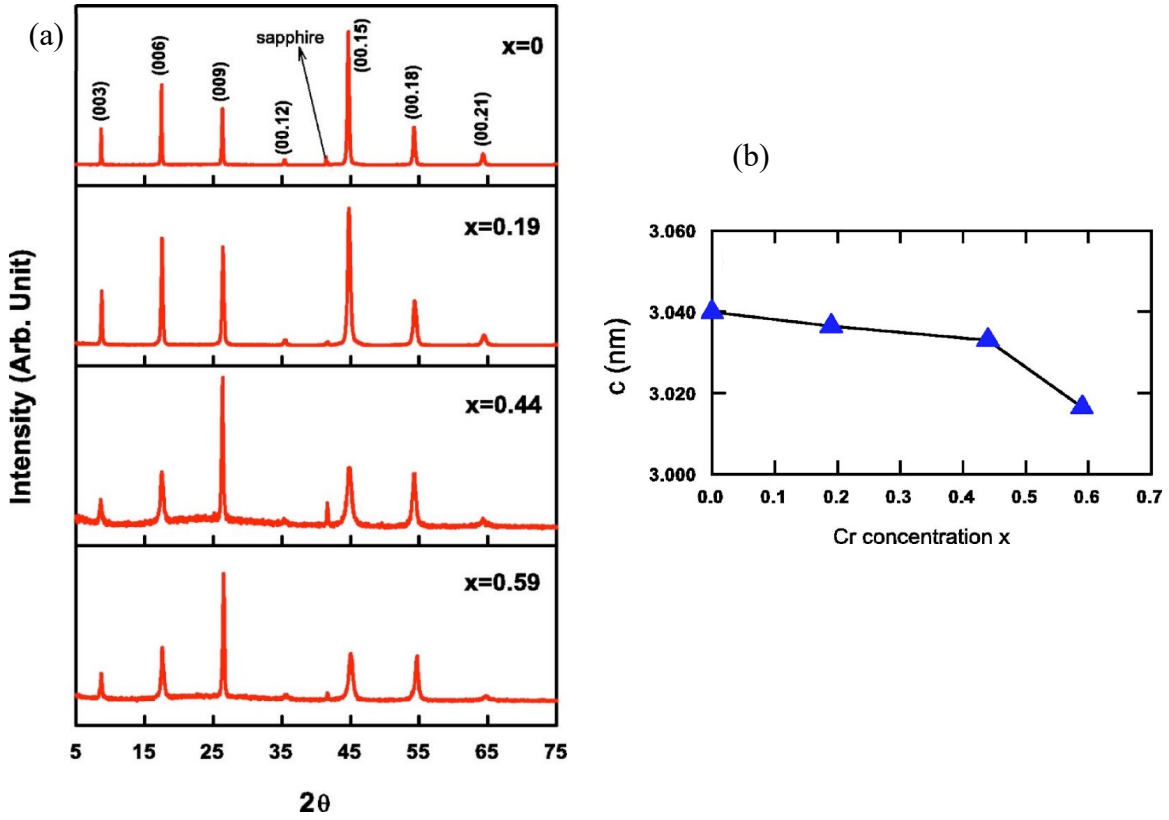

Figure 4.4 (a) X-ray diffraction patterns of Cr doped Sb_2Te_3 films on Sapphire (0001) substrates. (b) The *c*-lattice constant as a function of Cr concentration *x*.[92] Figure reproduced from ref. 92 without permission.

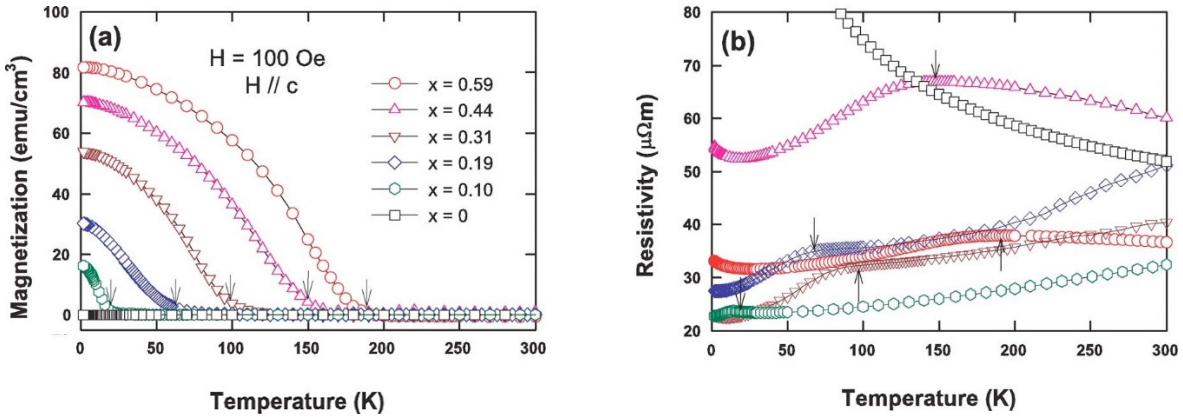

Figure 4.5 (a) Temperature dependent magnetization of Cr doped Sb_2Te_3 thin films with the field along the *c*-axis of Sapphire at 100 Oe. (b) The temperature dependent electrical resistivity at zero magnetic field[92]. The same legend is used in both figures. Figure adopted from ref. 92 without permission.

The sample with the highest doping of 26% , *i.e.* $x = 0.59$ had the highest T_c while the samples with the lower concentration of Cr showed upturns at progressively lower temperatures as shown in Figure 4.5 (a). Figure 4.5 (b) displays their temperature dependent resistivity. The resistivity of pure Sb_2Te_3 showed a typical semiconductor behavior, while all other curves for Cr doping displayed a local maximum hump around T_c. This maximum represent the paramagnetic to ferromagnetic phase transition, *i.e.* the magnetic ordering temperature of the films. They plotted the T_c as a function of Cr concentration x and observed a linear dependence as shown in Figure 4.6 (a). They also plotted the carrier density p on the concentration of Cr and observed only a weak dependence, hence could not comment if the mechanism of magnetism was based on carrier density.

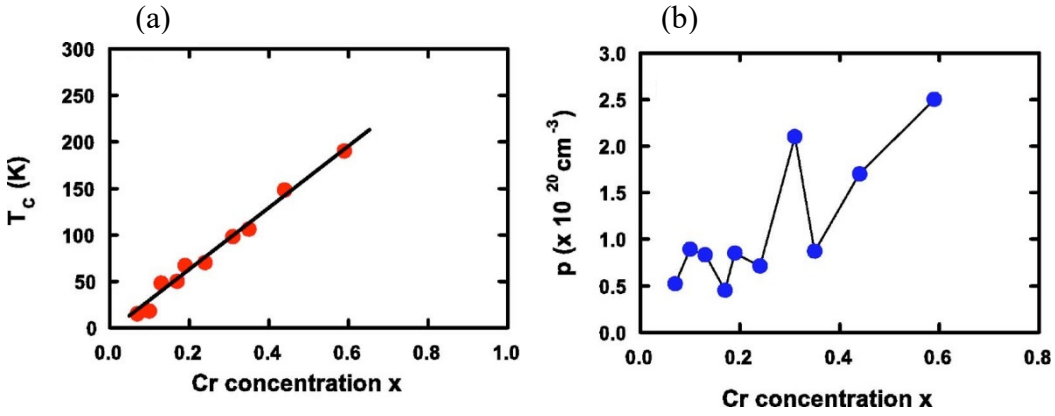

Figure 4.6 (a,b) Curie temperature T_c and carrier density p as a function of Cr concentration x.[92] Figure adopted from ref. 92 without permission.

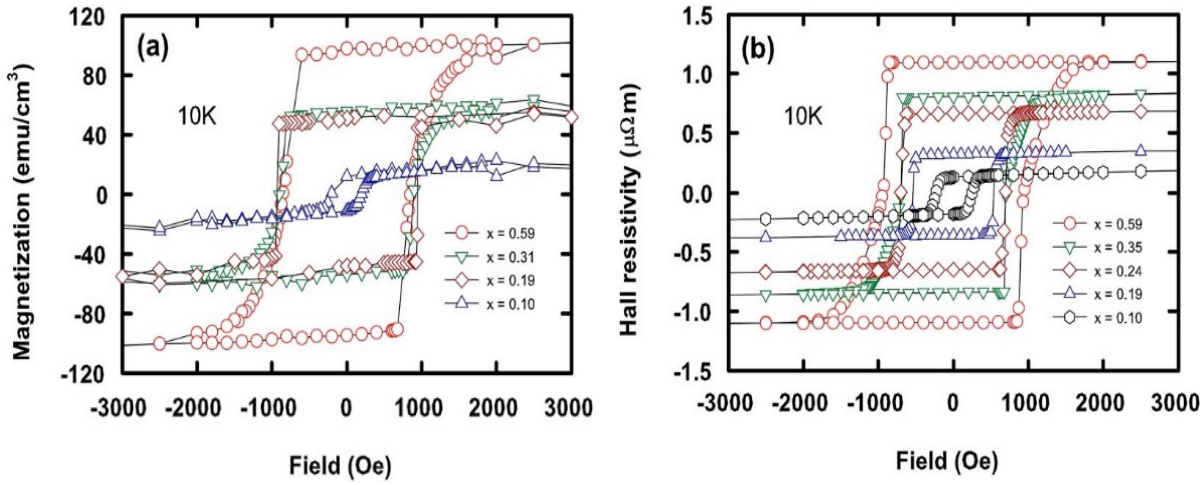

Figure 4.7 (a,b) In-plane magnetic hysteresis for all Cr doped samples measured using SQUID and electrical transport measurements of the AHE.[92] Figure reproduced from ref. 92 without permission.

Their final measurement was a comparison between SQUID magnetization and the Hall resistivity as displayed in Figure 4.7 (a) and (b). Upon analyzing the SQUID data, they observed that the value of the coercive field increases from about 200 Oe in a film with 5% doping to around 850 Oe for their highest doped sample with x = 0.59. The smooth loops indicated well- ordered films with a coherent rotation of spins. Similar results were obtained with resistivity measurements of the AHE which were a good match with the SQUID results.

4.3 Electric Transport and Optical Characterization of Cr Doped Sb_2Te_3 Thin Films

Hall bars were fabricated and wire bonded after which the samples were loaded into the cryostat one at a time as described in the experimental section 2.5.1. Hall bar fabrication and the circuit diagram for the experimental setup is described section 5.4 in great detail.
Once all the preliminary checks were made at room temperature, the sample was cooled down. While the sample was cooled to 1.8 K, the resistance of the sample was recorded. The results from the samples which were grown using MBE as described in section 3.5 are shown in table 4.1. This series was purposely chosen to study the doping trends in Sb_2Te_3. A nominal thickness of 20 nm was chosen for all samples to assure less bulk contribution.

Sample name	Nominal stoichiometry	Thickness ~ (nm)
1. M2-0574	$Cr_{0.15}Sb_{1.85}Te_3$	20
2. M2-0575	$Cr_{0.41}Sb_{1.59}Te_3$	19
3. M2-0576	$Cr_{0.58}Sb_{1.42}Te_3$	20
4. M2-0577	$Cr_{0.76}Sb_{1.22}Te_3$	20

Table 4.1 Samples on which transport measurements were carried out.

Figure 4.8 shows the longitudinal resistances R_{xx} for all Cr doped samples in the $Cr_xSb_{2-x}Te_3$ series for various values of x ranging from 0.15 to 0.76 as a function of temperature upon cooling. All samples behave differently. Starting with the lowest doped sample with $x = 0.15$, as the temperature was reduced from 300 K the resistance increased monotonically indicating a freezing of the bulk carries in the TI film down to ~ 35 K. However, below ~ 35 K, the resistance begins to gradually decrease with a further reduction in temperature. This insulator to metal transition at ~ 35 K displays the effect of doping magnetic impurities into TIs. Such a behavior can be attributed to the reduction in the spin disorder scattering that sets in at the paramagnetic to ferromagnetic phase transition[122,123]. It is important to note that the sample itself was not subject to an external magnetic field, but that microscopic ferromagnetic domains form in random directions which lead to ordering in the film. This transition is also known as the Curie temperature T_c. The resistance then saturates down to 1.8 K. A similar behavior was also perceived in the highest doped sample, *i.e.* for $x = 0.76$, where the insulator to metal transition was seen at a much higher temperature close to 176 K, corresponding to the T_c of $Cr_{0.76}Sb_{1.22}Te_3$. On further reducing the temperature the resistance showed a sharp increase, indicating the freezing of the bulk carriers. This may

suggest that the introduction of magnetic doping in TIs induces a gap in the surface states as the time reversal symmetry is broken. This has been theoretically predicted[33,57] and previously reported by various groups around the world using angle resolved photo emission spectroscopy[81,113]. The activation energy can be estimated from the Arrhenius plot of log (R_{xx}) vs 1/T, as shown in the inset of Figure 4.8 at high temperatures.

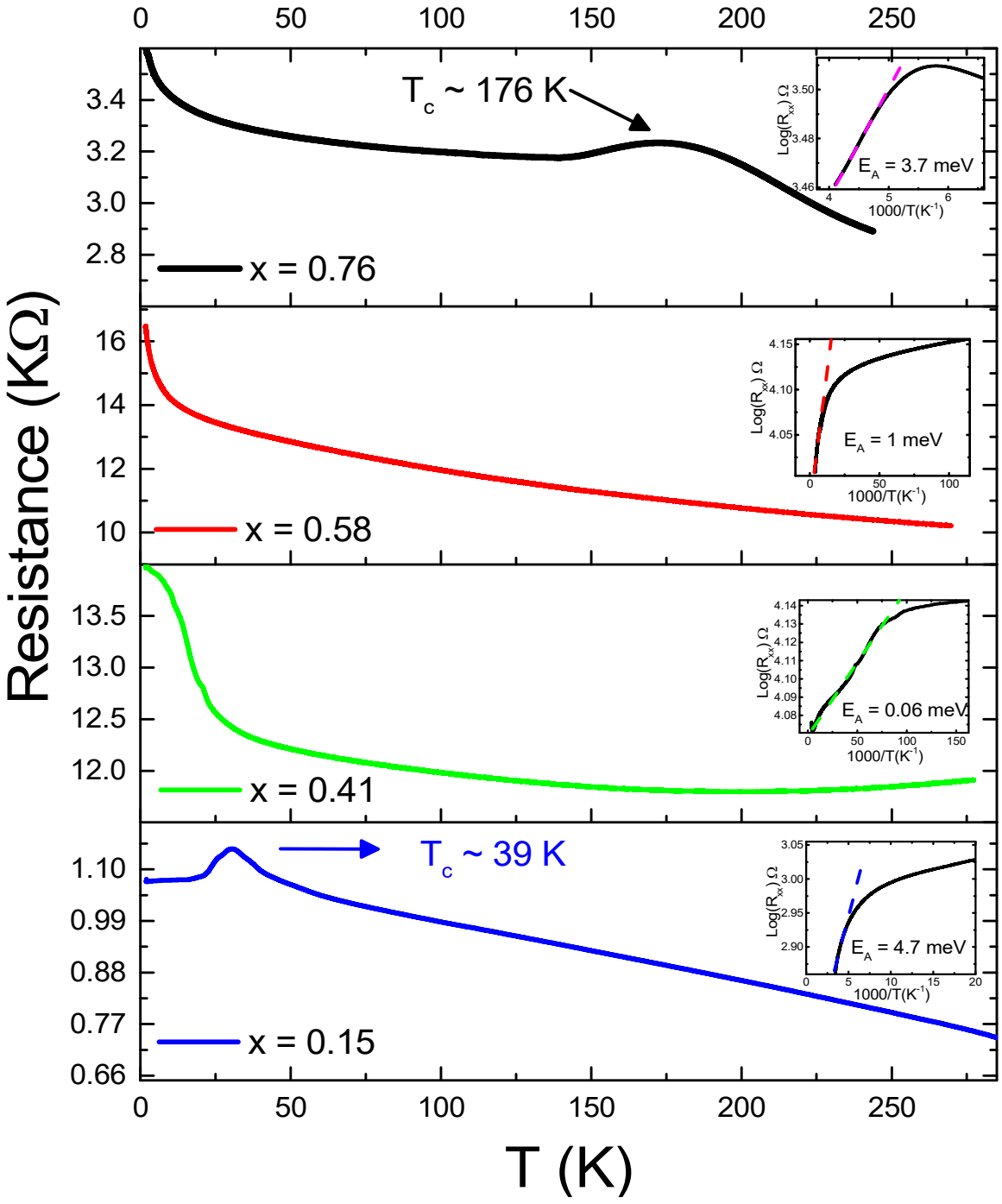

Figure 4.8 Longitudinal resistance R_{xx} as a function of temperature for all $Cr_xSb_{2-x}Te_3$ samples with x ranging from 0.15 to 0.76. Inset shows the Arrhenius plot of log (R_{xx}) vs 1/T.

Samples with x = 0.41 and x = 0.58 show between themselves similar trends. No metal to insulator transition was observed in these samples and the resistance increases with decreasing temperature as expected from a trivial semi-conductor. Similar trends have been reported by Chang *et al*. in their samples, while no signs of a paramagnetic to ferromagnetic phase transition were observed[118].This is in disagreement with Zhou *et al*. who observed transitions for their whole doping range from x = 0.1 to 0.59 as shown in Figure 4.5[92]. It is clear that in these samples the resistance trend does not get affected by doping, even if we presume that there is a cross over from a paramagnetic to ferromagnetic phase (not seen). While the mechanism of the magnetic interaction may be different in these samples, the resistance of them are clearly only temperature dependent and seemingly independent of the magnetic doping. Further magnetic field dependent characterization was carried out on all the samples as described below.

Figures 4.9 illustrates the B-dependent magneto-resistance ratio defined as : $\frac{\Delta Rxx(B)}{Rxx(0)} = \frac{R_{xx}(B)-R_{xx}(0)}{R_{xx}(0)}$ measured between 180 K to 1.8 K for all the samples with x = 0.15 to 0.76. A butterfly shaped hysteresis was observed in all the samples characterized by the negative *MR* caused by spin dependent scattering of carriers[124] as magnetically ordered domains form below T_c. The distance between the two peaks for all temperatures correspond to the coercive field H_c. T_c can be estimated by studying the temperature dependence and is defined as the temperature when H_c becomes zero. At this point the long range ferromagnetic order disappears and a positive *MR* may be observed corresponding to the weak anti-localization (WAL) commonly observed in pristine TI samples[125,126]. A detailed explanation of magneto-resistance and why the resistance reduces with increasing magnetic field can be found in section 1.4.3. Furthermore, a characterization study was performed using anomalous Hall effect measurements to study the ferromagnet ordering of the samples down to 1.8 K. Figures 4.10 shows the evolution of the Hall resistance R_{xy} as a function of temperature and magnetic field B for x = 0.76 to 0.15. Long range ferromagnetic ordering, indicating that the easy axis of magnetization pointing out-of-plane was observed through these transport measurements. Furthermore, all the $Cr_xSb_{2-x}Te_3$ films had hole-type carriers transport (p-type) with different slopes at high fields indicative of the normal Hall effect, once the magnetization of the ferromagnet is saturated. A few conclusions can be drawn when looking at these graphs. Firstly, the area of the hysteresis loop *i.e.* the coercive field H_c as well the overall magnetization expressed in terms of the magnitude of the residual resistance at zero field increased with increasing doping concentration besides for the highest doped sample.

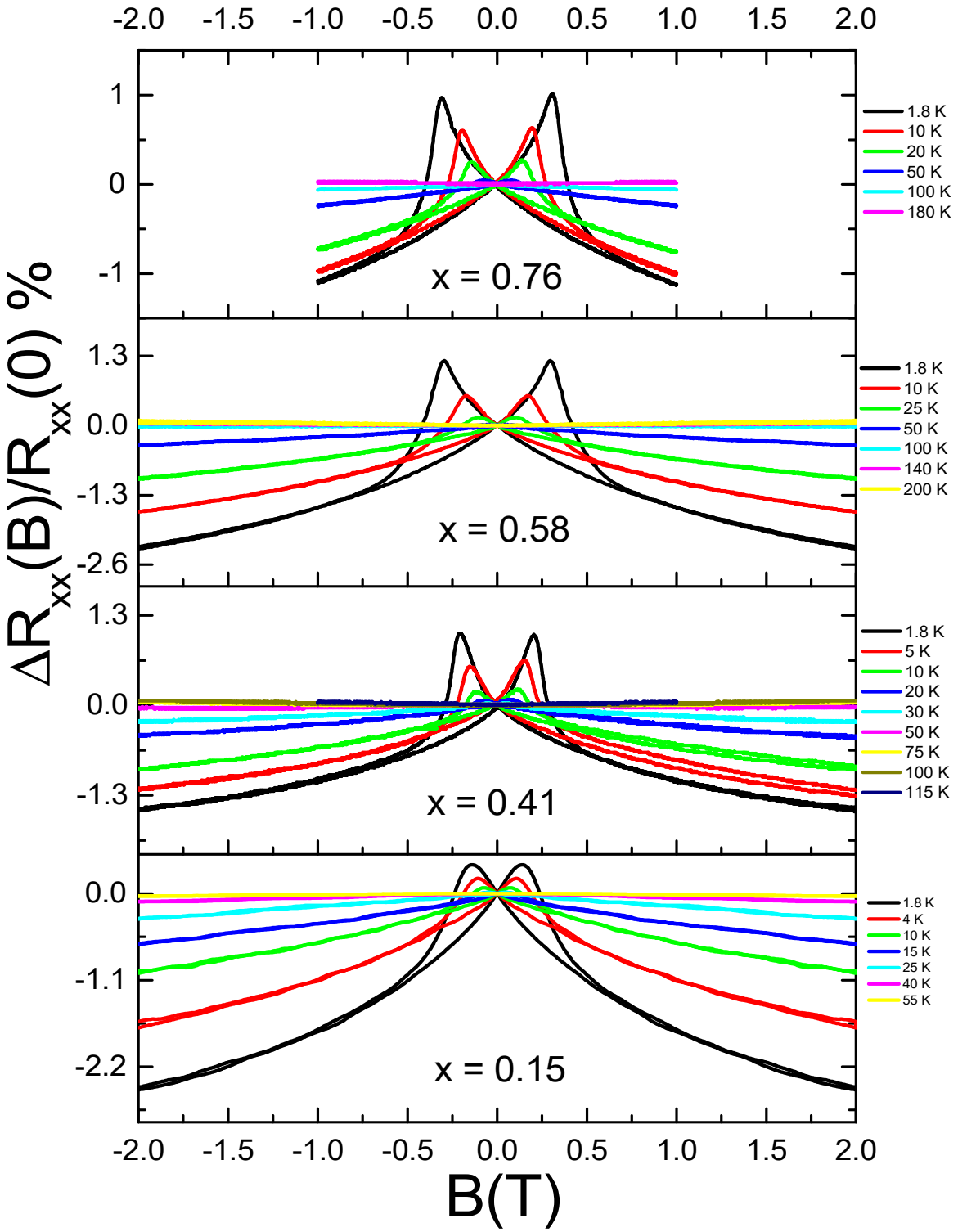

Figure 4.9 Temperature dependent *MR* ratio for 20-nm-thick samples with $x = 0.76$ to $x = 0.15$.

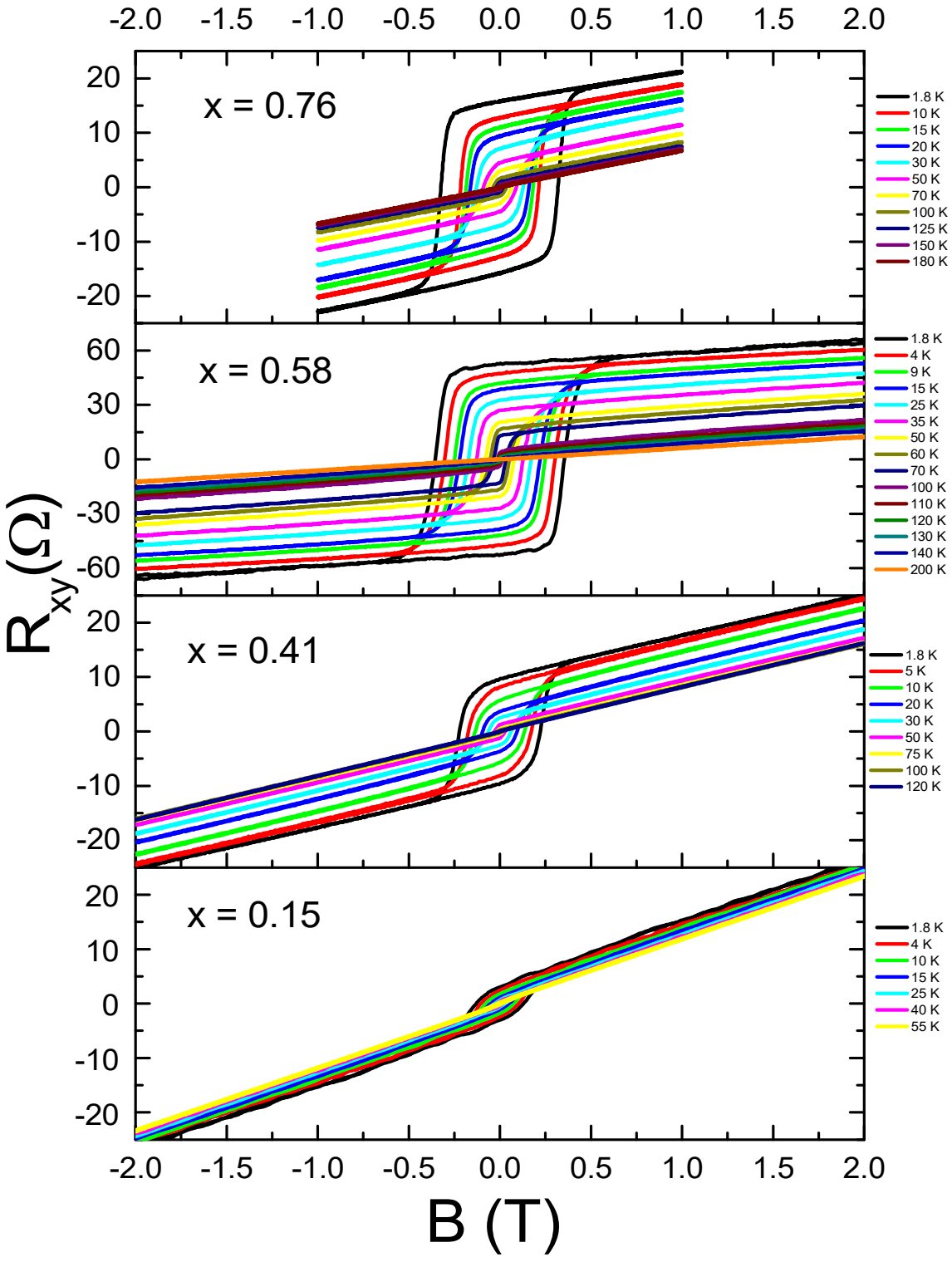

Figure 4.10 Magnetic field dependent Hall resistance R_{xy} in the samples with $x = 0.76$ to 0.15 exhibiting a hysteretic behavior, corresponding to the anomalous Hall effect, at different temperatures from 1.8 K to 180 K.

Secondly, the slope of the Hall resistance decreased with increasing doping levels. This will be discussed in detail later. It was also detected that the coercive field H_c and the saturated Hall resistance at $B = 0$ T were higher for the sample with $x = 0.58$ than for $x = 0.76$, although its Curie temperature T_c was lower, which will also be discussed in more detail later. Additionally, the Hall resistance R_{xy} dependent on different directions of the magnetic field B with respect to the sample surface normal direction was studied in $Cr_{0.76}Sb_{1.22}Te_3$ as shown in Figure 4.11 (a). As the angle θ of the sample changed from out-of-plane ($\theta = 90°$) to in plane ($\theta = 0°$), the value of R_{xy} reduced and the slope gradually changed from positive to negative until a parabolic (magnetic hard axis) dependence at $\theta = 0°$ was observed. This result for $\theta = 0°$ indicates an out-of-plane spontaneous magnetization at zero field, confirming that the magnetic moments of the sample prefer to be perpendicular to the surface normal. This feature may be favorable for spintronic applications, where perpendicular magnetic anisotropy is more useful than in plane magnetism[118,127].

Magneto-optical Kerr measurements were conducted first at 1.8 K on all Cr doped samples. These results are displayed in Figure 4.12. Similar to the transport measurements, MOKE also displayed an increasing out-of-plane hysteretic behavior with respect to increasing the Cr doping and also with decreasing the temperature in each case. Here, the Kerr rotation in radians increases with increasing doping while the coercivities H_c for $x = 0.15$ and 0.45 and for $x = 0.58$ and 0.76 at 1.8 K are very similar. To further investigate this, the diode laser used to power the MOKE setup was modulated while sweeping the magnetic field.

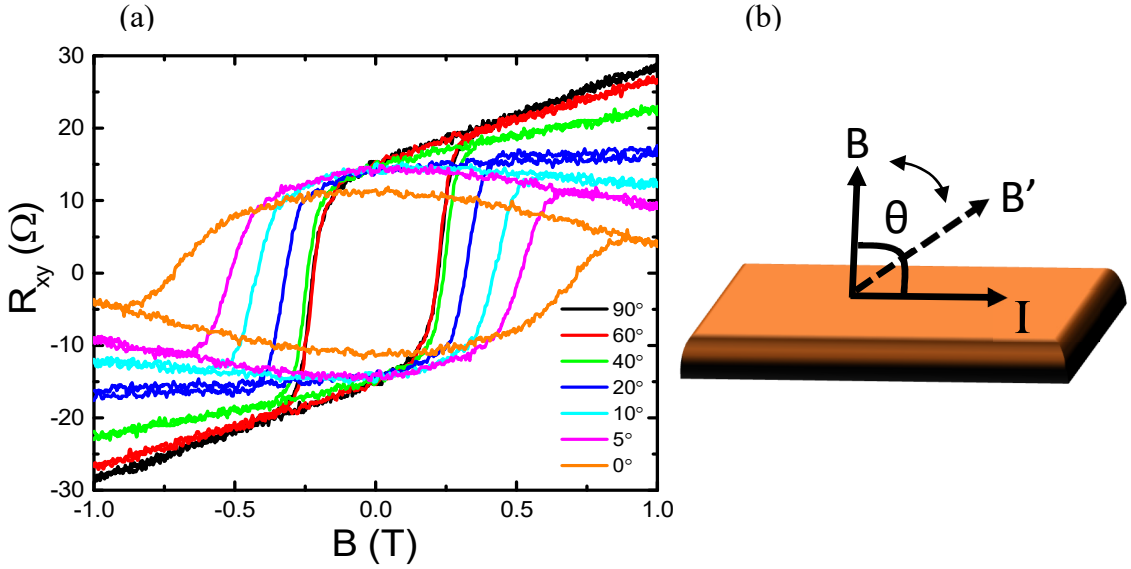

Figure 4.11 (a) Angular dependence of the Hall resistance R_{xy} at 1.8 K for a representative 20-QL-thick $Cr_{0.76}Sb_{1.24}Te_3$ sample. (b) Illustration of the out-of-plane angle theta θ with respect to the applied current I ($\theta = 0°$ along I).

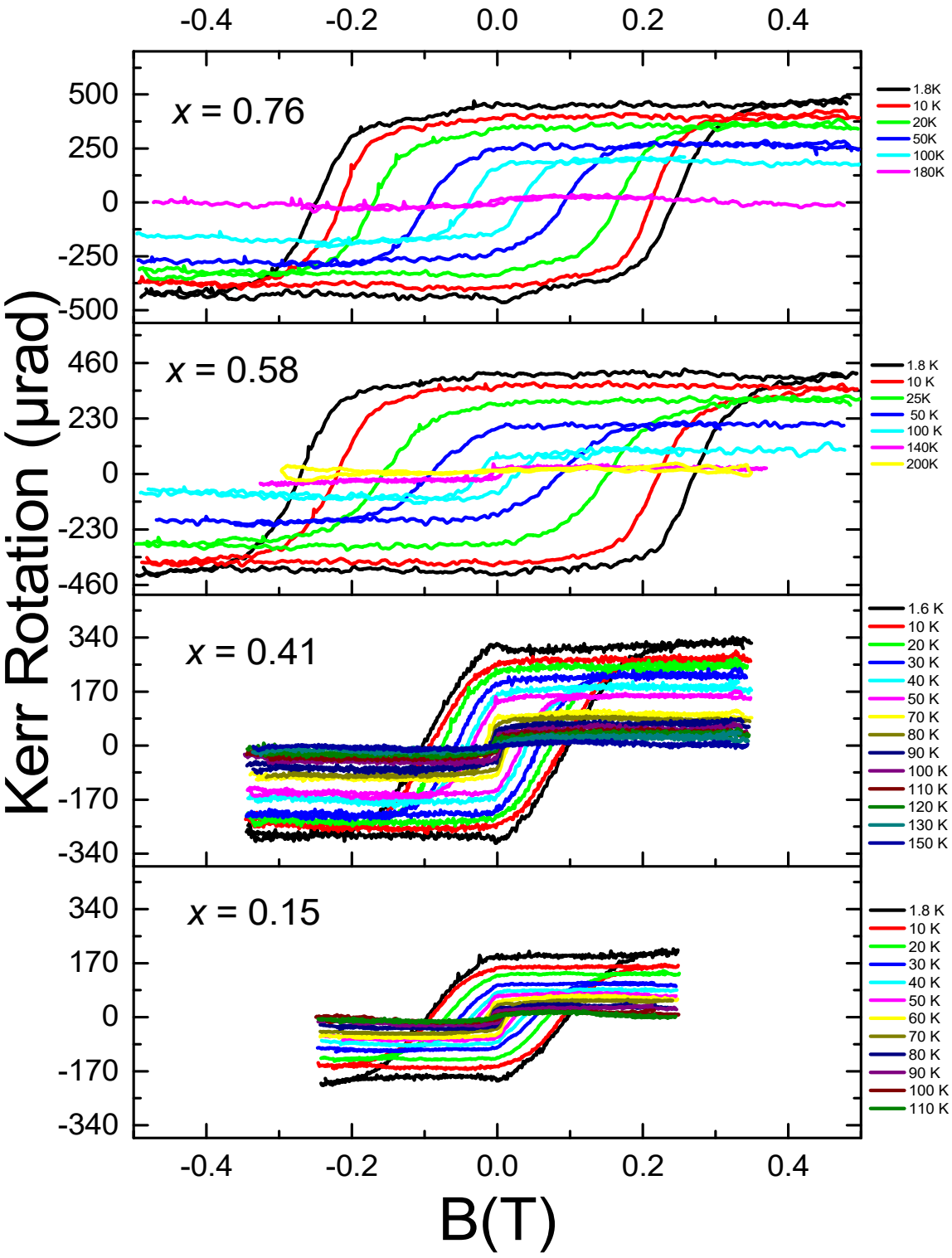

Figure 4.12 Kerr rotation in radians for samples with x = 0.15 to 0.76 showing hysteretic behavior below T_c at different temperatures from 1.8 K to 180 K.

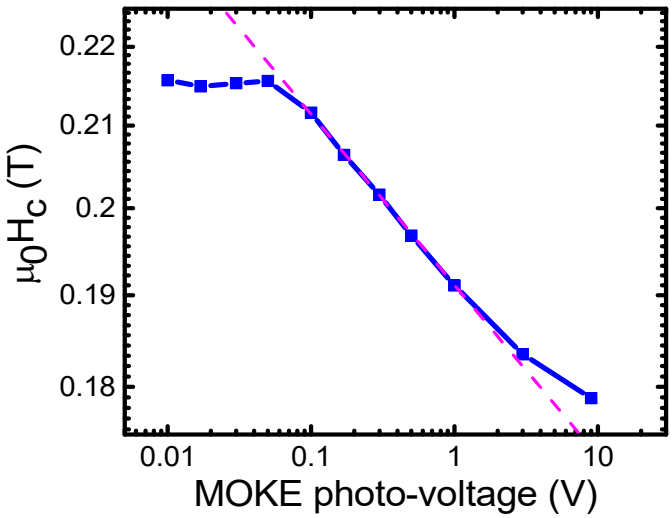

Figure 4.13 Coercivity H_c for the x = 0.76 film extracted from MOKE hysteresis loop measurements as a function of laser power. The photo-voltage is proportional to the light intensity incident on the film. 10 V corresponds to ~10 mW.

The magnetic properties of the $Cr_{0.76}Sb_{1.22}Te_3$ sample were affected by the laser power. When the laser was focused to a 3 μm spot size on the sample at T = 10 K, the coercivity decreased with increasing laser intensity as shown in Figure 4.13. This relation fitted well to a power law (dashed line) from 0.1 V to 3 V photo-voltage, which corresponded to approximately 0.1 mW to 3 mW incident energy on the film. Locally induced heat from the laser excited thermally the spins and accounts for this coercivity relation[128]. Below 0.5 mW laser power (0.05 V photo-voltage) the coercivity reached a plateau of ~0.215 T.

Figures 4.14 directly compares the MOKE signal θ_K and the AHE signal R_{xy} at 10 K and 50 K for all the doped samples with x = 0.76 to 0.15. The measurements on x = 0.76 and x = 0.58 [Figure 4.14 (c) and (d)] were taken at the lowest possible laser power (0.05V) while the samples with x = 0.15 and x = 0.41 [Figure 4.14 (a) and (b)] were taken at highest laser power (10 V) to compare the difference. The conclusions derived from the H_c values and R_{xy}/θ_K are summarized in table 4.2.

	10 K		50 K	
	H_C	R_{xy}/θ_K	H_C	R_{xy}/θ_K
$Cr_{0.15}Sb_{1.85}Te_3$	match	good match	good match	**different**
$Cr_{0.41}Sb_{1.59}Te_3$	**different**	good match	good match	**different**
$Cr_{0.58}Sb_{1.42}Te_3$	good match	good match	good match	good match
$Cr_{0.76}Sb_{1.22}Te_3$	good match	good match	good match	**different**

Table 4.2 Comparison of MOKE and transport measurements at 10 K and 50 K. A "good

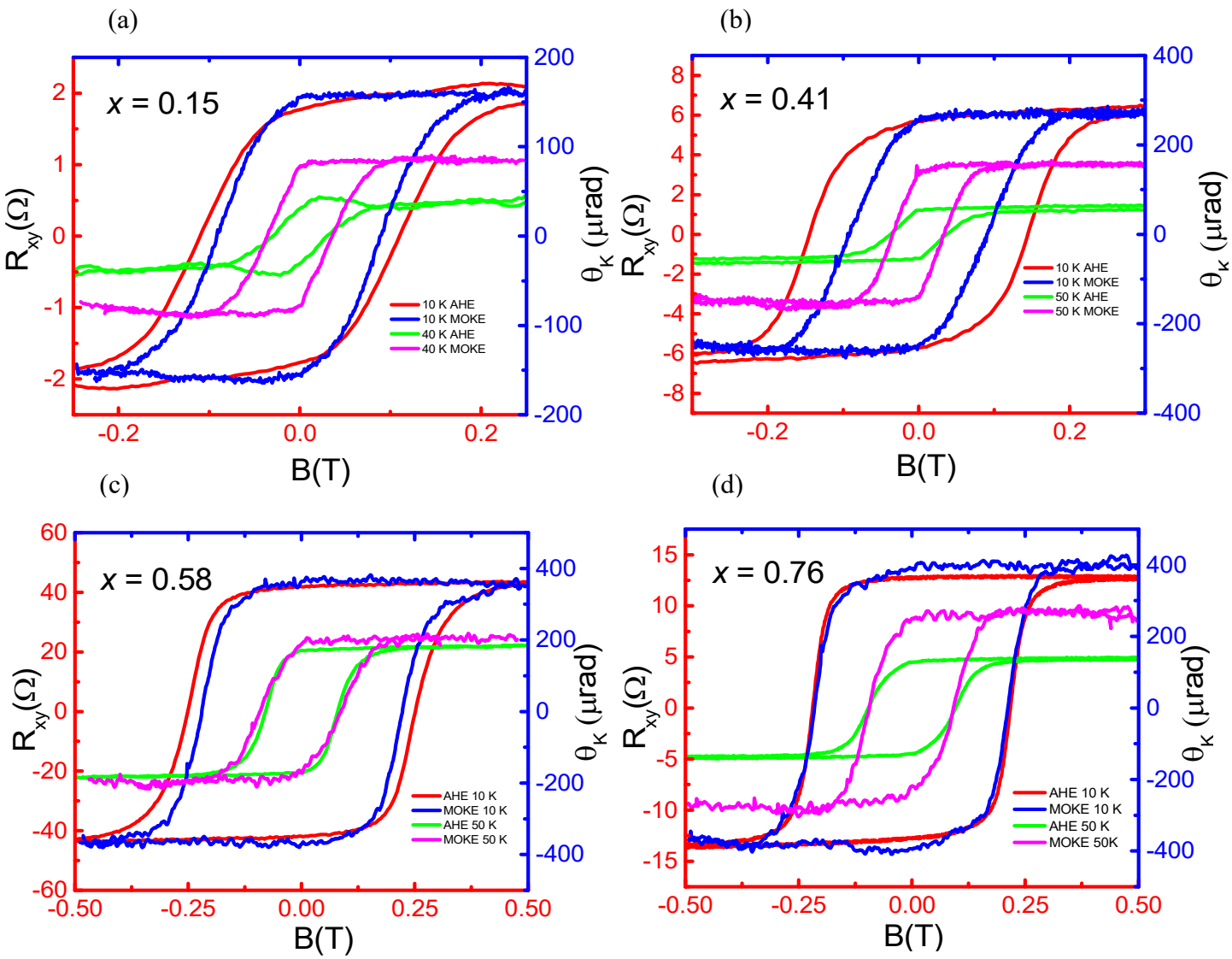

Figure 4.14 Magnetic hysteresis loops comparing the anomalous Hall resistance R_{xy} and Kerr angle θ_K as a function of magnetic field in all the films with $x = 0.15$ to $x = 0.76$ at 10 K and 50 K from (a) to (d) respectively, showing that both measurements are in reasonably good agreement with each other.

match" means that the coercivities and saturation values are consistent with each other while "different" would mean the opposite.

It is clear when looking at table 4.2, both MOKE and transport measurements were in relative good agreement with each other, while an anomaly was seen in R_{xy} and θ_K at 50 K for x = 0.15, 0.41 and 0.76. Furthermore, H_c was different for $x = 0.41$ at 10 K. The inconsistencies in H_c were related to the laser power of the MOKE, while the difference in R_{xy} and θ_K were investigated further. To understand these inconsistencies, the trend comparing the anomalous Hall conductivity $\sigma^A{}_{xy}$ / Kerr rotation θ_K and H_c as a function of temperature was studied.

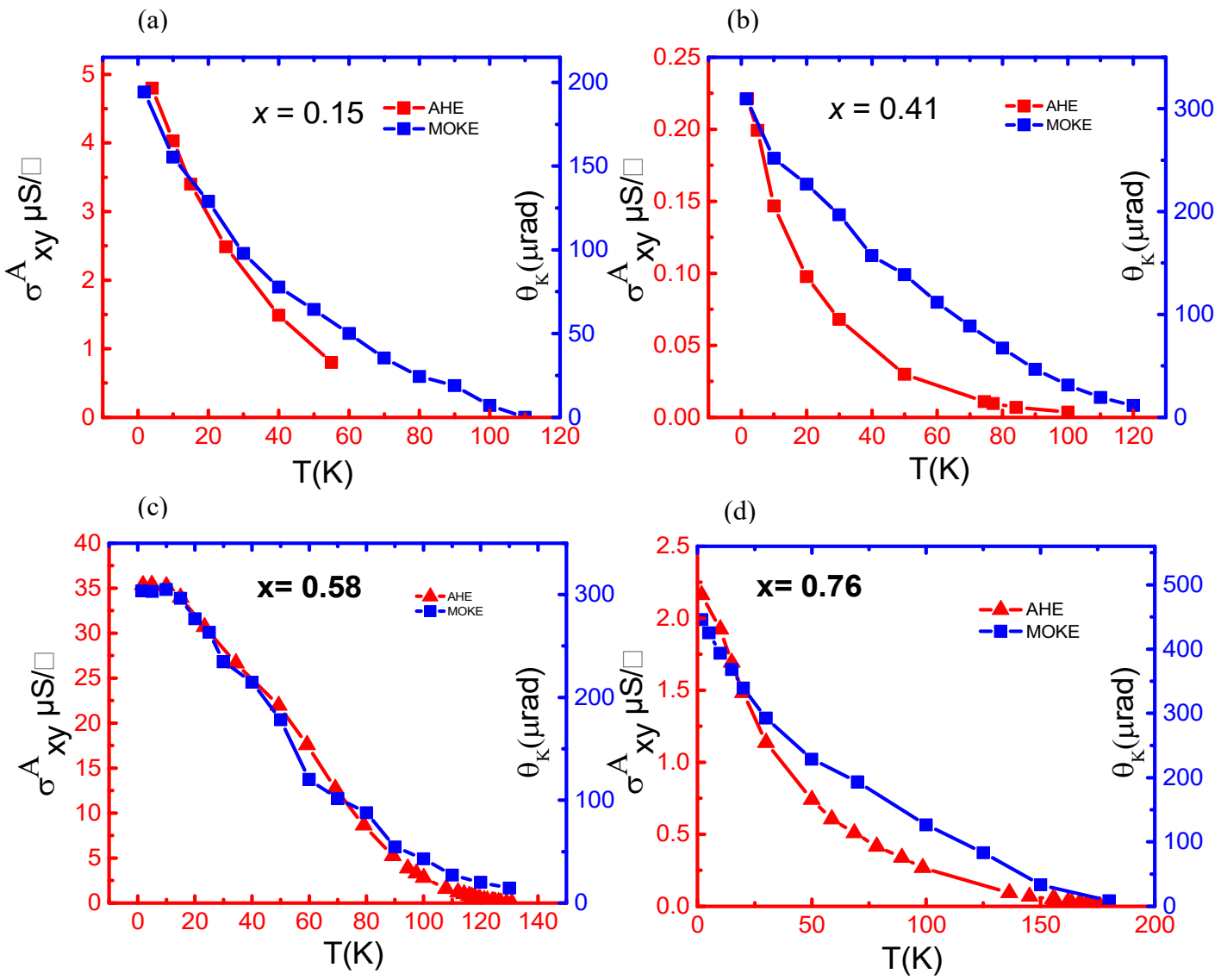

Figure 4.15 Comparing the results of zero-field anomalous Hall conductivity $\sigma_{xy}{}^{A}$ and optical Kerr rotation θ_K for samples with $x = 0.15$ to $x = 0.76$ as a function of T.

The evolution of the anomalous Hall conductivity with temperature and magnetic field can be linked to the magnetization M, of the sample through the following relationship[99]: $\rho_{xy} = R_oB + R_sM$, where ρ_{xy} is the total Hall resistivity, B is the applied magnetic field, $R_o = 1/nec$ (e being the electron charge and n the carrier concentration) is the ordinary Hall coefficient arising from the Lorentz force experienced by electrons/holes and R_s is the anomalous Hall coefficient. Upon dividing this equation by $\rho_{xx}{}^{2}$, we see that the equation expresses the additivity of the Hall currents, that is, the total Hall conductivity $\sigma^{T}{}_{xy}$.

As $\rho_{xy} \ll \rho_{xx}$, $\sigma^{T}{}_{xy} = \frac{\rho_{xy}}{\rho_{xx}{}^{2} + \rho_{xy}{}^{2}} \approx \frac{\rho_{xy}}{\rho_{xx}{}^{2}} = \frac{RoB + R_sM}{\rho_{xx}{}^{2}}$ with $\sigma^{T}{}_{xy} = \sigma^{O}{}_{xy} + \sigma^{A}{}_{xy}$,

where $\sigma^{O}{}_{xy}$ and $\sigma^{A}{}_{xy}$ are the ordinary and anomalous Hall conductivity, respectively. These result in: $\sigma^{A}{}_{xy} = \sigma^{T}{}_{xy} - \sigma^{O}{}_{xy} = \frac{R_S M}{\rho_{xx}{}^2}$. From this equation, an accurate determination of $\sigma^{A}{}_{xy}$ will indirectly yield the magnetisation M by carefully removing the ordinary Hall component $\sigma^{O}{}_{xy} = \frac{R_O B}{\rho_{xx}{}^2}$, hence enabling the field and temperature dependence of M to be extracted directly from magneto-transport data. Figure 4.15 (a-d) shows the variation of $\sigma^{A}{}_{xy}$ and θ_K with respect to temperature for all the doped samples. All the magnetization curves as measured with both techniques were strikingly concave over a broad range of temperatures in contrast to the convex Brillouin-function behavior of the mean field theory,[129] observed in most ferromagnetic metals. This outwardly concave feature of magnetization is often observed in DMS systems with low carrier densities, which can be explained by the polaron percolation theory[130], complimentary to the mean field theory. In the event that the carrier density is low, the carriers are treated as localized in the impurity band of the semiconductor, and exchange interaction between localized carriers and magnetic impurities help to form bound magnetic polarons. In reality a typical DMS system will have a magnetization curve exhibiting anything between a highly concave (low carrier density) and highly convex (high carrier density) shape[131]. This behavior was similar to that reported by Chang *et al*.[118] in their transport data but different to that of Zhou *et al*.[92] in their SQUID data, both for Cr doped TIs. Furthermore, the surface sensitivity of MOKE measurements might also account for the discrepancy with the transport measurements, which are depending on the bulk properties as well. The coercive field H_c as obtained from transport and MOKE were compared with each other. This displays a good match for all the samples except for the one with x = 0.15 and 0.41 as shown in Figure 4.16 (a-d). Various reasons could be the cause of this, a few suggested reasons are: doping inhomogeneity in the sample during MBE growth processing, and as mentioned before, the laser power was much higher in the case of x = 0.41 and 0.15.

Theoretically the Curie temperature T_c can be estimated as the point when $\sigma^{A}{}_{xy}$ and H_c both decrease to zero at zero magnetic field, but measurements in an applied magnetic field show a tail above the T_c. This may be due to sample inhomogeneity leading to slightly different T_c's or a remnant field arising from the superconducting magnetic coils in the cryostat.[107] Hence it is best practice to accurately determine the T_c by using Kouvel-Fisher (K-F)[132] and Arrott-Noakes[133] plots.

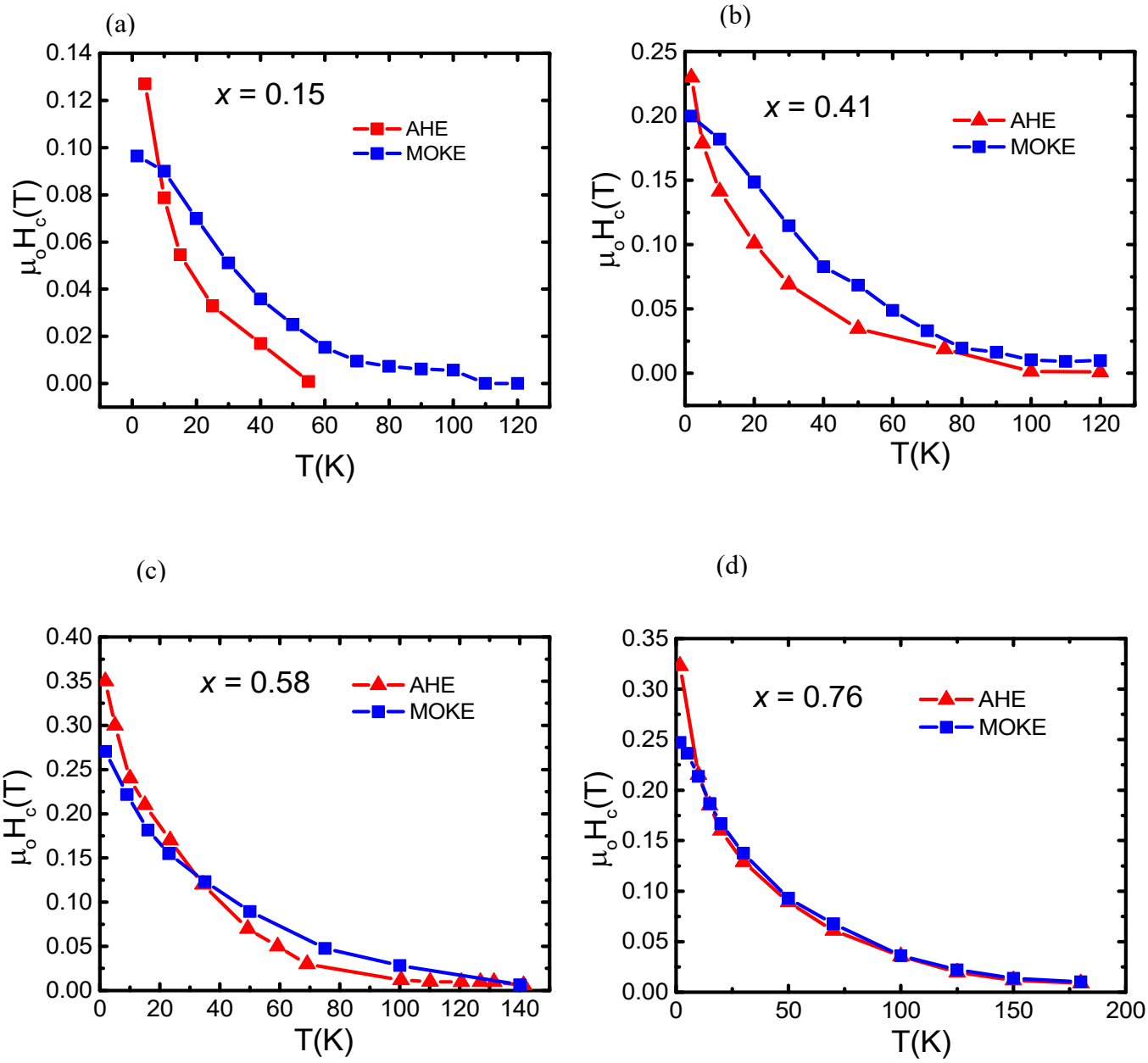

Figure 4.16 Comparing the values of the coercive field H_c from electrical transport and MOKE data for samples with $x = 0.15$ to $x = 0.76$ as a function of T.

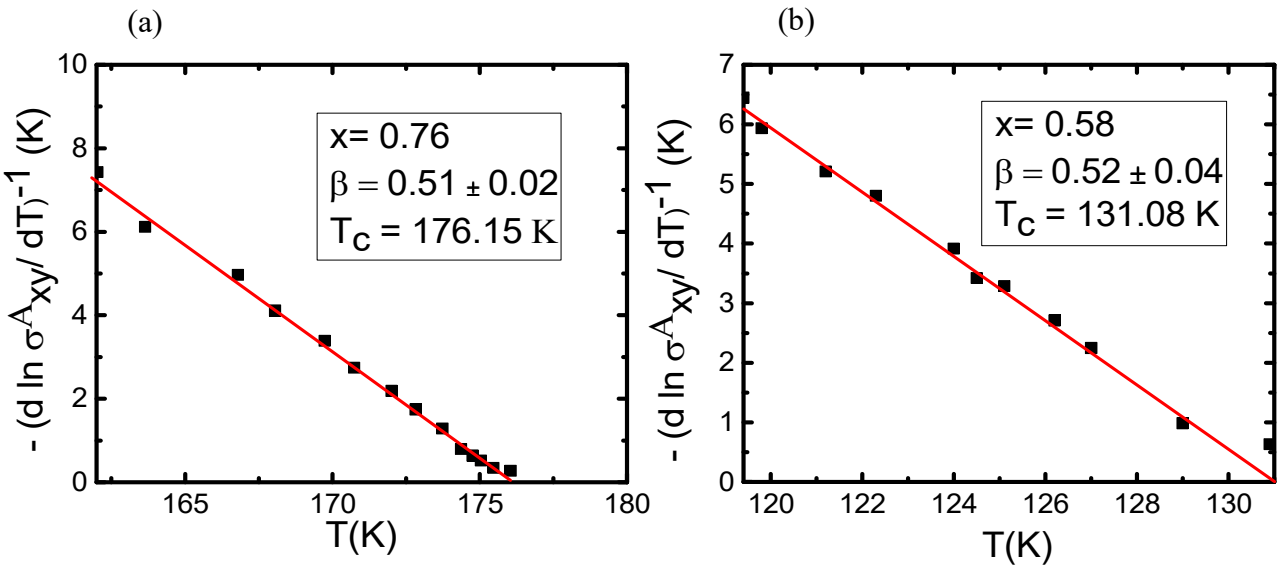

Figure 4.17 Kouvel-Fisher plots for samples with $x = 0.76$ and $x = 0.58$ showing the obtained values of β and T_C from the slope and intercept, respectively.

Close to T_c all ferromagnetic material properties are determined by critical fluctuations following power law dependences[134]. In the case for K-F plots the reduced magnetization follows: $\left(\frac{dln\, M}{dT}\right)^{-1} = -\frac{1}{\beta}(T_c - T)$, where β is the critical exponent. Replacing M with $\sigma^A{}_{xy}$ and plotting $\left(d\ ln\, \sigma^A{}_{xy}\ /dT\right)^{-1}$ against T yields β from the slope and the value of T_c from the intercept on the T axis. Figures 4.17 (a) and (b) show the K-F plots with linear fits performed over reduced temperature ranges for the samples with $x = 0.76$ and 0.58, giving a value of $\beta = 0.51 \pm 0.02$ and 0.52 ± 0.04 for both samples. These values are consistent with the value of 0.5 predicted in the mean-field model. The corresponding T_c values were (176.15 ± 0.02) K and (131.08 ± 0.02) K.

In the case of Arrott-Noakes plots, the equation takes the form: $\left(\frac{h}{\sigma^A{}_{xy}}\right)^{1/\gamma} = at + b(\sigma^A{}_{xy})^{1/\beta}$,where a and b are assumed to be temperature-independent coefficients related to the critical amplitudes, while β and γ are the implicit critical exponents. Figures 4.18 (a-d) show modified Arrot plots using the mean field exponents values of $\beta = 0.5$ (deduced from the K-F plots) and $\gamma = 1$ for the samples with value of $x = 0.78$ to 0.15. The plots give parallel straight lines for each T, with that for $T = T_c$ passing through the origin. The corresponding T_c values obtained were 176 K ,132 K, 74 K and 40 K for $x = 0.76$, 0.58, 0.41 and 0.15 respectively, hence justifying the use of the mean field critical exponent values.

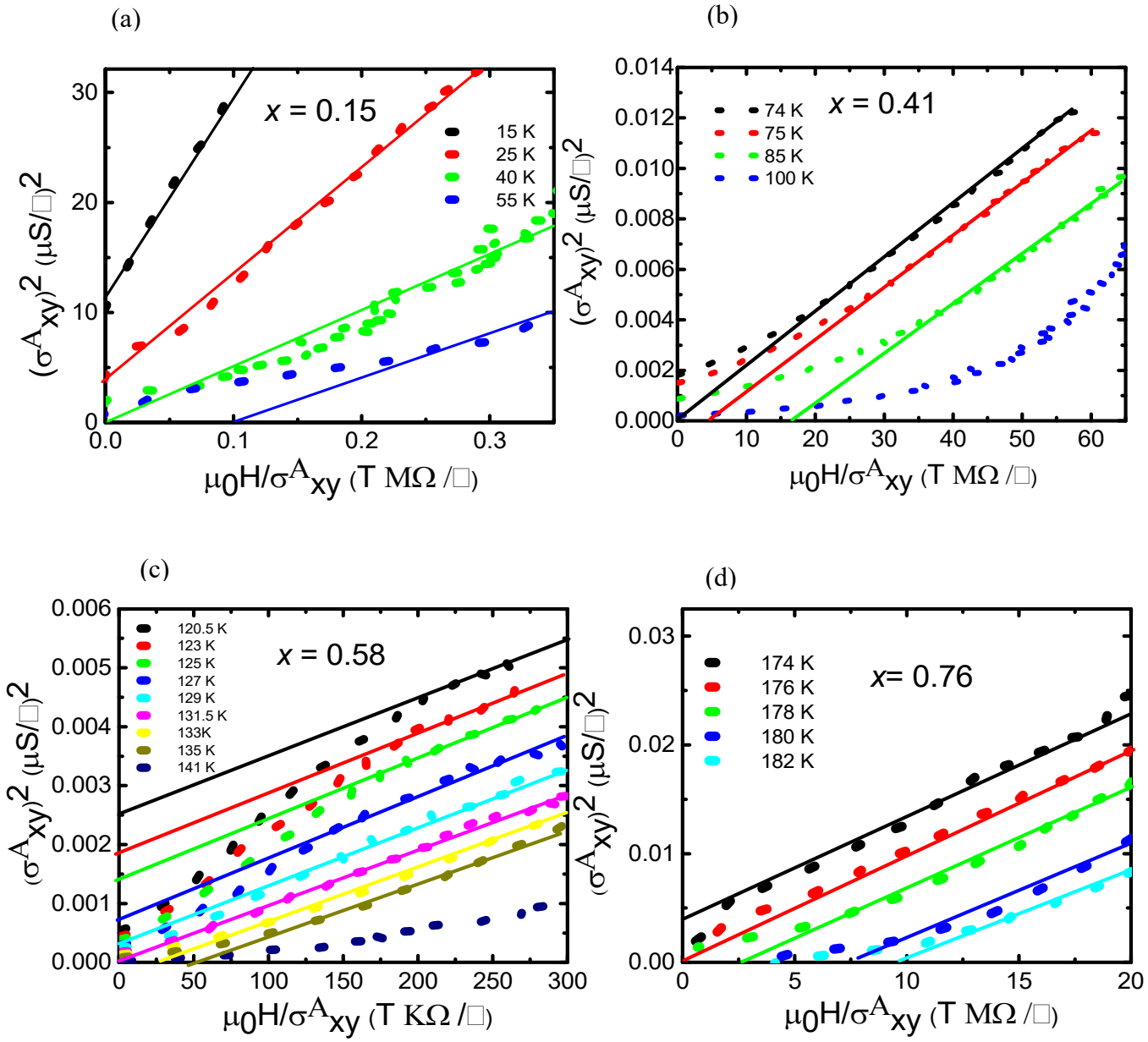

Figure 4.18 (a-d) Arrot plots for samples with x = 0.15 to 0.76 giving a T_c of 40 K, 74 K, 131.5 K and 176 K, respectively.

After estimating the Curie temperatures for all of the samples, the next step was to see if a gate modulation would change the magnetic properties of the film. Given this context, there is a strong motivation to understand the mechanism of the magnetic behavior in doped TIs. Two models have been proposed in literature: (i) the Van Vleck mechanism,[135] which is caused by the large spin susceptibility of the valence electrons in the band-inverted TI materials, and (ii) the Rudderman-Kittel-Kasuya-Yosida [33] coupling, where the magnetic ions can indirectly couple with the assistance of itinerant electrons(also refer to Figure 1.8).

Consequently, the former is independent of the carrier density and refers to "bulk ferromagnetism", while in the latter case the neighboring magnetic moments couple via a carrier-mediated mechanism.

Applying an ion gel as a gate dielectric allows an efficient control of the carrier densities at very low operating voltages, making it superior compared to other gating methods which suffer from high leakage currents, slow polarization responses and limited transistor operation speeds at less than 100 Hz[136,137]. Commercially purchased ionic-liquid *N*, *N*-diethyl-*N*-(2-methoxyethyl)-*N*-methylammonium bis (trifluoromethylsulphonyl-imide), DEME-TFSI was drop casted using a micropipette on top of the channel of the Hall bar as shown in Figure 4.19 (a). One of the arms of the Hall bar was isolated from the channel and used as a ohmic contact for the drop casted gate. By applying a positive gate voltage, the $DEME^+$ cations accumulate on the channel of the cleaved Hall bars flat surface and an electric double layer, which acts as a capacitor with nanoscale thickness, forms at the liquid/solid interface. The Figure 4.19 (b) shows the Hall resistance R_{xy} modulation with the gate bias fixed at -3 V, 0 V and +3 V at 200 K for the sample with $x = 0.58$ at 1.8 K. The amplitude of the hysteresis loop increased, showing an increase in the AHE, as the gate bias was lowered from +3 V to -3 V. The leakage current in the ion gel dielectric was less than 100 nA. The total carrier density p changed from 1.89 x10^{14} cm^{-2} at -3 V to 9.31 x10^{13} cm^{-2} at +3 V. The increase in the $\sigma^A{}_{xy}$ at -3 V is explained by the increase in the hole concentration on applying an electric field, resulting in an increase of the magnetization hinting towards a hole-mediated ferromagnetic interaction between localized Cr spins, although there is no apparent change in the T_c with gate dependence as evidenced by the $\sigma^A{}_{xy}$ vs T plot in the lower inset of Figure 4.19 (b). The inset on the top of Figure 4.19 (b) shows R_{xx} vs V_g sweep at 200 K (the temperature where gel modulation was possible before cooling to 1.8 K). R_{xx} increased with increasing V_g from -3V to +3V. The bottom inset of Figure 4.19 (b) shows the temperature dependent $\sigma^A{}_{xy}$ deduced from the saturated behavior at +3, 0 and -3 V.

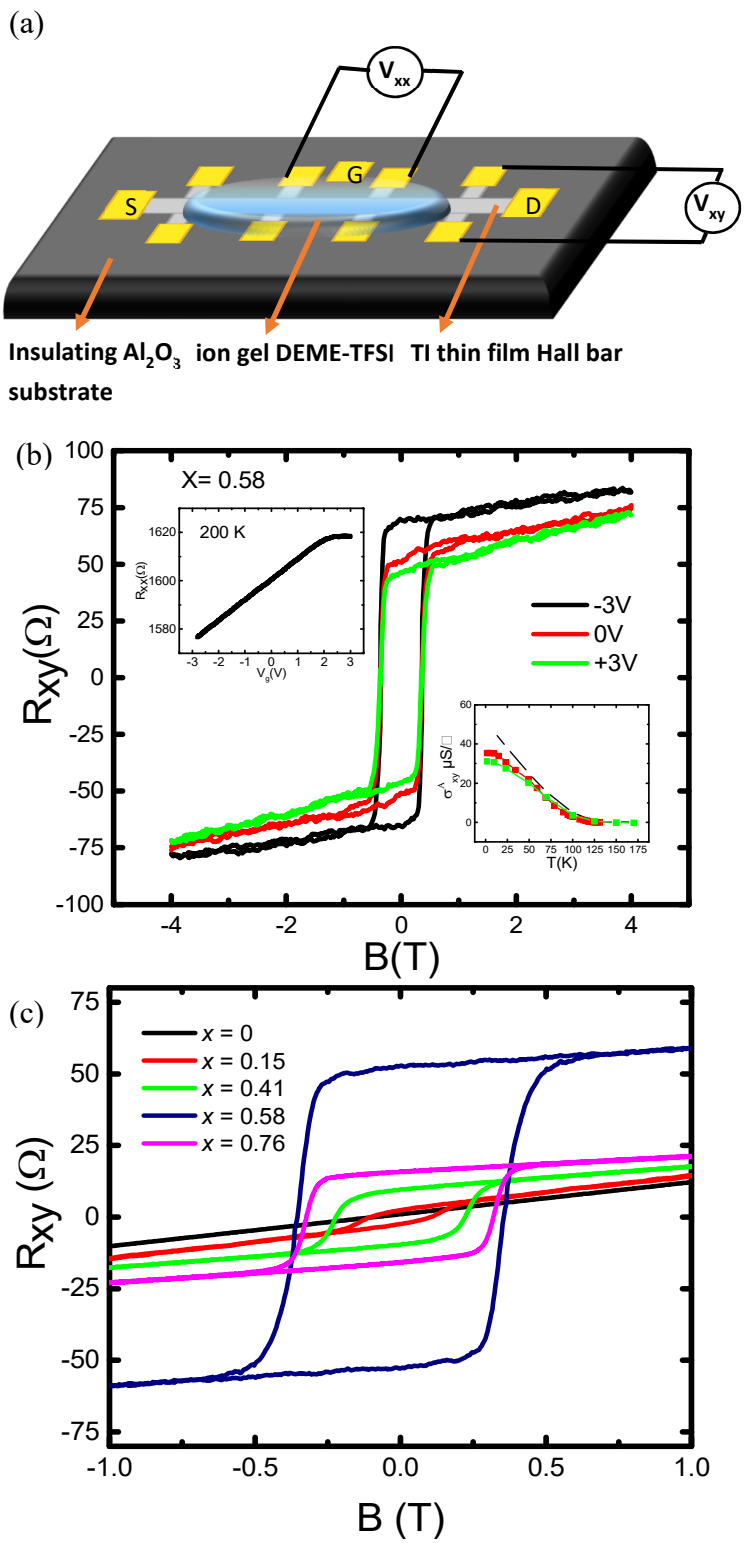

Figure 4.19 (a) A schematic of a Hall bar with an ion gel drop casted along the channel of the Hall bar (b) Gate bias dependence of the Hall traces R_{xy} in a sample with x = 0.58 at 1.8 K showing an decrease in the AHE from -3V to +3V. Top inset: R_{xx} vs V_g curve at 200 K. Lower inset: T dependence of the anomalous Hall conductivity $\sigma_{xy}{}^{A}$ for V_g = -3 V, 0 V and +3 V. (c) The AHE signal at 1.8 K for x varying from 0 to 0.76.

To visualize the effect of doping a plot showing the total Hall resistance versus perpendicular magnetic field at 1.8 K for all the samples was plotted in Figure 4.19 (c). The coercive field and saturated Hall resistance increased monotonically with higher Cr concentration except for the sample with $x = 0.76$. A similar trend was also reported by Lee *et al*. in Mn doped Bi_2Te_3, which they attributed to structural flaws arising from a Bi bilayer sandwiched between two QLs[138]. Our XRD data showed no parasitic peaks as presented in Figure 3.27 over the entire scan range even for the highest Cr doped sample where a reduction in the *c*-lattice parameter corresponded to Sb being replaced by Cr. The homogeneity of magnetic ordering in transition metal doped TIs has been debated for a while and a few possible scenarios were proposed such as super-paramagnetism[139], long-range ferromagnetism, antiferromagnetic coupling[140] and cluster formation[141]. These scenarios depend on the location and concentration of the Cr atoms in the crystal. For example, Cr atoms sitting at interstitial sites may form clusters and couple antiferromagnetically, while Cr replacing Sb sites couples ferromagnetically[142]. Hence, our results may be explained by the spontaneous coexistence of ferro–and antiferromagnetic coupling leading to a lower saturation magnetization at 0 T for $x = 0.76$. In order to further our understanding on the magnetic interaction and elucidate the mechanism of magnetism, a detailed study was carried out to comprehend the relationship between carrier densities, T_c and Cr concentration trends using THz - TDS.

It is a well-known that device processing makes it more challenging to probe the surface states of pristine TI thin films[143] as TIs are very sensitive to water and organic solvents. To circumvent this issue, a contact-free and non-invasive THz–TDS technique was employed to study optical conductivities and to determine the carrier densities and mobilities for all the samples. This allows us to compare them directly with the results obtained from electrical transport measurements. The carrier damping rate in TIs (typically $\sim 10^{-13}$ s^{-1}) lies in the THz frequency range (0.8-2.2 THz), making broadband THz spectroscopy a particularly sensitive probe of TI carrier dynamics. Moreover, the typical energies of collective quasi particles such as optical phonons have a fingerprint across the energetic range of the THz radiation (10 - 15 meV) making it a powerful technique to study TIs[144]. The time-resolved THz transmission through all the $Cr_xSb_{2-x}Te_3$ thin films was measured at 4 K as shown in Figure 4.20 (a). The primary transmitted THz field intensity shows a systematic reduction with increasing Cr concentration *x* [see inset in Figure 4.20(a)] which signifies an increased free carrier absorption potential in the film. To further quantify this behavior, we extracted the carrier densities of each sample.

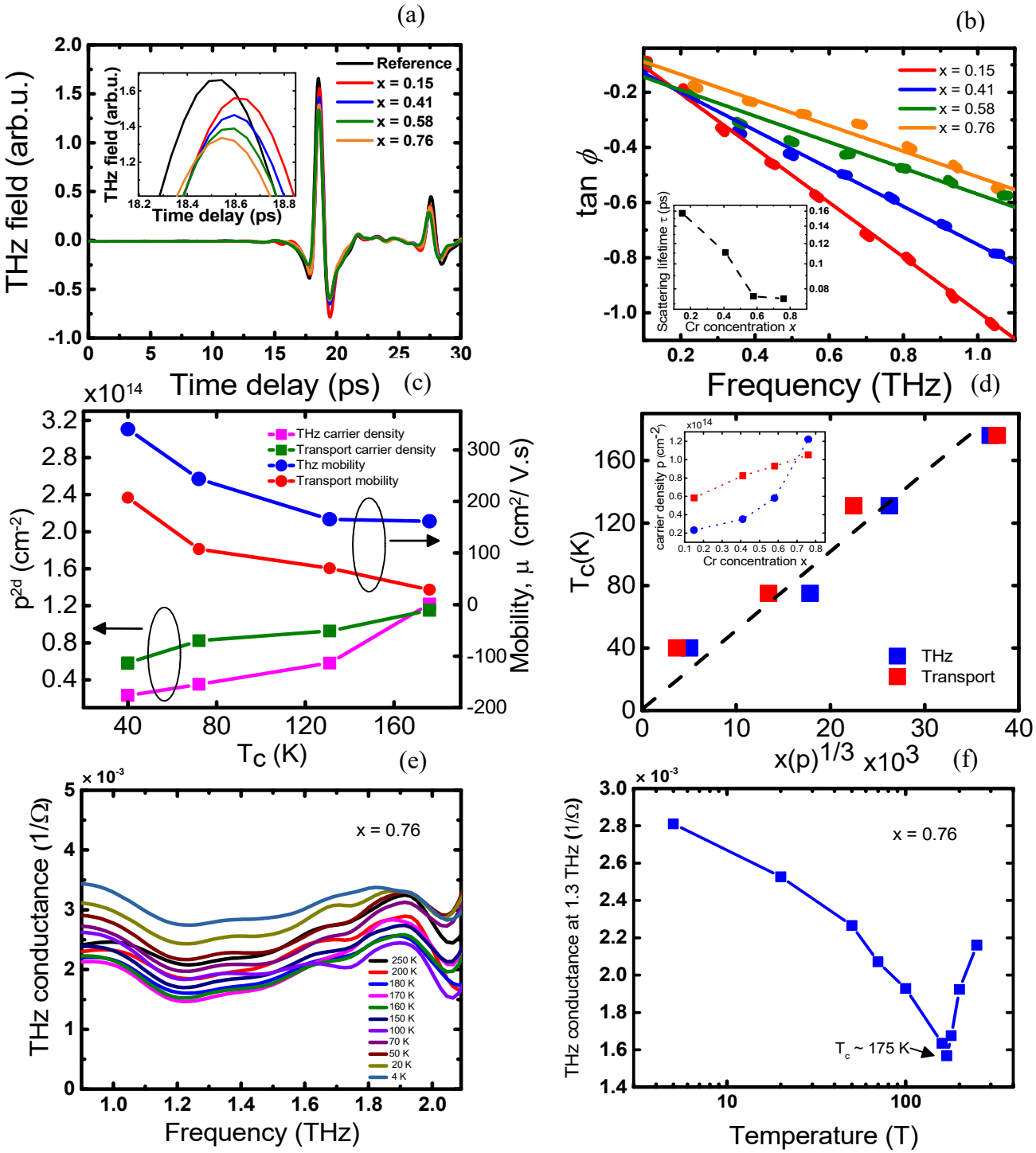

Figure 4.20 (a) Time domain picosecond pulse response transmitted through 20 QL of $Cr_xSb_{2-x}Te_3$ films with varying Cr concentrations x. The inset shows a magnified pulse response transmitted through the $Cr_xSb_{2-x}Te_3$ film and a reference transmission through a (0001) sapphire substrate at 4 K. (b) Plot of tan ϕ vs. frequency. The solid lines represent the linear fit to each data set. The inset shows the scattering lifetime τ vs x. (c) The plot of mobility μ and carrier density p^{2d} vs. Curie temperature T_c of each sample deduced from the THz measurements (blue and pink curves), and Hall measurements (red and green curves) respectively. (d) Sheet carrier density, $p^{1/3}$. x as a function of T_c obtained from the THz measurements (blue curve) and Hall measurements (red curve). The inset shows carrier density p^{2d} vs. carrier concentration x. (e) THz conductance spectra of $Cr_{0.76}Sb_{1.24}Te_3$ showing distinct features at ~1.9 THz which are indicative of an optical phonon. (f) THz conductance at 1.3 THz as a function of T displaying a minimum at the samples T_c. (THz measurement analyses was performed by Dr. Varun Kamboj)

Using the Tinkham's equation for thin films[145] and substituting for the complex Drude conductivity as $\tilde{\sigma}(\omega) = \sigma_0/(1 - i\omega\tau)$, the following relationship was obtained between the imaginary and the real parts of the transmission coefficient: $Im.\{\tilde{T}(\omega)\}/Re.\{\tilde{T}(\omega)\} = -\omega\tau = \tan\phi$, where ϕ is the phase angle between the sample and substrate waveforms, ω is the angular frequency and τ is the scattering lifetime for the carriers. Plotting $\tan\phi$ as a function of frequency [Figure 4.20 (b)] and fitting it with a linear regression, the slope yielded the scattering lifetime τ [inset to Figure 4.20 (b)] and hence the mobility μ, where $\mu = \tau e/m^*$(assuming that the bulk hole effective mass m^* in Sb_2Te_3 is 0.78 m_e, with m_e as the electron rest mass)[146].

The carrier concentration p^{2d} was then obtained using the following relationship between sheet conductance G_{2d} and p^{2d} as, $G_{2d} = G(\omega \to 0) = \mu e p^{2d}$. This yielded the plot shown in Figure 4.20 (c) directly comparing the values of p^{2d} and μ extrapolated from the slope of R_{xy} vs B at high fields [Figure 4.19 (a)]. The carrier densities (and mobilities) in both measurements increased (decreased) roughly linearly with the Curie temperature T_c [as obtained from Figure 4.18 (a-d)] yielding the carrier dependency on the magnetic ordering temperature of the samples. It is interesting to note that the values of p^{2d} obtained from the THz measurements tend to be smaller than those deduced from the Hall transport measurements besides from the highest doped sample. A bulk hole effective mass $m^* = 0.78$ m_e was used when calculating the values for the THz measurements[146]. Due to the anisotropic nature of the upper and lower valence bands in Sb_2Te_3 the effective mass varies from $m^* = 0.034$ m_e to $m^* = 1.24$ m_e[146,147]. This was likely to be one of the origins for the quantitative discrepancy in the parameters obtained from THz and transport measurements. Furthermore, Ar^+ ion milling used during the Hall bar processing has been reported to increase the transport carrier density in TIs[148]. Figure 4.20 (d) shows the relationship between T_c and $x(p)^{1/3}$. In the case when magnetism is mediated through carriers in the mean field approximation, the Curie temperature is given by[140]: $T_c = \frac{S(S+1)}{3k_B} nJ^2\chi$, where S is the spin quantum number of Cr, n is the number density of Cr in the material, J is the exchange interaction constant between localized Cr spins and itinerant holes, and χ is susceptibility of itinerant hole spins. In the above equation, χ is characterized as: $\chi = \frac{m^*}{h^2} k_F = \frac{m^*}{h^2}(3\pi^2 p)^{\frac{1}{3}}$, where m^* is hole effective mass, h is Planck constant and p is hole density. The above two equations indicate that in mean field theory T_c will be proportional to $x(p)^{1/3}$. The Curie temperature T_c with respect to $x(p)^{1/3}$ in all samples was plotted with results obtained from

electrical transport and terahertz measurements in Figure 4.20 (d). The results demonstrated a linear dependence between T_c and $x(p)^{1/3}$ consistent with the mean field approximation in the parabolic band model[140], strongly suggesting the RKKY mediated magnetism in our $Cr_xSb_{2-x}Te_3$ films. This behavior was similar to that reported by Zhou *et al*.[92] and Li *et al*[149]. The inset of Figure 4.20 (d) illustrates the proportionality between the Cr doping concentration x and the carrier density p with a monotonic increase in p with x also consistent with the mean field theory.

Temperature dependent THz - TDS was further performed on the $Cr_{0.76}Sb_{1.24}Te_3$ sample (largest Cr concentration) and the corresponding THz conductance spectra was deduced [Figure 4.20 (e)]. A detailed description of the method used to obtain the THz conductance is discussed elsewhere[144]. The THz conductance spectra in Figure 4.20 (e) showed a response with a characteristic phonon signature at 1.9 THz, consistent with previous reports of THz measurements on Sb_2Te_3 and other TIs[150,151]. Figure 4.20 (f) shows the THz conductance response of $Cr_{0.76}Sb_{1.24}Te_3$ at 1.3 THz plotted as a function of temperature. As the temperature was reduced from 300 K to 4 K, the THz conductance decreased rapidly indicating a freezing of the bulk carries in the TI film. However, the THz conductance began to gradually increase again with a further reduction in temperature due to an insulator to metal transition at ~175 K. Such a behavior is attributed to the spin disorder scattering that sets in at the paramagnetic to ferromagnetic phase transition.[122,123] The temperature (~175 K) obtained from the THz measurements was in close agreement with the T_c value obtained from the transport and MOKE measurements and was also consistent with the resistance vs. temperature plot for $Cr_{0.76}Sb_{1.24}Te_3$ (Figure 4.8). Introducing a magnetic dopant in TI breaks the time reversal symmetry[113] and a bulk type insulator response is expected from the film (*i.e.* conductance decreasing with decreasing temperature). However, below 175 K the THz conductance shows a metallic response as presented in Figure 4.20 (f), indicating that the magnetism could indeed be RKKY mediated. Table 4.3 summarizes all the set of samples and their properties.

Table 4.3 Summary of the physical parameters of the Cr-doped Sb_2Te_3. Cr atomic concentration measured and calculated using XPS, 2D carrier densities p and mobilities μ obtained from electrical transport and THz-TDS, and T_c deduced from electric transport.

Sample	p^{2d} **transport** (10^{13} cm^{-2})	p^{2d} **Thz** (10^{13} cm^{-2})	μ **transport** (cm^2/Vs)	μ **Thz** (cm^2/Vs)	T_c **(K)**
$Cr_{0.15}Sb_{1.85}Te_3$	5.83	2.33	207	340	39
$Cr_{0.41}Sb_{1.59}Te_3$	8.24	3.52	107	243	74
$Cr_{0.58}Sb_{1.42}Te_3$	9.28	5.81	70	165	132
$Cr_{0.76}Sb_{1.24}Te_3$	11.52	12.20	28	161	176

4.4 Electric Transport on Magnetically Doped Heterostructures of TIs

To take things further, an heterostructure was grown by Professor Thorsten Hesjedal at the University of Oxford using MBE and a wafer was sent to Cambridge university for device fabrication and measurements. The structure was an alternating ten layer stack of 6 nm of dysprosium doped Bi_2Te_3 followed by 6 nm chromium doped Sb_2Te_3 as shown in Figure 4.21 (a). The total thickness with ten layers comprising of Cr-doped Sb_2Te_3 and Dy-doped Bi_2Te_3 was 120 nms. Cr doped TIs are well known ferromagnets and their properties have been studied in great detail in the earlier section, while Dy doped TIs are relatively new with no studies performed on this material system related to electrical transport. By combining the two doped TIs into an heterostructure, the aim was to study the effect the layers had on each other via the proximity effect and perhaps probe ferromagnetism through the exchange bias (EB) effect. Dy in its elemental form although being a rare earth, is known to exhibit an anti-ferromagnetic phase below 179 K[152]. The combination of an antiferromagnet with a ferromagnet in a heterostructure may induce an EB effect which has become an integral part of modern magnetism with implications for numerous device applications. To name a few, the EB coupling is used in spin valves where one pinned and one free ferromagnetic layer is embedded in devices such as magnetic random access memory (MRAM), readout sensors and storage media. The EB effect was discovered 50 years ago by Meiklejohn and Bean[153]. Never the less more fundamental understanding needs to be unfolded which has further motivated the research field to explore the effect of EB in new material systems such as TIs[154]. The EB effect is an interlayer exchange coupling effect between a ferromagnet and an anti-ferromagnet while it manifests itself as a shift in the hysteresis loop from negative to positive direction with respect to the applied field. The origin of the effect is from the magnetic coupling between the common interface shared by the ferromagnetic layer and an anti-ferromagnetic layer. The essential part of an EB system is the different magnetic properties of the ferromagnetic layer and the anti-ferromagnetic layer.

Firstly, a Hall bar was fabricated in the clean room using an Ar^+ ion milling process to define the mesa and then Ti/Au ohmic contacts were thermally evaporated to form the source and drain of the bar. The sample had a two point resistance ~5KΩ at room temperature. The detailed overview on device processing is described in Section 5.4. The device was placed in a continuous flow cryostat and was measured up to a temperature of 1.8 K.

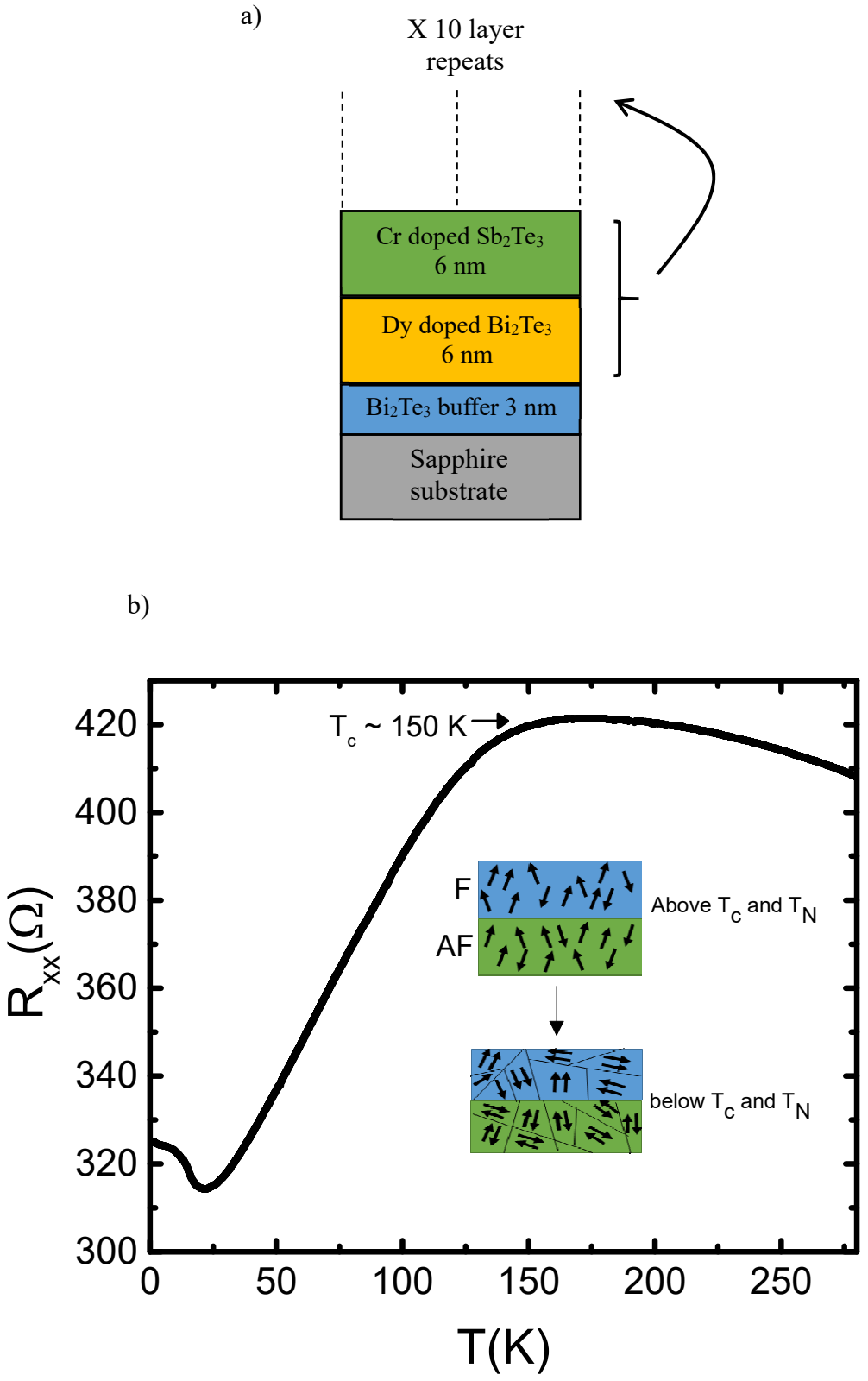

Figure 4.21 (a) Schematic of the heterostructure showing 10 layers each of Cr-doped Sb_2Te_3 and Dy-doped Bi_2Te_3 (b) Longitudinal resistance of the heterostructure Cr-doped Sb_2Te_3/ Dy-doped Bi_2Te_3 as a function of temperature from 300 K to 1.8 K.

The resistance of the sample was recorded as a function of temperature while cooling the cryostat from room temperature to 1.8 K as shown in Figure 4.21 (b). At first the resistance showed an insulator to metal transition around 150 K which may be associated with the ordering temperature, T_c of the Cr doped Sb_2Te_3 layer. Such a behavior is attributed to the reduction in the spin disorder scattering that sets in at the paramagnetic to ferromagnetic transition.[122,123]. The resistance then shows another transition around 18 K corresponding to a metal to insulator phase. This may be associated with the freezing of bulk carriers which may increase the resistance at low temperatures. The inset shows a model of what may be happening below and above the Curie temperature T_c and the Neel temperature T_N. Above the T_c and T_N , all the spins in both the Cr-doped layer (blue box) and the Dy-doped layer (green box) are disoriented as depicted with the black arrows inside the boxes. As the sample is cooled and reaches below T_c an T_N, F and maybe AF domains starts to form and ordering begins to take place in the sample, hence changing the resistance of the sample. It is difficult to ascertain the T_N as electrical transport only probes the ferromagnetic properties and not antiferromagnetic properties if they were any in the sample. Also the model displayed is only for the purpose of understanding and depicts the interface only (the boxes depict the behaviour at the interface only and not the full layer). In reality, the AF layer might only form on the interface of the Dy doped layer hence making the picture slightly more complicated to apprehend.

The temperature dependent magnetoresistance was then carried out and a magnetic field scan rate of 20 T/hour with a range of 0.6 T to -0.6 T was chosen. These numbers were chosen sensibly the reasons for which will be obvious as the chapter unfolds. Figure 4.22 displays the longitudinal resistance with respect to the external perpendicular field B at different temperatures. A change in resistance with respect to the magnetic field corresponding to the anisotropic magnetoresistance effect was observed. Interestingly the magnetoresistance effect was different for the up-sweep data (-0.6T to +0.6T) compared to the down-sweep data (+0.6T to -0.6T). This may mean that, not all the ten repeat layers of the ferromagnetic part were aligned with the field or some layers behave differently with field directions. It may also indicate that each Cr or Dy layer may be doped unintentionally slightly differently.

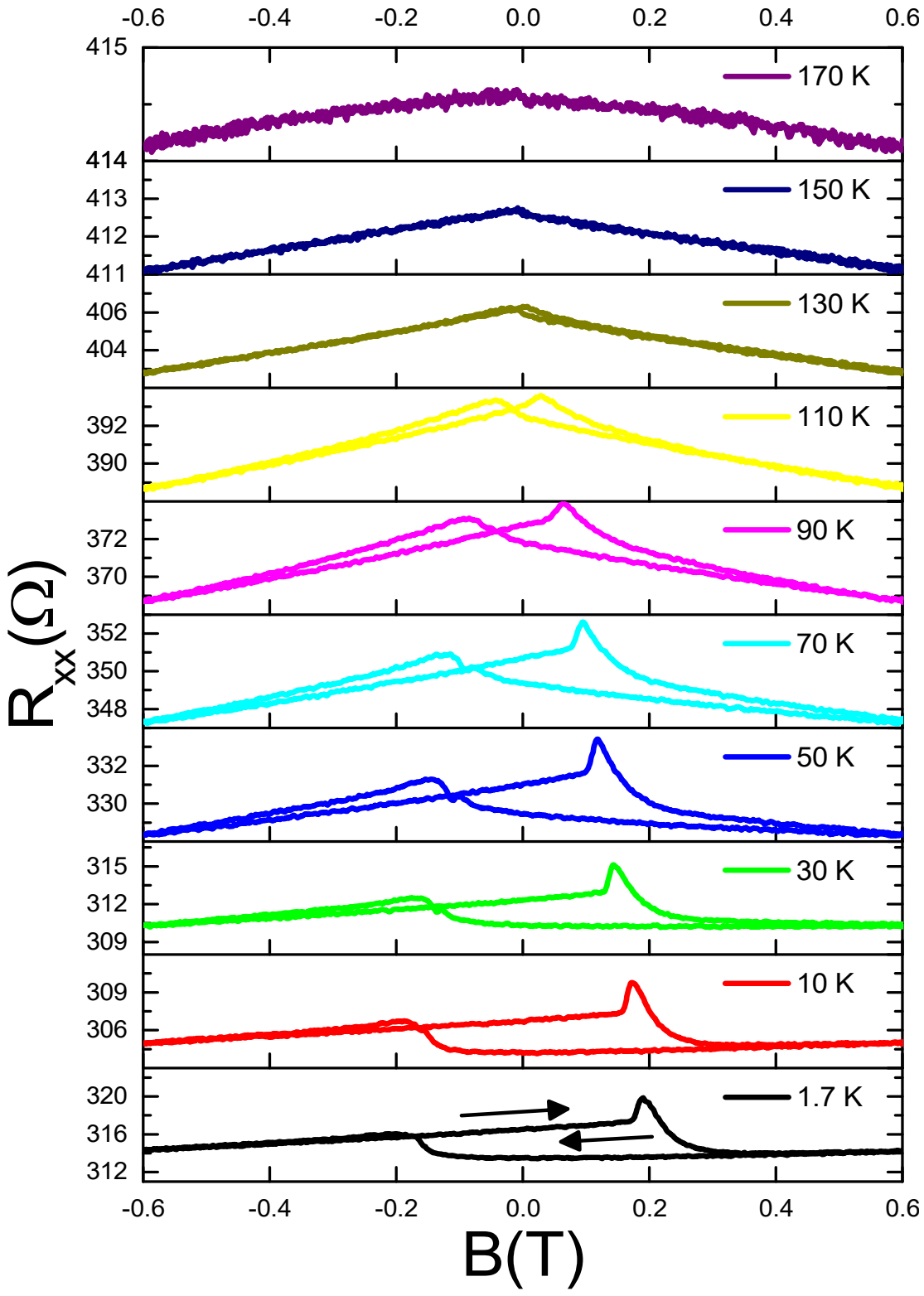

Figure 4.22 Temperature dependent Magnetoresistance within ± 0.6 T, with 20 K step size. Curie temperature was found to be around 150 K where the peak splitting vanishes.

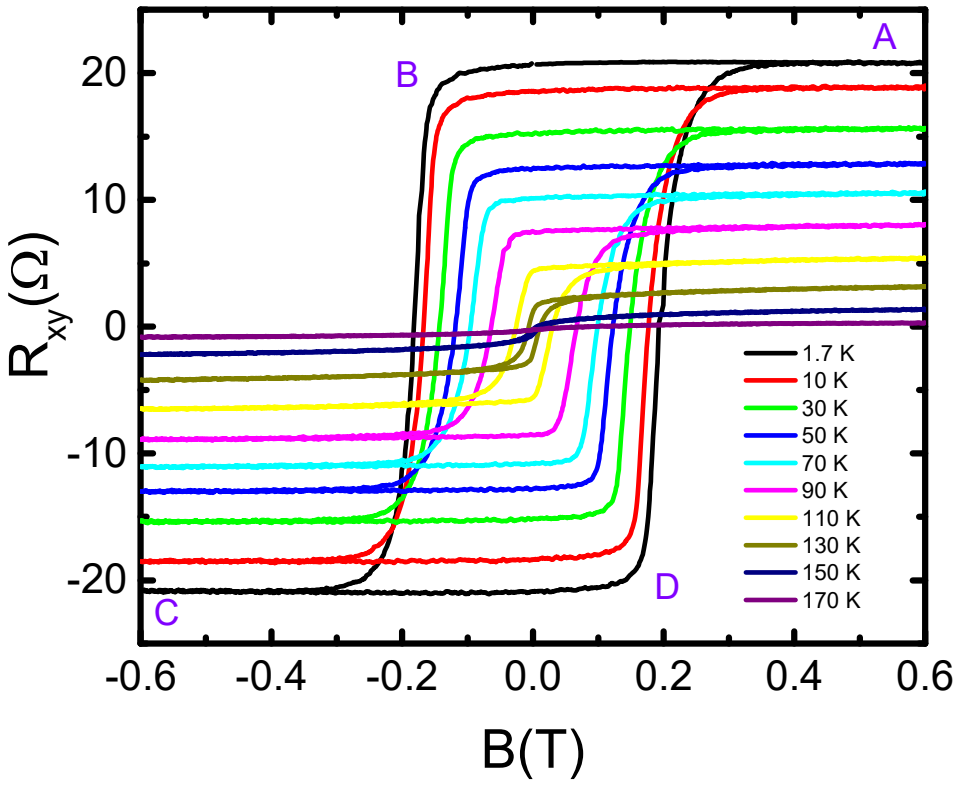

Figure 4.23 Temperature dependent AHE measurements within ± 0.6 T. Curie temperature was found to be around 150 K where the loop closes and no hysteresis is observed.

The Hall resistance was then swept within the same range: ± 0.6 T. The results displayed the anomalous Hall effect centered at 0 T as shown in Figure 4.23. The Curie temperature was found to be around 150 K where the hysteresis loop closes and the coercivity vanishes. There were a few important observations. Firstly, the loop is centered at zero field (the coercive field is equal on both sides of 0 T) and secondly at points B and D the switching of the curvature of the loop is rounded. A model was made to explain in more detail.

AT POINT A:

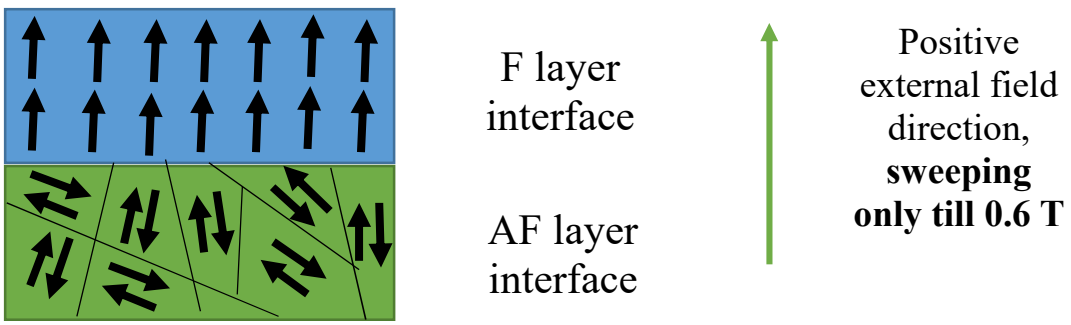

At point A, the magnetic field is at +0.6 T. This field was enough to saturate the ferromagnetic F layer spins in the positive field direction (blue box) with all spins pointing upwards, but not enough to generate enough antiferromagnetic spins at the interface of the Dy layer (green box), hence the AF spins remain semi-randomly oriented having no/very little effect on the F layer. An after effect of this can be seen by observing the rounded edges (B to C and D to A) on the hysteresis loops showing a coherent switching between spin up and spin down directions in the F layer. The loop is also centred at zero field as expected from a normal F response.

At Point C:

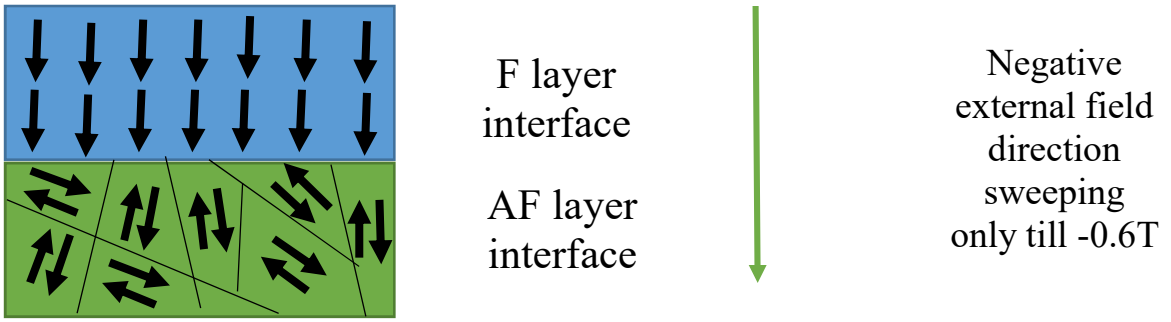

At point C, the field is now at -0.6 T. This field was enough to saturate the ferromagnetic F layer spins now in the negative field direction (blue box) with all spins pointing downwards, but not enough to saturate or create an antiferromagnetic AF interface, hence the AF spins remain randomly oriented having no effect on the F layer with the loop centred at zero field.

The magnetic field was now pre-set to +2 T. This was followed by a field sweep between +0.6 T to -0.6 T as shown in Figure 4.24. This time around, the results were different from what were observed without the preset. The longitudinal resistance R_{xx} with respect to external field B was measured and two important observations were made. Firstly the up-sweep and down-sweep curves did not match as before, but more importantly the curves were not centered at zero. There is an observation of a slight shift by ~ 0.06T to the left on comparing Figure 4.24 with Figure 4.22 at 1.9 K.

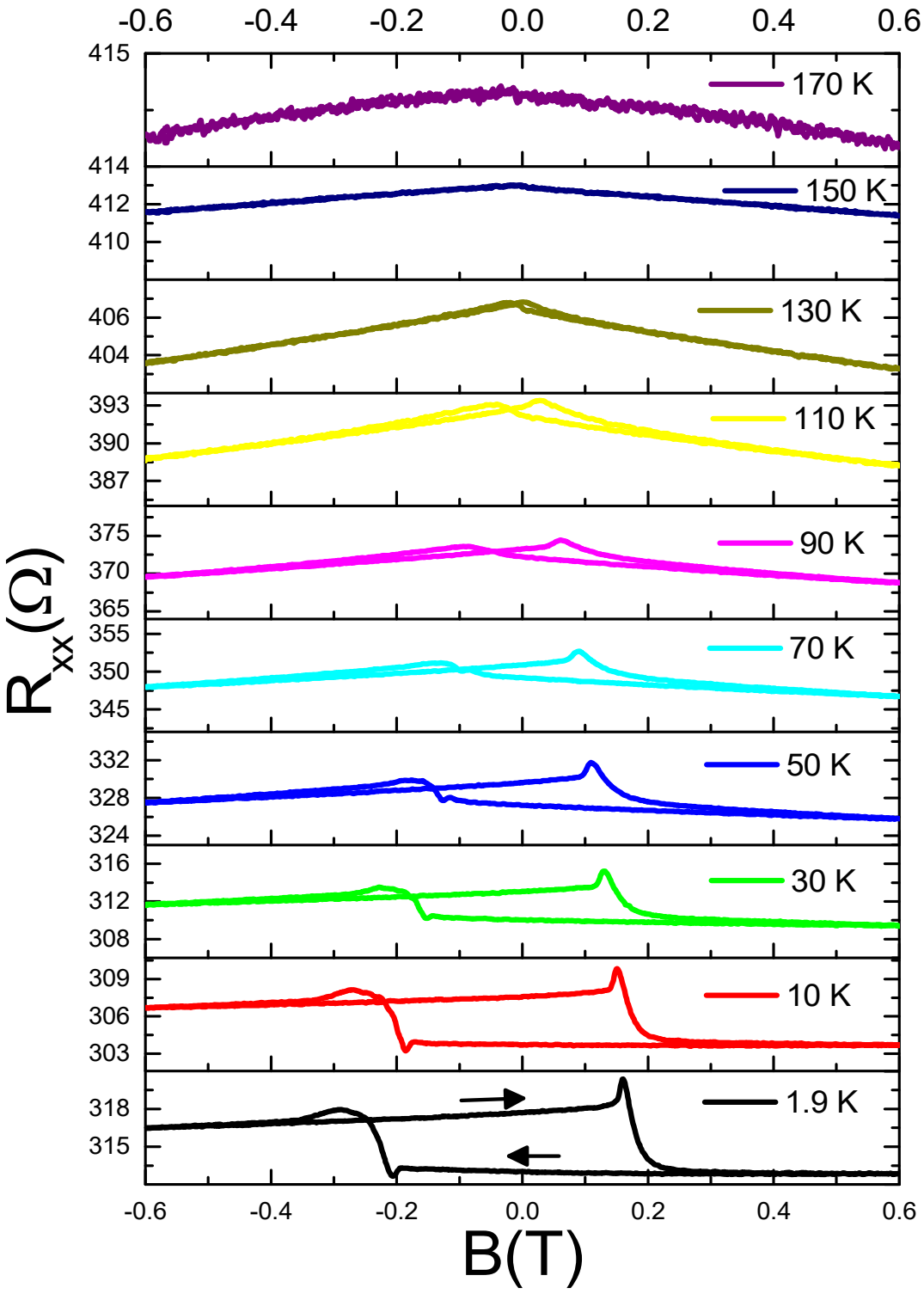

Figure 4.24 Temperature dependent Magnetoresistance within ± 0.6 T after presetting the magnetic field to +2T. Curie temperature was found to be around 150 K where the peak splitting vanishes.

A shift was also observed in the Hall data taken at different temperatures as shown in Figure 4.25.

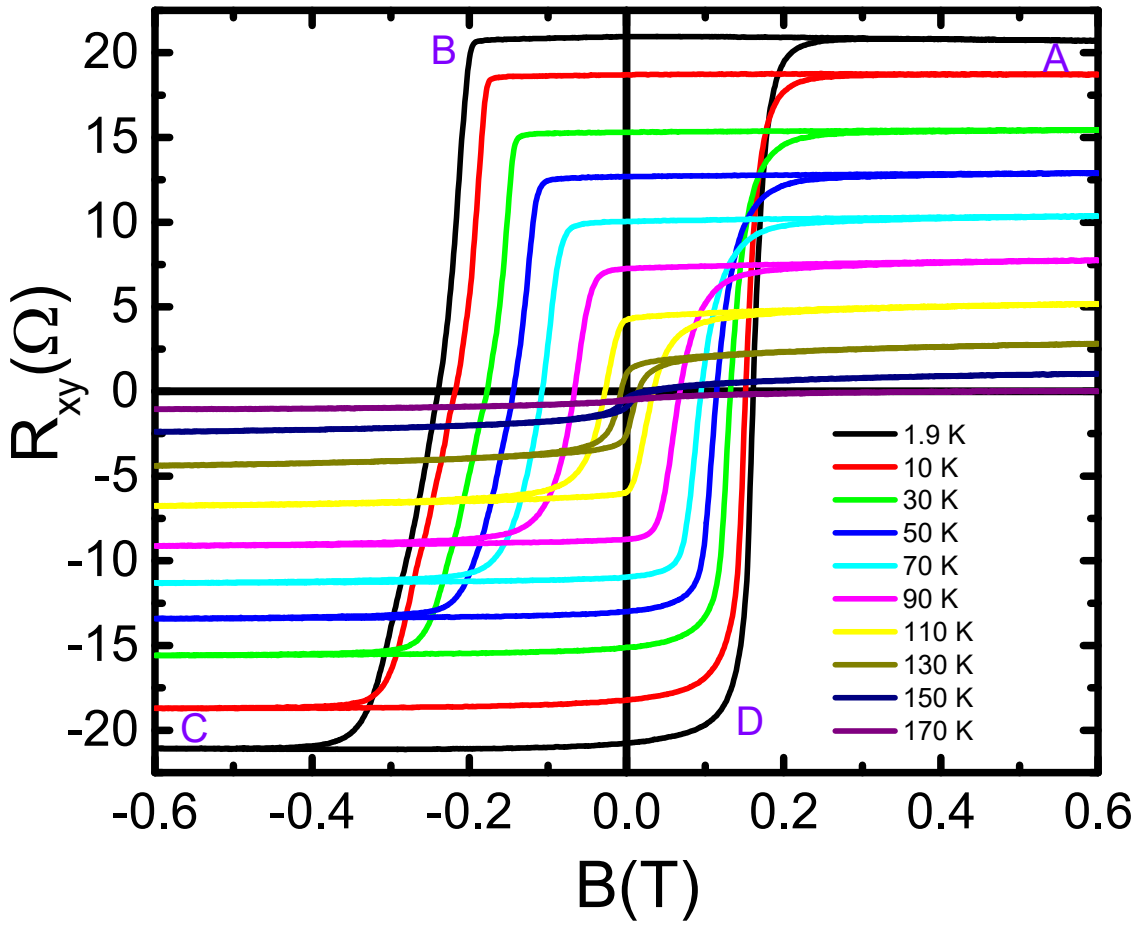

Figure 4.25 Temperature dependent AHE measurements within ± 0.6 T after presetting the external field to +2T.

The explanation is as follows: When the field is preset to +2T, then an antiferromagnet forms at the interface in the Dy doped layers. Now sweeping between ±0.6 T, the loop was shifted as expected from a hetero-structure showcasing the EB phenomenon. This observation was clearly noticeable below a temperature of 70 K. Above 70 K, no shift was observed. Also note: a sharp reversal was seen on the descending branch (+0.6T to -0.6T *i.e.* A to C via B) and a more rounded reversal was observed on the ascending one (-0.6T to +0.6T *i.e.* C to A via D). The explanation for this is as follows:

AT POINT A:

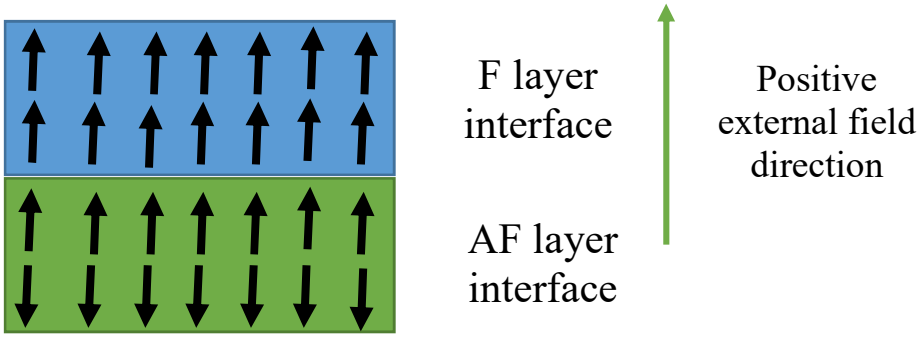

At point A, the field is at 0.6 T, which saturates the ferromagnetic layer interface (as depicted in the blue space above) where all the spins are aligned with the external positive field. Now since the external magnetic field was first pre-set to +2T, an antiferromagnetic layer is formed at the interface of the Dy doped layer. This causes the first monolayer of the Dy doped film to align parallel to the ferromagnetic interface of the Cr doped film while the second monolayer of the Dy doped film to align antiparallel to the pervious layer as to complete the AF order at the interface due to proximity effects (as shown in the green box).

FROM POINT B to C:

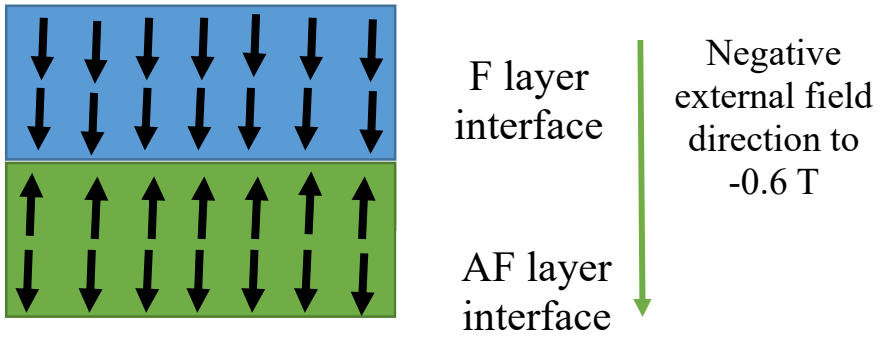

At point B, the field is now sweeping towards -0.6T. The ferromagnetic layer spins will try to rotate out-of-plane in the opposite direction (as shown in the blue box). Since the bottom F layer spins on the Cr doped layer were coupled to the top AF layer spins on the Dy doped layer interface, a bigger force and thereafter a stronger external field was required to overcome the coupling and to rotate the ferromagnetic spins. As a result of this, the transition is a sharp shift (not coherent *i.e.* the drop at point B) and the coercive field is higher. Since the coercive field is higher, a shift to the left is observed. On comparing Figure 4.25 with

Figure 4.23 at 1.9 K, a shift to the left in the curve was noticed by ~0.06 T in the former consistent with the EB effect.

At point D, the external field is now sweeping back towards +0.6T. As the field sweeps, the ferromagnetic layer will rotate back towards the positive direction of the field but this time much easily than before. This is because the top AF layer spins on the Dy doped layer interface are already pointing towards the positive field direction. So this time, lesser force will be required and the ferromagnetic spins will rotate coherently shown by the rounded reversal compared to a sharp one (point D). This is also consistent with the EB effect.

The magnetic field was now pre-set to -2T instead of +2T earlier and then field was swept from +0.6T to -0.6T like before. A similar EB effect was expected but in the opposite field direction. Figure 4.26 shows the R_{xx} vs. B data at different temperature after the field was pre-set to -2T. Similar observations were made as before: the up sweep curves and down sweep curves behave differently and the overall shift in the curves at 1.9 K is towards the right. Comparing Figure 4.26 with Figure 4.22, there is clear shift to the right hand side by ~ 0.03T.

A similar shift was also observed in the Hall data taken at different temperatures as shown in Figure 4.27.

The explanation is as follows: When the field is preset to -2T, then an antiferromagnet forms at the interface of the Dy doped layers. Now sweeping between $\pm$0.6 T, the loop was shifted as expected from a hetero-structure showcasing the EB phenomenon. This observation was noticeable at temperatures below 110 K. After 110 K, no shift was observed. Also note: the same sharp reversal was now seen on the ascending branch not the descending branch showcased earlier (-0.6T to +0.6T) and a more rounded reversal is observed on the descending one (+0.6T to -0.6T). Another important observation was that the EB phenomenon lasts till 110 K on the negative pre-set and lasts only till 70 K on the positive pre-set. (This may explain the asymmetry in the R_{xx} values on positive and negative sweeps for positive and negative presets).

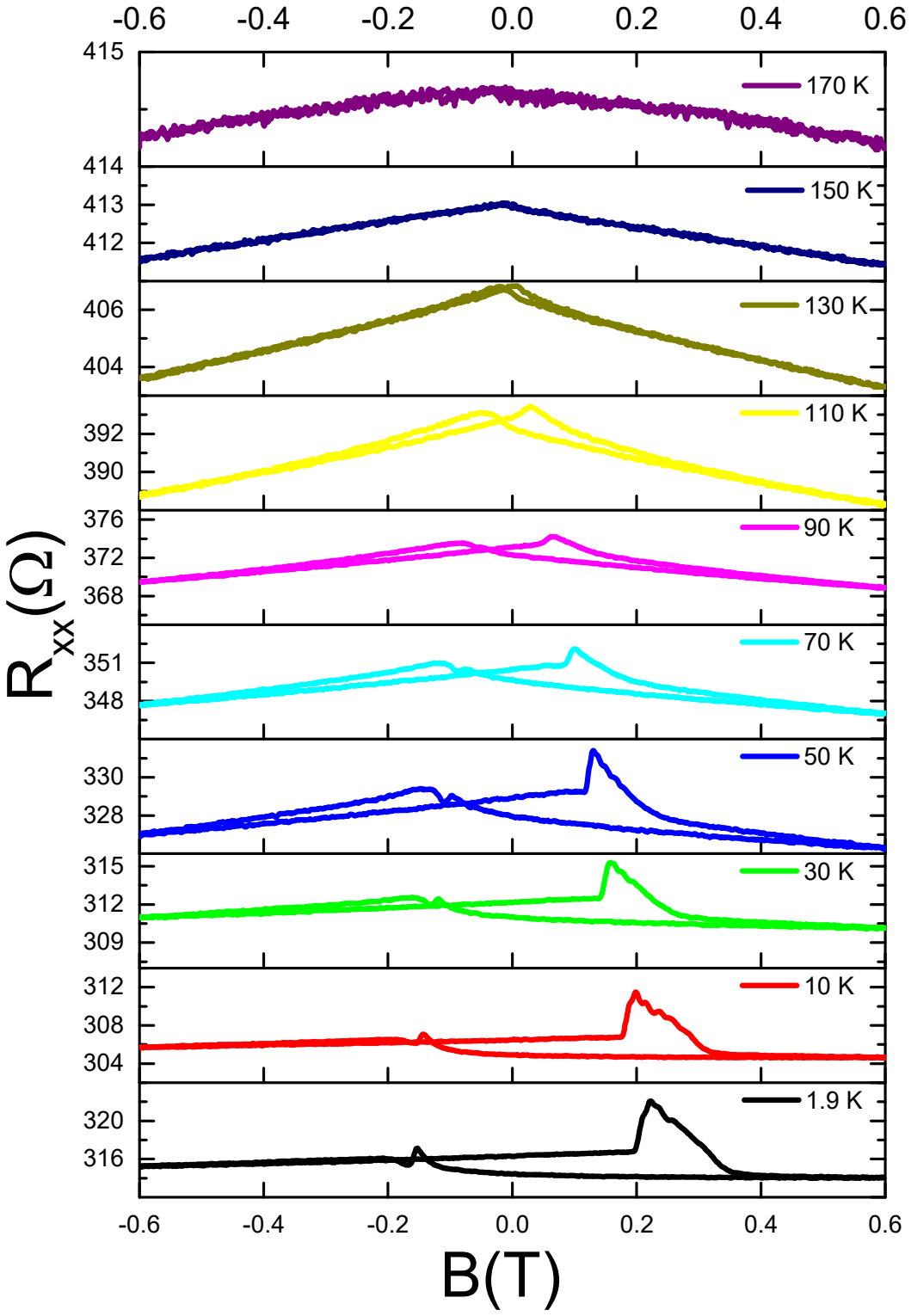

Figure 4.26 Temperature dependent Magnetoresistance within ± 0.6 T after presetting the magnetic field to -2T.

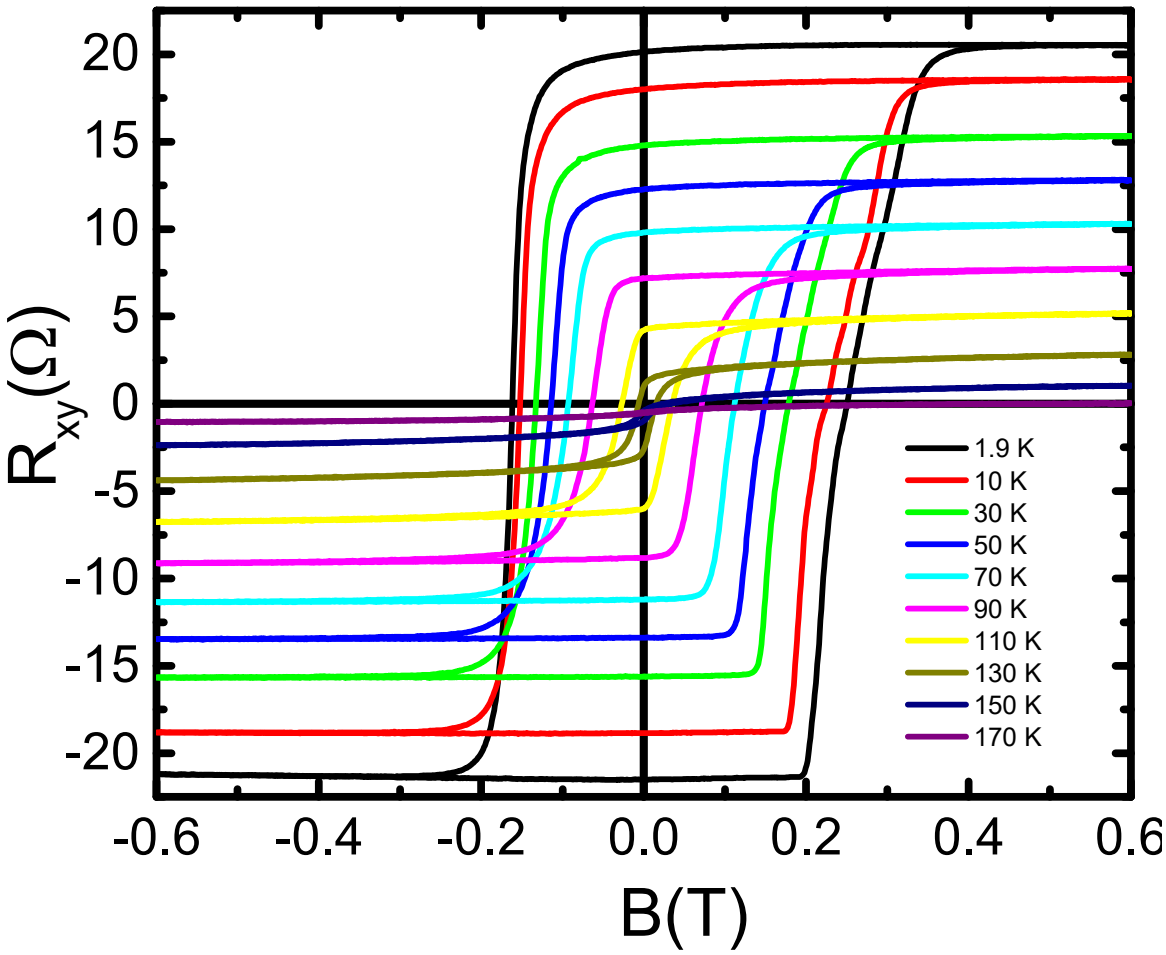

Figure 4.27 Temperature dependent AHE measurements within ± 0.6 T after presetting the external field to -2T.

Another measurement performed on this sample was a magnetic field sweep from +2T to -2T. The results for R_{xx} vs B and for R_{xy} vs B are displayed below in Figures 4.28 and 4.29 respectively. The longitudinal resistance R_{xx} shows the AMR effect as expected which disappears at 150 K corresponding to the T_c of the Cr doped layer like before. This time, the up-sweep and down-sweep were aligned to the centre of the field. The results for R_{xy} display the anomalous Hall effect centred at 0T. The loops size reduces with increasing temperature and disappears at 150 K corresponding to the ordering temperature T_c. All the temperatures are centred at zero as expected, but in this case affected by the proximity of the anti-ferromagnetic interface as the antiferromagnetic spins remain oriented as explained in more detail below.

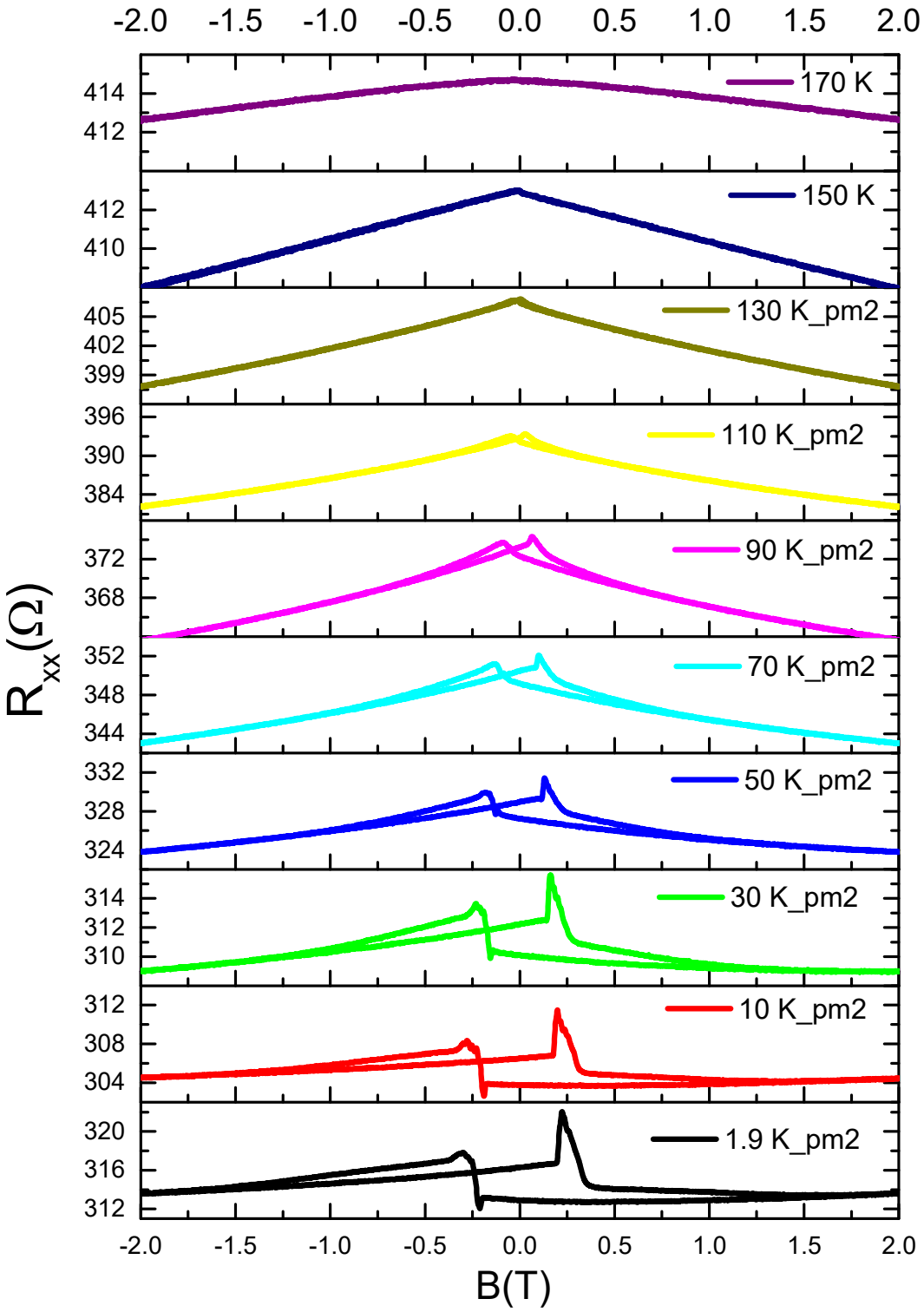

Figure 4.28 Temperature dependent Magnetoresistance within ± 2 T.

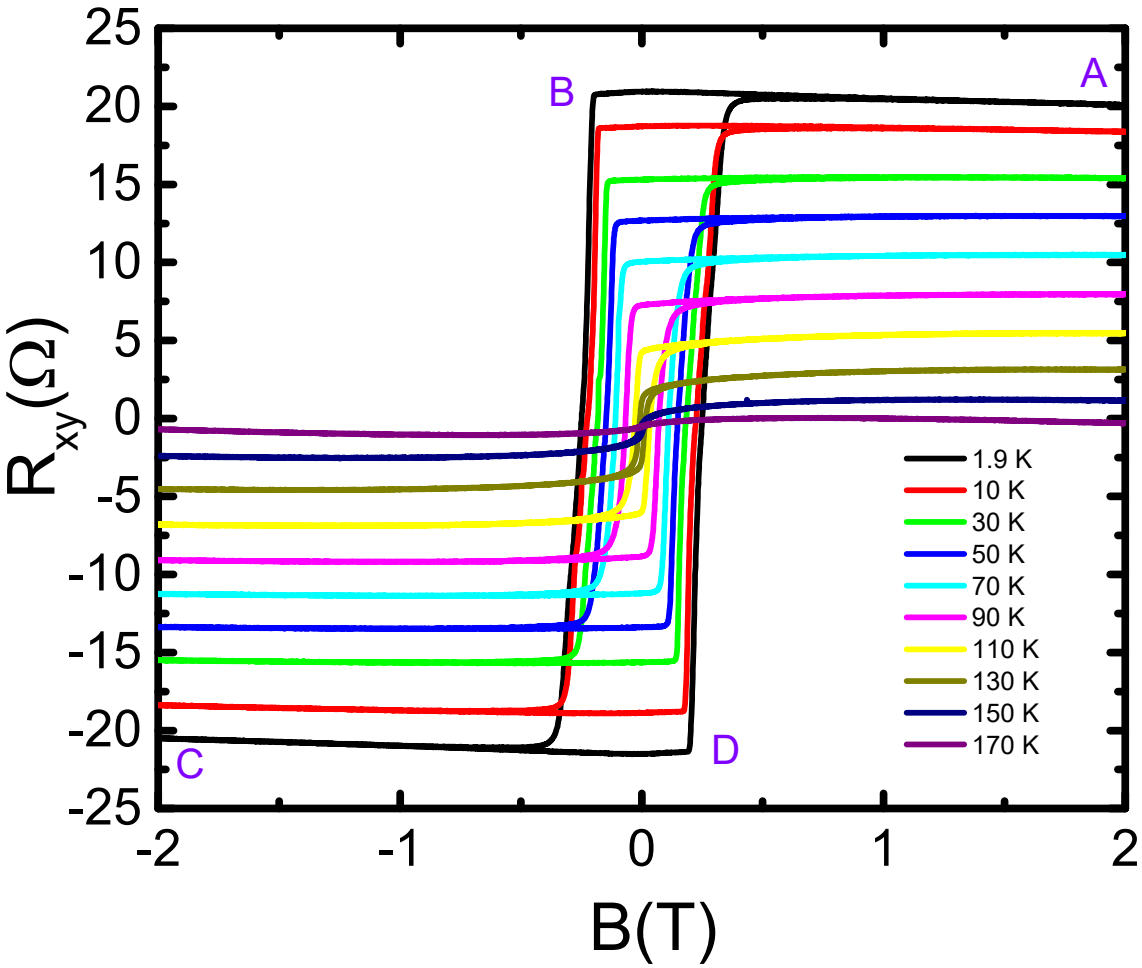

Figure 4.29 Temperature dependent AHE measurements within ± 2T.

AT POINT A:

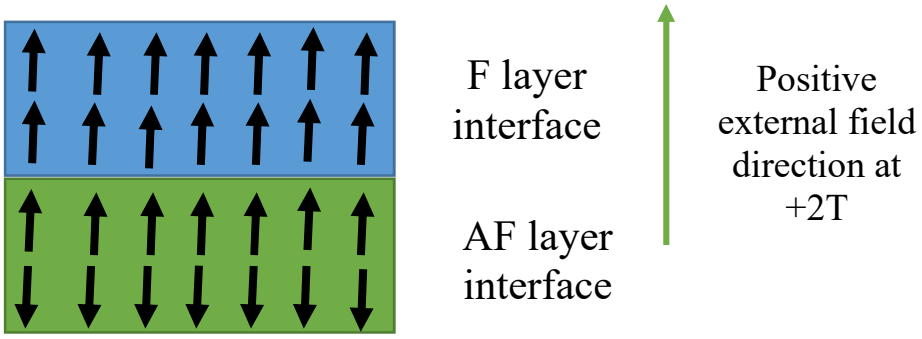

At point A, the field is at 2 T, hence both the F layer spins along with the AF layer spins are aligned strongly with the magnetic field. This also pins/couples the lower F layer spins with the upper AF layer spins.

FROM POINT B TO C:

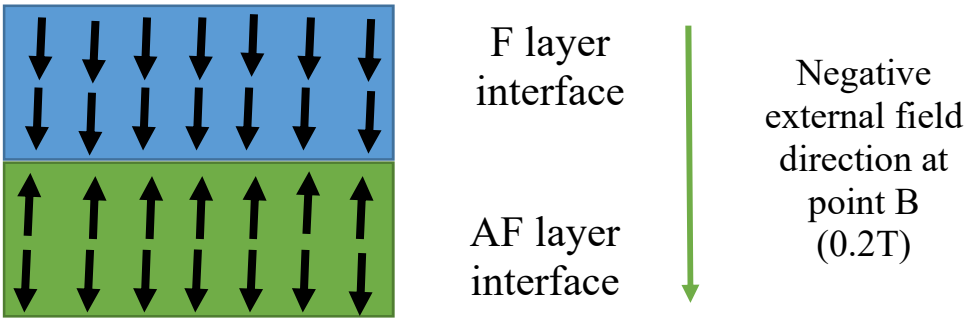

As the magnetic field sweeps from B to C, the F layer spins will try to rotate out-of-plane in the negative field direction. Since the bottom F layer spins were coupled to the top AF interface spins, a bigger force and thereafter a stronger external field is required to overcome the coupling and to rotate the ferromagnetic spins. As a result of this, the transition is a sharp shift (not coherent) and the coercive field is higher.

AT POINT C:

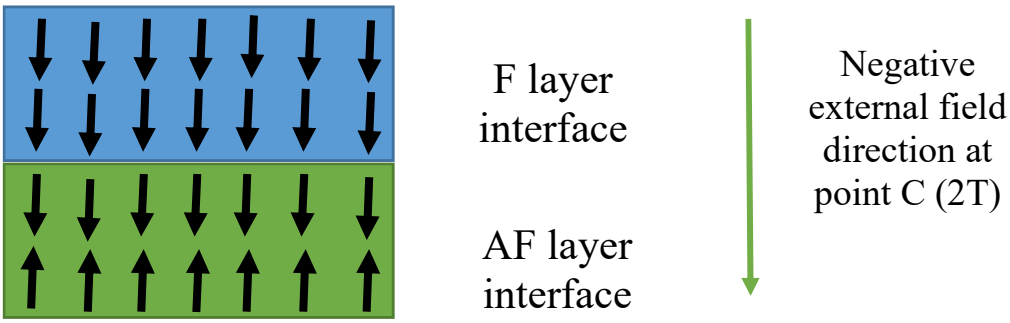

At point C, the field reaches -2T, this sets the AF interface now in the opposite direction as shown in the green layer. The F layer spins get pinned/ coupled in the opposite direction from before, with the top AF layer.

FROM D TO A:

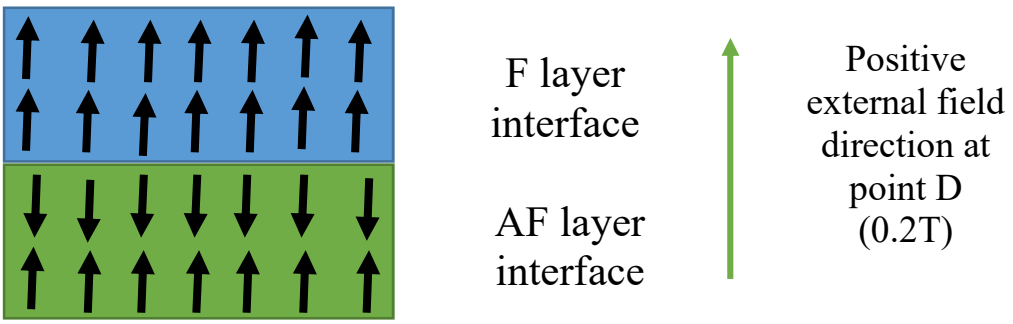

As the magnetic field sweeps from D to A, the F layer spins will try to rotate out of plane in the opposite direction. Since the bottom F layer spins were coupled to the top AF layer spins, a bigger force and thereafter a stronger external field is required to overcome the coupling and to rotate the ferromagnetic spins. As a result of this, the transition is a sharp shift (not coherent) and the coercive field is higher.

Overall, this ends up with both sides of the hysteresis loops having sharp transitions and centred at zero (different from sweeping just from +0.6T to -0.6T without pre-setting the field to 2T). This shows the EB effect on pinning the AF layer in both directions.

After performing so many different magnetic field sweep ranges, it was clear that the range of the magnetic field sweeping had an effect on the coercivity and the EB effect. Further studies were performed to understand this. The sample was first warmed to room temperature and then cooled to 10 K under zero field cooling conditions and then, at 10 K different sweeping ranges in an increasing order (from ±0.1 T to ±4 T) were applied to investigate this relationship. It was found that from ±0.3 T a hysteresis loop is formed with a closed loop, and at ±2 T the soft antiferromagnetic interface fully saturates/polarizes as the coercivity did not change on further increasing the sweep range as shown in Figure 4.30 (a and b).

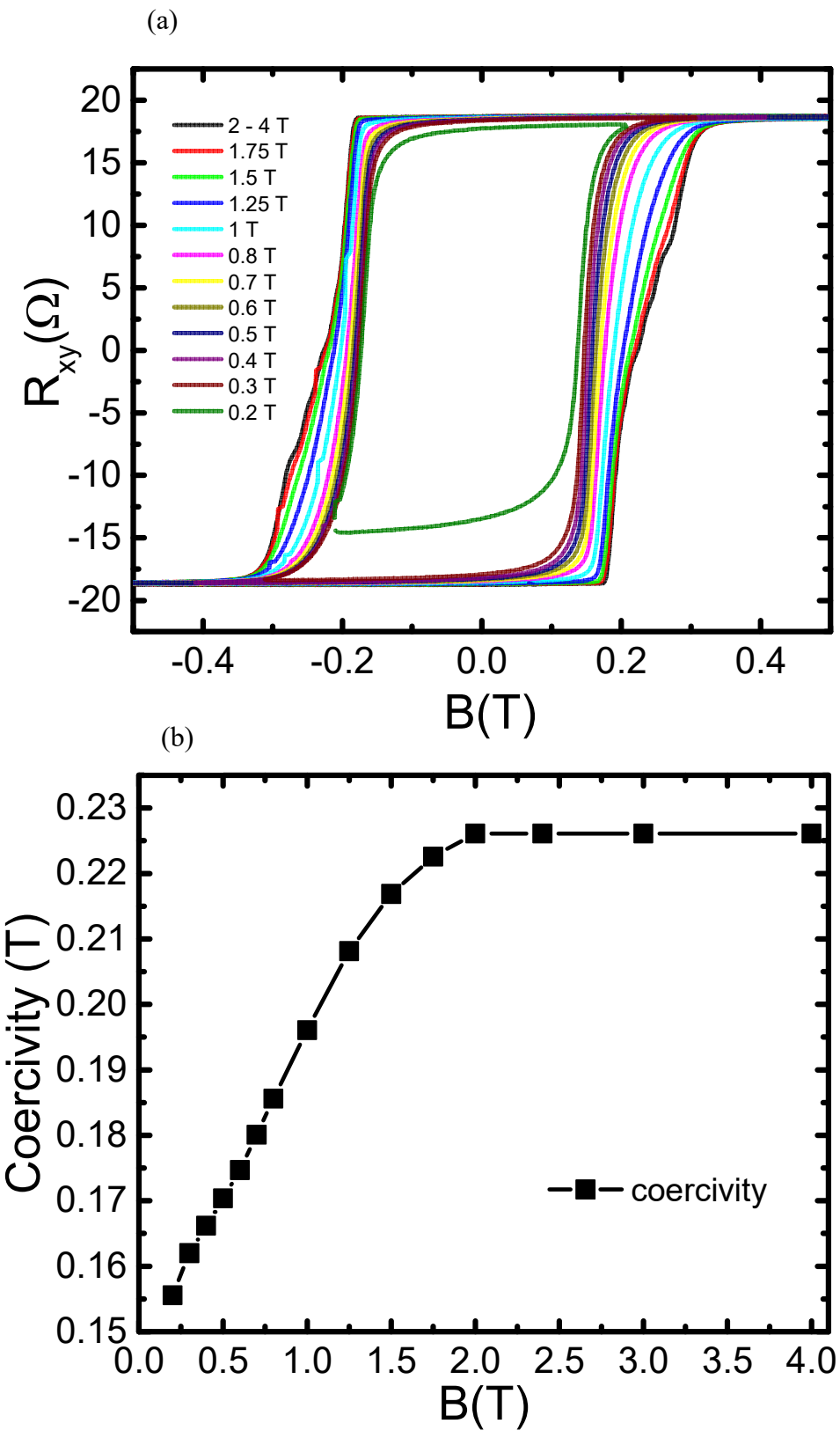

Figure 4.30 (a) The AHE at 10 K for different sweeping ranges in an increasing order (from ± 0.1 T to ± 4 T) (b) The change in coercivities at different magnetic field ranges showing a saturation after 2 T.

Also when a magnetified image of Figure 4.30 (a) was created, an interesting finding was made. An oscillatory pattern was observed in both R_{xx} and R_{xy} data as shown in Figure 4.31. These wiggles correspond to the coercivity for different heterostructure layers. Each layer seems to switch one-by-one with respect to the field in a systematic ordered manner and hence we observe different coercivities. This is an extremely important finding as the exchange bias is widely used in different magnetic sensors and read heads for spintronic applications therefore having a direct impact on magnetoelectrical devices. Having more coercivities is advantageous as more sensors could be incorporated in existing technology.

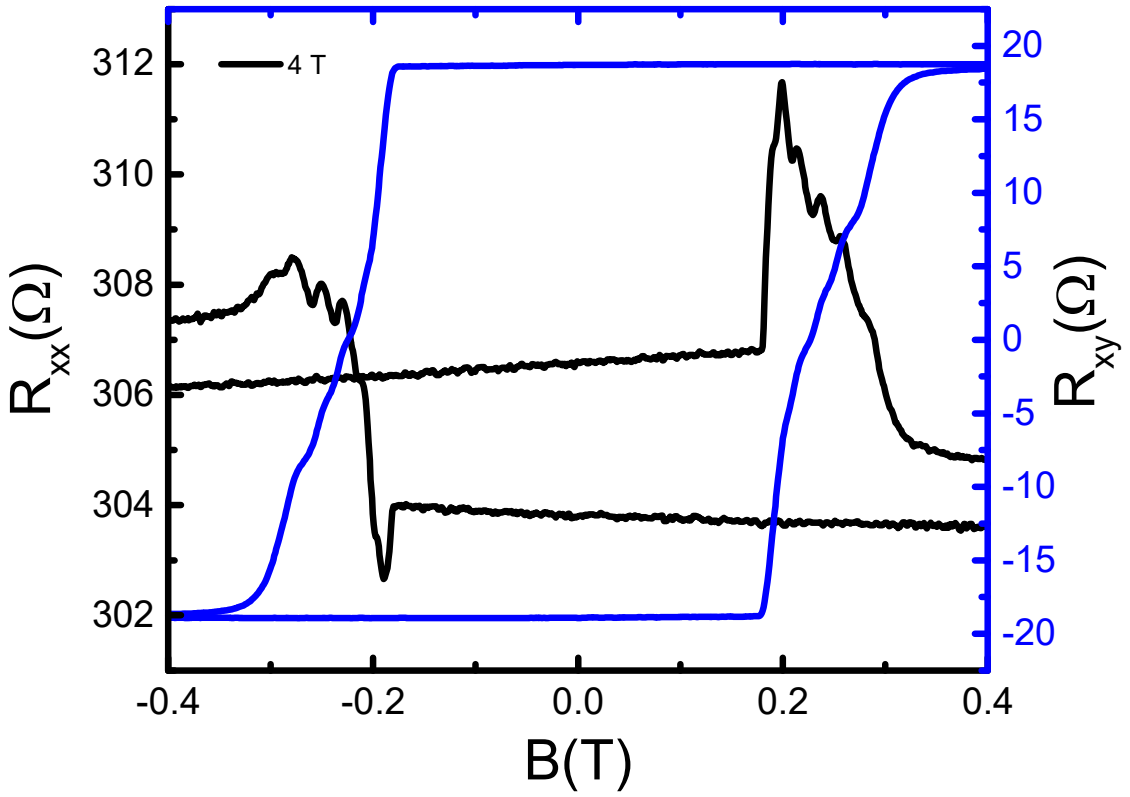

Figure 4.31 Wiggles seen in both R_{xx} and R_{xy} data with respect to the external magnetic field B, corresponding to the switching of each layer in the heterostructure in an ordered fashion.

All in all apart from the wiggles seen in R_{xx} and R_{xy}, there are four situations with clearly different coercivities as shown in Figure 4.32:

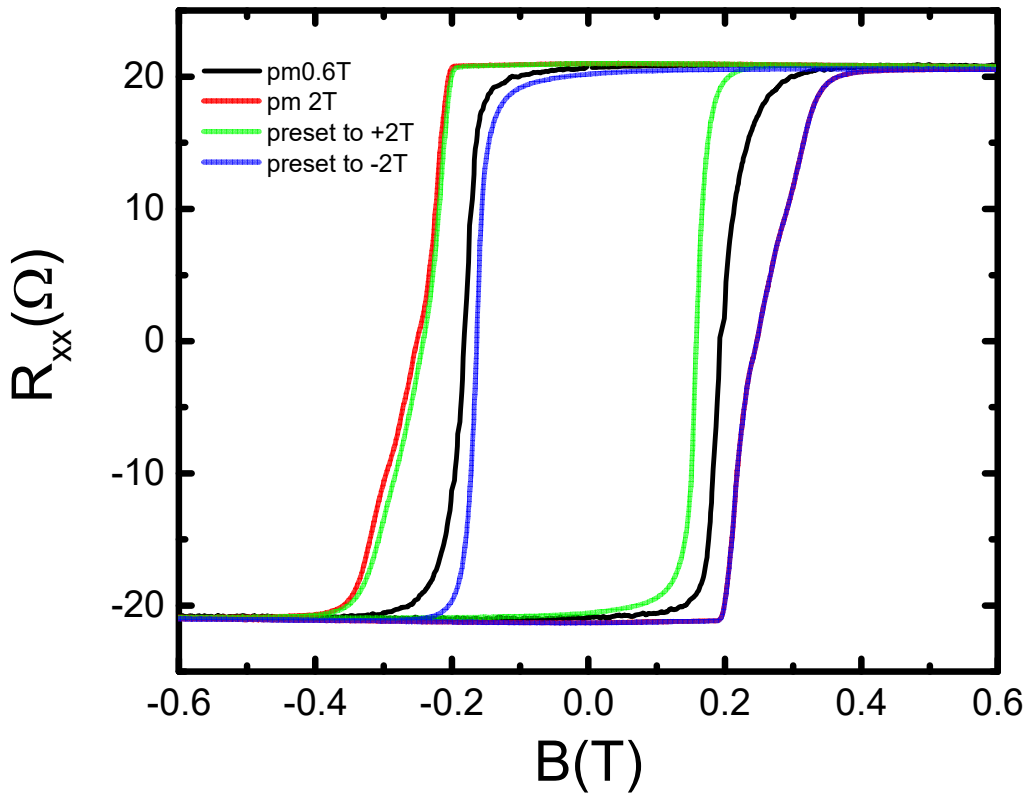

Figure 4.32 The Hall resistance of the samples with different sweep ranges and preset values.

a. The black hysteresis loop, shows a simple scan from +0.6 T to -0.6 T. In this case the F layer saturates but no AF interface is developed or oriented hence not involved in EB.
b. The red hysteresis loop (hidden behind the blue curve on the positive field sweep side), shows a scan from +2T to -2T. In this case, both the F layer and AF layer are saturated, the EB is seen on both sides of the hysteresis loop hence the highest coercivity state is observed.
c. The green hysteresis loop, shows the AF layer pinned to the F layer in the positive direction (pre-set to +2T).
d. The blue hysteresis loop, shows the AF layer pinned to the F layer in the negative direction (pre-set to -2T).

In principle, depending on the sweep range, we can have four different hysteresis patterns with four different coercivities which has never been showcased before in any material system.

Angle dependence measurements were performed by rotating the sample on the rotator probe to zero degrees with respect to the magnetic field. The anomalous Hall effect shows a parabolic dependence on the magnetic field. This parabolic behavior indicates a strong out-of-plane spontaneous magnetization at zero field confirming that the magnetic moments of the sample prefer to be in the perpendicular direction as shown in Figure 4.33.

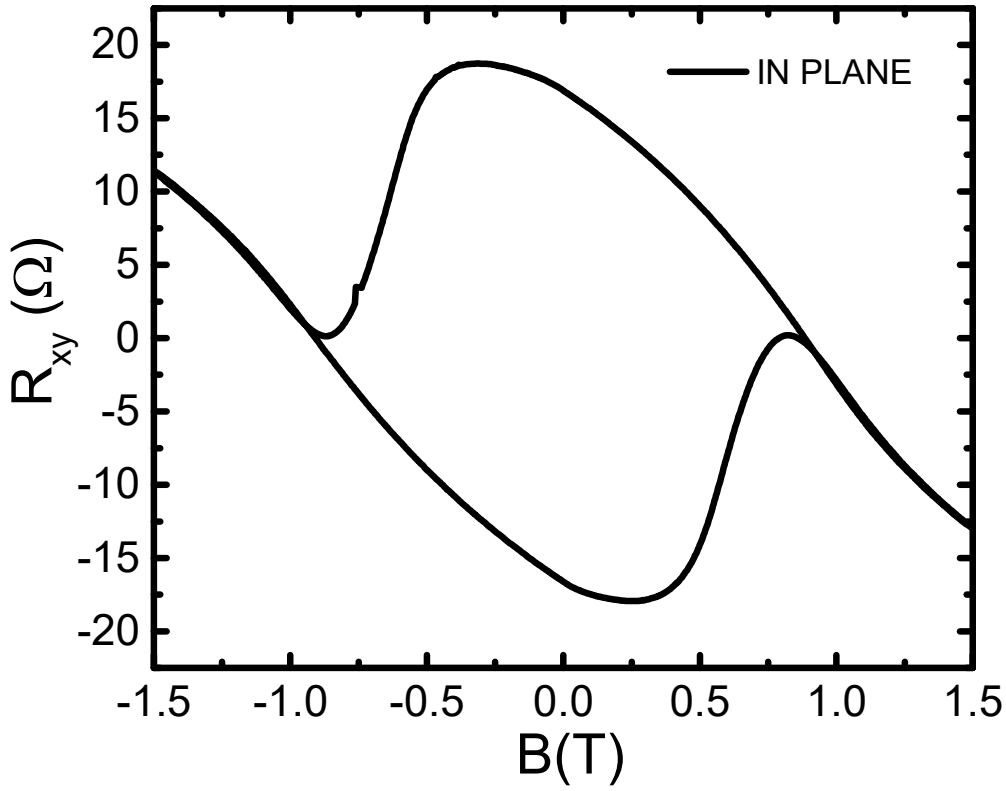

Figure 4.33 An in-plane measurement of the AHE showing a parabolic dependence.

4.5 Conclusion

In conclusion, electrical and optical measurements were carried out on magnetic impurity doped $Cr_xSb_{2-x}Te_3$ TI thin films by using AC lock-in transport measurements, MOKE, and THz-TDS. AHE and MOKE measurements were measured as a function of magnetic field and temperature which showed an out-of-plane ferromagnetic ordering. The Curie temperatures for all samples ranging from $x = 0.76$ to 0.15 was estimated yielding a T_c of 176 K for the highest doped and 40 K for the lowest doped sample. Ion gel gating was then employed on a sample with $x = 0.58$ to vary the chemical potential. An increase in the magnitude of the AHE was observed as the level of hole doping was increased by up to 50% with a gate bias variation of $\pm$ 3V, which corresponded to an increase in carrier density by 50%. This directly suggested a strong correlation between carrier concentration and ferromagnetism originating from RKKY interaction. On studying carrier densities and mobilities for all Cr doped samples using THz-TDS and comparing them directly to transport measurements, it was found that the T_c obtained from transport was proportional to $x(p)^{1/3}$, further supporting a mean field approximated RKKY interaction scenario. By using transport, MOKE and THz spectroscopy to understand the ferromagnetic properties of $Cr_xSb_{2-x}Te_3$ a new pathway was provided to explore novel quantum phenomena caused by the magnetically induced gap opening at the Dirac point in a TI.

Furthermore, the Cr doped Sb_2Te_3 was grown on top of Dy doped Bi_2Te_3 to form an heterostructure while a complete transport study was carried out. It was found for the first time that the Dy layer acted as an antiferromagnetic at the interface which led to an EB effect. Four different magnetic states were achieved with respect to different field sweep ranges which could hold very promising applications in magnetoelectronic devices. Furthermore the heterostructure which contained 10 layers each of Cr doped TIs and Dy doped TIs showed an oscillatory pattern in its longitudinal resistance which meant each layer could be tuned into a unique ferromagnetic state independently.

5. Chapter 5

Device Processing and Electrical Transport in Bi_2Se_3 and Sb_2Te_3 Thin Films

5.1 Introduction and Motivation

In the past few years, TIs have emerged as a new platform for coherent spin-polarized electronics. These exotic materials are predicted to have spin-momentum-locked metallic surface states and an insulating bulk state[14,30,31,35,101,155–157]. Their band structure topology and unique spin-momentum locking mechanism are foreseen to prevent the metallic states from localization due to backscattering, which is forbidden[158]. Among the TIs discovered so far, Bi_2Se_3 is considered the most promising due to its near- ideal surface band structure, *i.e.* a single Dirac cone which has been confirmed by a number of surface-sensitive probes[14,159,160]. However, electrical properties in this material have been very different from the theoretical prediction of surface metallic states with a so-called insulating bulk state[161,162]. Considering that the bulk and surface transport display different properties, the motivation behind this work was to be able to distinguish the surface states from the bulk states using electrical transport while looking into various device processing techniques, mainly etching through argon ion milling or chemical etching with regards to clean-room fabrication.

This chapter covers a brief literature review on the transport properties of MBE grown thin films of Bi_2Se_3 followed by electrical transport measurements on two Bi_2Se_3 thin films. The Ar^+ milled sample was measured with Thierry Ferrus from Hitachi Cambridge. A thickness dependent study was then carried out on its sister material Sb_2Te_3.

5.2 Literature Review

The 3D TI Bi_2Se_3 is the most widely studied TI material at present and hence it is worth reviewing magneto-transport properties in Bi based 3D TIs. Studying transport properties in an externally applied magnetic field is a powerful probe and can reveal information regarding the topological nature of the surface states. For example, a Berry phase shift may

appear in the magnetoresistance oscillations at very high magnetic fields or quantum corrections to the conductivity are observed at low magnetic fields. There is an ongoing debate on both of the above mentioned effects with regards to liaising them to the origin of the surface states. The Berry phase shift in the magnetoresistance oscillations and change in the conductivity at low fields are discussed in detail below.

Weak antilocalization (WAL) is commonly observed in magnetoresistance measurements at zero magnetic field and a lot of scientists have performed in-depth studies of this effect. In 2011 Kim *et al*. reported magneto-transport on Bi_2Se_3 thin films with various thicknesses ranging from 3 nm to 170 nm and observed WAL in all their films[163]. They carried out van der Pauw measurements on all of their samples with Indium contacts and reported a metallic behavior at high temperatures. As the temperature dropped below 30 K, the resistance tended to increase slightly due to strong electron-electron interaction or due to an impurity band in the bulk as seen in Figure 5.1 (a). They further plotted mobility vs. thickness data displaying a linear increase until a saturation at 3000 cm^2/Vsec [Figure 5.1 (b)]. The results made the community realize that Bi_2Se_3 was not a perfect TI in-fact the bulk was never insulating, regardless of the thickness. A true TIs sample properties should not change with regards to its thickness for example its mobility for as long as the bulk remains insulating. The very observation of the conventional thickness dependence implied that the observed mobilities were dominated by the bulk instead of the surface.

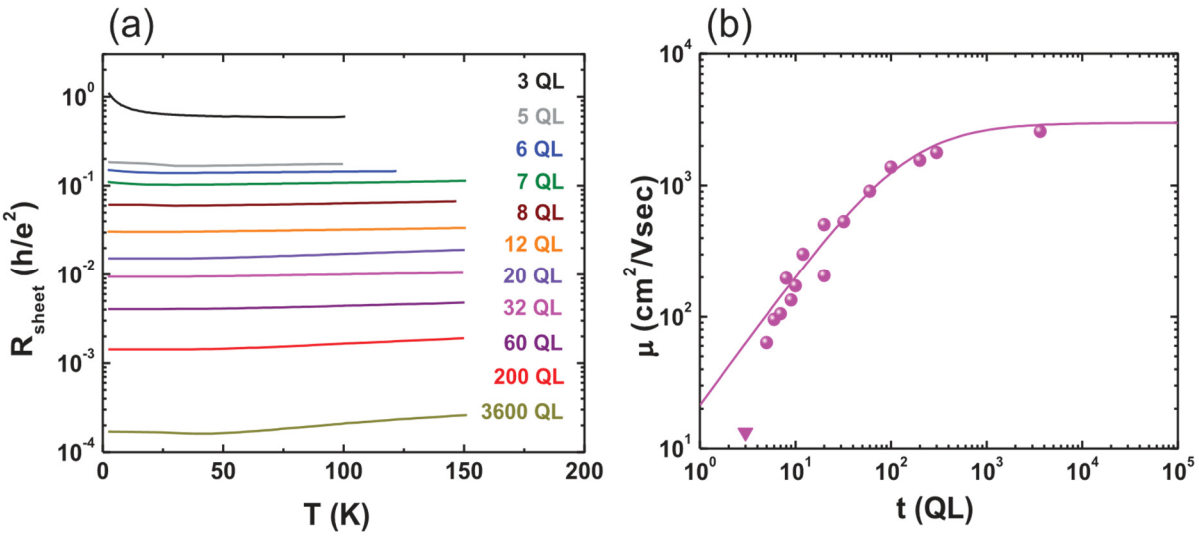

Figure 5.1 Thickness dependence of the transport properties of Bi_2Se_3. (a) Sheet Resistance and mobility of Bi_2Se_3 films as a function of temperature with thickness ranging from 3 to 3600 QL. (b) Mobility as a function of thickness obtained from Hall measurements at 1.5 K.[163] Figure reproduced from ref. 163 without permission.

WAL studies now forms the basis of understanding of the physics in Bi_2Se_3. Liu *et al*. in the same year tried to change the name from WAL to "topological delocalization" which occurs only in TIs, but did not get a very positive response from the community[164].

The HLN equation describes the quantum correction to the 2D conductivity due to localization or anti-localization effects as[43]:

$$\Delta\sigma_{xx}^{2D} \equiv \sigma_{xx}^{2D}(B) - \sigma_{xx}^{2D}(0) = \alpha\frac{e^2}{2\pi^2\hbar}\left[ln\left(\frac{\hbar}{4eBL_\varphi^2}\right) - \Psi\left(\frac{1}{2}+\frac{\hbar}{4eBL_\varphi^2}\right)\right]$$

where $\Delta\sigma_{xx}^{2D}$ indicates the normalized 2D sheet conductivity, B is the magnetic field perpendicular to the plane of the film, e is the electronic charge, $\hbar$ is the reduced Planck constant, Ψ is the digamma function, α is the number of topological surface modes (TSM) and L_φ is the phase coherence length. In 2011, it was widely accepted that strong spin–orbit interactions (or topological effects) gives rise to WAL with an α value equal to - 0.5 while weak spin–orbit scattering typically gives weak localization (WL) effects with a value of α = 1. More studies revealed that the value of α = - 0.5 depend on the sample thickness and the modulation of the bulk conductivity via gating. This was confirmed by various groups[163–168]. Figure 5.2 shows results of MBE grown samples displaying magneto-transport data by Kim *et al*. over a range of thicknesses from 3-100 QL[163]. Except for the 3 QL sample, the fitting parameter A (in this case A = α / π) remained constant ~ 1/(2π) as shown in Figure 5.2 (b), while the phase coherence length parameter l_φ monotonically increased with sample thickness (Fig. 5.2 (c). The parameter A equaled 1/(2π), as compared to 1/π implied that the WAL effect for 5–100 QL was dominated by a single 2D channel.

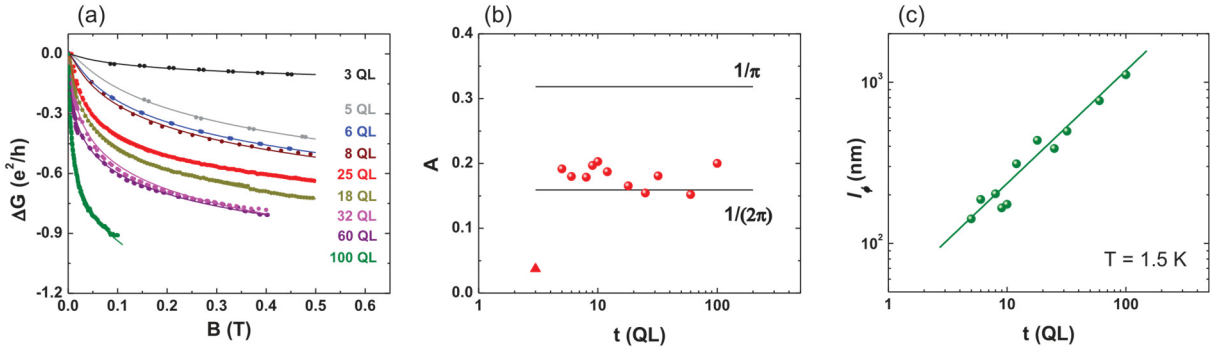

Figure 5.2 Weak antilocalization effect. (a) The HLN fitting of the change in conductance in the low-field regime from 3 to 100 QL. (b) Above 5 QL, the coefficient A is almost thickness independent, close to a single channel WAL contribution, that is 1/(2π). (c) The phase coherence length increases as $t^{0.7}$ with the sample thickness.[163] Figure reproduced from ref. 163 without permission.

Another measurement, this time by tuning carrier densities by Dohum Kim *et al*. was made on exfoliated Bi_2Se_3 single crystals with ranging thickness of 5, 7, 12 and 17 QLs[169]. Figure 5.3 (e) shows a representative device (thickness 12 QL), where height profiles across the width direction of the 17, 12, 7 and 5 QL are shown.

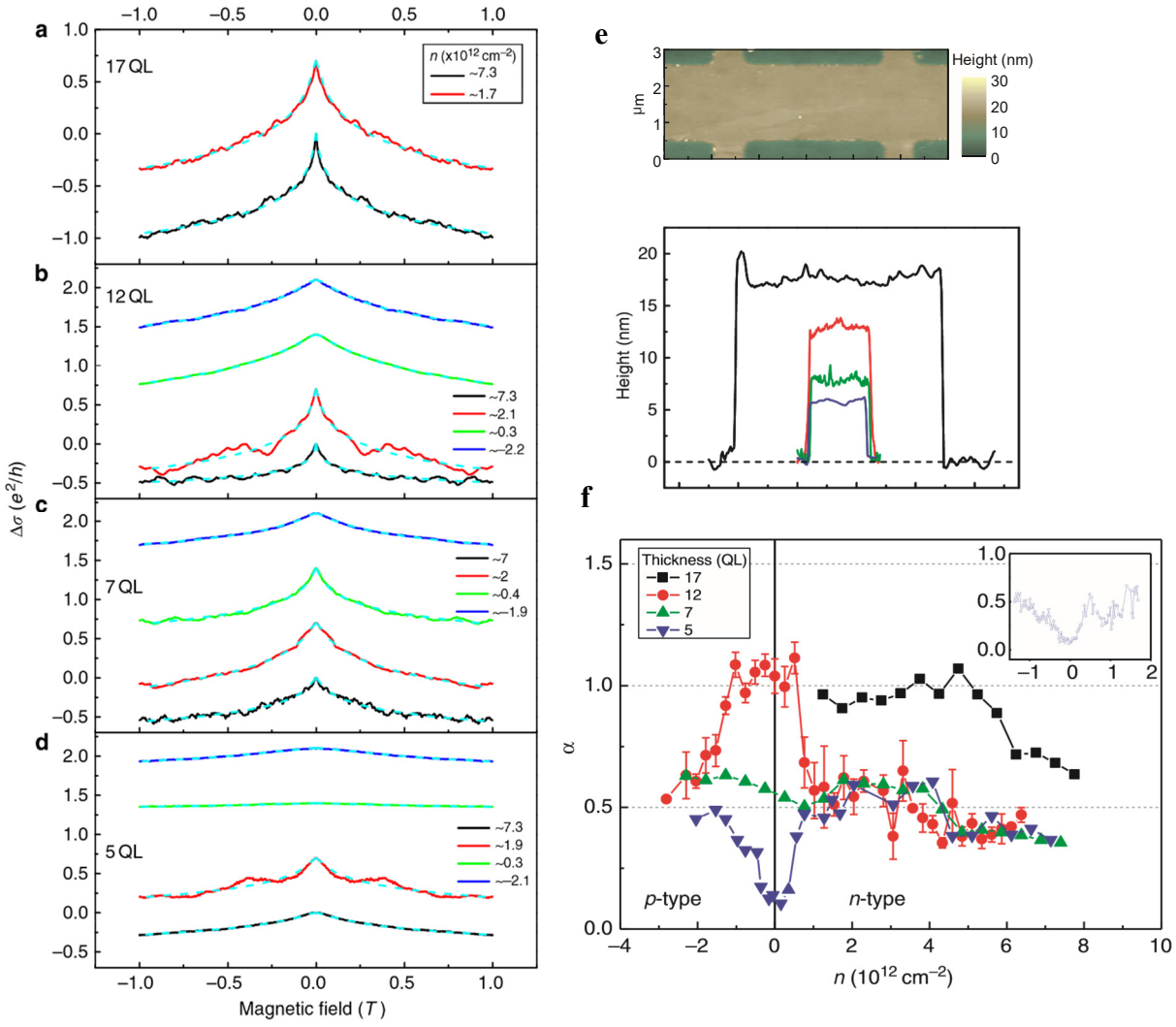

Figure 5.3 (a,b,c,d), WAL in the TI regime. Magneto-conductivity $\Delta\sigma$ as a function of perpendicular magnetic field B in 17, 12, 7 and 5 QL devices measured at 2 K at gate-induced carrier densities indicated in the legends. Dashed curves show the fits to the HLN equation. Zeros of all curves are offset by 0.7 e^2/h for clarity. (e) Characterization of Bi_2Se_3 Hall bar devices. Atomic force microscopy image of 12 QL Bi_2Se_3 Hall bar device and height profiles along width directions of the devices used in this study.(f) The variation of WAL parameter α as a function of carrier density n for 17 (black square), 12 (red circle), 7 (green triangle) and 5QL (blue triangle) thick devices measured at 2K.[169] Figure adopted from ref. 169 without permission.

Figure 5.3 (a-d) shows the magneto-conductivity $\Delta\sigma$ for all of their four devices. Curves were taken at comparable carrier densities ranging from $\approx 7\times10^{12}$cm^{-2} (n-type) to 2×10^{12} cm^{-2} (p-type) excluding the 17 QL device where only n-type carrier density could be tuned due to high initial doping. They fitted all their curves to the HLN equation which provides a physical description of the WAL behavior in particular for α = m/2, which probes the number of channels m. The variation of α obtained was plotted as a function of carrier density n for 17 (black), 12 (red), 7 (green) and 5 (blue) QL devices measured at 2 K as shown in Figure 5.3 (f). In all their devices α was close to ½ at high carrier density *i.e.* 8×10^{12} cm^{-2}, which was interpreted as a single coherent channel. But what was different from previous studies was their gate dependence, which showed very different behaviors related to the thickness of the device. Their thickest device (17 QL) showed WAL consistent with an α value ≈ 1, which was explained as two decoupled top and bottom topological surfaces starting at $n \approx 6 \times 10^{12}$ cm^{-2}, maintained down to the minimum achievable n. In their 12 QL device, they observed a sharp transition of α from ½ to 1 near $n \approx 1 \times 10^{12}$ cm^{-2} (n-type) and back to ½ at $n \approx -1 \times 10^{12}$ cm^{-2} (p-type). This transition was absent in the 7 QL device, where WAL in the entire range of n indicated a strongly coupled single channel ($\alpha \approx 1/2$). Finally, for their smallest thickness (5 QL), they observed a suppression in WAL for -1×10^{12} cm^{-2} < $n < 1 \times 10^{12}$ cm^{-2}. [inset of Fig. 5.3 (f)]. In summary, a value of $\alpha \approx 1/2$, suggests one coupled channel and $\alpha \approx 1$ suggested two channels (top and bottom) decoupled. A few other groups around the world also reported an α value between 0.7 and 1[169,170]. This lead to the open question about the meaning of the value of α with regards to topological surfaces states. To conclude, a lot of researchers have spent time in characterizing different thickness of Bi_2Se_3 samples and have found very different inconsistent results. In 2014, Brahlek *et al.*[171] displayed a schematic (Figure 5.4) describing their model about the top and bottom surface states. They suggested that below 10 QL the topological surface states (TSS) on the top and bottom surfaces can communicate via hopping or tunneling through the thin bulk, even if bulk states are suppressed and remain strongly coupled, thus behaving as one channel. Between 10–20 QL, the TSS start to decouple as the communication dies out, and above 20 QL, which is too thick for inter-surface coupling to occur, the two TSS are completely decoupled from each other and behave as two isolated channels, as expected for bulk insulating systems. While this model provides a first reasonable picture, a lot needs to be done with respect to temperature and field measurements regarding WAL where there is currently not a lot of literature.

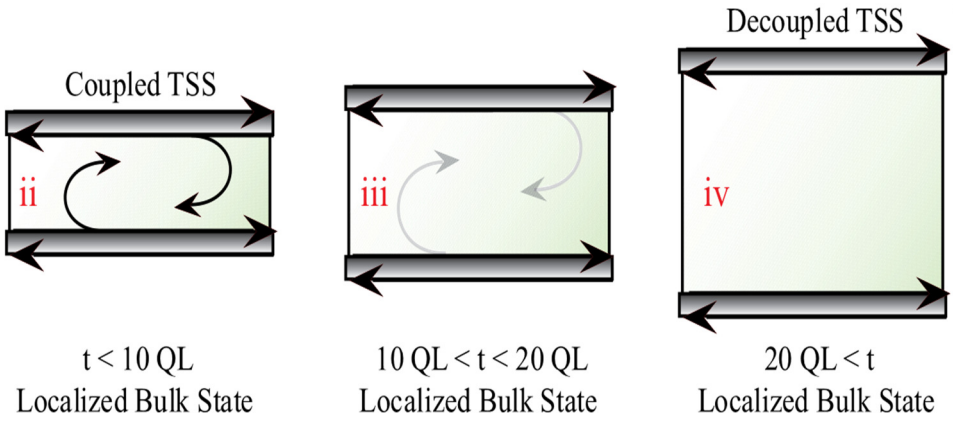

Figure 5.4 (ii) A model showing top and bottom surface coupled, if the thickness of the sample <10 QL. (iii –iv) decoupled surface states as the film becomes thicker.[171] Figure reproduced from ref. 171 without permission.

Other debates on the subject include a Berry phase shift appearing in the magneto-resistance oscillations. In 2010, James G. Analytis *et al*. observed quantum oscillations in Bi_2Se_3 for the first time[162]. They characterized a number of thin films of Bi_2Se_3 with different carrier concentrations at pulse fields up to 55 T. Figure 5.5 (a) and (b) illustrate their longitudinal and transverse resistances R_{xx} and R_{xy}, respectively, in a sample called Σ1at 1.5 K exhibiting strong features. To confirm the 2 dimensional surface effect of their TI, they measured the dimensionality of these features by rotation of the sample with respect to the field. They observed that the quantum oscillatory phenomena depended only on the perpendicular component of the field $B\perp$ and were periodic in $1/B$. Figure 5.5 (c) shows the linear background subtracted signal exhibiting an increase in the oscillation features with increase in field as expected if these were Shubnikov-de Haas type oscillations. On examining Figure 5.5 (c) they assigned Landau indices N = 1, 2 and 3, as the second and third minima in the oscillations occurred at twice and three times the $1/B$ value of the first. Plotting the indices against $1/B$ connected a straight line which passed through the origin [black curve in Figure 5.5 (e)]. Theory suggests that in TIs the quantization of conductance follows $\sigma_N = 2\left(N + \frac{1}{2}\right)e^2/h$, hence leading to the slope of the line in Figure 5.5 (e) passing through the intercept ½. Sample number Σ1did not seem to match this criteria which they attribute to parallel channels in the bulk. To confirm if the experiment matched the theory, they measured another sample called Σ3 the results of which are also displayed in Figure 5.5 (d) and (e) (blue curve). In this sample they found an intercept which passed through -0.17, a first of its kind distinguishing this Dirac system from earlier measurements on graphene.

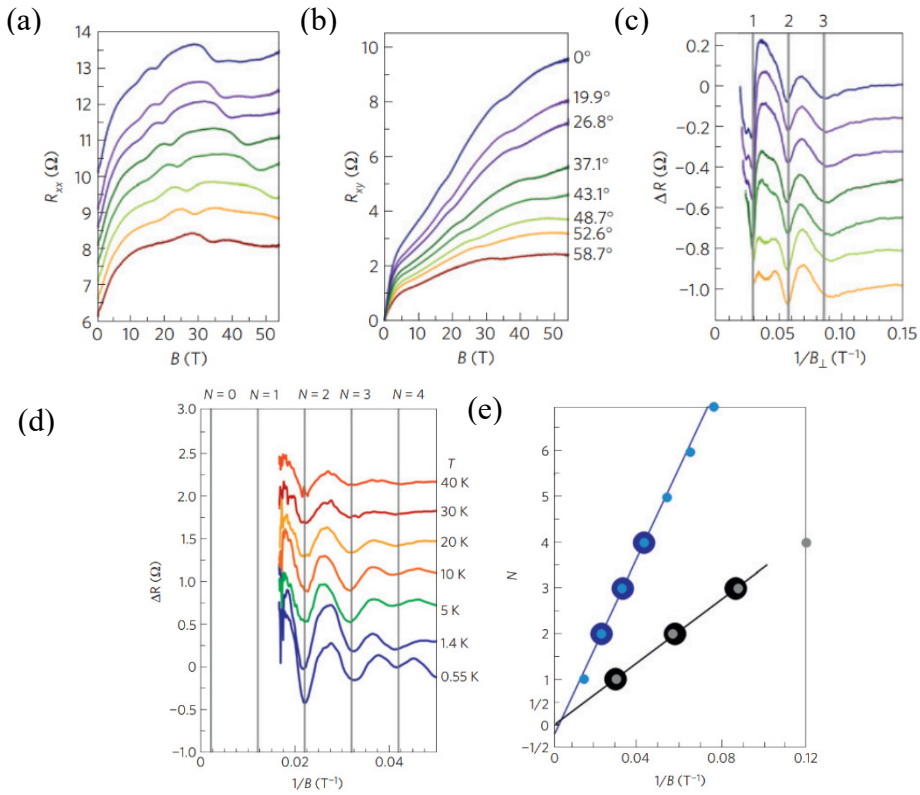

Figure 5.5 (a) Transport properties of a 2D surface state. (a) R_{xx} which are at an offset for clarity (b) R_{xy} as a function of tilt angle of the sample with respect to the magnetic field (c,d) Normalized value for R_{xx} with a linear background subtracted in samples Σ1 and Σ3. (e) The landau level index N as a function of inverse field for two Bi_2Se_3 samples showing different intercepts.[162] Figure reproduced from ref. 162 without permission.

This led to many scientists looking for the Berry phase signature = ½ to confirm the topological non-trivial surface state.

In 2012, Professor Wang's group at the University of California presented for the first time quantum oscillations in a 6 nm thin film of Bi_2Se_3 at very low magnetic fields[172]. This observation as they claim was a direct evidence for a surface state dominated conduction. They presented their field dependent longitudinal resistance R_{xx} acquired at 1.9 K for their 6 QL sample as shown in Figure 5.6 (a). Strong oscillations in R_{xx} at various temperatures, after subtracting a smooth background, were observed [Figure 5.6 (b)]. This was the first time, any group observed quantum oscillations in Bi_2Se_3 at such a low external magnetic fields. The amplitude of oscillations became stronger with an increase in magnetic field and decreased with temperature.

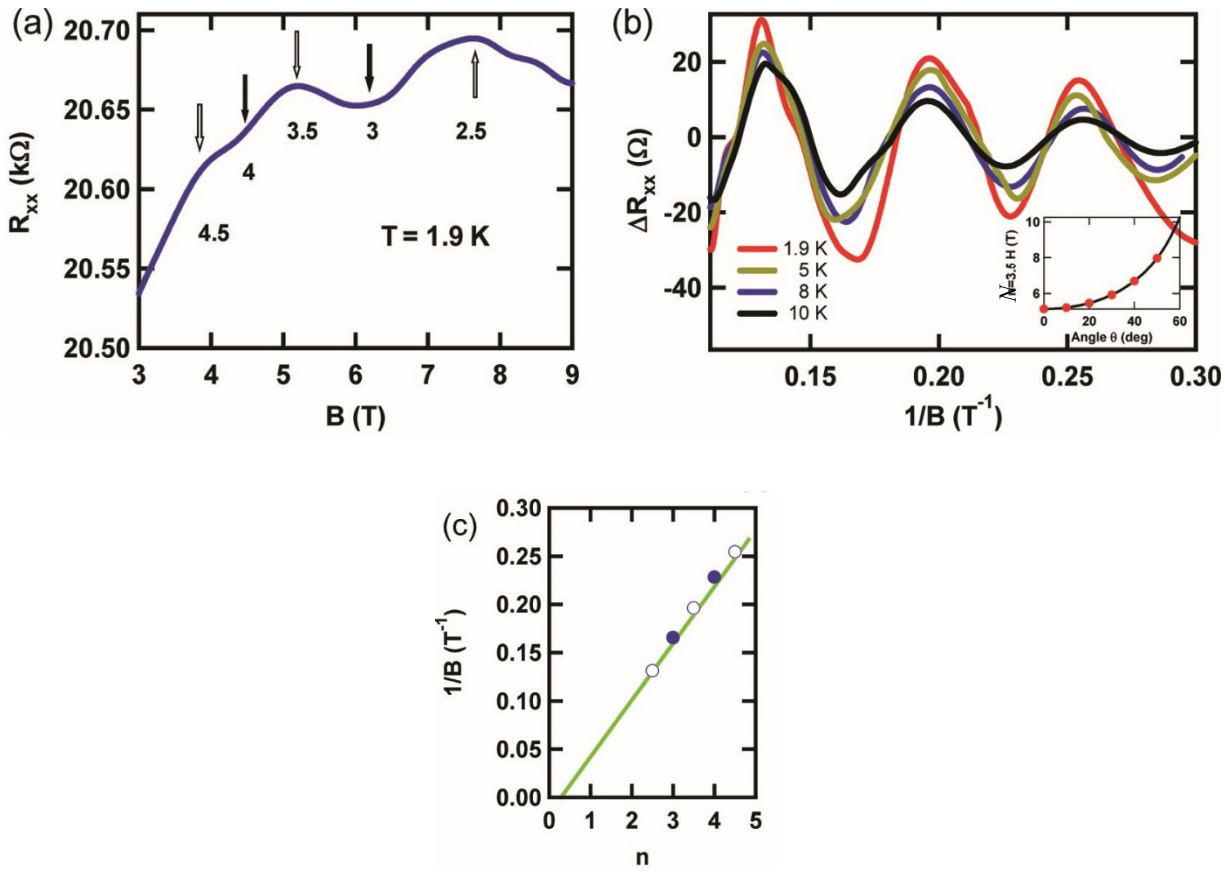

Figure 5.6 Shubnikov-de Haas oscillations of the surface states of a 6 QL sample. (a) Longitudinal resistance R_{xx} vs magnetic field at T = 1.9 K. Solid arrows indicate the integer Landau levels (LL) from the valley values; open arrows give the peak values. (b) ΔR_{xx} vs $1/B$ at different temperatures. The inset shows the field position of the $N = 3.5$ LL peak which varies with θ as $1/\cos\theta$ (solid black line), suggesting a 2D Fermi surface. (c) Landau level index plot: $1/B$ vs N. The open (close) circles are the Landau level of the maxima (minima) of ΔR_{xx}.[172] Figure reproduced from ref. 172 without permission.

Similar to previous work, the positions of the peaks only depended on the perpendicular component of the B field, *i.e.* $B\perp = B\cos(\theta)$ (where θ is the tilt angle between B and the perpendicular axis) confirming that their oscillations originated from a 2D system. The inset of Figure 5.6 (b) shows the second peak in Figure 5.6 (a) plotted at different field angles which follows a $1/\cos(\theta)$ trend perfectly. They then went on to plot the Landau level index number N vs. $1/B$ [Figure 5.6 (c)] which is related to the cross sectional area of the Fermi surface (S_F) by $2\pi(n+\gamma) = S_F\,\hbar/eB$, where e is the electron charge, ħ is the Plank's constant divided by 2π, B is the magnetic flux density and $\gamma = 1/2$ or 0 represents the Berry phase of π or 0. Their intercept revealed a value for $\gamma \sim 0.35 \pm 0.08$ which was very close to the 0.5 value representing a π-Berry phase.

5.3 Growth and Characterization of Bi_2Se_3

MBE was used to grow a thin film of Bi_2Se_3. The sample was fabricated by Liam Collins Mcintyre and shipped to me from Professor Thorsten Hesjedal's laboratory. As mentioned in Chapter 4, all chalcogenide TI materials, for example Bi_2Se_3, Bi_2Te_3 and Sb_2Te_3 grow via a van der Waals epitaxy mechanism. A similar two-step growth recipe as mentioned in Chapter 4 was followed for the growth of Bi_2Se_3. The Bi_2Se_3 thin film was deposited by first growing a lower temperature seed layer of approximately 5 nm at a substrate temperature of 250°C followed by an annealing step in a Se overpressure for 30 minutes while raising the substrate temperature to 300°C. This was followed by growing the remaining film thickness at a higher substrate temperature of 300°C. This approach has yielded the highest quality film in the past, as the use of the seed layer is a critical step to establish the correct stoichiometry and crystal structure.

X-ray studies were carried out by me in Cambridge. XRD was performed with a Bruker D8 diffractometer using Cu-Kα radiation. The 2θ scan (Figure 5.8) shows peaks of the (00l) family of Bi_2Se_3. The diffraction spectrum clearly indicates that the grown film is well ordered, confirming the correct phase (peak positions) and high crystalline quality.

The XRR plot is shown in Fig. 5.8. The modelling was done by considering a two layers slab model of Bi_2Se_3 with the density varying slightly at the substrate interface to account for proximity effects (inset of Figure 5.7). The model shows a total Bi_2Se_3 layer thickness of 22 nm, consisting of a 5.8-nm-thick seed layer and a 16.2 nm thin film with a surface roughness of 1.7 nm. The fitting is marked with the red dotted line.

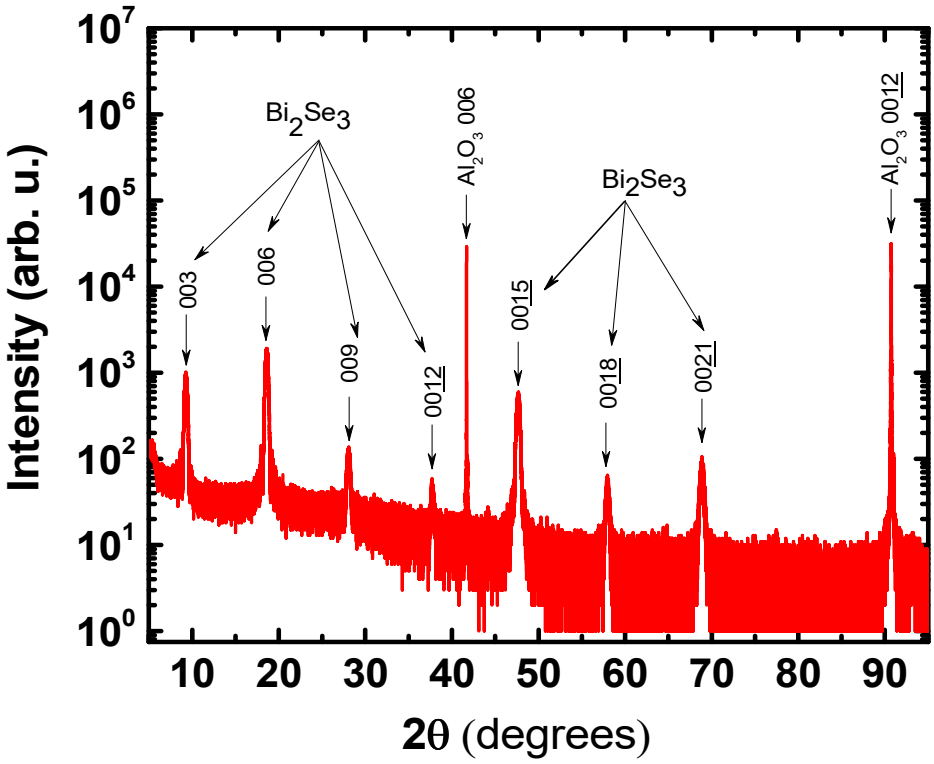

Figure 5.7 X-ray studies of an epitaxial Bi_2Se_3 thin film on a Sapphire (0001) substrate. All the relevant peaks are labelled.

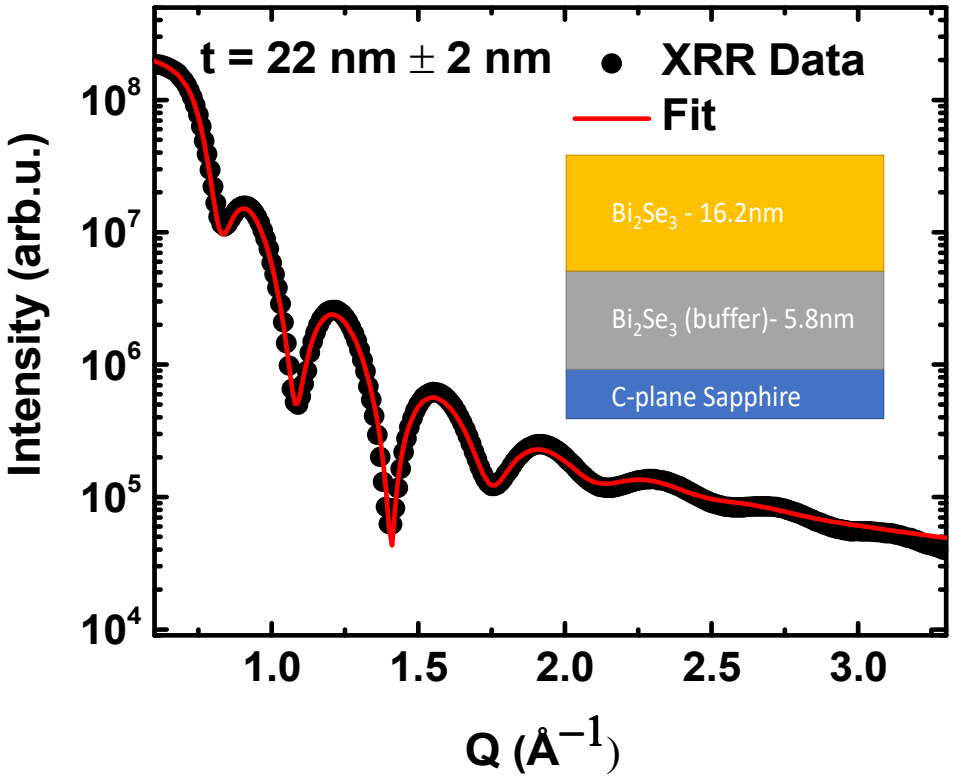

Figure 5.8 X-ray reflectivity of the measured film (black) and fitted model in GenX (red) showing a thickness of 22 nm total with a two layer slab fitting model as shown in the inset.

5.4 Preparation of Hall Bar Devices

The motivation behind this work was to use lithography as a tool to eliminate uncertainties in evaluating resistivities encountered due to irregular shaped samples. All devices were prepared in a class 100 clean room using a sequence of optical lithography steps described in detail. The skill of device fabrication lies in having very stable hands, an eye for perfection, a lot of patience and of course experience. For example using an incorrect kind of tweezer while handling the chips can lead to cross contamination or cleaving the chips using a contaminated diamond cutter can lead to un-intentional doping.

A new lithography mask was designed in the AutoCAD software along with Thuy-Anh Nguyen for the sole purpose of making the fabrication steps easy and to avoid narrow junctions and corners which can be a cause of failure if not handled with precaution. The design of the mask is shown in Figure 5.9. The mask contains several patterns with a central bar which forms the conduction channel with various widths ranging from 50, 80, 100, 150 to 200 μm. All the bars have arms perpendicular to the conduction channel which are of the same dimension as the bar itself. The ends of the bar and the arms are called contact pads and a separate pattern was designed to cover the ends of the Hall bar as shown in the Figure 5.10 (b). A gate pattern was also designed as shown in Figure 5.10 (c) and (d). During all these steps extreme care to detail has to be taken.

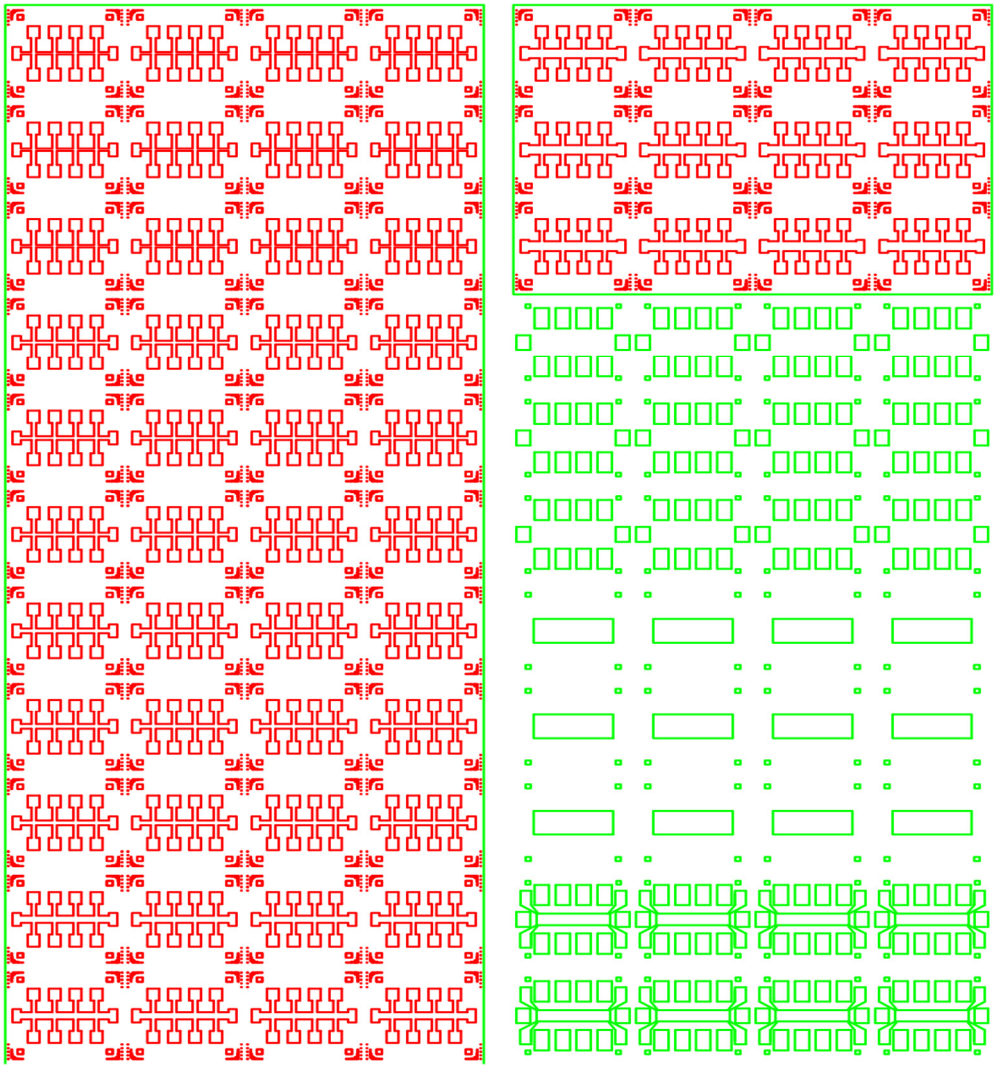

Figure 5.9 An optical mask designed in AutoCAD showing several Hall bars with different widths ranging from 50, 80, 100, 150 to 200 μm (in red). The length of each Hall bar was fixed at 1200 μm. The patterns in green show the contact pads and gate contacts.

The mask was designed for the purpose of following a positive resist lithography, where the areas which were exposed to light could be developed. In this case the area under the Hall bars were covered in chromium, while the rest of the areas were clear glass. The opposite was the case for the contact pads and gate pattern where all areas outside the pattern were covered in chromium so that no light could pass through it. From past experience and many trials at failed attempts with device fabrication, we chose the size of the contact pads to be much bigger than the Hall bar pattern ends. The idea was to facilitate the wire bonding in such a way that the ball bond forms on top of the substrate and not the desired material itself. This also prevents the risk of the film peeling off while trying to wire bond, hence damaging the surface.

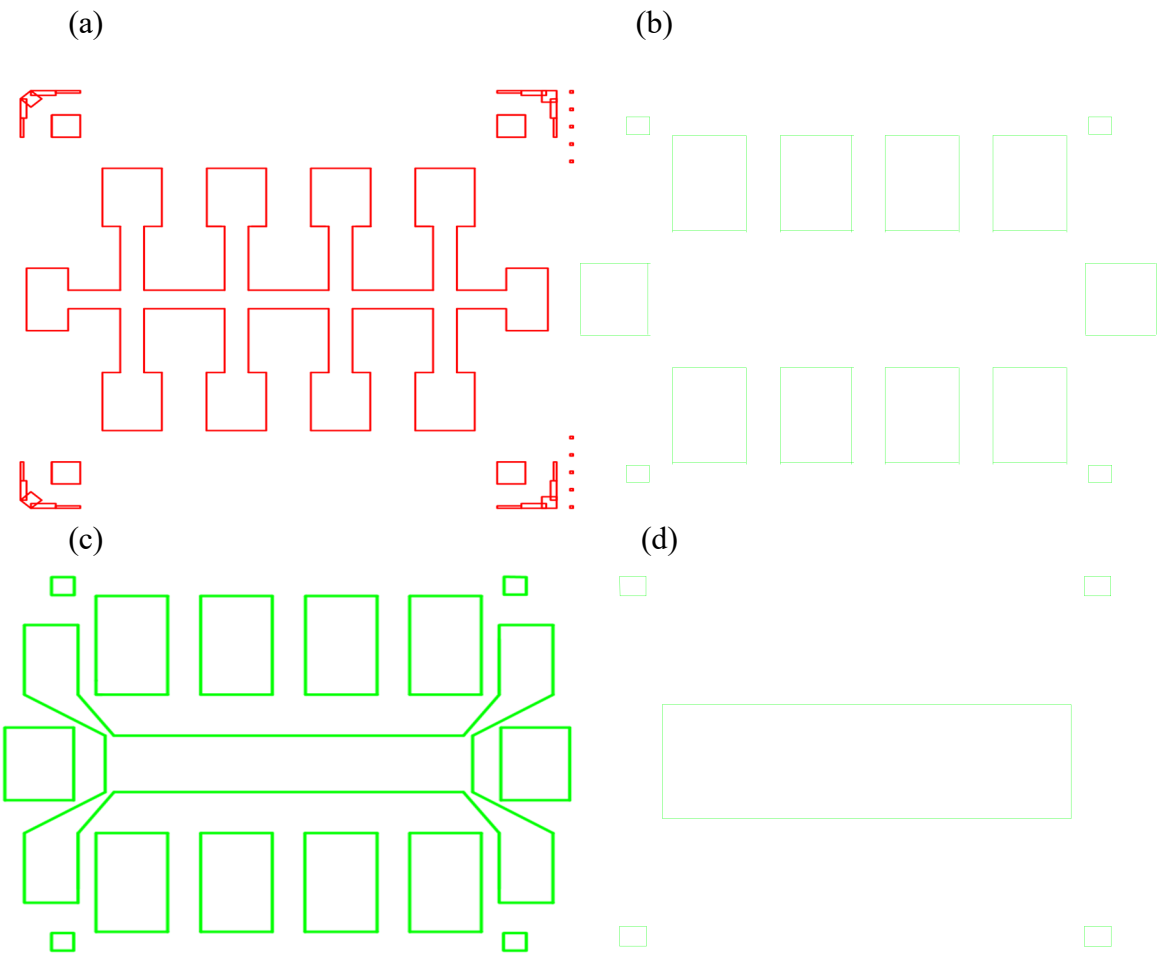

Figure 5.10 Details of the optical mask designed in AutoCAD showing: (a) A Hall bar pattern (b) ohmic contact pads, (c) gate pattern and ohmic pads (d) dielectric gate pattern

To be able to tune the carrier density by using a gate, we also designed a pattern to top-gate a Hall bar as shown in Figure 5.10 (c).

The Bi_2Se_3 sample was grown on a *c*-plane (0001) Sapphire substrate. The substrate was transparent while the film had a shiny silvery appearance. It was soon realized that even touching the film slightly smudged the surface, hence it was a good idea never to put any sort of pressure onto the sample. The film was first cleaved into several 5 mm by 5 mm chips by means of a mechanical arm used to move the sample stage underneath a diamond tip cutter. The sample was held in place under vacuum while aligning it beneath a microscope lens. The force and tilt of the diamond cutter was adjusted while the arm was mechanically moved to scratch the Sapphire substrate [shown in Figure 5.11 (a)]. Since sapphire was *c*-plane oriented, it only has one easy axis direction to cleave. It was important to cleave the chips in the direction of its easy axis else Sapphire can end up breaking into many different fragments. After the cleave marks were made, the piece was blow dried with N_2 gas to

remove the accumulation of Sapphire dust. The sample was then placed in such a way that the cleave mark was aligned right on top of the knife edge followed by mechanically pressing down on the two corners to snap it as shown in Figure 5.11 (b). This procedure was repeated until a few 5 mm by 5 mm chips were created.

First the chip was cleaned with acetone, isopropanol (IPA), methanol and deionized (DI) water in an ultrasonic bath for a few seconds followed by N_2 drying. Acetone acts as a simple organic stripper that is commonly used in the chemical industry. It tends to leave residues on the wafer which were then removed with IPA, followed by a methanol dip and then DI water.

(a)

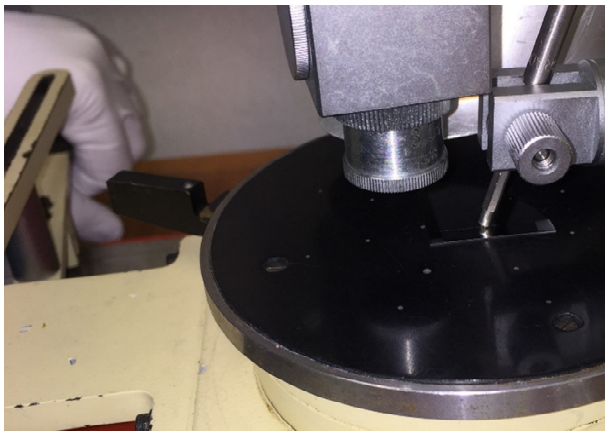

(b)

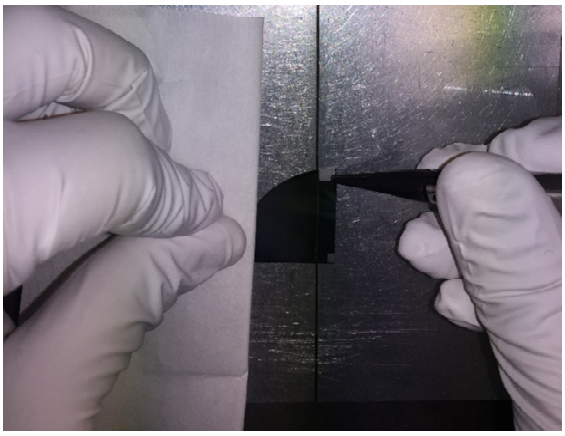

(c)

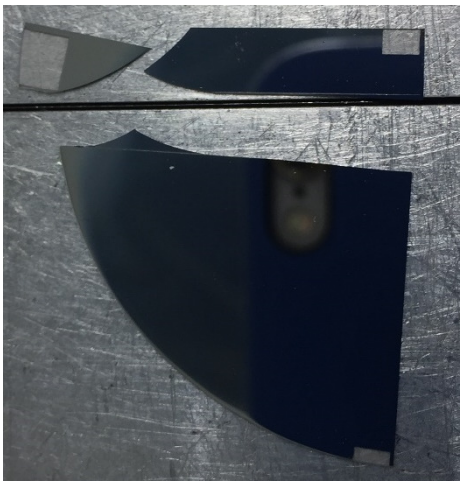

Figure 5.11 Cutting of a Bi_2Se_3 sample with a diamond cutter with the sample stage underneath a mechanical arm. (b) The sample placed on a knife edge on top of the cleave mark. (c) Cleaving gone wrong breaking the Sapphire into two pieces.

The purpose for this was to have the cleanest surface to facilitate the next step. In the next step, commercially available S1813 photoresist was drop casted on top of the chip, placed on a spinner. It was important to observe that the drops which falls on top of the chip does not contain any bubbles and covers the entire chip. This ensured an even distribution as shown in Figure 5.12 (a). The chip was spun for 1 minute at 5500 rotations per minute. This further ensured the uniformity of the photoresist except for the corners where the edge beads were uneven. After spinning, the chip was baked at 120°C for 2 minutes to ensure the resist was hardened and all its solvent content reduced. As the name suggests, S1813 has a thickness of ≈ 1.3 micrometres. So, one should roughly have that resist thickness at this stage.

The chip was then exposed to UV light through a mask following the procedure below. Our custom designed mask was aligned in such a way that at least 6 Hall bar patterns (3 × 2) on the mask positioned themselves precisely above our chip, keeping away from the edges [as seen in figure 5.12 (b)]. It is important to note that once the final alignment was made, the chip is pushed upwards until it comes in contact with the mask. The chip was then exposed to ultra violet light through the mask for an optimized time of 6.5 seconds. S1813 is a positive resist, which means that the areas exposed to light get affected and become soluble in a developer while unexposed regions stay un-affected.

(a)

(b)

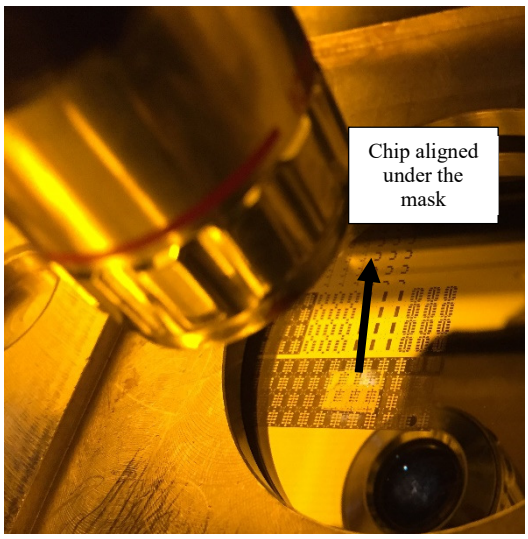

Figure 5.12 (a) S1813 photoresist drop casted on top of the sample inside a spinner. (b) Alignment of the chip underneath a photomask before exposure to UV light.

As mentioned in the design section of the mask, the Hall bar pattern was covered with chromium underneath the glass, while the rest of the mask was transparent glass. Therefore when the UV light passed through the mask, all regions were exposed except for the Hall bar pattern itself. The lithography procedure is described in detail in the experimental section 2.4.1. After exposure, the sample was dipped in MF319 resist developer for a total time of 30 seconds, followed by a rinsing in DI water (with a resistance > 10 mega ohms) and N_2 blow dried. The chip was afterwards taken under the microscope for inspection. It was made sure that the microscope lens had a UV filter on it, in case the film was not properly exposed in the earlier step. We are left thereafter with resist in the shape of bar on top of the film and substrate as shown in Figure 5.13 (a). A Dektak profile was also taken at this stage at various positions on the chip to confirm the height ≈ 1.2453 micro meters of the photoresist [Figure 5.13 (b)]. At this point, two very important procedures were followed independently, the results of which are compared in this chapter. To transfer the resist pattern onto the thin film we used Argon ion beam etching and chemical etching both of which were successful and are described in detail. The was not performed in the clean room and hence the sample was transferred into a milling chamber on the same day as the earlier performed steps. Once the sample was placed in the chamber, it was pumped down to 1×10^{-2} mbar using a dry pump. This was followed by switching "ON" a turbo pump which further took the pressure down to below 2×10^{-6} mbar. At this point Ar gas was inserted into the chamber which raised the pressure to ~ 10^{-4} mbar. The Ar gas is passed through an aligned high DC voltage grid and gets ionized to Ar^+. The sample holder was then placed at a high negative voltage, which helped the Ar^+ ions strike the film.

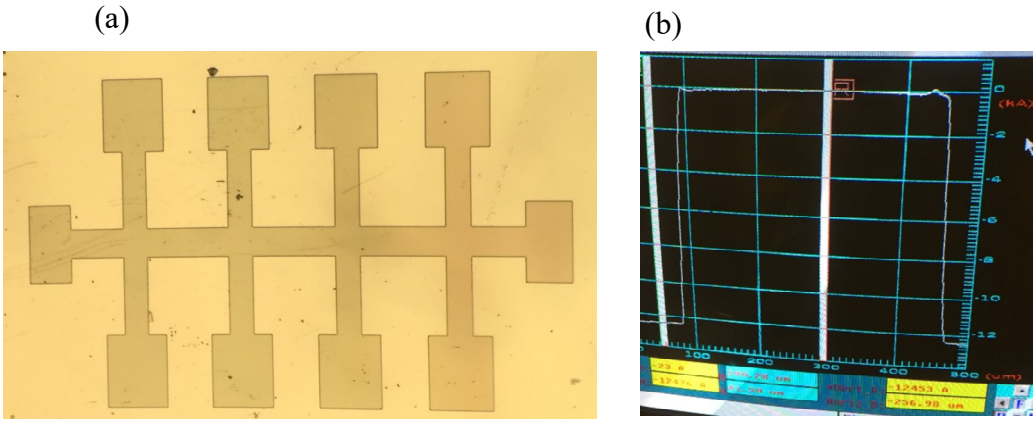

Figure 5.13 (a) A Hall bar made of photoresist on top of the Bi_2Se_3 film. (b) A Dektak profile image showing a height of 1.2453 microns across the bar.

The ions bombard the sample causing an anisotropic milling. As the thickness of the photoresist was more than 10 times the thickness of the film on the substrate, there was a low risk of over etching. Hence the exact milling rate was not measured for this sample, however, from pervious samples, being etched in the chamber, an etching time of 15 minutes was sufficient to remove 100 nm. The sample was milled for a total of 10 minutes in three steps. First for 3 minutes followed by a pause of 1 minute then for 3 mins followed by another break for 2 minutes finally ending with a 4-minute milling. These pauses are crucial and the objective was to allow the sample to cool down, preventing the photoresist from hardening and becoming difficult to remove later. Once the procedure was finished, the Ar gas inlet was closed and the chamber was vented. On visually inspecting the sample, it became clear that the Ar ion milling had successfully etched everything away except for the regions which were covered by photoresist, *i.e.* the shape of a bar. Figure 5.14 (a) shows a picture of the pieces that were just taken out of the milling chamber. A clear contrast is seen as the substrate was transparent. The samples were then taken back into the clean room and dipped into Acetone followed by IPA to remove the resist. Figure 5.14 (b) and (c) shows a failed attempt at removing the photoresist. The sample starts to peel off while the resist still stays intact in some places, due to a continuous milling process without taking breaks.

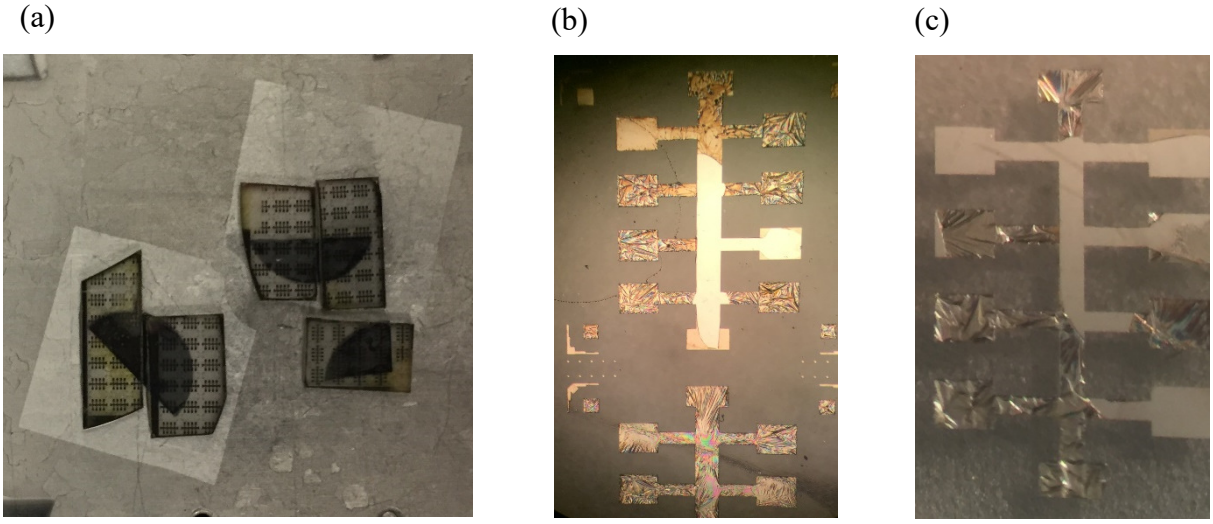

Figure 5.14 (a) Pieces of Bi_2Se_3 just taken out of the milling chamber. (b,c) Milling procedure overdone, leading to the resist not properly peeling off.

Although dry etching was very successful, there have been reports suggesting that carbonization of photoresist occurs due to the long term exposure to high energy ion beams[173] along with the fact that the Ar ions might cause disorder in the system[148]. To look for an alternative approach, a chemical etching process was also carried out on the same batch of Bi_2Se_3 pieces. Wet etching stands as a superior alternative due to its high etching rate, low cost and high selectivity. A literature survey suggested that iodine and/or bromide based chemistries promised a selective surface etching but at low etching rates[174]. On the other hand, Gao *et al.*[173] tried etchants based on $K_2Cr_2O_7$– H_2SO_4 and $K_2Cr_2O_7$– HCl solutions for patterning Bi_2Se_3 thin films on Si substrates successfully. However they noted that a Se depletion layer at the surface was formed on the etched Bi_2Se_3 as confirmed by using XPS.

For a quick chemical etching of bismuth chalcogenides, I first attempted a wet etchant using an aqueous solutions of HNO_3 and HCl mixture (diluted aqua regia).This is perhaps the most common and popular etchant recipe used by various groups in the world[175–178]. However, even after leaving the sample for prolonged periods in the etchant, it seemed like Bi_2Se_3 did not etch. On addition of H_2O_2 into the aqua regia solution, the etch was successful. H_2O_2 acts as an oxidizing agent and helps to oxidize the surface which then reacts with the acid in the solution. The results of this are shown in Figure 5.15 (a-c) taken in real time while the etching was underway. The total etching time was 30 seconds and the three images were taken 10 seconds apart from each other starting with (a) to (c). It was observed that the solution was highly corrosive and caused a uncontrollable reaction with Bi_2Se_3, resulting in severe undercutting at the edges [Figure 5.15 (c)].

(a) (b) (c)

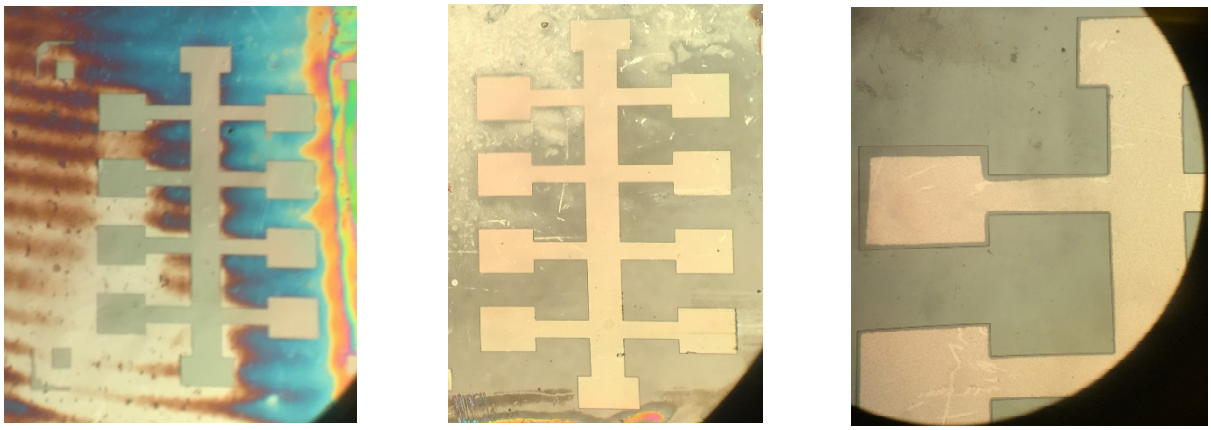

Figure 5.15 (a) The sample dipped in an acid solution after 10 seconds, (b) 20 seconds (c) and 30 seconds.

Another less stronger acid recipe was carried which showed promising results. A wet chemical etching solution containing 1 ml HCl, 0.8 ml hydrogen peroxide, 8 ml acetic acid with 16 ml distilled water was prepared with the sample dipped in it for 1 minute. The pattern was transferred onto the Bi_2Se_3 film very cleanly with no signs of undercutting or rapid etching. Figure 5.16 (a) shows an image of the film dipped in this acid after the first 30 seconds, while (b) and (c) were taken after 1 minute. Optical images confirmed that the sample was in good condition. After a successful chemical and dry etching step, the samples were taken back into the clean room and dipped in Acetone, IPA and blow dried with N_2 gas. The second stage of lithography began by spinning a fresh batch of photoresist S1813 for 1 minute at 5500 RPM followed by baking the resist at 90°C for 2 minutes. It should be noted that the baking temperature was lower than for the first time, the reason of which will become clear later. The sample was then transferred onto the mask aligner but this time aligned with a different pattern, *i.e.* the contact pads. Since the pads were not covered by chromium and all other regions of this pattern were covered, the UV light would only shine through the pad windows. The exposition was slightly more complicated than before as the contact pads pattern had to be perfectly aligned with the Mesa below. The exposure was followed by a dip in chlorobenzene for 2 minutes. The chlorobenzene diffuses into the resist and lowers the rate at which the resist develops. This leads to an undercutting in the resist profile which will be useful at a later stage during lift off. To assist this process, the resist was baked at a slightly lower temperature (90°C) in the previous step. After the chlorobenzene dip, the resist was developed in MF319 developer for a total time of 2 minutes (much longer than in the previous step) followed by DI water and blow drying in N_2 gas.

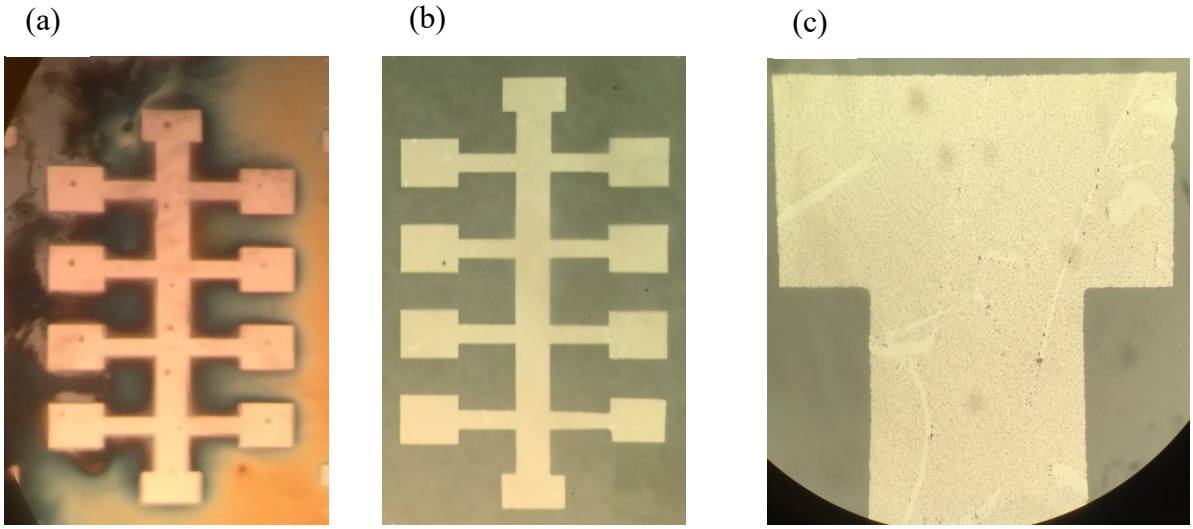

Figure 5.16 (a) The sample dipped in an HCl, H_2O_2 and acetic acid solution for 30 seconds (b) 60 seconds and (c) a zoomed image showing no signs of undercutting.

The result of the exposure and development is shown in Figure 5.17 (a). Clear open windows are seen on the contact pads whilst all other regions are covered with photoresist. The sample pieces were then placed in a radio frequency asher in an oxygen plasma environment for 30 seconds. The purpose of this step was to remove all residual resist on the open windows, whilst oxidising the surface. Finally, the samples were dipped into a 10% dilute HCl solution for 30 seconds to remove any oxidation layer which may have formed on top of the open windows. Titanium and gold of thickness 25 nm and 100 nm, respectively, were deposited one after the other by physical vapor deposition. A thermal evaporation chamber reaching a base pressure below 1×10^{-7} mbar was used. Pieces in the form of small cylinders of Ti and Au were cut and placed on W-boats. These boats were heated until the material in them started to sublimate. Metallic atoms condense directly on the sample surface while the rate of deposition was controlled by adjusting the current which passed across the boat terminals. After the procedure, the chamber was vented and the sample taken out. It is important to note that on a few occasions, the TI boat or Au boat broke due to the high currents which pass across them. If the Ti boat breaks while preparing the device, the chamber might need to be vented and hence the half grown Ti is exposed directly to air. The Ti in this case will immediately react to oxygen to form TiO_2 which will create a Schottky barrier. To avoid this, there was an extra boat in the evaporator with extra Ti.

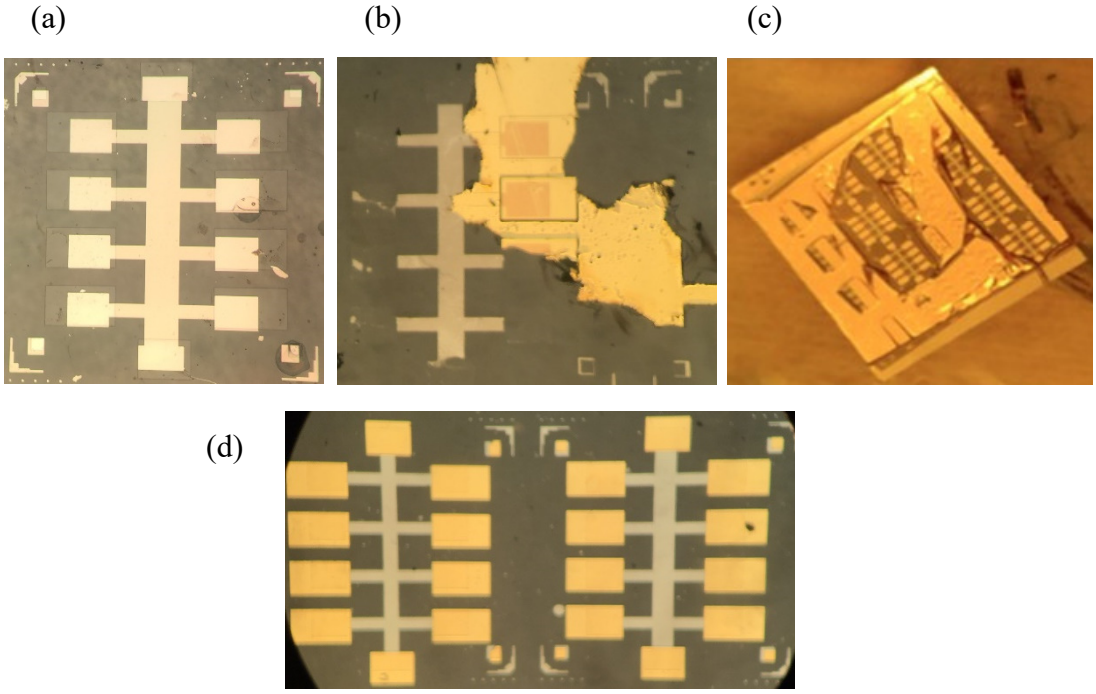

Figure 5.17 (a) Contact windows open on a Hall bar pattern of Bi_2Se_3, whilst all other regions are covered with photoresist.(b) the effect of ultrasonicating a film (c) a lift off process showing the gold peeling off (d) Hall bars after the lift off process.

The deposited metal film covered the whole sample, *i.e.* the resist and the window area. The photoresist under the film was removed with Acetone and taking the extra metal bits away by leaving the Ti/Au that was previously deposited directly on top of the Bi_2Se_3 layer [shown in Figure 5.17 (d)]. In many cases, the resist did not peel off and it was found that ultrasonicating the lift-off solution and device displaces the film underneath. Since Bi_2Se_3 is weakly bonded to the substrate, it is prone to displacement. Figure 5.17 (b) shows the effects of ultrasonicating the film. The contact pads peel off along with the gold metal deposited on the top.

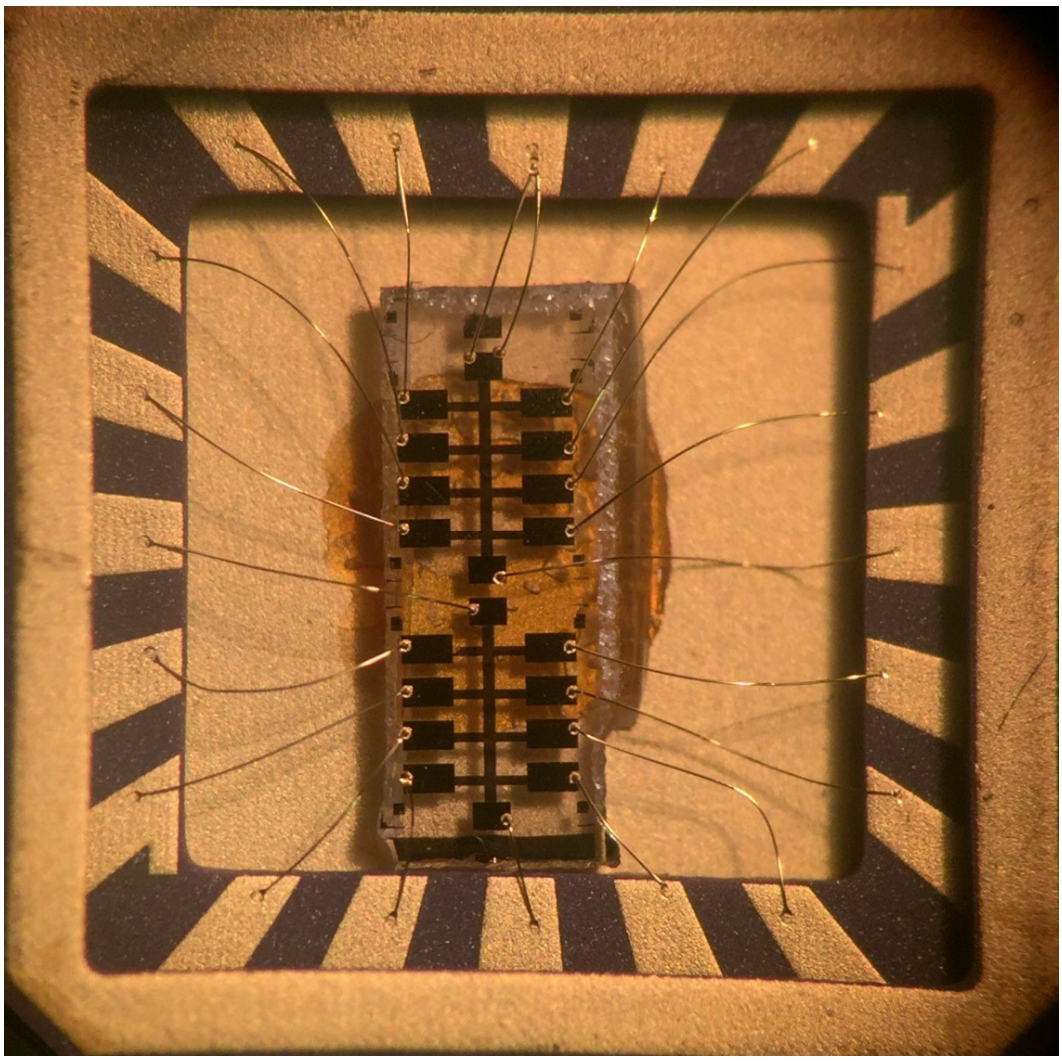

Figure 5.18 Two Hall bars after sticking onto a chip carrier with GE varnish and then wire bonded to the chip carrier.

Finally, using the diamond scriber again, the chip was further cut down into individual pieces and glued onto chip carriers. They were fixed by using GE varnish which is electrically insulating and can also withstand very low cryogenic temperatures. After this, wire bonds were made to connect the contact pads to the pads on the chip carrier as shown in Figure 5.18.

The final step was the gate pattern. But I soon realized that the design of the gate mask as shown in Figure 5.10 (c) was not compatible with the hall bar and would have involved many complicated steps. Hence I tried to fabricate a gate with just the mask design as shown in Figure 5.10 (d). First a window was opened in the resist using an UV light and MF319 as described earlier, following a similar procedure. Figure 5.19 (a) shows the open window. Then 60 nm of Al_2O_3 was deposited onto the sample using atomic layer deposition (ALD) with the help of Dr Ateeq Nasir from the Semiconductor Physics group. This dielectric layer acts as a capacitor and helps in creating an electric field during gated measurements. After this, Ti/Au of thickness 25/100 nm was deposited onto the sample followed by a dip in Acetone and IPA as described earlier. The final device is shown in Figure 5.19 (b).

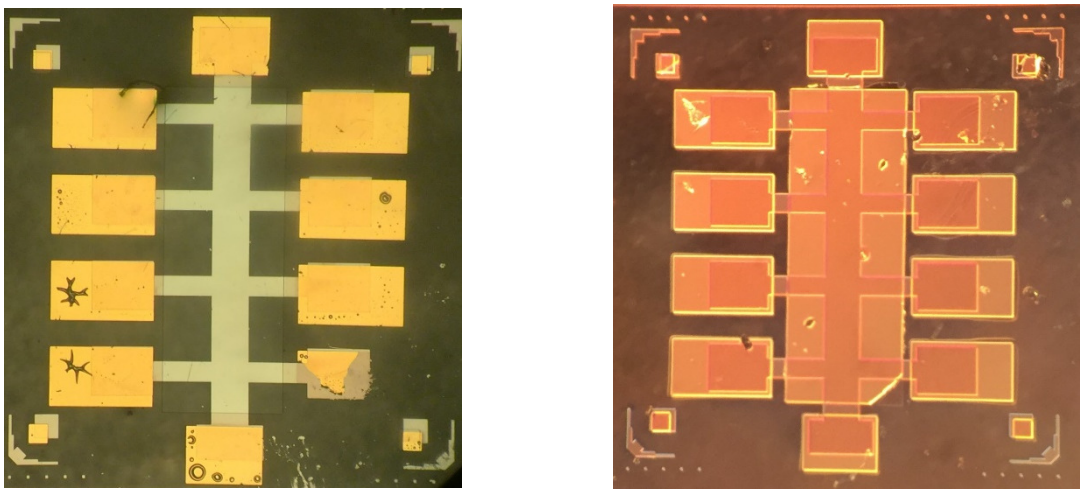

Figure 5.19 (a) A Hall bar device with photoresist everywhere except for the central length of the Hall bar where an open window can be seen. (b) A gated Hall bar device with a layer of Al_2O_3 dielectric.

5.5 Electric Transport in Bi_2Se_3 Devices

Once the Hall bars were fabricated and wire bonded, the sample was loaded into the cryostat as described in section 2.5.1. This section contains results from two working Hall bars, one fabricated using Ar^+ ion milling and one made using chemical wet etching. For convenience, the sample fabricated using chemical wet etching was called "Sample A" while the other was called "Sample B".

We started with all the preliminary checks to see if the devices were working, for example checks were made to see if a current was passing from the source to the drain, whilst also checking if the current was passing through the arms of the Hall bars. The circuit used for the measurement setup is described below.

In order the avoid contact resistances, a four terminal setup was wired as shown in the schematic of Figure 5.20. A lock-in amplifier was used to source a voltage, for example 1V through a 10 MΩ resistor followed by the device under test (DUT), then through to a 10 KΩ resistor and then grounded to earth. The arms of the device were connected to two lock-in amplifiers to measure the longitudinal V_{xx} and transverse V_{xy} voltages. Another lock-in was used to measure the voltage (V_{sd}) across the 10 KΩ resistor which provided the value of a constant current of I_{sd} = 100 nA flowing inside the circuit. Provided that the 10 MΩ is very large as compared to the device resistance then a constant current can be maintained. A very small current for I_{sd} was chosen to avoid sample heating and also to get a good signal-to-noise ratio. All electrical measurements were carried out on a *Labview* assisted program layout, designed and written by Professor Chris Ford, the details of which are in section 2.5.1.

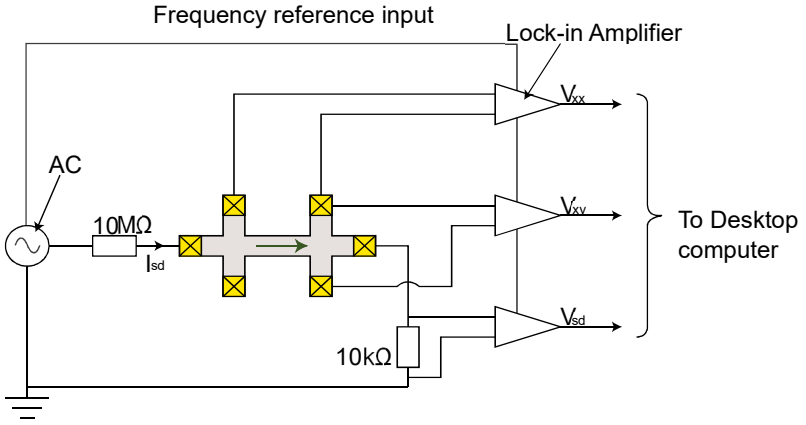

Figure 5.20 Schematic of the setup used for 4-terminal resistance measurements. The arrow indicates the current I_{sd} flow direction, V_{xx} and V_{xy} are the voltages measured along the longitudinal and transverse while V_{sd} is the voltage drop across a 10 KΩ resistor.

Once all the checks were carried out at room temperature, the needle valve of the cryostat was opened slightly while a vacuum was maintained inside the inner chamber where the sample sits. This allows liquid He to flow into the sample space at a controllable rate, monitored using a pressure gauge. While the sample is cooled to 1.5 K or 300 mK, the resistance of the sample was recorded upon cooling.

Figure 5.21 shows the longitudinal resistances R_{sheet} of the chemical etched Sample A and of the Ar^+ ion etched Sample B as a function of temperature. For sample A, the resistance reduces as the temperature decreases, suggesting a metallic behaviour as observed widely in Bi_2Se_3 thin films[162,172]. This decrease can be explained by the alleviation of phonon scattering when the temperature is reduced. On further reducing of temperature, the resistance flattened out down to 1.5 K. This region may be dominated by a combination of surface as well as bulk conduction. Interestingly, Sample B exhibits a contrasting behaviour. As the temperature is reduced, an increase in resistance is observed with a kink just below 5 K. This increase is most likely associated with the freezing-out of the bulk behaviour of the sample. The kink around 5 K may be associated with impurity band conduction also commonly observed in TIs[74].

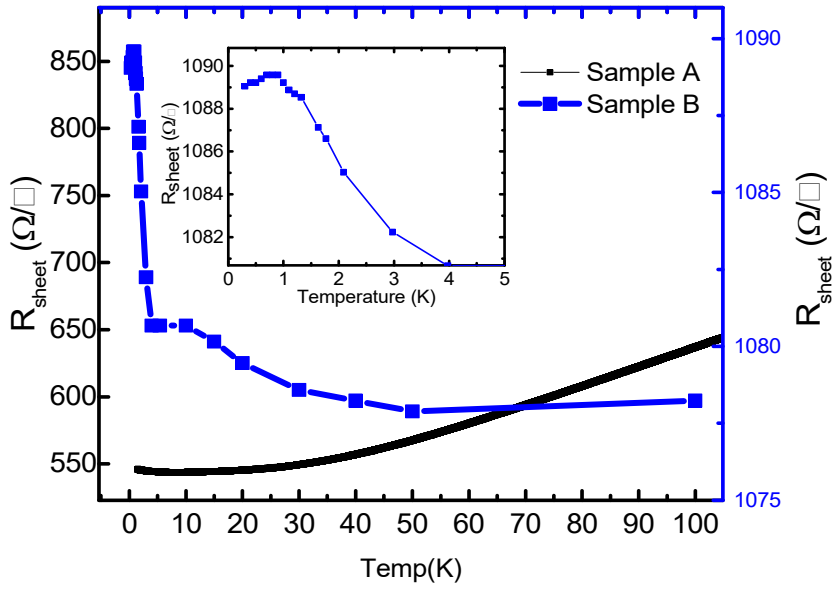

Figure 5.21 Longitudinal resistance as a function of temperature for a chemical etched Sample A and Ar^+ ion etched Sample B. Sample A shows a monotonic reduction in the resistance with decreasing temperature while it stabilizes at low temperature (around 20 K). Sample B shows an increase in the resistance as the temperature reduces to 1 K, after which it decreased as shown in the inset.

Similar behaviour was also observed by Analytis *et al.*[162]. but with changing the carrier concentration in the sample. At temperatures below 1 K, the resistance falls off displaying a metallic behaviour down to 300 mK. This region is presumably dominated by surface conduction. In summary, the behaviour of the exact same sample changes drastically when treated with Ar^+ ions compared to wet etching. To further understand the transport mechanism, magnetotransport measurements were carried out whilst comparing sample A and B. The longitudinal resistance R_{xx} was recorded in both samples while sweeping the magnetic field B. The sweep rate was fixed for both samples, while multiple measurement averages were taken to plot the results as shown in Figure 5.22. Both samples display a WAL behaviour at low field, while the resistances of the samples were different. In materials with strong spin-orbit coupling the spin of electrons is locked to it momentum, the presence of an external magnetic field may interfere with the electrons and cause destructive or constructive interference. If the spin of the electrons are locked to their momentum, (such as for surface state electrons in TIs) a suppression of backscattering occurs which cause a Berry phase of π to be acquired by electrons while executing time-reversed paths. If the electrons interfere destructively, the WAL phenomenon is observed and a quantum correction to the resistance is detected resulting in a dip in the resistance at zero magnetic field. Such a phenomenon reflects both the Dirac nature of the surface states as well as the strong spin−orbit interaction in TI materials[165].

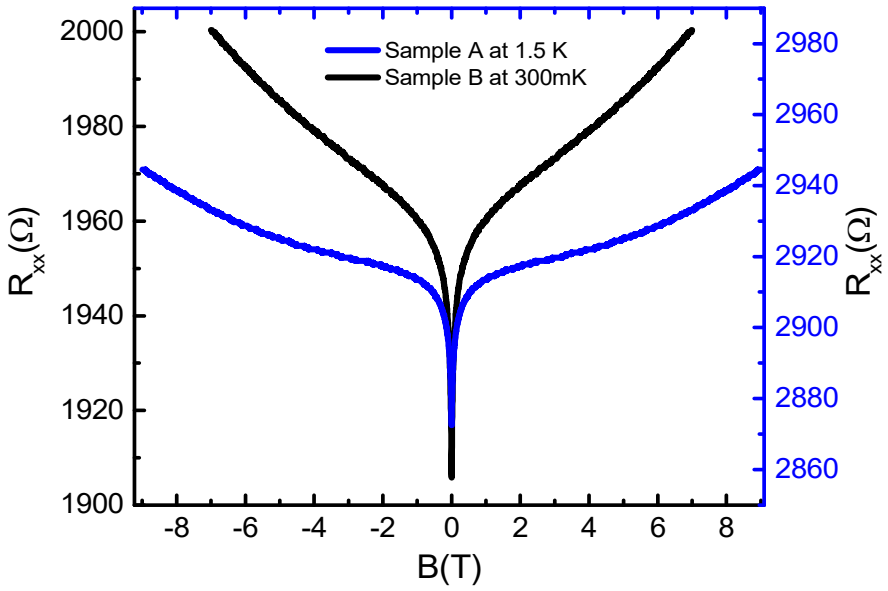

Figure 5.22 Longitudinal resistance R_{xx} as a function of sweeping the magnetic field in a chemical etched Sample A, compared to an Ar^+ etched Sample B at 1.5 K and 300 mK respectively.

At high fields both samples behave differently. The *MR* for Sample A exhibits a certain degree of non-linearity compared to Sample B which shows a nearly linear dependence at high fields. Such a linear dependence in Sample B is predominantly caused by the coupling of the spin momentum locked electrons to the external field *B*, hence showing a more surface dominated response. A similar behaviour was also observed by Qu *et al.* in Bi_2Te_3[179]. The non-linearity in Sample A may be associated with a more bulk-like contribution[180–182]. It was also observed that both samples exhibit non saturated *MR* at high fields. It has been known that regular metals display a quadratic *MR* (*i.e.* $\Delta R \propto B^2$) at low fields and this *MR* saturates at high field[183]. Observing a non-saturating *MR* at high fields is useful for both the fundamental magneto-transport phenomena and for magnetic sensor applications[40]. Another powerful technique, which can be used to distinguish the 2D weak anti-localization effect from 3D bulk effects, is to perform tilted magnetic field measurements. The inset of Figure 5.23 shows the *MR* effect with respect to the magnetic field angle at 1.5 K for Sample A.

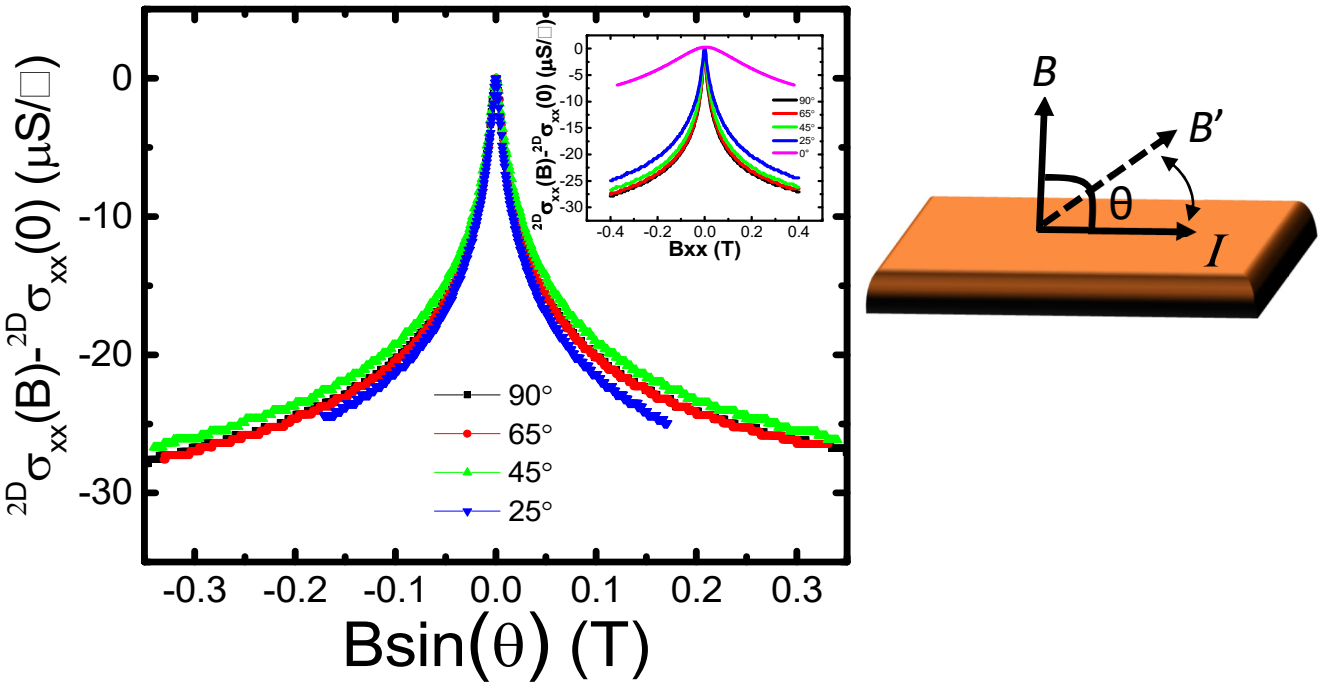

Figure 5.23 A normalized magneto-conductivity $\Delta\sigma_{xx}^{2D} = \Delta\sigma_{xx}^{2D}(B) - \sigma_{xx}^{2D}(0)$ for Sample A measured as a function of the normal *B* component at T = 1.5 K. $\theta = 0$ ° corresponds to the field *B* parallel to the sample current direction *I*. The inset shows the normalized magneto-conductivity as a function of *B* at different sample tilt angles θ.

At $\theta = 0°$, *i.e.* when the sample is parallel to the magnetic field tilt, the *MR* almost completely disappears (pink curve in the inset) and the *MR* shows an almost parabolic *B*-field dependence. This semiclassical dependence results from the Lorentz deflection of carriers. Figure 5.23 shows the normalized magneto-conductivity as a function of the normal component of the *B* field *i.e.* $B\,sin\theta$ for various angles. It can be clearly observed that at low fields all the curves coincide with each other. This behaviour suggests that the observed WAL effect results from the orbital motion of carriers since the orbital term only depends on the normal component of the magnetic field indicating the 2D nature of the strong spin-orbit coupled topologically protected surface states. Although this is the case, in systems where the dephasing length L_φ is much larger than the sample thickness *t*, bulk transport could also show a 2D weak antilocalization behaviour hence showing a parabolic dependence even at $\theta = 0°$.

Figure 5.24 displays the normalised magneto-conductivity for Sample A and Sample B defined as $\Delta\sigma_{xx}^{2D} = \Delta\sigma_{xx}^{2D}(B) - \sigma_{xx}^{2D}(0)$ as a function of temperature. A sharp increase in the conductivity is observed at low magnetic field B when increasing the temperature in both samples A and B. This demonstrates weak antilocalization behaviour as explained above. Although both samples show similar cusp shapes at low temperatures (1.5 K-20 K) , the conductivity for Sample A almost flattens out at 50 K, while for Sample B, it still shows a prominent WAL behaviour even at 100 K. This is consistent with Sample A showing more bulk type characteristics at 50 K compared to Sample B at the same temperature. Fitting the data to the HLN equation as described in section 5.2 yields a value of the number of surface

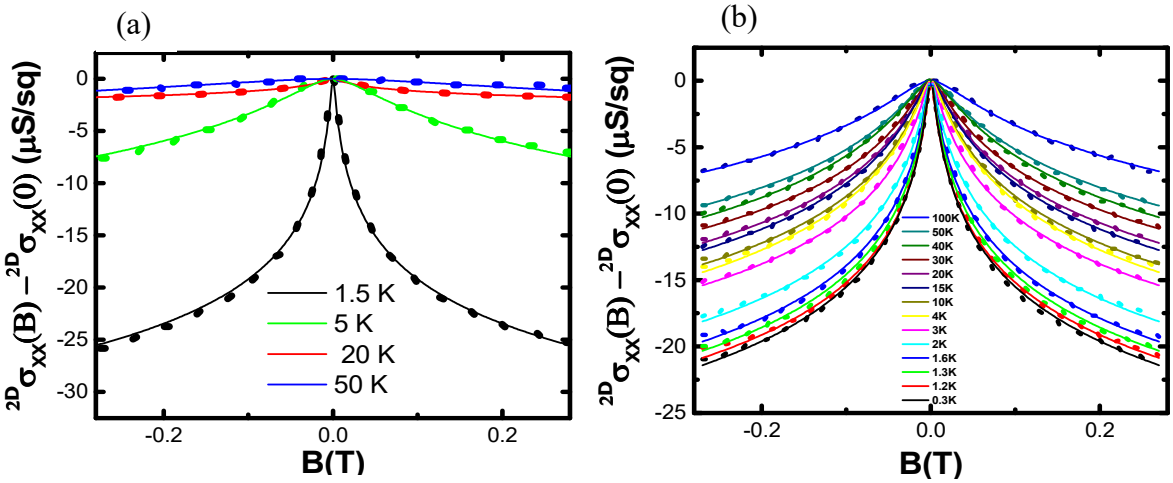

Figure 5.24 Weak antilocalization effect in Bi_2Se_3 for samples A and B. (a) Normalized conductivity changes as a function of magnetic field measured at different temperatures. Each data set is fitted (dots) to the HLN formula described in the text. The cusp in conductance is a characteristic feature of the WAL effect.

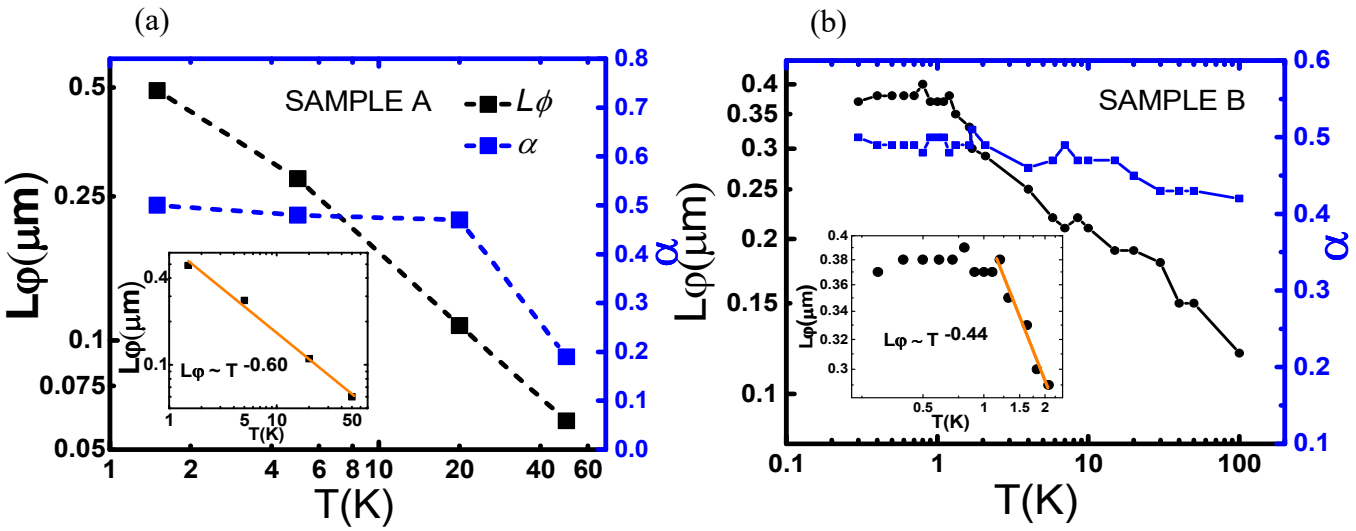

Figure 5.25 Plot of the parameters L_φ and α as a function of temperature as obtained from the WAL fit to both (a) Sample A and (b) Sample B. The inset shows the power law fit of $L_\varphi \sim T^{-0.60}$ for Sample A and $T^{-0.44}$ for Sample B.

state modes/channels α and the dephasing length L_φ. Figures 5.25 (a) and (b) show the variation of α and L_φ as a function of temperature in both samples A and B, extracted from the fit to the HLN equation in the WAL regime. A value for prefactor $\alpha \approx 0.5$ was obtained, which remains largely unchanged from 1.5 K to around 20 K for Sample A and from 0.3 K to 15 K in Sample B (blue curves). The result of 0.5 for α suggests a single conducting channel. In an ideal case scenario, *i.e.* a perfect TI sample, surface dominated transport should exclusively take place in two symmetric channels corresponding to $\alpha = 1$. This allows for a straightforward calculation of the dephasing length L_φ from the HLN equation. The regime requires the bulk to be perfectly insulating and at the same time the top and bottom surfaces decoupled, having identical dephasing fields. Unfortunately, most measurements reported do not fullfill this criteria owing to bulk conduction[163,165–167,169–171,181,184]. The result of $\alpha = 0.5$ may suggest that the top surface is contributing significantly more to the WAL than the bottom surface. This might be due to a somewhat reduced phase coherence length L_φ, at the bottom interface, owing to the defects present at the TI−substrate interface[184,185]. The TI-substrate interface is affected by the lattice mismatch between the Bi_2Se_3 and the substrate[166,185]. Above 20 K in both samples, α starts to drop with temperature, indicating increasing bulk interference. The sharpness of the WAL cusp determines the phase coherence length L_φ. This length characterizes the phase coherent behavior of carriers before an inelastic scattering event, indicating thereby the quality of the film. The obtained L_φ shows a strong temperature dependence (black curves). The phase coherence length increases with

decreasing temperature, with a value of 500 nm at 1.5 K for Sample A and a saturated value of 380 nm at 300 mK for Sample B. The observed saturation in Sample B for L_φ may result from strong electron−electron interaction in the low- temperature regime[186]. A power law fit of the phase coherence length at low temperatures shows a $L_\varphi \sim T^{-0.60}$ and $T^{-0.44}$ dependence for Sample A and Sample B. In general, a power law dependence of $T^{-0.50}$ represents a two-dimensional (2D) system, while a $T^{-0.75}$ represents a three-dimensional (3D) system[187]. Hence, the observed temperature dependence of L_φ suggests that the WAL at low temperatures in Sample B could possibly originate from a 2D surface state, while the L_φ dependence of Sample A might suggest more bulk contribution. Although the transport measurements reveal useful parameters such as $\alpha \approx 0.5$ and $L_\varphi \approx 380$ nm and 500 nm, they do not demonstrate that the observed WAL originates exclusively from the TSS. In conclusion, the *MR* response could be due to coupling of the top and bottom TSS through the bulk or could be due to a significant response from the top only TSS for both samples. In both cases, however, $\alpha = 0.5$ is consistent with the presence of topological surface state.

The Hall resistance R_{xy} for samples A and B as a function of magnetic field were taken at different temperatures as shown in Figure 5.26 (a) and (b). By making a linear fit to the data the sample carrier densities and mobilities were estimated by using the semiclassical value of the Hall resistivity: $R_{xy} = B/nec$ and $\sigma_{xx} = ne\mu$. A comparison of the Hall mobilities and carrier densities obtained from the two samples are shown in Figure 5.26 (c) and (d) respectively. The mobilities were much lower in Sample B compared to sample A, which was processed using the wet chemical etch method. This could be attributed to the increase in the density of defect states in Bi_2Se_3 after being exposed to the ion milling process due to an increased disorder in the system. This may suggest that Ar^+ milling dopes the sample more compared to a chemically etched sample. On the other hand, both samples display very little change in the carrier densities with respect to temperature, confirmed by an insignificant change in the gradient in Figure 5.26 (a) and (b). The carrier density of Sample B is higher than the density of Sample A at all temperatures following roughly the same temperature trend as shown in Figure 5.26 (c). This is consistent with the observation that the mobilities obtained from the samples processed with Ar^+ ion milling were approximately half of those obtained from the chemically etched Sample A as shown in Figure 5.26 (d). Although, both samples were processed in similar ways during device fabrication apart for the etching process, they were both exposed to clean room chemicals (MF319 developer and S1813 resist), solvents and deionized (DI) water. There is some evidence that using MF319

developer (tetramethylammonium hydroxide) and DI water may modify the surface of the TI with the possible chemical reaction occurring at the surface, following: $Bi_2Se_3 + 6H_2O \rightarrow 3H_2Se\uparrow + 2Bi(OH)_3$. The H_2Se gas escapes, leaving Se vacancies[143] and bismuth hydroxide behind[66], which cause an overall *n*-doping of the Bi_2Se_3 film. Even though this should not directly affect the topological surface state, the increased doping makes it more challenging to distinguish the surface from the bulk response[144].

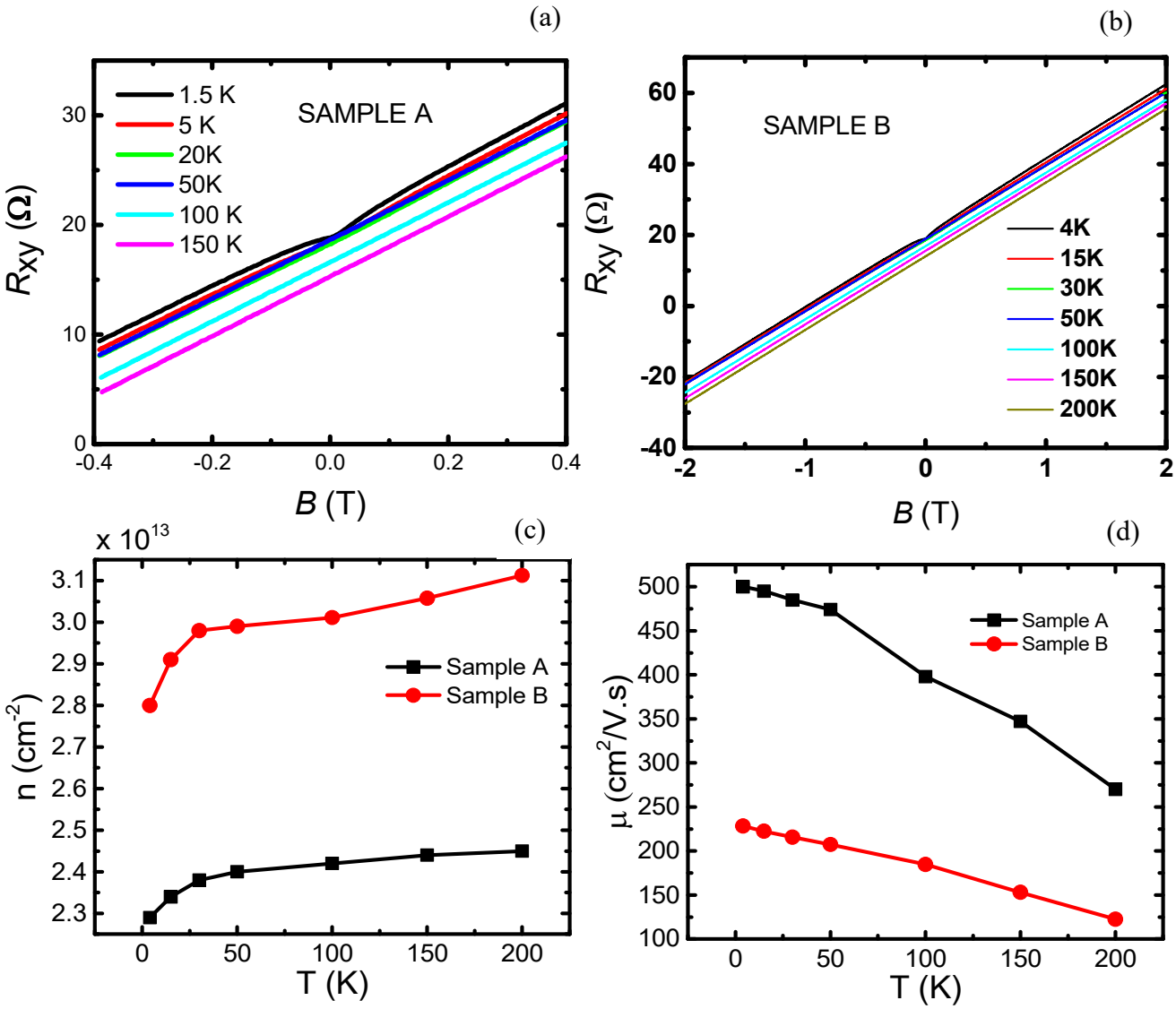

Figure 5.26 (a.b) Hall resistance R_{xy} for samples A and B as a function of magnetic field. (c) The carrier densities *n* and (d) mobilities μ as a function of temperature for samples A and B.

In summary, a 22 nm nominal thickness of Bi_2Se_3 thin film was grown using MBE and two Hall bars were fabricated using wet chemical etching and Ar^+ milling processes respectively. Their differences are summarized in tabular form below.

Table 5.1 Table below summarizing the differences in the results from Sample A and Sample B.

SAMPLE A (Chemical etched)	**SAMPLE B (Ar^+ ion milled)**
Resistance *R* vs. Temperature *T* plot shows a decrease in *R* with decrease in *T* up to 20 K after which it saturates. This may be explained by a combination of surface and bulk conduction.	Resistance *R* vs. Temperature *T* plot shows an increase in *R* from 100 K up to 1 K after which it decreases with decreasing *T*, consistence with a metallic behaviour. This may show predominant surface conduction.
MR at 1.5 K in low field regions show WAL while *MR* at high fields show an unsaturated non-linearity consistent with bulk conduction.	*MR* at 300 mK at low fields also shows WAL while high field results display an unsaturated linear dependence consistent with a surface type response.
WAL cusps flatten out at 50 K with an α value of 0.5 consistent with one conducting channel which may be the top surface state.	WAL cusps don't flatten out even at 100 K giving an α value of 0.5 consistent with a single surface state mode.
L_φ = 500 nm at 1.5 K follows a power law temperature dependence as: $L_\varphi = T^{-0.60}$ close to the expected value of $T^{-0.75}$ for bulk conduction. The result might be explained by a combination of surface and bulk conduction.	L_φ = 380 nm at 300 mK follows a power law temperature dependence as: $L_\varphi = T^{-0.44}$ close to the expected value of $T^{-0.50}$ for surface conduction. The result shows a surface type response.
The carrier densities are lower following a similar temperature trend as compared to Sample B.	The carrier densities are higher following a similar temperature trend as compared to Sample A. Ar^+ may be responsible for creating more disorder in the material system caused due to ion implantation.
The mobilities are almost double at all temperatures compared to Sample B.	The mobilities are almost half as compared to Sample A consistent with a higher carrier density.

5.6 Electric Transport in Sb_2Te_3 Devices

A closely related material to Bi_2Se_3 is Sb_2Te_3. Although the underlying physics is very similar, not many researchers have studied this material. Here I present results from MBE grown samples synthesized by Dr Gregor Musler at the Peter Grünberg Institute Jülich, Germany, on Si(111) substrates. Two thin films with thicknesses of 12 nm and 25 nm were studied. The results are a thickness dependent comparison of the transport properties in Sb_2Te_3. A similar procedure was followed for device processing and Hall bars were fabricated using Ar^+ ion milling as described in section 5.3, while the cryostat and circuit connections were also the same as described earlier in Figures 2.14 and 5.20.

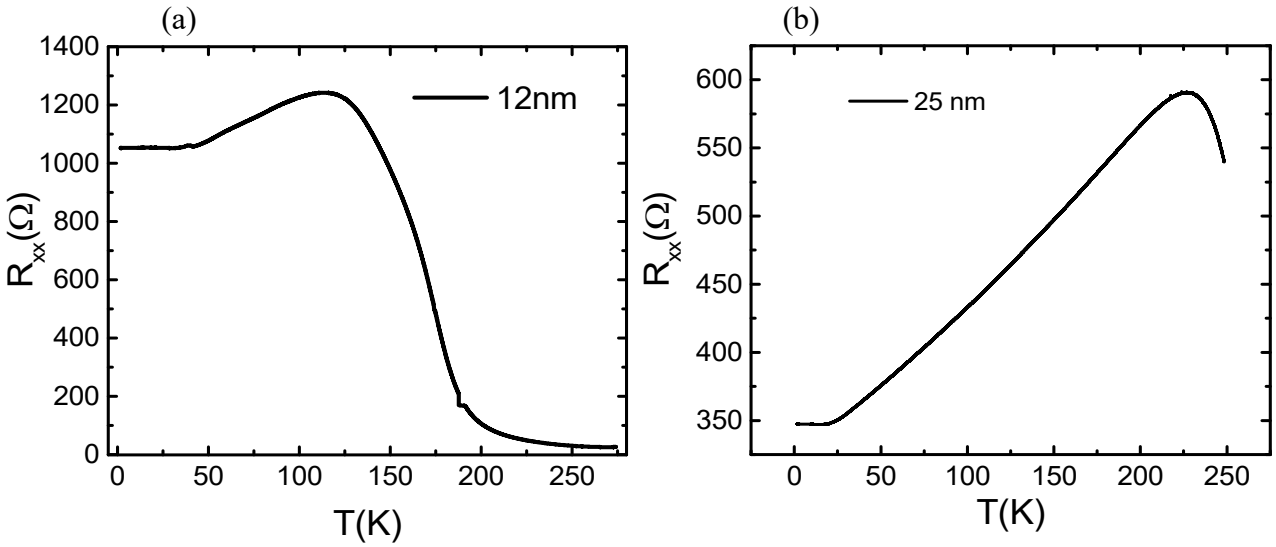

Figure 5.27 (a,b) Longitudinal resistance R_{xx} as a function of temperature for a 12 nm (Sample C) and 25 nm (Sample D) Sb_2Te_3 thin film. Sample C shows an increase in the resistance as the temperature reduces to 120 K, after which it reduces up to 50 K and then saturates. After an initial increase between 250 K to 225 K, Sample D shows a monotonic reduction in the resistance with decreasing temperature where it stabilizes at 20 K.

Figure 5.27 (a) and (b) display the temperature dependent longitudinal resistance R_{xx} for two Sb_2Te_3 samples with thicknesses 12 nm and 25 nm. Both samples show a different behaviour. The 12 nm sample shows an increase in resistance from room temperature to 120 K consistent with freezing out the bulk carriers after which the resistance reduces and stabilizes reminiscent of a metallic surface state response. For the 25 nm sample the resistance increases with decreasing temperature (indicating freezing of the bulk or perhaps the Si substrate parallel conduction) followed by a monotonic decrease in the resistance down to 20 K, consistent with a metallic behaviour. The resistance saturates below 20 K. In both cases, the saturation of the resistance at 20 K can be associated with electron-electron interaction. The metallic behaviour in both samples are attributed to the surface state responses.

The normalized longitudinal resistance defined as: $R_{xx}(B)$- $R_{xx}(0)$ at 1.8 K was directly recorded while sweeping the magnetic field B in both samples. Exactly the same sweep rates were used for both samples, while multiple measurement were taken and averaged to plot the results in Figure 5.28. The magnitude of the resistance and shape of the curves show a strong dependence on thickness.

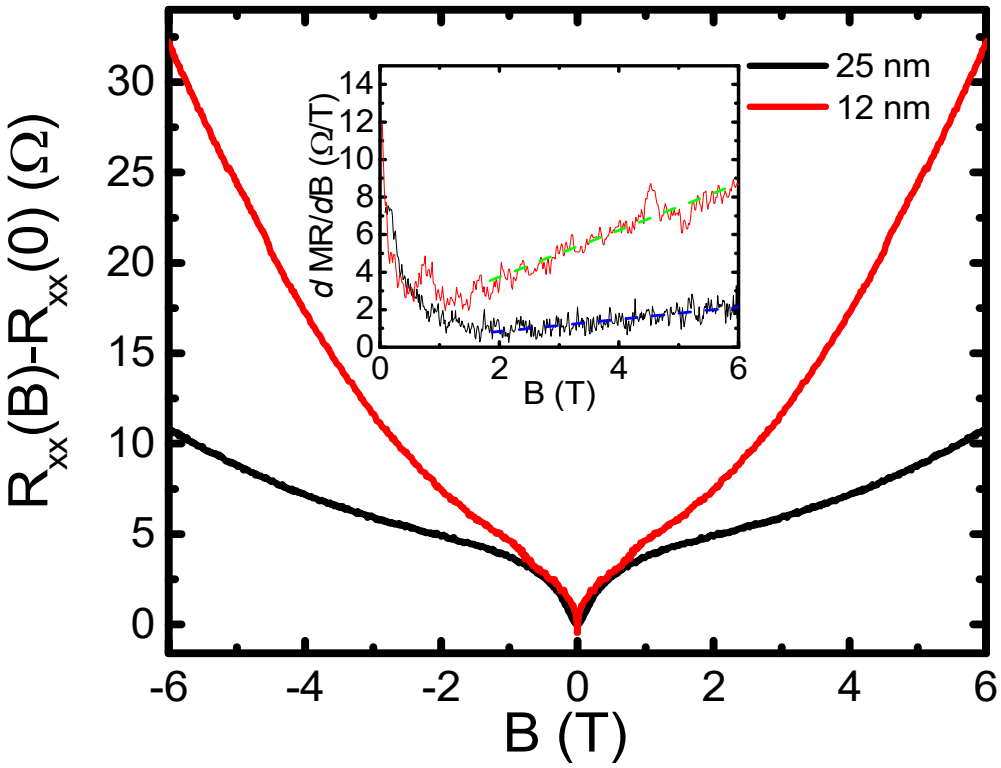

Figure 5.28 Normalised longitudinal resistance R_{xx} as a function of magnetic field B in a 25 nm and 12 nm thin film of Sb_2Te_3 at 1.8 K. The inset shows the derivatives $d\,MR/d\,B$ of the magneto-resistance with respect to field B.

At low magnetic fields (<±1T), the resistance exhibits a WAL cusp, as expected from TI samples. In addition, at high fields (>1T) the resistance increases with increasing field in a non-saturating trend up to $B = 6$ T. The 12 nm sample has a much higher resistance compared to the 25 nm sample while both curves show a parabolic B-field dependence. Similar to Bi_2Se_3, this semiclassical B^2 dependence results from the Lorentz deflection of the carriers which forces them into cyclotron orbits. The derivatives of the longitudinal resistance with respect to the magnetic field, defined as $d\,MR/d\mathrm{B}$ is shown in the inset. Generally the resistance saturates or is proportional to B^2, depending if the corresponding orbits are closed or open respectively. The condition for closed orbits is given by $\omega_c\tau > 1$, where $\omega_c = qB/m^*$ is the cyclotron frequency and τ is the relaxation time. Both the resistance curves obtained do not saturate, indicating that the cyclotron orbits are open in the range of the applied magnetic field and temperature. The orbit radius $r = \hbar k_F/qB$, where $k_F = (3\pi^2 p)^{1/3}$ is the wave vector at the Fermi surface and p is the carrier density. The radius corresponds to 333 nm for the 12 nm sample and 216 nm for the 25 nm sample at a magnetic field of 4 T. Therefore the radius in both cases exceeds the thickness in the whole range of the applied magnetic fields. Looking at the inset, the derivative for both samples is linear after 2 T (showing a B^2 dependence). This indicates that the scattering mechanism may not be changing qualitatively in the region of the magnetic field. A similar behavior was also reported by Harutyunyan in Sb_2Te_3 nano-flakes[188]. A temperature dependent study was conducted on both samples with the results displayed in Figure 5.29 (a) and (b) for the 12 nm and 25 nm film respectively. As the temperature is increased, the cusps in both samples weaken as a result of the decreasing coherence length, as suggested in the case of Bi_2Se_3, and eventually gives rise to a stronger parabolic-like B-dependence at higher temperatures and low fields. At higher fields, both samples show a roughly linear behaviour. The slope changes very little over the complete temperature range (from 1.7 K to 150 K) for the 25 nm sample, while a variation in the slope for the 12 nm is seen as it deviates from 130 K upwards. The deviation in the slopes are consistent with resistance vs. temperature plots showing a metallic surface state response below ~ 120 K in the 12 nm sample and below 200 K in the 25 nm sample with decreasing temperature.

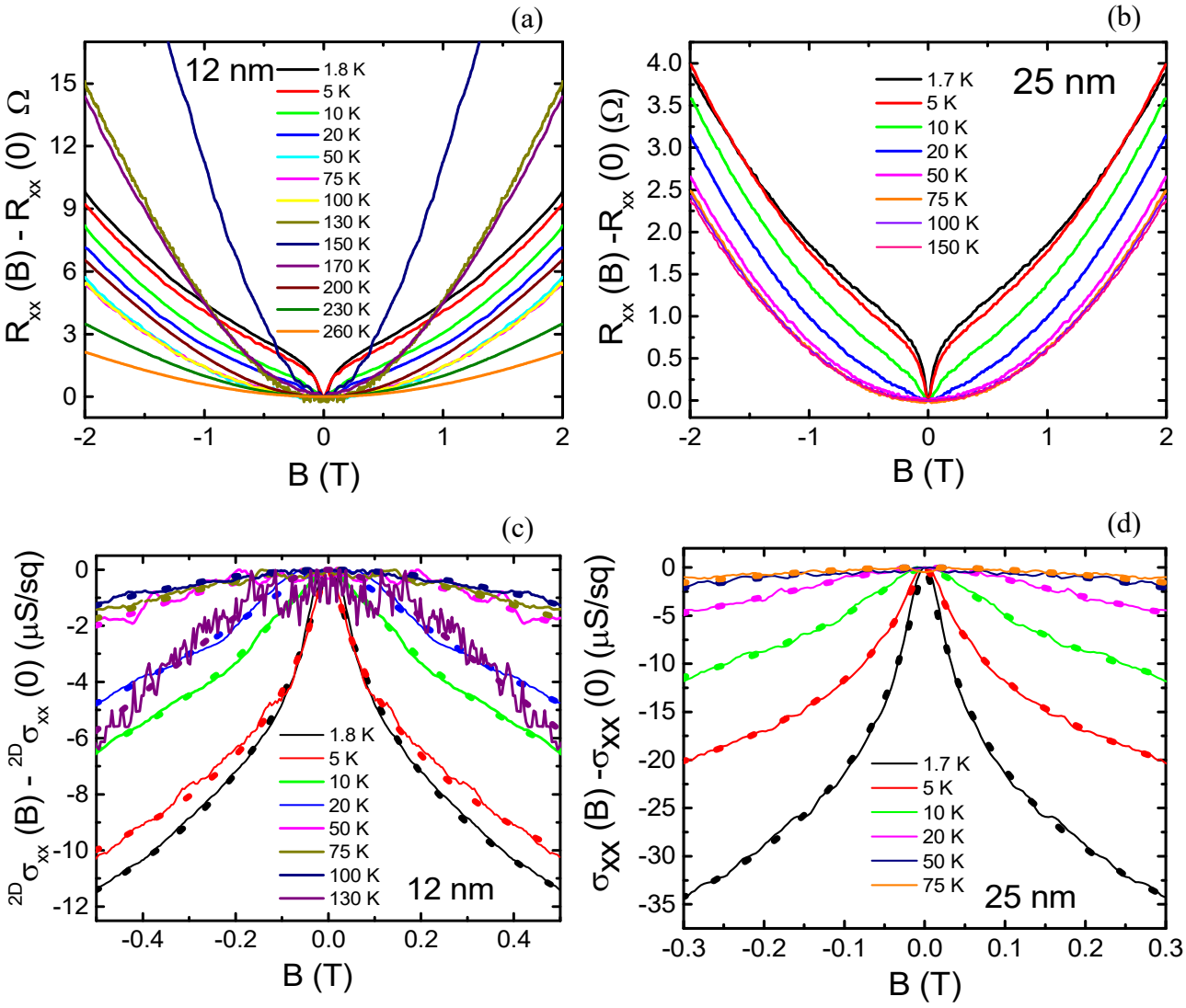

Figure 5.29 (a,b) normalized longitudinal resistance versus applied magnetic field for a 12 nm and 25 nm thick Sb_2Te_3 film at temperatures up to 1.7 K. (c,d) Magneto-conductance (solid lines) versus applied magnetic field for a 12 nm and 25 nm thick Sb_2Te_3 film along with the HLN fits (dotted lines) at various temperatures.

Fits (dotted lines) to the HLN equation as described section 5.2 on the normalized magneto-conductance (solid lines) for both samples are shown in Figures 5.29 (c) and (d). The number of surface state modes/channels α and the dephasing length L_φ were obtained as previously performed for the case of Bi_2Se_3.

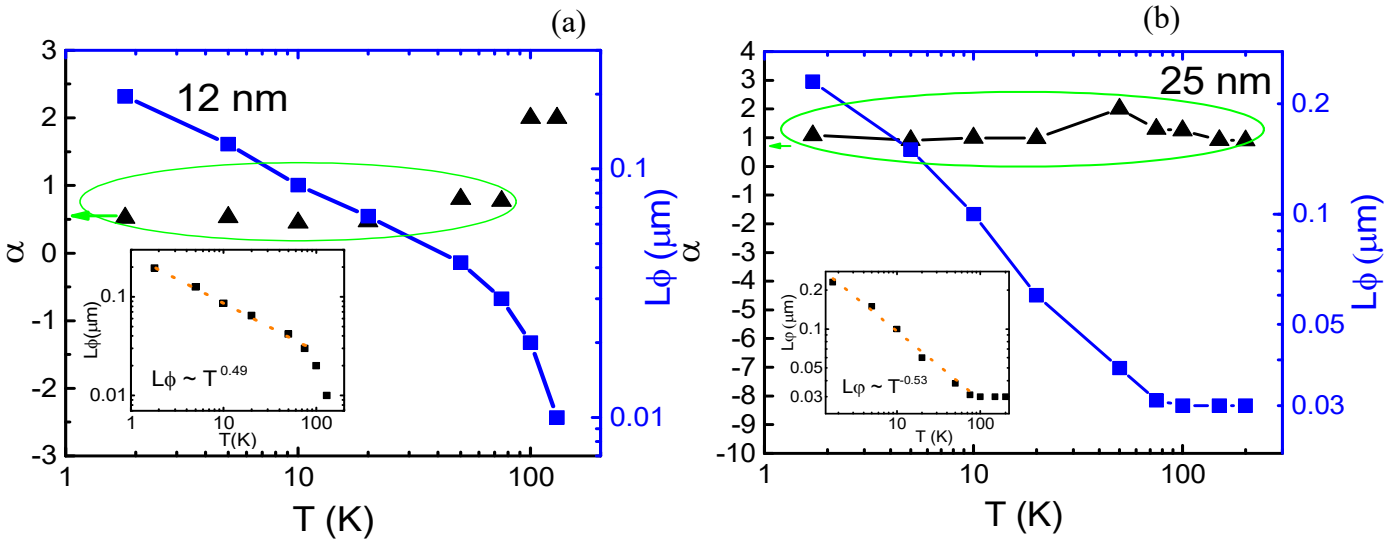

Figure 5.30 Plot of the fitted parameters L_φ (squares) and α (triangles) as a function of temperature as obtained from the WAL fit in (a) 12 nm sample and (b) 25 nm sample. The inset shows the power law fit of $L_\varphi \sim T^{-0.49}$ for the 12 nm sample and $T^{-0.53}$ for the 25 nm sample.

Figure 5.30 (a) and (b) shows the variation of α and L_φ as a function of temperature in both samples 12 nm and 25 nm respectively, extracted from the fit to the HLN equation. A value for the prefactor $\alpha \approx 0.5$ - 0.75 (black triangles marked inside the green circle) was obtained for the 12 nm sample, which remains largely unchanged from 1.5 K to around 80 K and then jumps to $\alpha \approx 2$ for 100 K and 140 K. The result of 0.5 - 0.75 for α suggests a single conduction channel. The value of $\alpha = 0.5$ as before may suggest that the top surface is contributing significantly more to the WAL than the bottom surface. Another possible scenrio is the coupling of the top and bottom surface states through the bulk. This was also reported by Brahlek *et al.*[171] in their Bi_2Se_3 model for samples with thicknesses below 10 QL. The topological surface states on the top and bottom surfaces can communicate via hopping or tunneling through the thin bulk and remain strongly coupled, even if the bulk states are suppressed, thus behaving as one single channel as described in Figure 5.4. This seems the most likely scenario since the 12 nm sample is close to the critical thickness of 10 nm. It has been reported previously in literature using scanning tunneling microscopy, that the critical thickness in Sb_2Te_3 below which the surface states start to couple is 4 nm[189]. Above 100 K, $\alpha \approx 2$ which is consistent with many conducting channels, which suggests a combination of bulk and surface carriers. This agrees with R vs T in figure 2.7 (a) which shows a metallic surface state below ~ 120 K, above which an insulating behaviour is seen. In the case of the 25 nm sample, $\alpha \approx 1$ (black triangles inside the green circle) was obtained

at all temperatures up to 200 K, which suggests surface dominated transport exclusively takes place with two symmetric decoupled channels (top and bottom). This is also in agreement with Figure 2.7 (b) which shows a metallic response up to 200 K followed by an insulating behaviour with increasing temperature. An estimation of the phase coherence length L_φ from the HLN equation was carried out. As mentioned earlier, the sharpness of the WAL cusp determines the phase coherence length L_φ. This length characterizes phase coherent behavior of carriers before an inelastic scattering event, indicating the quality of the film. The obtained L_φ shows a strong temperature dependence for both samples (blue curves).

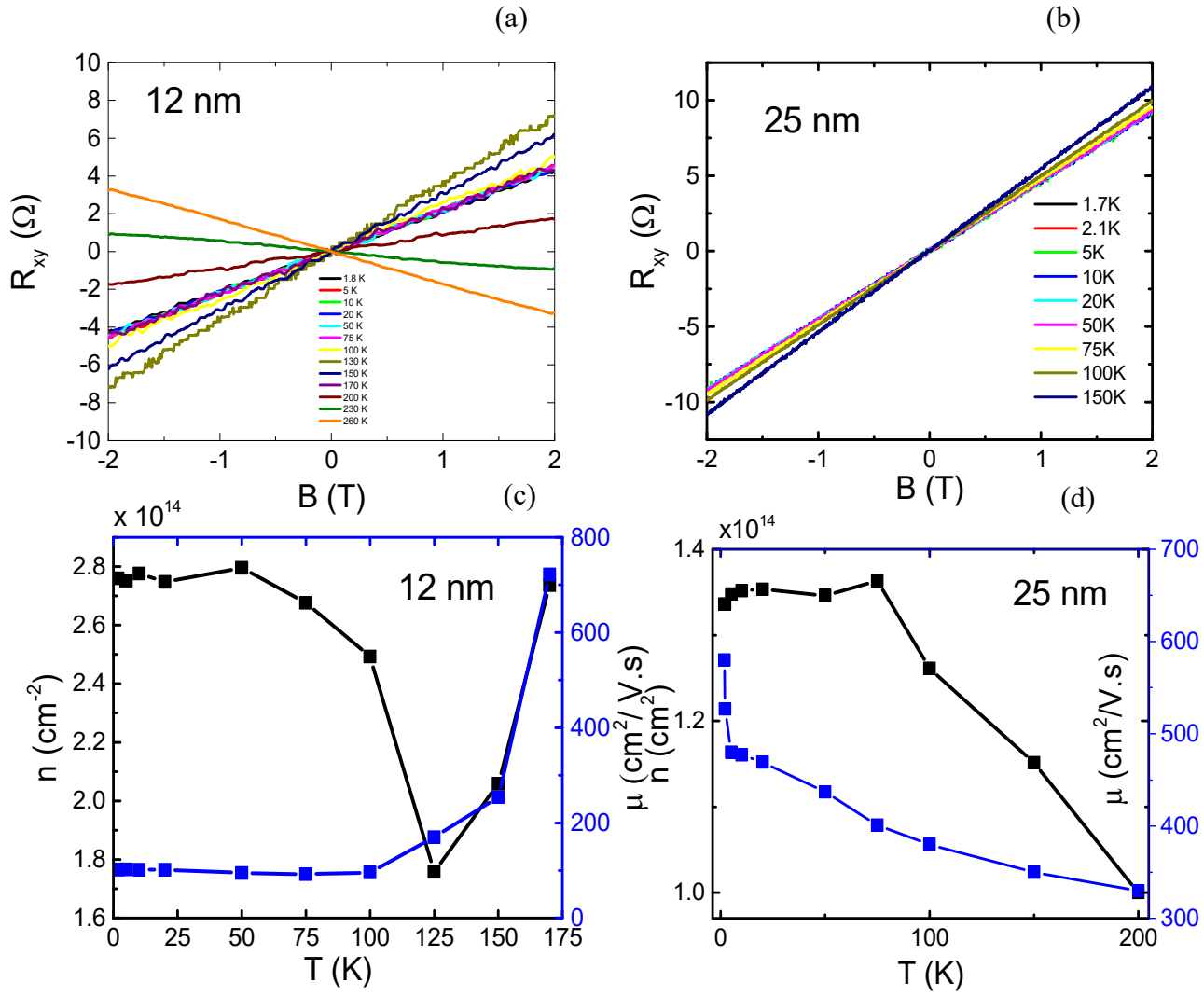

Figure 5.31 (a.b) R_{xy} vs B for the 12 nm sample and 25 nm sample. (c) The carrier densities n and (d) mobilities μ as a function of temperature for both samples.

For the 12 nm and 25 nm samples, the phase coherence length increases with decreasing temperature, with a value of 200 nm and 286 nm at 1.8 K, respectively, with no sign of saturation in both cases. A power law fit to the phase coherence length at low temperatures shows $L_\varphi \sim T^{-0.49}$ and $T^{-0.53}$ dependence for the 12 nm and 25 nm sample respectively. In general, a power law dependence of $T^{-0.50}$ represents a two-dimensional (2D) system, while $T^{-0.75}$ represents a three-dimensional (3D) system[187]. Hence, the observed temperature dependence of L_φ in both samples suggests that the WAL at low temperatures (<40 K) originate from a 2D surface state.

Here it is assumed the dephasing length L_φ for the top and bottom surfaces are identical leading to the correct fitting in the WAL formula. Figure 5.31 shows the Hall resistance R_{xy} vs T for both samples. It is expected that Sb vacancies and Sb_{Te} anti-site defects in the Sb_2Te_3 lattice generate free carriers, hence increasing the p-type conduction, Therefore all Sb_2Te_3 samples are expected to be p-type[190]. By making a linear fit to the data the sample carrier densities n and mobilities μ were estimated using the semiclassical value of the Hall resistivity: $\rho_{xy} = B/ne$ and $\sigma_{xx} = ne\mu$.

A comparison of the Hall mobilities and carrier densities obtained from the two samples are shown in Figure 5.31 (c) and (d) respectively. The mobility trend for the 12 nm sample decreases with decreasing temperature down to 100 K after which is saturates until 1.8 K with a value close to 100 cm^2/Vs. This value is rather low, but consistent with the fact that the top and bottom surface states might be coupled with each other through the bulk, increasing the scattering effects. On the other hand, the 25 nm behaves quite the opposite. The mobility increases with decreasing temperature and then shows a sharp increase for 1.8 K with a value of 580 cm^2/Vs. This is consistent with the surface states being completely decoupled. The mobilities of the 25 nm sample are much higher than those for the 12 nm sample. Similar to Bi_2Se_3, Sb_2Te_3 samples also display very little change in the carrier densities with respect to temperature, confirmed by an insignificant change in the gradient in Figure 5.31 (a) and (b) over the temperature range 1.8 K – 100 K. The changes in the carrier densities above 170 K can be attributed to unfreezing of bulk carriers or conduction from the Si substrate. In summary, the differences in the two samples are is written below in table 5.2.

Table 5.2 summarizes the difference in the results from a 12 nm and 25 nm thin film of Sb_2Te_3.

12 nm Sb_2Te_3	**25 nm Sb_2Te_3**
Resistance *R* vs. Temperature *T* plot shows an increase in *R* with decrease in *T* up to 120 K after which it goes down, up to 1.8 K. This may be explained by a freezing of bulk carriers and leading to purely surface conduction.	Resistance *R* vs. Temperature *T* plot shows an increase in *R* from RT up to 220 K after which it decreases with decreasing *T* up to 1.8 K, consistence with a metallic behaviour. This may show predominant surface conduction from a much higher temperature.
MR at 1.8 K in low field regions show WAL while *MR* at high fields show an unsaturated B^2 dependence.	*MR* at 1.8 K at low fields also shows WAL while high field results display an unsaturated B^2 dependence.
WAL cusps flatten out at 50 K with an α value of 0.5 consistent with one conducting channel which may be the top surface state or a coupled state (2 surface states + bulk state).	WAL cusps give an α value of 1 up to 150 K consistent with a two decoupled surface states.
L_φ = 200 nm at 1.8 K follows a power law temperature dependence as: $L_\varphi = T^{-0.49}$ close to the expected value of $T^{-0.50}$ for 2D conduction.	L_φ = 286 nm at 1.8 K follows a power law temperature dependence as: $L_\varphi = T^{-0.53}$ close to the expected value of $T^{-0.50}$ for 2D conduction.
The carrier densities are overall higher than the 25 nm sample, consistent with a coupled surface state, while the trend saturates below 50 K.	The carrier densities are lower overall compared to the 12 nm sample, while the trend also saturates below 100 K.
Overall lower mobilities compared to the 25 nm sample. The trend flattens out below 100 K.	The mobilities are higher compared to the 12 nm sample, the trend is the opposite, showing an increase in mobility with decreasing temperature up to 1.8 K.

5.7 Conclusion

In conclusion, a photo lithography mask was designed and Hall bars were successfully fabricated using a wet chemical etch process as well as an Ar^+ milling procedure on MBE grown Bi_2Se_3 with a thickness of 22 nm. XRD revealed a high quality epitaxial (00l) growth. Electrical transport measurements were successfully carried out on various Hall bars comparing results from the two etching processes. Both samples displayed WAL at low magnetic fields ($\pm$1T) which reflected both the Dirac nature of the surface states as well as the strong spin−orbit interaction in this material system. The chemically etched sample showed a degree of non-linearity at high fields consistent with more bulk behaviour compared to the Ar^+ milled sample showing a more surface-type response. The temperature dependent phase coherence length for both samples were also consistent with the fact that the chemically etched sample showed a more bulk response compared to the Ar^+ milled sample. The number of surface state modes in both samples showed one conducting channel which may be the top surface state only. The carrier densities were lower for the chemically etched sample with their mobilities double as compared to the Ar^+ milled sample.

A thickness dependent study was also carried out on MBE grown Sb_2Te_3 with thicknesses 12 and 25 nm. Both samples exhibit WAL at low magnetic fields ($\pm$1T) while their resistances display an unsaturated B^2 dependence at high fields. The 12 nm sample displays a single conducting channel attributed to a coupled surface and bulk state while the 25 nm sample shows two conducting channels attributed to decoupled surface states. The phase coherence length in both samples are consistent with 2D conduction. The carrier densities are overall higher for the 12 nm sample compared to the 25 nm sample, consistent with a coupled surface state while overall the mobilities are lower for the 12 nm sample compared to the 25 nm sample. The studies have helped understand TI material's electrical properties in great detail.

6. Chapter 6

Device Processing and Electrical Transport in Cd_3As_2 Nanowires

6.1 Introduction and Motivation

Three-dimensional (3D) Dirac semimetals[191] (DS) are quantum materials in which the conduction and valence bands touch each other at distinct points known as Dirac points (DP). Like in TIs where the linear dispersion along the directions near the DP is protected by time reversal symmetry, in DSs, the linear dispersion in three directions near the DP is protected by rotational crystalline symmetry[192,193]. In DSs, if the symmetry breaks the DP may split into a pair or nodes known as Weyl nodes and a DS changes to a Weyl semimetal[194]. The unique band structure of DSs can also give rise to many other topological phases like TIs[195] and topological superconductors[196]. In the family of 3D DSs, bulk Cd_3As_2 is a model DS material which has a pair of Dirac points near the Γ point in the Brillouin zone[193]. This has been confirmed by ARPES where a linear dispersion near the Dirac points was observed[197,198]. Cd_3As_2 also demonstrates an ultrahigh carrier mobility probed using transport measurements[199–203] while a very large linear positive *MR* has also been observed in its bulk form[204]. To make things more advantageous for devices, its Fermi surface is also very close to the Dirac points[205]. Considering all the properties in Cd_3As_2, it is highly desirable to investigate and conduct electrical transport measurements and push the material towards device applications.

6.2 Literature Review

Although many transport studies on Cd_3As_2 have been carried out in the bulk[199,201,203–205] and thin film form[200], not many researchers have concentrated on nanostructures such as wires[202]. Lie *et al*.[200] grew Cd_3As_2 single crystal thin films in an MBE system and made Hall bars with an electrolyte gel used as a gate for the first time. They performed magneto-transport measurements up to 9 T while also performing theoretical band structure calculations.

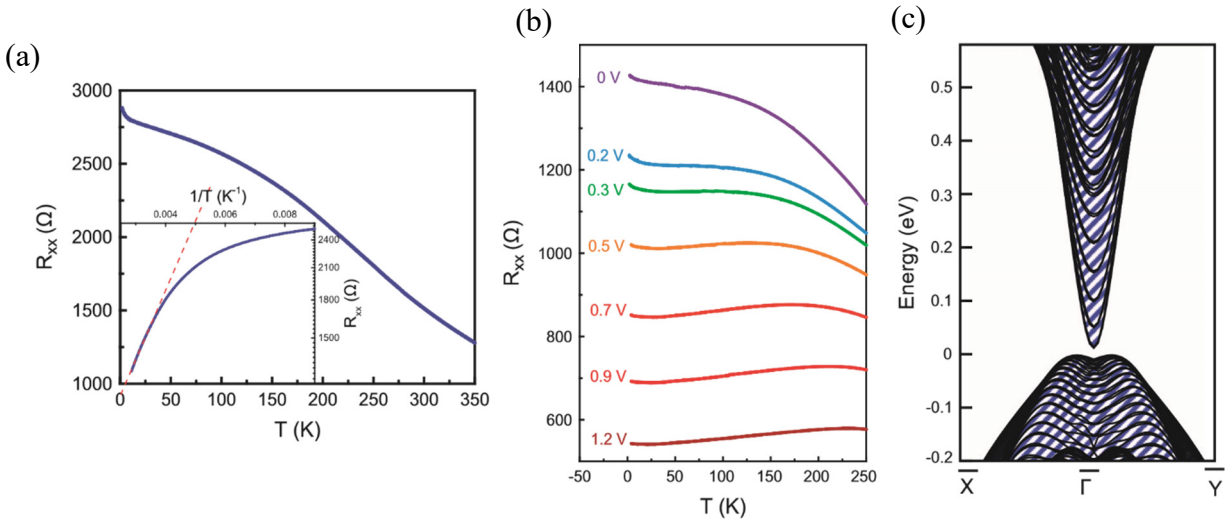

Figure 6.1 Electrical transport in a 50 nm thin film of Cd_3As_2. (a) Temperature vs. resistance measurement showing an increase in resistance as the sample is cooled. Inset: the Arrhenius plot of R_{xx}. (b) A temperature dependent R_{xx} with different positive gate voltages V_G showing a gate-induced metallic behaviour. (c) The electronic band structure of the Cd_3As_2 thin film.[200] Figure reproduced from ref. 200 without permission.

Figure 6.1 (a,b) shows a temperature and gate dependent longitudinal resistance measurement from them. The result displayed a semiconductor like behaviour which changes to a metallic like behaviour as the gate bias was increased from 0 V to positive 1.2 V [Figure 6.1 (b)] consistent with the fact that the Fermi level moves into the conduction band. They also extracted the activation energy (E_a) by fitting the high temperature on the Arrhenius plot which was ~ 12.45 meV [inset of Figure 6.1(a)]. Their theoretical band structure model suggested that the bulk Dirac cone was fully opened, with a sizable gap of 20 meV displayed in Figure 6.1 (c). They then performed a detail study of quantum oscillations to probe the Fermi surface of the band structure. On applying a positive gate bias V_G, they were able to resolve the Fermi level into the conduction band which led to an increase of electron conduction where a relatively high mobility was observed. Figure 6.2(a) shows their gate-dependence Shubnikov-de Hass oscillations (SdH) at 4 K. They calculated the oscillation frequency B_F at different gate voltages and found that B_F changed from 18.1 to 42.5 T as V_G changed from 0 to 1.2V by taking the Fourier transform of Figure 6.2 (b) . This translated to a change in the Fermi surface area A_F from 1.72×10^{-3} to 4.05×10^{-3} Å^{-2}. The enlargement of the Fermi surface suggested that the Fermi level moved deeper into the conduction band as V_G became larger. From this they extracted the Fermi wave vector K_F, the results of which are summarized in the table 6.1. They also plotted a Landau fan diagram

and found the intercept of the plot close to 0.5 proving that the material had a non-trivial behaviour as shown in Figure 6.2 (c). The SdH amplitude as a function of temperature were further analyzed to obtain more important parameters of the carrier transport such as the cyclotron mass m_{cyc} , the Fermi energy E_F, and from the Dingle plot shown in Figure 6.2 (d), the transport lifetime and then the mobility μ_{SdH} were obtained. All these parameters are summarized in table 6.1. In summary, they used an electrolyte ion gel to demonstrate for the first time a gate-tunable working of a Cd_3As_2 transistor device.

Table 6.1 Estimated parameters from the SdH oscillations at T= 4 K

V_G (V)	B_F (T)	K_F (Å)	m_{cyc}(m_e)	v_F (10^5 ms^{-1})	E_F (meV)	t (10^{-13} s)	L (nm)	μ_{SdH} (cm^2 V^{-1} s^{-1})
0	18.1	0.0234	0.0292	9.3	143	1.25	116	7537
0.2	20.6	0.0252	0.0311	9.4	155	1.51	141	8524
0.3	21.2	0.0254	0.0317	9.3	157	1.49	138	8241
0.5	24.9	0.0275	0.0321	9.9	180	1.26	125	6910
0.7	27.7	0.0290	0.0343	9.8	187	0.86	84	4416
0.9	32.9	0.0316	0.0358	1.0	213	0.75	76	3664
1.2	42.5	0.0359	0.0387	1.1	254	0.60	65	2736

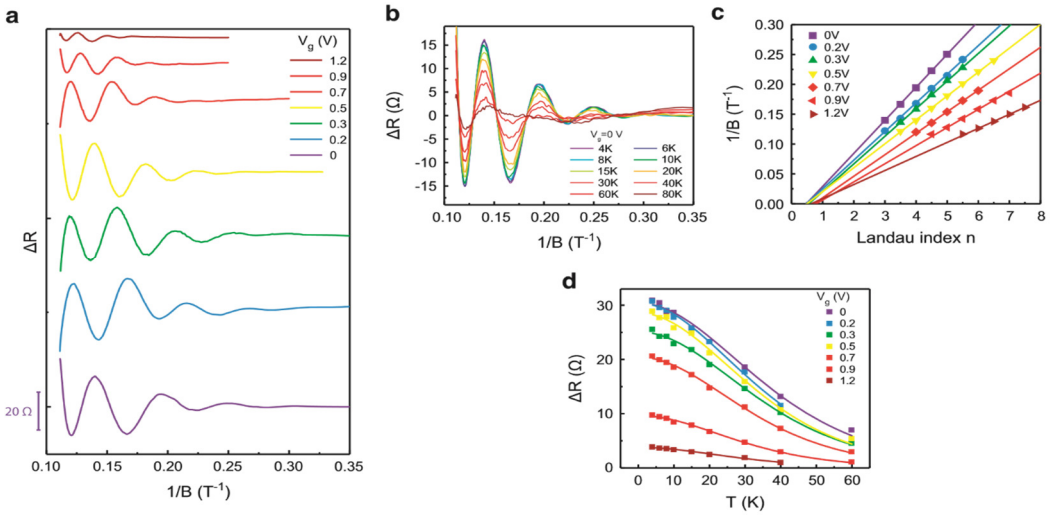

Figure 6.2 SdH oscillations of Cd_3As_2 thin films. (a) Gate-dependent SdH oscillations at 4 K. The amplitude decreased as the gate voltage increased. (b) Temperature-dependent SdH oscillations at 0 V. (c) Landau level index n with respect to 1/*B* under different gate voltages. The intercepts are close to 0.5 (d) Temperature-dependent amplitude of SdH oscillations under different gate voltages. With the best fit, the effective mass was obtained.[200] Figure reproduced from ref. 200 without permission.

6.3 Preparation of Cd_3As_2 Nanowire Devices

Cd_3As_2 nanowires were grown at the University of Oxford by Dr. Piet Schönherr who used chemical vapor deposition prepared on Si substrates. Briefly speaking, these wires were grown in a self-catalyst process from surfaces of Cd_2As_3 clusters, where a tip-induced vapour-solid growth mechanism was employed. The growth of the wires was controlled by the carrier gas flow where a high gas flow led to the formation of microwires. More details of the growth can be found in Dr Schönherr's PhD thesis[206]. The samples looked like a cluster of tiny hairs under an optical microscope. A special microtool was first used to transfer a few wires onto a new Si substrate as shown in Figure 6.3. This procedure required very stable hands and a lot of practice. A failed transfer attempt is also shown in the Figure 6.3 in green. Thousands of wires can be seen displaced on the substrate.

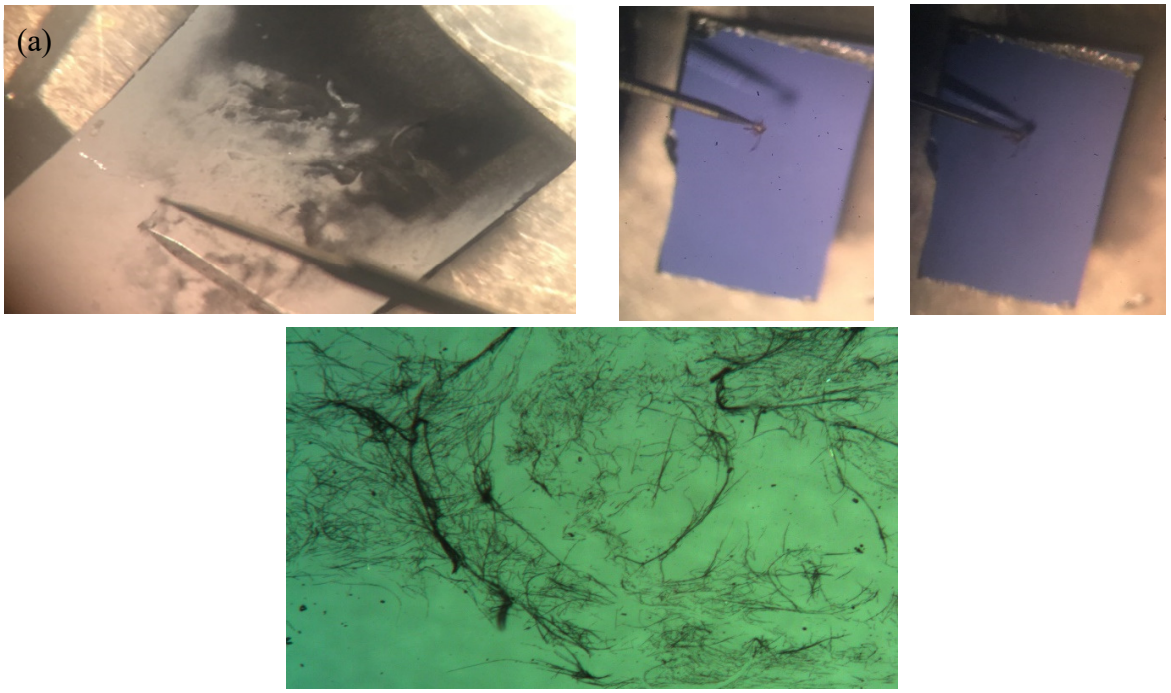

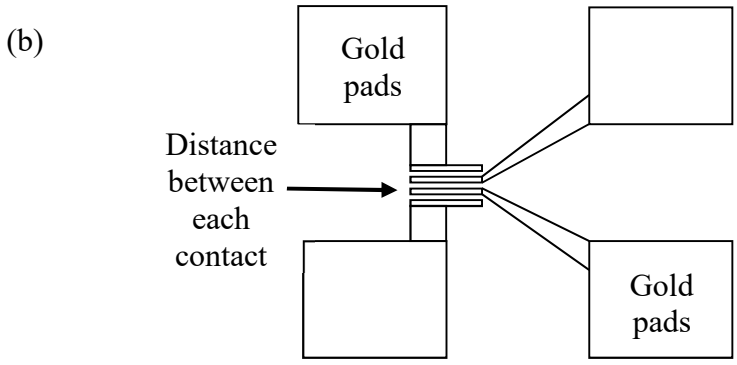

Figure 6.3 (a) Isolation of Cd_3As_2 nanowires from a cluster using a microtool. (b) A photolithography mask design showing contact pads 5μm apart.

The aim was to pick up as few wires as possible and displace them back onto another substrate using the microtool. This would help identifying a wire under test and would make patterning easier at a later stage. Once a wire was placed onto a new substrate, a few scanning electron microscope (SEM) images were taken with the help of Dr Jon J. Rickard as shown in Figure 6.4 (a-c). A cluster of wires of various sizes can be seen in Figure 6.4 (a) while an isolated wire of dimensions 5 microns × 120 nm can be seen in Figure 6.4 (b). A high resolution image showing another wire 300 nm wide is shown in Figure 6.4 (c) while Figure 6.5 (d) shows a tilted SEM image of the same wire displaying charging effects.

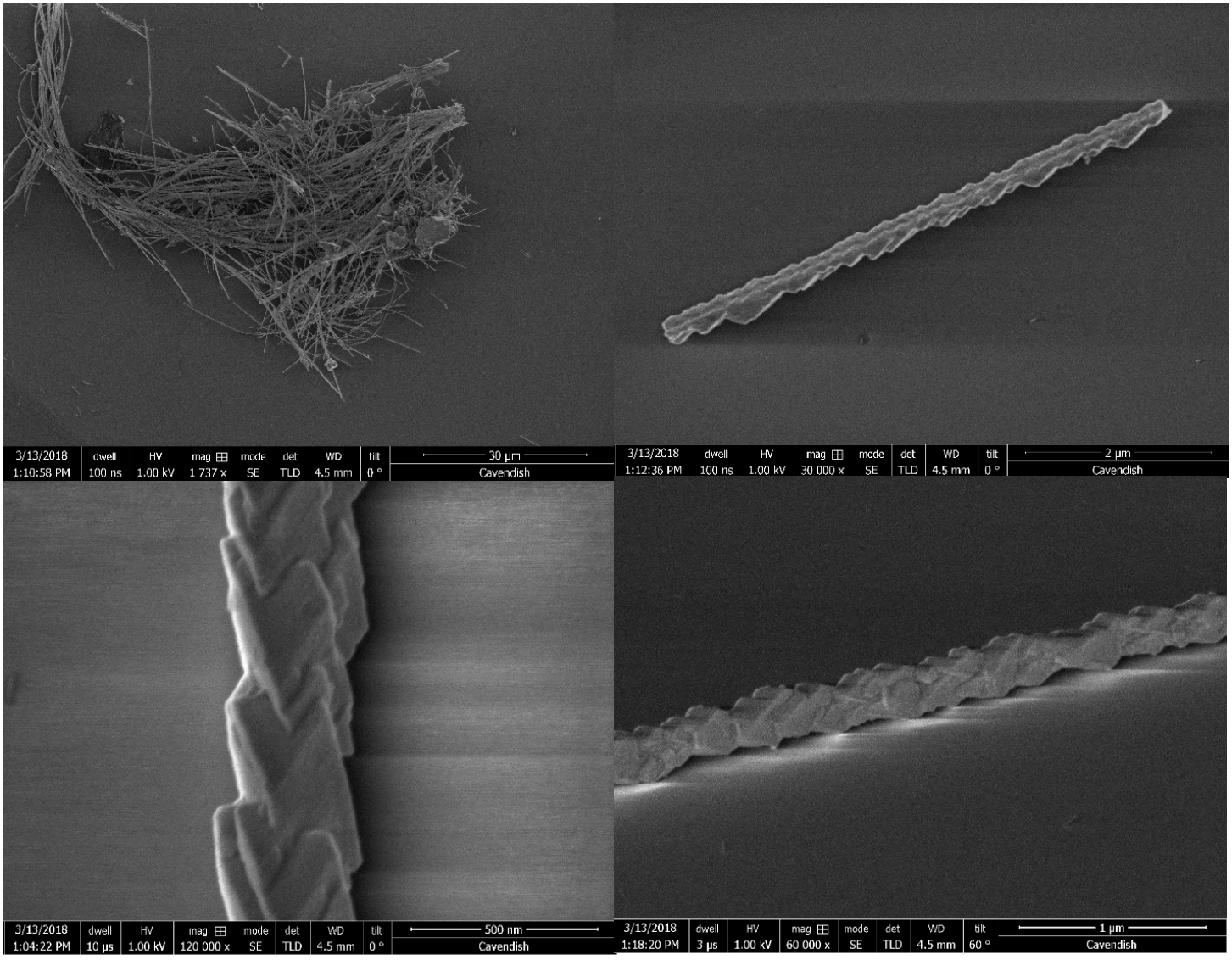

Figure 6.4 Scanning electron microscope images of (a) a cluster, (b) an isolated nanowire of dimensions 5.2 µm × 120 nm. (c) A magnified image of another wire with a width of 60 nms. (d) A tilted SEM image of a wire.

Clean room device processing consisting of photolithography and metallization was performed to make devices. The photomask used is shown in Figure 6.3 (b) designed by Dr Stuart Holmes from Toshiba. Four contact pads were present which were connected onto four rods 5 µm apart from each other. The idea was to place a wire in the middle of the rods and then pass a current/voltage through the contact pads. A lot of devices were successfully fabricated, bonded to chip carriers and then measured in a cryostat. The results shown in this chapter are from one of the successful devices fabricated. A similar procedure was followed for device fabrication as performed earlier in chapter 5 apart from using a different mask. Figure 6.5 shows pictures of a few devices successfully fabricated.

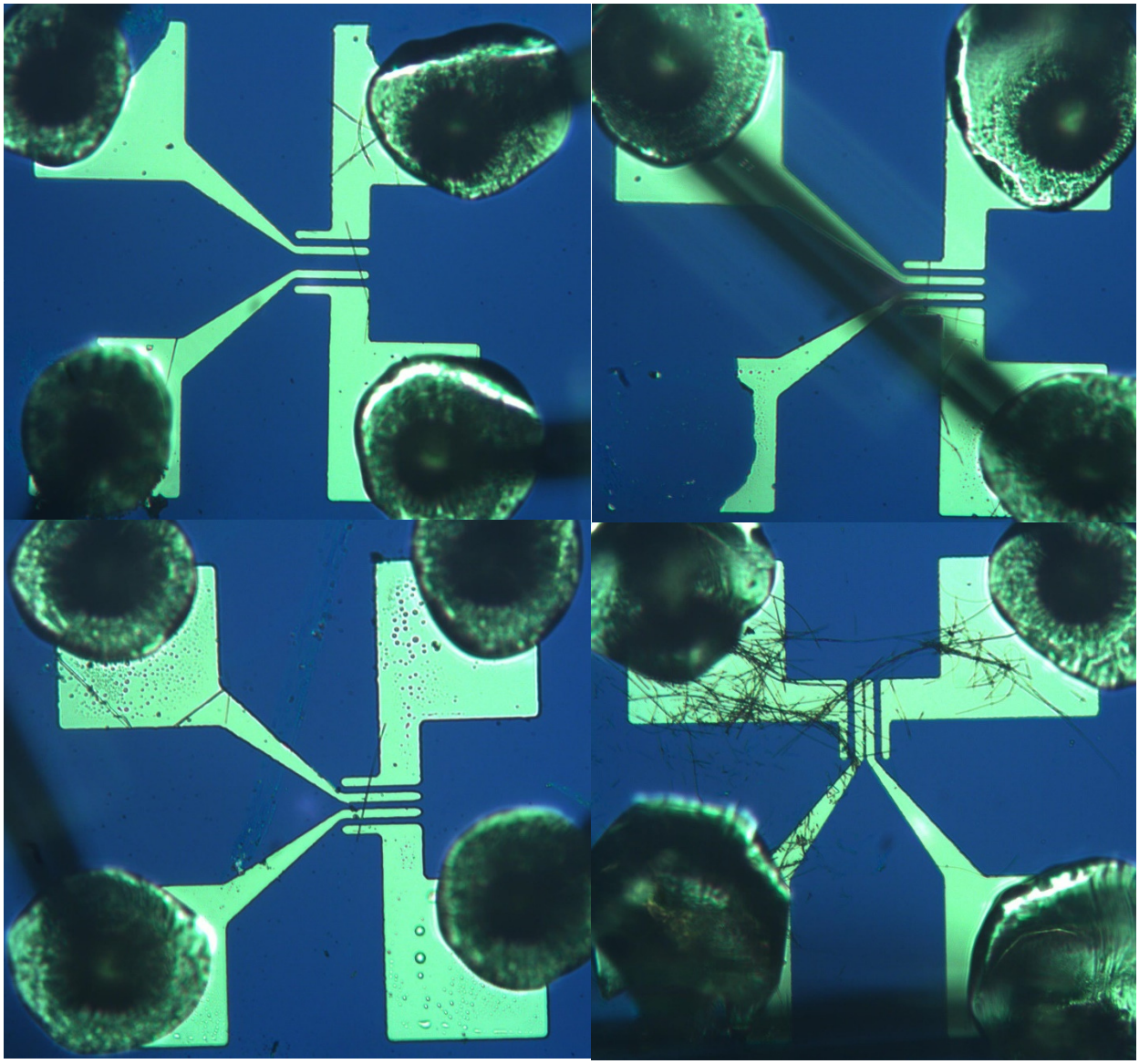

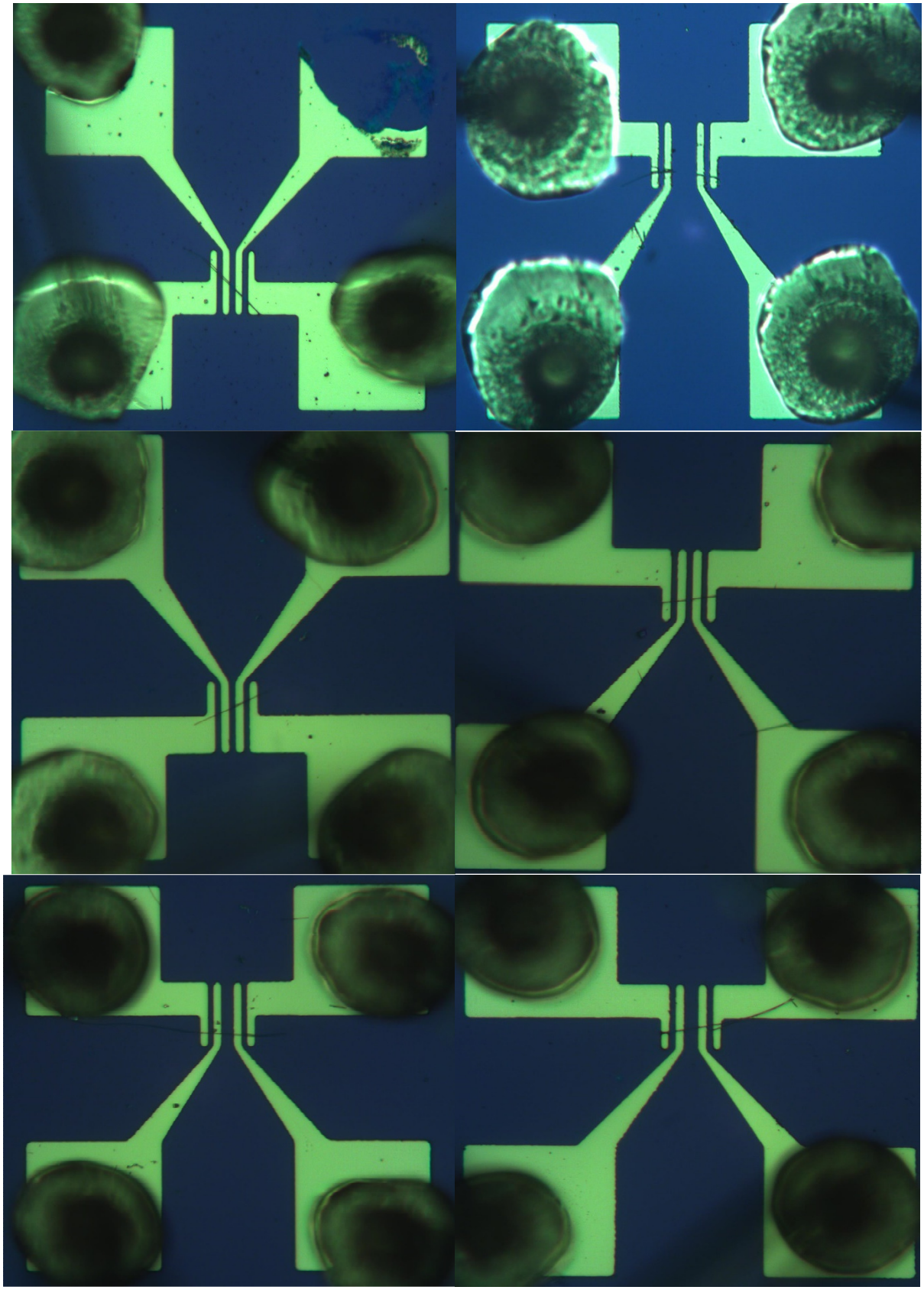

Figure 6.5 four point probe devices of Cd_3As_2 nanowires in between contact rods 5μm apart.

6.4 Electrical Transport on Cd_3As_2 Nanowires

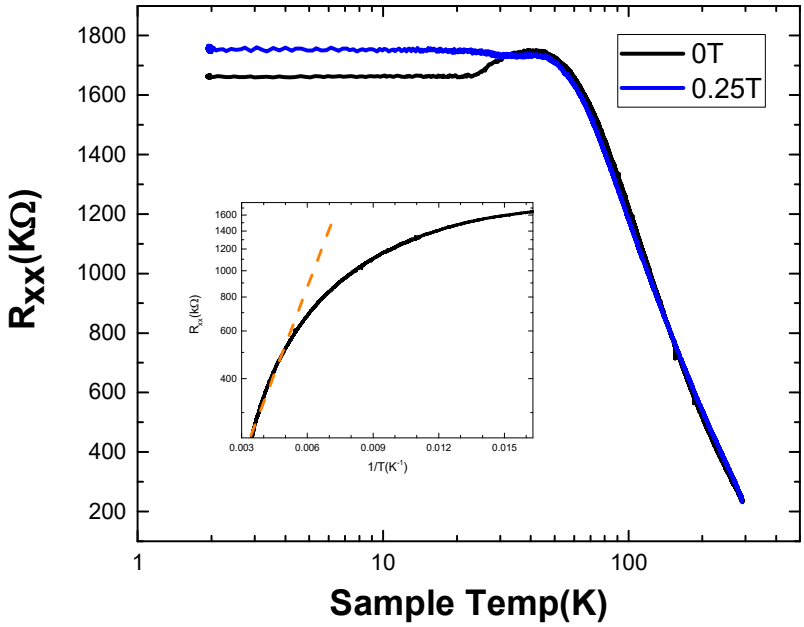

Figure 6.6 Resistance R_{xx} vs Temperature T for Cd_3As_2 at 0T and 0.25T field.

A chip carrier with a device was placed inside a cryostat and cooled to 1.8 K. DC measurements were conducted on sample with a constant current of 100 nA passing through the wire's four contacts while measuring the voltage drop across the pads.

Figure 6.6 shows the resistance of the device with respect to temperature with zero field cooling $B = 0$T and field cooling $B = 0.25$ T. Both curves show a semiconductor like behavior as the temperature is reduced (resistance increasing with decreasing temperature). The zero field cooled curved shows a metallic response close to ~ 40 K which then flattens out below 20 K while the field cooling results do not show any signs of a metallic behavior. In an ideal semimetal system, for example bulk crystals of Cd_3As_2, a metallic behavior is expected from room temperature to low temperatures. A semiconductor like response in Figure 6.6 suggests that the bulk band gap is open which is due to quantum confinement, as the measurement was performed on a nanowire. The activation energy was acquired by fitting the high-temperature resistance to the equation $R_{xx} \propto \exp(E_a/K_BT)$, where E_a is the activation energy and K_B is the Boltzmann constant (inset of figure 6.6). E_a was extracted to be ≈ 20 meV.

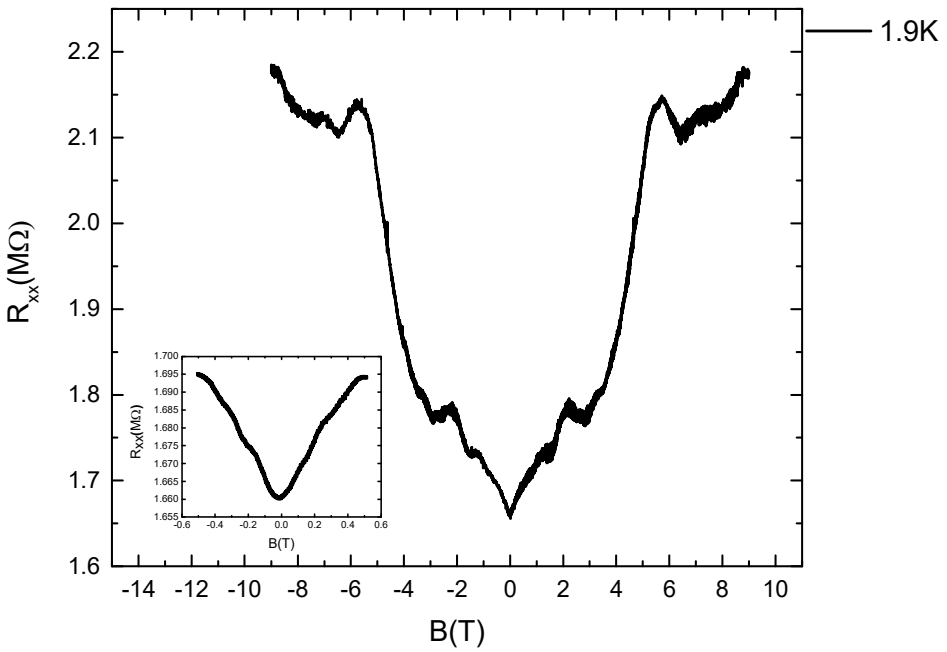

Figure 6.7 R_{xx} vs. B at 1.9 K, showing quantum oscillations. The inset shows a zoom in on the weak-antilocalization behaviour at 0T confirming strong spin orbit coupling.

Figure 6.7 displays the longitudinal resistance R_{xx} as a function of magnetic field B at 1.9 K. Quantum oscillations were clearly visible with a feature at zero field corresponding to weak WAL. WAL occurs in systems with strong spin orbit interaction and shows that Cd_3As_2 has topologically protected surface states. This is also consistent with the metallic response observed in the R_{xx} vs. T plot in Figure 6.6. To further understand the quantum oscillations, a temperature dependent magnetic field sweep was performed on R_{xx}. Pronounced SdH oscillations were observed up to 50 K after which they disappeared as shown in Figure 6.8. A linear background was then subtracted from these graphs and the plots of oscillation amplitude ΔR_{xx} versus $1/B$ from 1.9 K to 50 K were obtained as depicted in Figure 6.9. The oscillations became stronger with the increase of magnetic field and decrease of temperature. A landau fan diagram for 1.9 K was plotted by taking the maximum and minimum of the oscillations amplitude as the half integer and integer respectively as shown in Figure 6.10. Since not a lot of oscillations were observed, only four points could be extracted from Figure 6.9. According to the Lifshitz-Onsagar rule, it is also well known that in the SdH oscillations, the Landau level index n is related to the cross section area of the Fermi surface S_F by: $2\pi(n+\gamma) = S_F \frac{\hbar}{eB}$, where e is the electron charge, ħ is the Plank's constant divided by 2π, B is the magnetic flux density and γ represents the Berry phase. The intercept was fitted which passed through the origin corresponding to a trivial Berry phase with $\gamma = 0$.

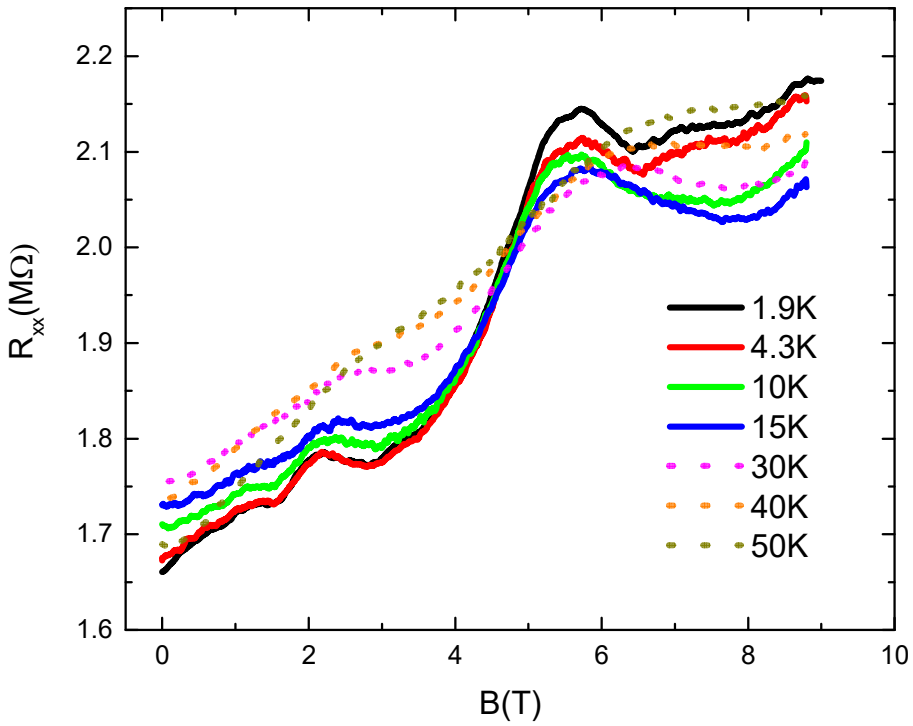

Figure 6.8 R_{xx} vs. B at various temperatures, showing quantum oscillations in a Cd_3As_2 microwire. Oscillations disappearing at 50 K.

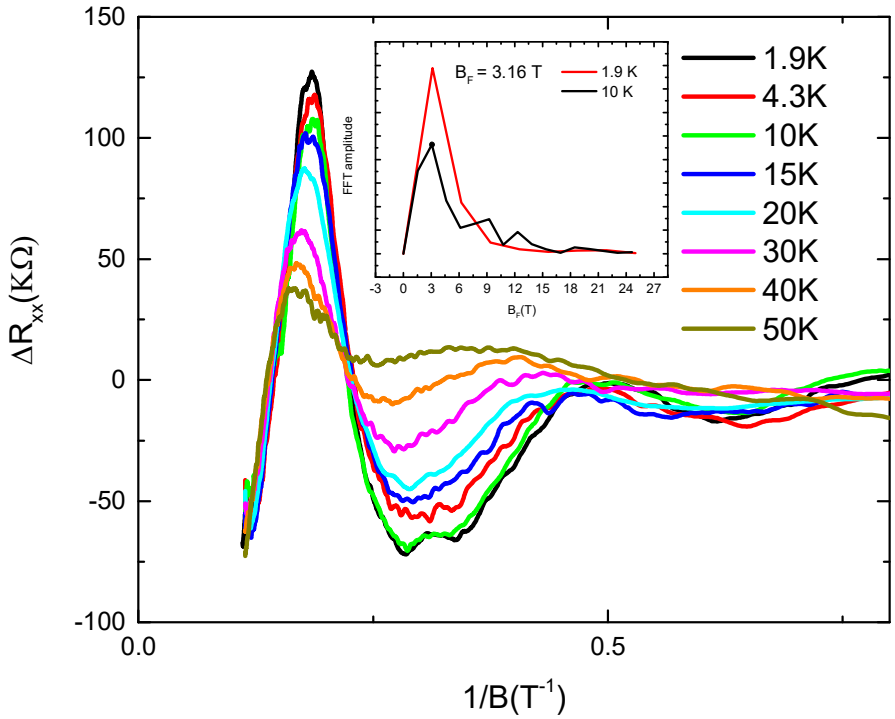

Figure 6.9 Temperature dependent SdH oscillation amplitude ΔR_{xx} as a function of $\frac{1}{B}$ after subtracting the background from figure 6.8 raw data. Inset shows the FFT of the oscillation with B_F = 3.16 T at 1.9 K and 10 K.

There may be some inaccuracy in the extrapolated intercept as there may be an error in the slope and in choosing the maxima and minima's. Therefore it is difficult to give an accurate value for the Berry phase. The observation of SdH oscillations is important to calculate the parameters of the carrier transport. To find the oscillation frequency B_F, a fast Fourier transform (FFT) was performed on the SdH oscillations giving a value of 3.16 T as shown in the inset of Figure 6.9. By using the equation $B_F = \left(\frac{\varphi_o}{2\pi^2}\right) S_F$, where $\varphi_o = \frac{h}{2e}$, the Fermi surface S_F = 0.33×10^{-3} Å^{-2} was acquired. Here, if we assume that the Fermi surface is circular *i.e.* a Dirac type band dispersion, the relations $S_F = \pi {K_F}^2$(K_F: Fermi wave vector) and $n_{2d} = \frac{{K_F}^2}{4\pi}$ (n_{2d}: two dimensional carrier density) can be used. Therefore K_F was estimated to be 0.0097 Å and n_{2d} = 8 x 10^{10} cm^{-2}.

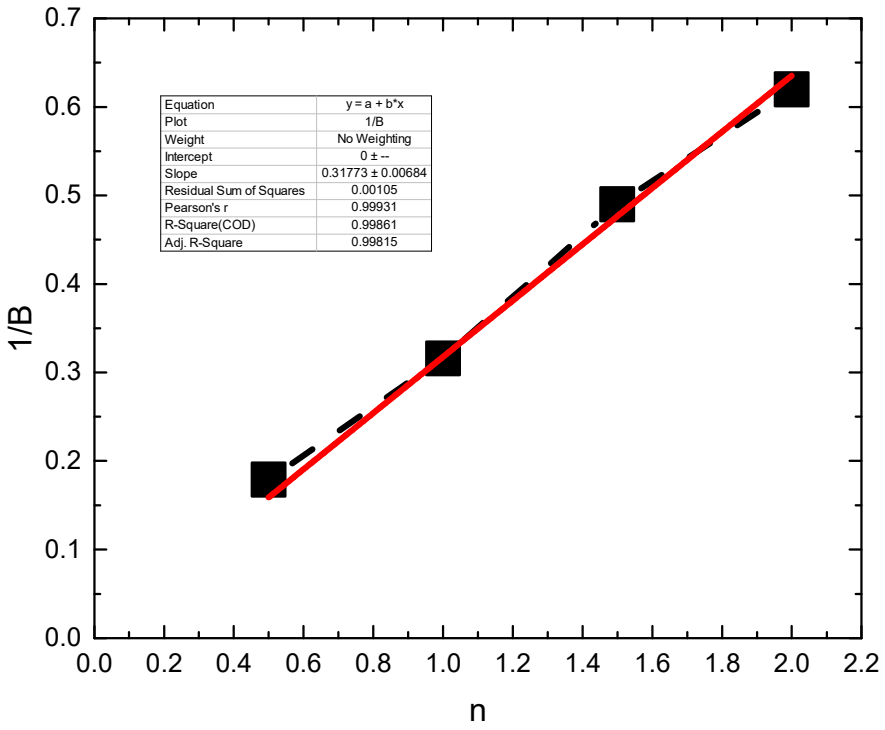

Figure 6.10 Landau fan diagram for the SdH oscillations. The slope of the line also gives the fundamental frequency B_F. (error bars in the figure are smaller than the size of the points)

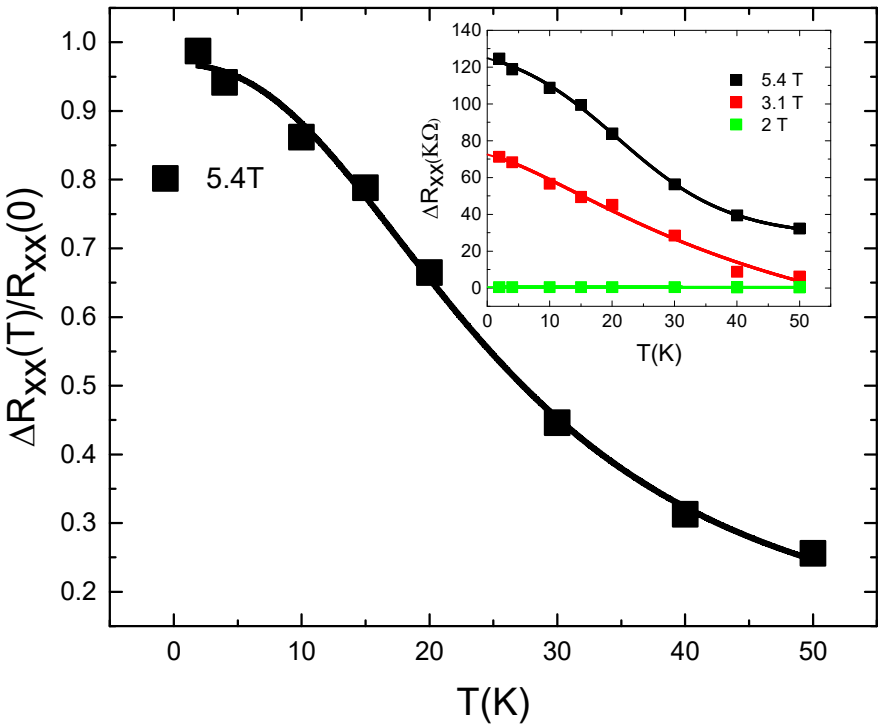

Figure 6.11 Normalized resistance amplitude ΔR_{xx} (T)/ ΔR_{xx} (0) vs. Temperature at 5.4 T. Inset shows ΔR_{xx} as a function of temperature at different fields from which the effective mass, m_{cyc} can be determined.

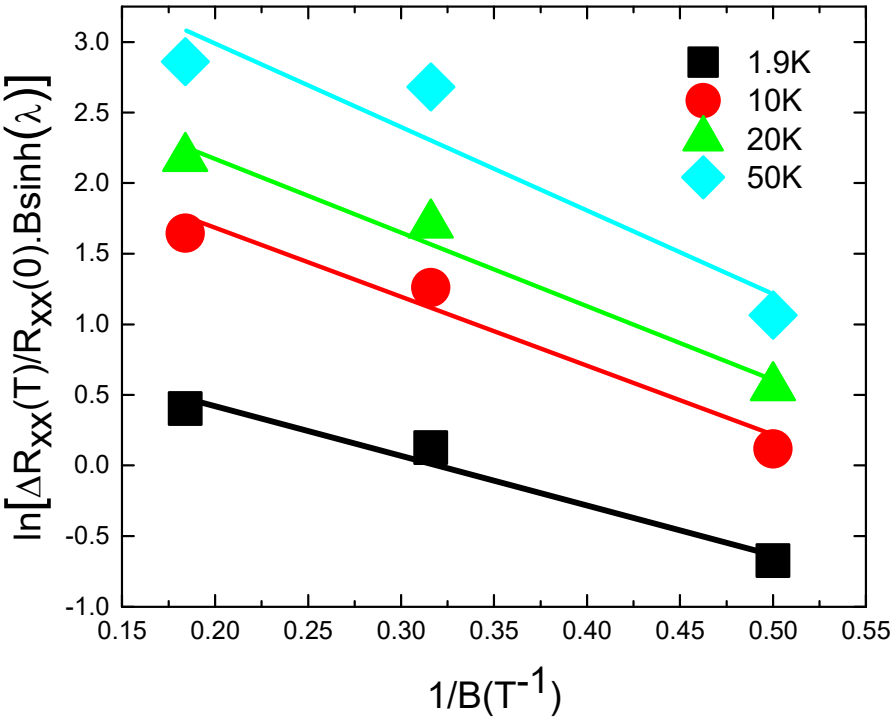

Figure 6.12 Dingle plot for the extraction of the quantum lifetime τ and mobility μ.

To analyze the characteristics of transport further, the cyclotron mass (m_{cyc}) was calculated. The temperature dependent SdH oscillations amplitude ΔR_{xx} was first extracted by following the Lifshitz-Kosevich (LK) theory[207] given by: $\frac{\Delta R_{xx}(T)}{R_{xx}(0)} = \lambda(T)/\sinh(\lambda(T)$, where the thermal factor is given by $\lambda(T) = 2\pi^2 K_B T m_{cyc}/\hbar eB$, K_B being the Boltzmann's constant, ħ is the reduced plank constant and $m_{cyc} = \frac{E_F}{{V_F}^2}$, is the effective cyclotron mass. As shown in Figure 6.11, the best fit gives the cyclotron mass $m_{cyc} = 0.053\ m_e$, where m_e is the free electron mass. The Fermi velocity $v_F = \frac{\hbar K_F}{m_{cyc}}$ and $E_F = m_{cyc}{v_F}^2$ can be calculated as 2.12 ms^{-1} and 13.5 meV.

Moreover, from the Dingle plot, the quantum lifetime τ time can be calculated from the Dingle factor e^{-D}, where $D = \frac{2\pi^2 E_F}{\tau e B {v_F}^2}$. Since $\Delta R_{xx}(\mathrm{T})/\ \Delta R_{xx}(0)$ is proportional to $\frac{e^{-D_{\lambda(\mathrm{T})}}}{\sinh(\lambda(\mathrm{T}))}$, the quantum lifetime τ can be found from the slope of the logarithmic plot of $\Delta R_{xx}(\mathrm{T})/\ \Delta R_{xx}(0).Bsinh(\lambda)$ versus $1/B$. By using the cyclotron mass, the quantum lifetime τ was estimated to be 1.73×10^{-12} s. Other important parameters such as mean free path $l = v_F\tau$ and the mobility μ_{SdH} were calculated and summarized in table 6.2 and 6.3.

Table 6.2 Calculated electrical parameters at 1.9 K.

Device	B_F (T)	S_F (10^{-3} Å^{-2})	K_F (Å^{-1})	V_F (10^5 ms^{-1})	E_F (meV)	l (nm)	$m_{cyc}(m_e)$	τ(10^{-12} s)
Cd_3As_2 microwire	3.16	0.33	0.0097	2.12	13.5	366	0.053	1.73

Table 6.3 Mobility for Cd_3As_2 calculated at different temperatures.

Other temperature mobility's

Temperature (K)	μ_{SdH} cm^{2}V^{-1}s^{-1}
1.9	56884
4	40129
10	36386
20	37897
50	33599

Even though Figure 6.4 shows that the wires are very rough (20 % of the diameter of the length scale of 300 nm) with steps of ⍰250 nms, the mobilities can still be very high as facets of good quality material could be coupled through these low quality steps. Furthermore, the B value at which the radius of the cyclotron motion was approximately equal to the radius of the nanowire ⍰125 nm was calculated. This value was rather small ≈ 0.5 T, which implies

that at fields greater than 0.5 T, no 1D confinement effect would be observed. This is much lower than the field at which the first oscillation was seen. To further probe the nature of SdH oscillations, the angular dependent magnetotransport measurements were performed by tilting the sample from θ = 0° to 90° where θ is the tilt angle between B and the sample surface as shown in the inset of Figure 6.13. For a two dimensional Fermi surface the peak positions of the oscillations only depend on the perpendicular component of B with $B_{\text{perpendicular}} = B\cos(\theta)$.

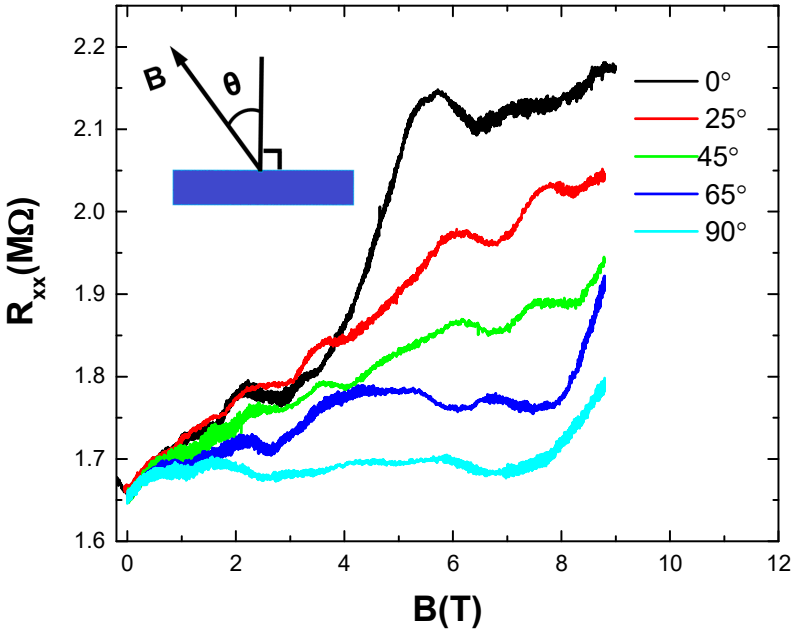

Figure 6.13 Angular-dependent oscillations up-to 9 T. R_{xx} as a function of B at different tilt angles shown in the inset.

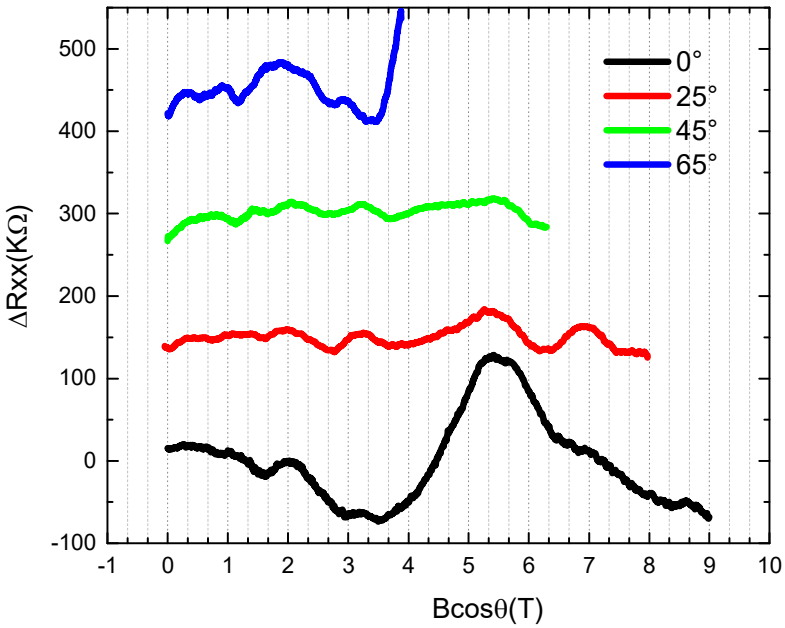

Figure 6.14 SdH oscillations amplitude ΔR_{xx} as a function of $B\cos(\theta)$ after removing the background. Each reading has an equally spaced offset for clarity.

Figure 6.13 shows the angular dependence of the longitudinal resistance R_{xx} with respect to the field B. A linear background was removed and each curve was shifted by an equal offset to produce Figure 6.14. Looking at Figure 6.14 it is clear that the oscillations follow $1/\cos(\theta)$ suggesting the SdH oscillations originate from a 2D Fermi surface.

6.5 Conclusion

In summary, Cd_3As_2 nanowires were processed into four point probe devices using photolithography and DC electrical measurements were carried out on them. The results display a semiconductor like behaviour with a clear metallic response at low temperatures consistent with a topological surface state. Weak antilocalization was observed which confirms strong spin orbit coupling in the material system. Clear SdH oscillations were visible at low temperatures from 1.8 K to 50 K. The analysis of the oscillations reveal various electrical transport parameters with a ultra-high mobility at 1.8 K corresponding to 56884 $cm^2V^{-1}s^{-1}$. The results shed light to understand the fundamental properties of nanowires which are very important to push the material system towards versatile and practical device applications.

7. Chapter 7

7.1 Future work

The work carried out during my PhD has formed a strong experimental grounding on developing new opportunities in condensed matter and device physics for practical applications with Dirac materials. This chapter covers in brief the details of the directions the field is moving towards for future applications.

Low power dissipation: Since topological materials are expected to possess very high mobilities these materials are ideal candidates for low power consumption electronics. Furthermore, the Dirac nature of surface electrons with forbidden backscattering properties due to strong spin momentum locking provides a pathway to run TI-based devices at low power. In addition, the insulating properties of the bulk may prevent leakage of electricity solving the heating problem.

Spintronics: The surface electrons in a TI has a spin-polarized structure where the spin is divided into two directions (up and down). This could increase the degree of freedom by making it possible to control the spin-polarization in two different directions.

Field-effect transistors: Voltage or current controlled semiconductor devices such as transistors hold the key to most micro-electronic devices. A schematic of a typical FET is displayed in Figure 7.1. In principle, the operation of an FET is based on the control of carrier density at the transport layer by capacitive coupling with external gate voltage. A typical device consists of a gate, source, drain electrodes, a semiconducting layer and an insulating layer. The source-drain electrodes are used for charge-injection, while the charge-transport occurs through the semiconductor upon applying a gate voltage. A thin dielectric layer separates the gate electrode from the active semiconductor, which is employed to induce charges at the semiconductor-dielectric interface under the effect of the applied gate bias. When a positive gate bias is applied at the gate electrode, a high electric field at the interface results in the bending of the band gap in the semiconductor. This energy level bending creates an accumulation of majority charge carriers at the interface, providing a highly conducting (on) state, called the accumulation mode. On the other hand, upon applying a negative gate bias, the majority carriers are pushed away from the interface due to opposite band bending, and carriers are depleted from the interface. This corresponds to low conduction and is called the depletion mode of operation.

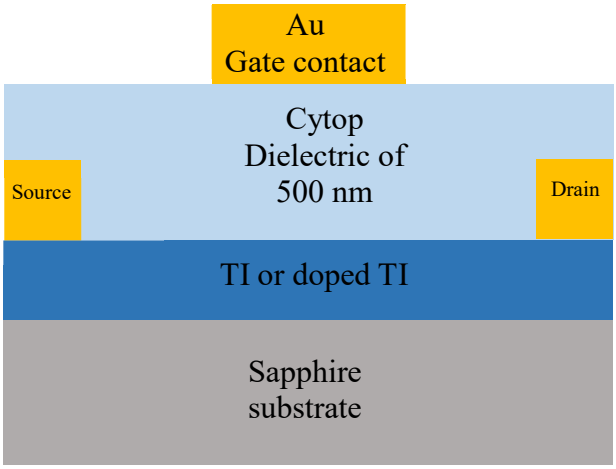

Figure 7.1 Schematic of a typical FET device made from a TI or a doped TI.

Based on the two regimes of an FET operation, the performance of an FET is mainly parameterized by the field-effect mobility (μ_{FET}) and on/off ratio.

Making a transistor from a TI material is advantageous due to the surface only metallic conduction, low leakage and low power dissipation properties. Utilizing a magnetically doped TI as an active material in a FET further provides an additional handle of magnetic control to the spin polarized channel. Considering these advantages, FET devices were fabricated as follows with the help from Dr Satya Senanayak in the optoelectronic group: Au Source-Drain electrodes were evaporated on the TI surfaces of Bi_2Te_3 and Mn-doped Bi_2Te_3. This was followed by the introduction of the cytop dielectric layer (~ 500 nm) by spin coating. The device was then completed with the deposition of an Au gate electrode. Temperature dependent I-V characteristics were performed using the S-D electrode to estimate the variation in resistance [Figure 7.2(a-d)]. The I-V characteristics displayed a linear trend and the R_{xx} values were obtained from the linear fit to the slope. In Bi_2Te_3, a clear metallic transition was observed at low temperature confirming the topological metallic surface states. However, at temperatures higher than 50 K a typical activated behavior consistent with the bulk insulator was observed. In comparison, the Mn-doped Bi_2Te_3 exhibited an insulating behaviour thorughout the complete temperature range indicating a possibility of a finite band gap originating from the Mn doping.

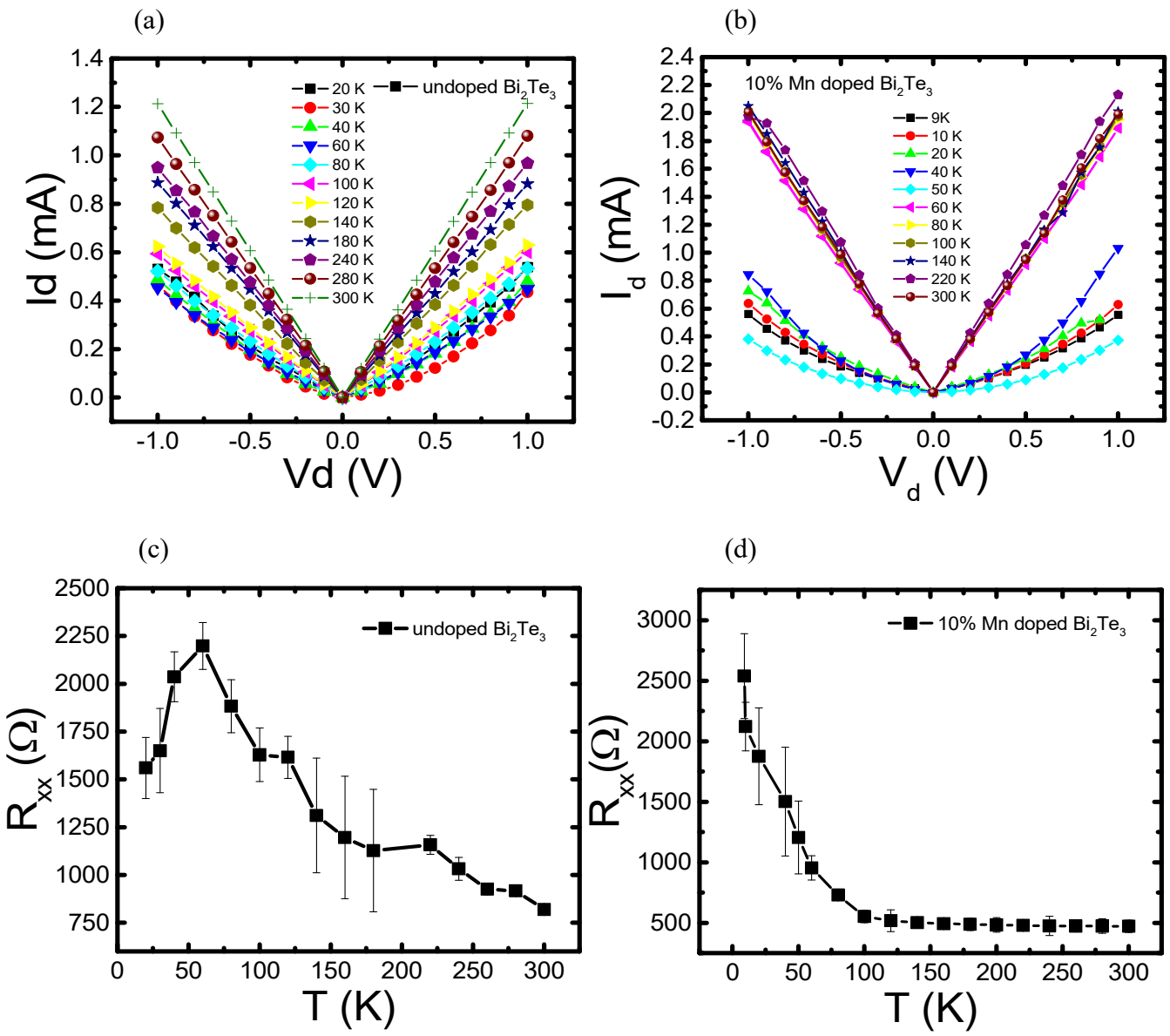

Figure 7.2 (a,b) Comparing the (a,b) I-V characteristics and (c,d) the resistance of an undoped Bi_2Te_3 thin film and a 10% doped Mn sample of Bi_2Te_3 both 60 nms of thickness.

As a next step, transfer characteristics were performed in FET devices over a temperature range of 10 K -300 K [Figure 7.3(a-d)]. A clean modulation of channel current was observed with the gate bias indicating a *n*-type transport characteristics in both Bi_2Te_3 and Mn doped Bi_2Te_3 [Figure 7.3(a and c)]. Since, FET characterizes the surface layers of the channel material, the existence of the metallic states at the TI surface results in a low on-off ratio ranging from 8 to 30. Mobility was estimated from the saturation characteristics using the expression: $I_{DS} = \frac{\mu_{FET} W C_0}{2L}\left(V_g - V_{TH}\right)^2$, where I_{DS} is the S-D current, μ_{FET} is the FET

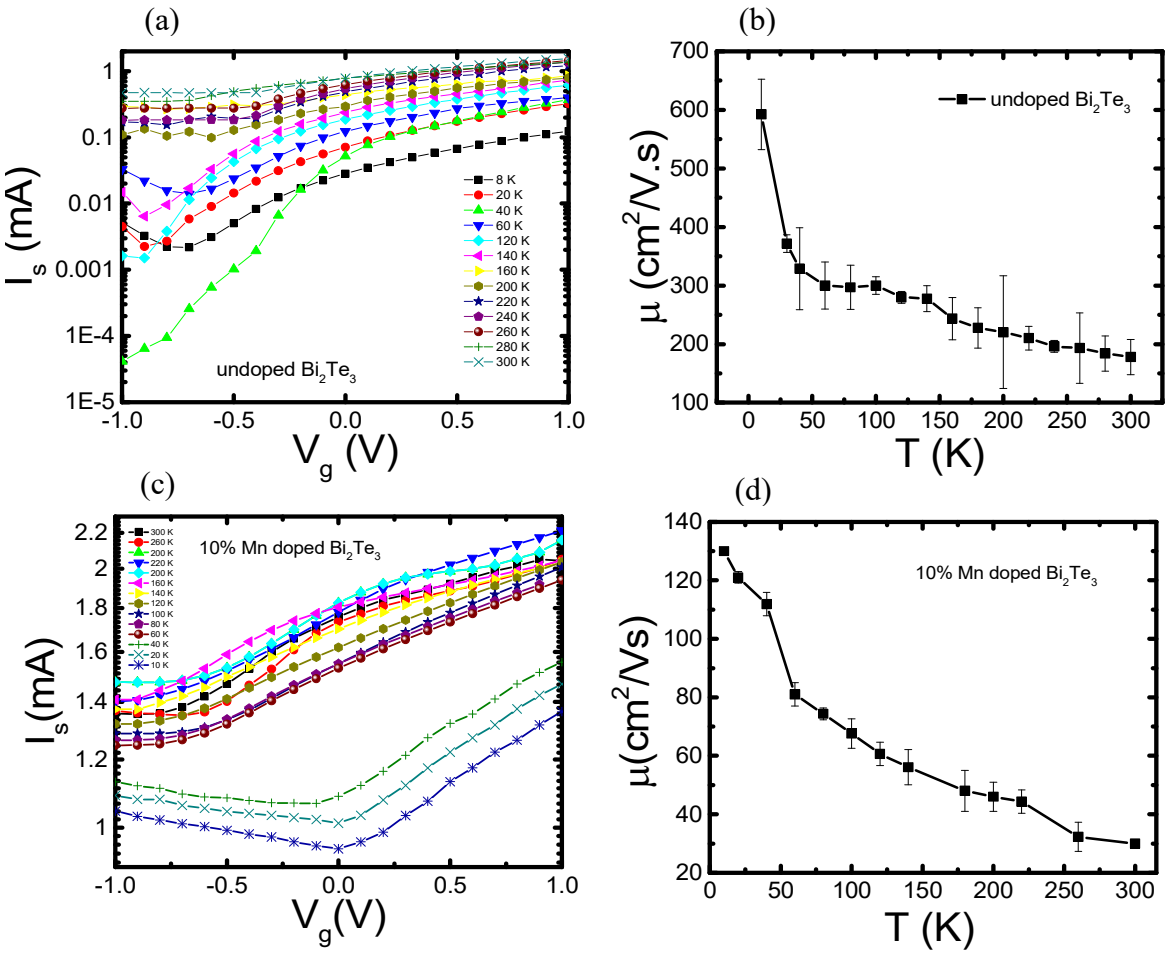

Figure 7.3 (a,c) The transfer characteristics in Bi_2Te_3 and Mn doped Bi_2Te_3 showing a variation in I_{sd} on sweeping the gate voltage V_g. (b,d) The change in the mobility as a function of temperature for Bi_2Te_3 and Mn doped Bi_2Te_3 respectively.

mobility, W is the width of the channel, C_0 is the capacitance per unit area of the dielectric layer, L is the channel length, V_g is the gate voltage and V_{TH} is the threshold voltage. The capacitance per unit area was estimated using a two terminal Au/Cytop/Au structure measured from an impedance analyzer. In the measurement a small sinusoidal AC voltage of 50 mV was applied to the capacitance structure while the frequency was swept from 100 Hz to 10 MHz. The capacitance per unit area magnitude was estimated from the capacitance value at 100 Hz. The typical trend of the μ_{FET} versus T for Bi_2Te_3 is shown in Figure 7.3(c,d). The μ_{FET} exhibits an increase in magnitude upon decreasing the temperature for both samples. For the Bi_2Te_3 sample, as the temperature decreased below 50 K a clear distinctive change in the slope was observed indicating a transition to a purely metallic state conduction. This behavior is consistent with the observed transition in the resistance for the two terminal device [Figure 7.2(c)]. In comparison, the Mn doped Bi_2Te_3 samples exhibited an activated

behavior throughout the complete temperature range [Figure 7.3(d)]. Thus indicating the absence of metallic surface states in Mn doped Bi_2Te_3 sample. From these preliminary studies it can be concluded that FETs can be used effectively to probe the surface states in these class of materials.

Magnetic devices: TIs have a non-zero spin density at the surface. If a TI is clubbed with a FM to form a heterojunction, the surface current may be used to control the FM layer thus can be used to study magnetic tunnel junctions by means of the tunneling magnetoresistance effect. The spin-orbit coupling state may enhance the spin-related tunneling effect. Also discussed in section 4.4 is another application for heterostructures. If a FM and AFM layer are combined to form a stack, many spin modes can be achieved which can be used to sense different states depending on the range of the applied external field hence suitable for an efficient sensor. Another possible advantage is magnetic doping of TIs as discussed in chapter 3 and 4. Doping in TIs has already lead to the discovery of the QAHE and magnetic monopole. Pushing these properties to room temperature is a step forward for electronic device applications. On this basis, a Co-doped sample was grown by Liam Duffy at Oxford using MBE consisting of V and Cr doped Sb_2Te_3. The motivation was as follows: Vanadium is known to have a much higher T_C , an order of magnitude larger coercivity and a much lower carrier density compared to Cr therefore realization of the QAHE maybe much easier in a material system with V in it[208]. Figure 7.4 (a) shows the temperature vs. resistance of the co-doped sample displaying a metallic response from room temperature down to 40 K after which an insulating behaviour confirming the opening of the bulk band gap due to magnetic doping. Figure 7.4 (b) displays the temperature dependent AHE showing a disappearance of the Hysteresis loop close to 90 K. Figure 7.4 (c) and (d) displays the temperature dependent *MR* effect. Interestingly a very clear transition from the WAL effect to the AMR effect was observed in this film from 60 K to 70 K. This was confirmed by a dip in the resistance at zero field above 70 K to a peak in the resistance below 60 K. Overall the addition of V into the Cr-doped Sb_2Te_3 matrix does not seem to have any significant advantages in terms of enhancment of the T_c or H_c while a clear transition from WAL to the AMR effect signifies the strength of the material system and the need to understand the basic fundamental concepts that govern magnetically doped Dirac materials.

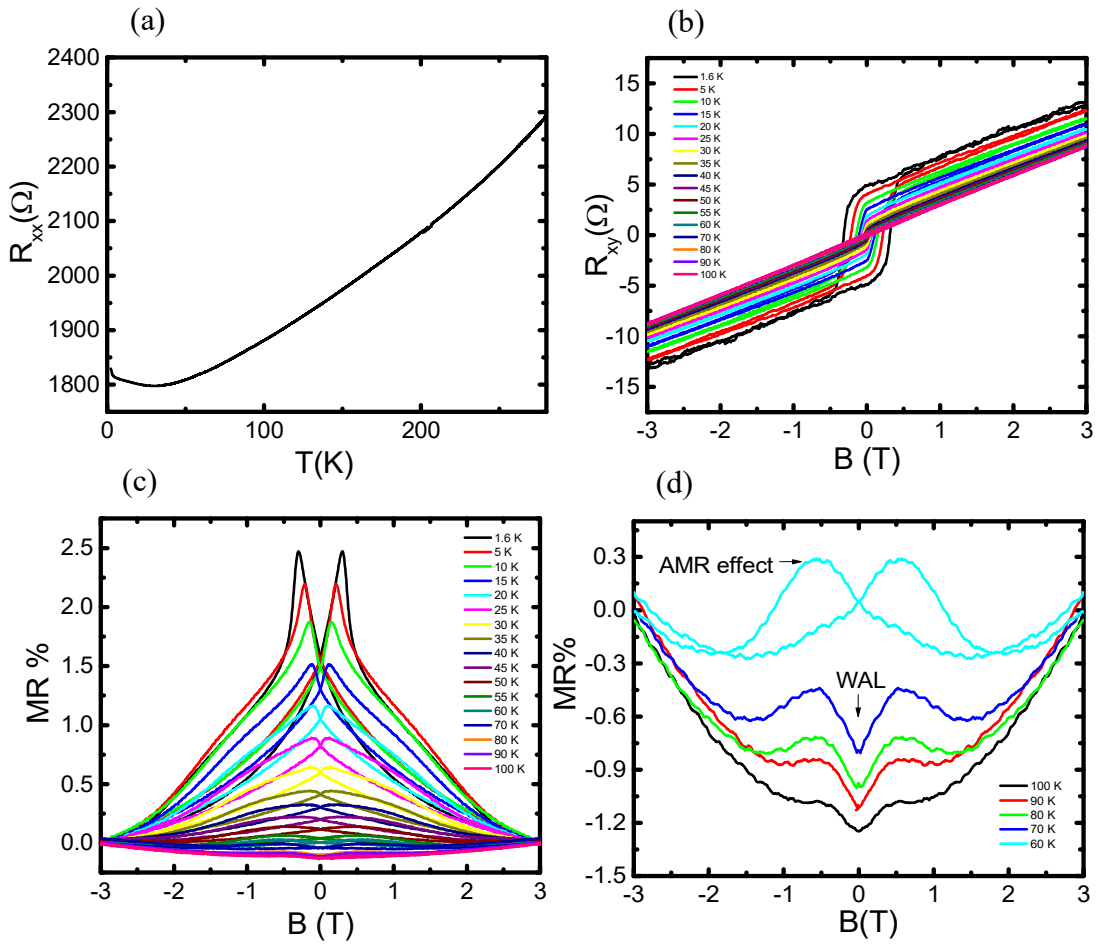

Figure 7.4 (a) The resistance Vs. Temperature plot for a Cr-V doped sample of Sb_2Te_3. (b) The temperature dependent AHE effect in a Cr-V doped Sb_2Te_3 sample. (c,d) The temperature dependent *MR* effect showing a clear transition from WAL to AMR at 60 K.

7.2 Summary of Thesis

Epitaxial Thin Film Growth and Structural Characterization of Magnetically-Doped Topological Insulators

Thin films with various thicknesses of $Cr_xSb_{2-x}Te_3$ were successfully prepared using molecular beam epitaxy as a growth technique on *c*-plane sapphire substrates. During the growth, a two-step process was followed where a 5 nm seed layer of pure Sb_2Te_3 was crucial to attain high quality epitaxial films. The Cr concentration *x* was varied by adjusting the Cr effusion cell to achieve a wide range of doping concentrations with *x* varying from 0.15 to

0.76. On analyzing the x-ray diffraction peaks for the Cr-doped samples, it was concluded that the Cr substitutes the Sb sites. This was confirmed by a reduction in the *c*-lattice parameter as the Cr doping increased. Ferromagnetism was achieved in 60 nm $Cr_xSb_{2-x}Te_3$ thick films probed using SQUID magnetometry. A Curie temperature T_c of 186 K was realized for the doped sample with $x = 0.71$ which is the highest T_c reported in literature. Furthermore, thinner films of ~20 nm of Cr-doped Sb_2Te_3 were grown for the sole intension to reduce bulk conduction for electrical transport measurements. These films had roughly reproducible Cr concentrations as for thicker samples showing similar reductions in the *c*-lattice parameters as the Cr concentration increased. The highest doping levels of Cr concentration with $x = 0.76$ (38%) was achieved keeping the crystal structure intact.

Electrical Transport of Magnetically-Doped Topological Insulator Thin Films and Heterostructures

Electrical and optical measurements were carried out on ~ 20 nm thin films of $Cr_xSb_{2-x}Te_3$ with varying Cr concentrations *x* using AC lock-ins, MOKE and THz-TDS measurements. All samples displayed magnetic behaviour with spins pointing in the out-of-plane direction on application of an external magnetic field. A temperature dependent comparison of the magnetization was made using electrical transport and MOKE measurements. Both results based on studying the anomalous Hall effect and the magneto-optic Kerr rotation were in good agreement with each other while the T_c achieved for the highest doped sample was 176 K. Ion gel gating was employed for the first time on a sample with $x = 0.58$ with a clear increase in the magnitude of AHE by 50% and an increase in the carrier density by 50% on applicating of just -3 V gate bias. This clearly suggested a RKKY type magnetic interaction among Cr spins. THz TDS measurements were conducted on all the samples at RT and the results for carrier densities and mobilities were directly compared to electrical transport. It was found that the T_c obtained was proportional to $x(p)^{1/3}$, further supporting a mean field approximated RKKY interaction scenario. By combining thin film growth, structural characterization, device fabrication, electrical transport and optical characterization of $Cr_xSb_{2-x}Te_3$ in great detail, a new pathway to exploit its material properties at room temperature for industrial applications as well as to explore novel quantum phenomena was provided. Furthermore, thin films of $Cr_xSb_{2-x}Te_3$ were grown on top of a Dy doped Bi_2Te_3 layer to form a ferromagnetic/antiferromagnetic bilayer. This sandwich structure was characterized through electrical transport, the results of which showed a clear exchange-bias

coupling between the two layers. Moreover, four different magnetic states were achieved with respect to different field sweep ranges which can hold very promising applications in magnetoelectronic devices.

Device Processing and Electrical Transport in Bi_2Se_3 and Sb_2Te_3 Thin Films

Thin films of Bi_2Se_3 and Sb_2Te_3 suffer from bulk conduction in comparison to a purely surface conduction expected from a TI due to intrinsic unintentional doping. The aim of this chapter was to distinguish between the surface and bulk conduction channels and study the effects of device processing using a wet chemical etch and Ar^+ milling procedure in Bi_2Se_3. Moreover, performing a thickness dependent study on Sb_2Te_3 thin films. Hall bars were successfully fabricated using wet chemistry as well as dry etching, with electrical transport showing WAL behaviour at low fields ($\pm$1T). The WAL effect reflected the Dirac nature of the surface states and the strong spin-orbit interaction in Bi_2Se_3. The low field behaviour in Bi_2Se_3 revealed a single topological surface state channel which may be the contribution from only the top surface along with a saturated phase coherence length at low temperatures. Overall the wet chemical etched sample showed a more bulk type characteristic compared to the Ar^+ milled sample.

The Sb_2Te_3 thin films consisting of 12 nm and 25 nm showed contrasting results. A single conducting channel associated with a coupled surface and bulk state was deduced by fitting the WAL curves in the 12 nm sample whereas two conducting channels associated with the top and bottom surfaces were deduced from the WAL fitting curves in the 25 nm sample. The fundamental studies on both Bi_2Se_3 and Sb_2Te_3 has helped understand their electrical characteristics in great detail paving the pathway towards practical device applications such as field effect transistors.

Device Processing and Electrical Transport in Cd_3As_2 Nanowires

DC electrical transport measurements were carried out on Dirac semimetal Cd_3As_2 nanowires. WAL was observed at low temperatures consistent with strong spin-orbit interaction in this material system. SdH oscillations were observed and analyzed in detail revealing an ultra-high mobility of 56884 $cm^2V^{-1}s^{-1}$ at 1.8 K. The work provides new physical insights into the unique transport characteristics essential for unlocking further properties of interest. By studying the fundamental properties of Dirac materials, new

avenues can be looked into by exploiting their unique properties for spintronics and magnetoelectronic devices.

References

1. Harris John. “Ten Million British Jobs Could Be Gone in 15 Years. No One Knows What Happens next by John Harris.” *The Guardian, Guardian News and Media,* (2018). doi:www.theguardian.com/commentisfree/2018/apr/30/reality-automation-terrifying
2. Tanmay Sinha. “IBM Watson Knowledge Studio – Teach Watson about Your Domain-Watson.” *IBM Cognitive Advantage Reports* (2017). Available at: www.ibm.com/blogs/watson/2016/06/alchemy-knowledge-studio/. (Accessed: 1st March 2018)
3. Thayer Watkins. The History of the Transistor. Available at: http://www.sjsu.edu/faculty/watkins/transist.htm. (Accessed: 19th June 2018)
4. David A.Laws. “A Company of Legend”: The Legacy of Fairchild Semiconductor. *IEEE Annals of the History of Computing* (2008). Available at: https://ieeexplore.ieee.org/stamp/stamp.jsp?arnumber=5255178. (Accessed: 20th June 2018)
5. Adrian Kingsley-Hughes. Inside Apple’s new A11 Bionic processor. *Hardware 2.0* (2017). Available at: https://www.zdnet.com/article/inside-apples-new-a11-bionic-processor/. (Accessed: 20th June 2018)
6. CNET. End of Moore’s Law: It’s not just about physics. *Scientific American* Available at: https://www.scientificamerican.com/article/end-of-moores-law-its-not-just-about-physics/. (Accessed: 20th June 2018)
7. Sankar Das Sarma. Spintronics. *Sigma Xi, Sci. Res. Honor Soc.* **89,** 516–523 (2001).
8. Oleg, V. Y., Joel, E. M. & Steven, G. L. Spin Polarization and Transport of Surface States in the Topological Insulators Bi_2Se_3 and Bi_2Te_3 from First Principles. *Phys. Rev. Lett.* **105,** 266806, 1–4 (2010).
9. Pan, Z. H. *et al.* Measurement of an Exceptionally Weak Electron-Phonon Coupling on the Surface of the Topological Insulator Bi_2Se_3 Using Angle-Resolved Photoemission Spectroscopy. *Phys. Rev. Lett.* **108,** 187001, 1–5 (2012).
10. Bianchi, M. *et al.* The electronic structure of clean and adsorbate-covered Bi_2Se_3: An angle-resolved photoemission study. *Semicond. Sci. Technol.* **27,** 124001, 14 (2012).
11. Jozwiak, C. *et al.* Photoelectron spin-flipping and texture manipulation in a topological insulator. *Nat. Phys.* **9,** 293–298 (2013).
12. Qi, X.-L., Li, R., Zang, J. & Zhang, S.-C. Inducing a Magnetic Monopole with Topological Surface States. *Science* ` **323,** 5918, 1184–1187 (2009).
13. Linder, J., Tanaka, Y., Yokoyama, T., Sudbø, A. & Nagaosa, N. Unconventional Superconductivity on a Topological Insulator. *Phys. Rev. Lett.* **104,** 067001, 1–4 (2010).
14. Xia, Y. *et al.* Observation of a large-gap topological-insulator class with a single Dirac cone on the surface. *Nat. Phys.* **5,** 398–402 (2009).
15. Hyde, G. R., Beale, H. A., Spain, I. L. & Woollam, J. A. Electronic properties of Bi_2Se_3 crystals. *J. Phys. Chem. Solids* **35,** 1719–1728 (1974).
16. Wang, G. *et al.* Topological Insulator Thin Films of Bi_2Te_3 with Controlled Electronic Structure. *Adv. Mater.* **23,** 26, 2929–2932 (2011).
17. Volykhov, A. A. *et al.* Rapid Surface Oxidation of Sb_2Te_3 as Indication for a Universal Trend in the Chemical Reactivity of Tetradymite Topological Insulators. *Chem. Mater.* **28,** 24, 8916–8923 (2016).
18. Figueroa, A. I., van der Laan, G., Harrison, S. E., Cibin, G. & Hesjedal, T. Oxidation Effects in Rare Earth Doped Topological Insulator Thin Films. *Sci. Rep.* **6,** 22935

(2016).
19. Checkelsky, J. G. *et al.* Quantum Interference in Macroscopic Crystals of Nonmetallic Bi_2Se_3. *Phys. Rev. Lett.* **103,** 246601, 3–6 (2009).
20. Hong, S. S., Cha, J. J., Kong, D. & Cui, Y. Ultra-low carrier concentration and surface-dominant transport in antimony-doped Bi_2Se_3 topological insulator nanoribbons. *Nat. Commun.* **3,** 757 (2012).
21. Kong, D. *et al.* Ambipolar field effect in the ternary topological insulator $(Bi_xSb_{1-x})_2Te_3$ by composition tuning. *Nat. Nanotechnol.* **6,** 11, 705–709 (2011).
22. Wang, Z., Qiu, R. L. J., Lee, C. H., Zhang, Z. & Gao, X. P. A. Ambipolar Surface Conduction in Ternary Topological Insulator $Bi_2(Te_{1-x}Se_x)_3$ Nanoribbons. *ACS Nano* **7,** 3, 2126–2131 (2013).
23. Qu, D.-X., Hor, Y. S., Xiong, J., Cava, R. J. & Ong, N. P. Quantum Oscillations and Hall Anomaly of Surface States in the Topological Insulator Bi_2Te_3. *Science`* **329,** 5993, 821–824 (2010).
24. Chang, C.-Z. *et al.* Experimental Observation of the Quantum Anomalous Hall Effect in a Magnetic Topological Insulator. *Science`* **340,** 6129, 167–170 (2013).
25. Teo, J. C. Y., Fu, L. & Kane, C. L. Surface states of the topological invariants in three-dimensional topological insulators:Application to $Bi_{1-x}Sb_x$. *Phys. Rev. B* **78,** 045426, 1–15 (2008).
26. Yamaguchi, H. & Sogawa, T. The Arrival of a New Era in Quantum Information Processing Technologies. *NTT Tech. Rev.* **15,** 7 (2017).
27. Berry, M. *Some geometric phases transparencies for three lectures at CERN*. *CERN academic training programme* (1993).
28. Gehring, P. Magnetotransport properties of Topological Insulator thin films(PhD thesis). **6073,** (Ecole Polytechnique Federale De Lausanne, 2014).
29. Fu, L. & Kane, C. L. Topological insulators with inversion symmetry. *Phys. Rev. B - Condens. Matter Mater. Phys.* **76,** 045302, 1–17 (2007).
30. Hsieh, D. *et al.* A topological Dirac insulator in a quantum spin Hall phase. *Nature* **452,** 970–974 (2008).
31. Zhang, H. *et al.* Topological insulators in Bi_2Se_3, Bi_2Te_3 and Sb_2Te_3 with a single Dirac cone on the surface. *Nat. Phys.* **5,** 438–442 (2009).
32. Luo, W. & Qi, X. L. Massive Dirac surface states in topological insulator/magnetic insulator heterostructures. *Phys. Rev. B - Condens. Matter Mater. Phys.* **87,** 085431, 1–7 (2013).
33. Liu, Q., Liu, C. X., Xu, C., Qi, X. L. & Zhang, S. C. Magnetic impurities on the surface of a topological insulator. *Phys. Rev. Lett.* **102,** 156603, 1–4 (2009).
34. Qi, X. L. & Zhang, S. C. Topological insulators and superconductors. *Rev. Mod. Phys.* **83,** 1057 (2011).
35. Hasan, M. Z. & Kane, C. L. Colloquium: Topological insulators. *Rev. Mod. Phys.* **82,** 3045–3067 (2010).
36. Wray, L. A. Topological transistor. *Nat. Phys.* **8,** 705–706 (2012).
37. Vobornik, I. *et al.* Magnetic Proximity Effect as a Pathway to Spintronic Applications of Topological Insulators. *Nano Lett.* **11,** 4079–4082 (2011).
38. Li, M. *et al.* Proximity-Driven Enhanced Magnetic Order at Ferromagnetic-Insulator – Magnetic-Topological-Insulator Interface. *Phys. Rev. Lett.* **115,** 087201, 2–6 (2015).
39. Nickel, J. Magnetoresistance Overview. *HP Labs Tech. Reports* HPL-95-60 (1995).
40. Parish, M. M. & Littlewood, P. B. Non-saturating magnetoresistance in heavily disordered semiconductors. *Nature* **426,** 162–165 (2003).
41. Gu, H. *et al.* An overview of the magnetoresistance phenomenon in molecular systems. *Chem. Soc. Rev.* **42,** 5907 (2013).

42. Peter Newton. Spintronic Device Physics in Germanium/Silicon Heterostructures (PhD thesis). (Cambridge, 2017).
43. Hikami, S., Larkin, A. I. & Nagaoka, Y. Spin-Orbit Interaction and Magnetoresistance in the Two Dimensional Random System. *Prog. Theor. Phys.* **63,** 707–710 (1980).
44. Stefan Blugel, Yuriy Mokrousov, Thomas Schapers, Y. A. *Topological matter-Topological Insulators, Skyrmions and Majoranas*. (48th IFF Spring School 2017 lecture notes, 2017).
45. Presentation slide show, Part II: Molecular Beam Epitaxy. *VEECO,* 8 (2018). doi:slideplayer.com/slide/3397945/
46. Markov, I. V. *Crystal Growth for Beginners: Fundamentals of Nucleation, Crystal Growth, and Epitaxy*. *World Scientific Singapore* (1995). doi:10.1142/5172
47. Shuji Hasegawa. *Characterization of Materials*. (John Wiley and Sons, Inc, 2012). doi:https://doi.org/10.1002/0471266965.com139
48. Klein, J. Epitaktische Heterostrukturen aus dotierten Manganaten. *Ph. D. Thesis* (Cologne, 2001). doi:http://kups.ub.uni-koeln.de/400/
49. Ewald, P. P. Introduction to the dynamical theory of X-ray diffraction. *Acta Crystallogr. Sect. A* **A25,** 103–108 (1969).
50. Collins-mcintyre, L. J. Transition-Metal Doped Bi_2Se_3 and Bi_2Te_3 Topological Insulator Thin Films (PhD thesis). (Oxford, 2015).
51. Waseda, Y., Matsubara, E. & Shinoda, K. *X-Ray Diffraction Crystallography*. (Springer, 2011).
52. Elective Course on x-Ray Diffraction. (2016). doi:chme.nmsu.edu/elective-course-on-x-ray-diffraction/
53. Yasaka Miho. X-ray thin film measurement techniques. *Rigaku J.* **26,** 1–9 (2010).
54. European Action towards Leading centre for innovative Materials XPS equipment. (2018). Available at: http://www.eagle-regpot.eu/EAgLE-Equipment_XPS.html. (Accessed: 20th June 2018)
55. Strehle, M. X-Ray Photoelectron Spectroscopy (XPS) Study of Single Crystal UO_2 and U_3O_8 on R-Plane Sapphire and Yttrium Stabilized Zirconium (YSZ) Substrates (PhD Thesis). (2011). doi:10.1017/CBO9781107415324.004
56. Jaklevic, R. C., Lambe, J., Silver, A. H. & Mercereau, J. E. Quantum interference effects in Josephson tunneling. *Phys. Rev. Lett.* **12,** 7, 159–160 (1964).
57. Chen, Y. L. *et al.* Massive Dirac Fermion on the Surface of a Magnetically Doped Topological Insulator. *Science`* **329,** 659–662 (2010).
58. Dziom, V. *et al.* Observation of the universal magnetoelectric effect in a 3D topological insulator. *Nat. Commun.* **8,** 15197, 6–13 (2017).
59. Yu, R. *et al.* Quantized Anomalous Hall Effect in Magnetic Topological Insulators. *Science`* **329,** 5987, 61–64 (2010).
60. Fujita, T., Jalil, M. B. A. & Tan, S. G. Topological insulator cell for memory and magnetic sensor applications. *Appl. Phys. Express* **4,** 094201 (2011).
61. Wang, Q. *et al.* Characterization of Cr-doped Sb_2Te_3 films and their applications to phase-change memory. *Phys. status solidi - Rapid Res. Lett.* **9,** 8, 470–474 (2015).
62. Huang, Y. Q., Song, Y. X., Wang, S. M., Buyanova, I. A. & Chen, W. M. Spin injection and helicity control of surface spin photocurrent in a three dimensional topological insulator. *Nat. Commun.* **8,** 15401, 1–8 (2017).
63. Fu, L., Kane, C. L. & Mele, E. J. Topological Insulators in Three Dimensions. *Phys. Rev. Lett.* **98,** 106803, 1–4 (2007).
64. Moore, J. E. & Balents, L. Topological invariants of time-reversal-invariant band structures. *Phys. Rev. B - Condens. Matter Mater. Phys.* **75,** 121306, 3–6 (2007).
65. Xiu, F. *et al.* Manipulating surface states in topological insulator nanoribbons. *Nat.*

Nanotechnol. **6,** 216–221 (2011).
66. Hor, Y. S. *et al. p*-type Bi_2Se_3 for topological insulator and low-temperature thermoelectric applications. *Phys. Rev. B - Condens. Matter Mater. Phys.* **79,** 195208, 2–6 (2009).
67. He, L. *et al.* Surface-dominated conduction in a 6 nm thick Bi_2Se_3 thin film. *Nano Lett.* **12,** 3, 1486–1490 (2012).
68. Yan, Y. *et al.* Synthesis and Quantum Transport properties of Bi_2Se_3 Topological Insulator Nanostructures. *Sci. Rep.* **3,** 1264 (2013).
69. Jia, S. *et al.* Low-carrier-concentration crystals of the topological insulator Bi_2Te_2Se. *Phys. Rev. B - Condens. Matter Mater. Phys.* **84,** 235206, 1–7 (2011).
70. Wang, Y. *et al.* Gate-Controlled Surface Conduction in Na-Doped Bi_2Te_3 Topological Insulator Nanoplates. *Nano Lett.* **12,** 3, 1170–1175 (2012).
71. Koma, A. Van der Waals epitaxy- a new epitaxial growth method for a highly lattice-mismatched system. *Thin Solid Films* **216,** 72–76 (1992).
72. He, L., Kou, X. & Wang, K. L. Review of 3D topological insulator thin-film growth by molecular beam epitaxy and potential applications. *Phys. Status Solidi - Rapid Res. Lett.* **7,** 1–2, 50–63 (2013).
73. Mzerd, A., Sayah, D., Tedenac, J. C. & Boyer, A. Optimal crystal growth conditions of thin films of Bi_2Te_3 semiconductors. *J. Cryst. Growth* **140,** 365–369 (1994).
74. He, L. *et al.* Epitaxial growth of Bi_2Se_3 topological insulator thin films on Si (111). *J. Appl. Phys.* **109,** 103702 (2011).
75. Canham, L. T. Silicon quantum wire array fabrication by electrochemical and chemical dissolution of wafers. *Appl. Phys. Lett.* **57,** 10 (1990).
76. Wang, Z. Y., Li, H. D., Guo, X., Ho, W. K. & Xie, M. H. Growth characteristics of topological insulator Bi_2Se_3 films on different substrates. *J. Cryst. Growth* **334,** 96–102 (2011).
77. Bansal, N. *et al.* Epitaxial growth of topological insulator Bi_2Se_3 film on Si(111) with atomically sharp interface. *Thin Solid Films* **520,** 1, 224–229 (2011).
78. Bringans, R. & Olmstead, M. Bonding of Se and ZnSe to the Si (100) surface. *Phys. Rev. B* **39,** 17, 985–988 (1989).
79. Ueno, K., Abe, H., Saiki, K. & Koma, A. Heteroepitaxy of Layered Semiconductor GaSe on a GaAs(III)B Surface. *Jpn. J. Appl. Phys.* **30,** 8A, L1352–L1354 (1991).
80. Ginley, T. P. & Law, S. Growth of Bi_2Se_3 topological insulator films using a selenium cracker source. *J. Vac. Sci. Technol. B, Nanotechnol. Microelectron. Mater. Process. Meas. Phenom.* **34,** 02L105 (2016).
81. Kou, X. F. *et al.* Magnetically doped semiconducting topological insulators. *J. Appl. Phys.* **112,** 063912 (2012).
82. Tsui, F. *et al.* Novel Germanium-Based Magnetic Semiconductors. *Phys. Rev. Lett.* **91,** 177203(4) (2003).
83. Ohno, H. Making Nonmagnetic Semiconductors Ferromagnetic. *Science`* **281,** 5379, 951–956 (1998).
84. Ueda, K., Tabata, H. & Kawai, T. Magnetic and electric properties of transition-metal-doped ZnO films. *Appl. Phys. Lett.* **79,** 7, 988–990 (2001).
85. Chen, Y. L. *et al.* Massive Dirac Fermion on the Surface of a Magnetically Doped Topological Insulator. *Science`* **329,** 5992, 659–662 (2010).
86. Chen, Z. *et al.* Molecular Beam Epitaxial Growth and Properties of Bi_2Se_3 Topological Insulator Layers on Different Substrate Surfaces. *J. Electron. Mater.* **43,** 4, 909–913 (2014).
87. Eddrief, M., Atkinson, P., Etgens, V. & Jusserand, B. Low-temperature Raman fingerprints for few-quintuple layer topological insulator Bi_2Se_3 films epitaxied on

GaAs. *Nanotechnology* **25,** 245701(8pp) (2014).
88. Harrison, S. E. *et al.* Two-step growth of high quality Bi_2Te_3 thin films on Al_2O_3 (0001) by molecular beam epitaxy. *Appl. Phys. Lett.* **102,** 171906, 2011–2015 (2013).
89. Liu, X. *et al.* Characterization of Bi_2Te_3 and Bi_2Se_3 topological insulators grown by MBE on (001) GaAs substrates. *J. Vac. Sci. Technol. B, Nanotechnol. Microelectron. Mater. Process. Meas. Phenom.* **30,** 02B103 (2012).
90. Das, D. *et al.* Defect induced structural and thermoelectric properties of Sb_2Te_3 alloy. *J. Appl. Phys.* **118,** 045102 (2015).
91. Collins-McIntyre, L. J. *et al.* Structural , electronic , and magnetic investigation of magnetic ordering in MBE-grown $Cr_xSb_{2-x}Te_3$ thin films. *Eur. Lett.* **115,** 27006 (2016).
92. Zhou, Z., Chien, Y. & Uher, C. Thin film dilute ferromagnetic semiconductors $Sb_{2-x}Cr_xTe_3$ with a Curie temperature up to 190 K. *Phys. Rev. B* **74,** 224418 (2006).
93. Björck, M. & Andersson, G. GenX: An extensible X-ray reflectivity refinement program utilizing differential evolution. *J. Appl. Crystallogr.* **40,** 6, 1174–1178 (2007).
94. Arne F. Andersen. A Neutron Diffraction Investigation of Cr_2Te_3 and Cr_5Te_6. *Acta Chem. Scand.* **17,** 5, 1335–1342 (1963).
95. Figueroa, A. I. *et al.* Magnetic Cr doping of Bi_2Se_3: Evidence for divalent Cr from x-ray spectroscopy. *Phys. Rev. B - Condens. Matter Mater. Phys.* **90,** 134402, 1–9 (2014).
96. Figueroa, A. I. *et al.* Local Structure and Bonding of Transition Metal Dopants in Bi_2Se_3 Topological Insulator Thin Films. *J. Phys. Chem. C* **119,** 30, 17344–17351 (2015).
97. Haldane, F. D. M. Model for a Quantum Hall Effect without Landau Levels: Condensed-Matter Realization of the 'Parity Anomaly'. *Phys. Rev. Lett.* **61,** 18, 2015–2018 (1988).
98. Onoda, M. & Nagaosa, N. Quantized Anomalous Hall Effect in Two-Dimensional Ferromagnets: Quantum Hall Effect in Metals. *Phys. Rev. Lett.* **90,** 20, 4 (2003).
99. Nagaosa, N., Sinova, J., Onoda, S., MacDonald, A. H. & Ong, N. P. Anomalous Hall effect. *Rev. Mod. Phys.* **82,** 2, 1539–1592 (2010).
100. Wang, Q. *et al.* Reversible Phase Change Characteristics of Cr-Doped Sb_2Te_3 Films with Different Initial States Induced by Femtosecond Pulses. *ACS Appl. Mater. Interfaces* **8,** 32, 20885–20893 (2016).
101. Moore, J. E. The birth of topological insulators. *Nature* **464,** 194–198 (2010).
102. Liu, C. X., Qi, X. L., Dai, X., Fang, Z. & Zhang, S. C. Quantum Anomalous Hall Effect in $Hg_{1-y}Mn_yTe$ Quantum Wells. *Phys. Rev. Lett.* **101,** 146802, 1–4 (2008).
103. Hirohata, A., Xu, Y. B., Guertler, C. M. & Bland, J. A. C. Spin-dependent electron transport at the ferromagnet / semiconductor interface. *J. Appl. Phys.* **85,** 8, 5804–5806 (1999).
104. Kasuya, T. & Yanase, A. Anomalous Transport Phenomena in Eu-Chalcogenide Alloys. *Rev. Mod. Phys.* **40,** 4, 684–696 (1968).
105. Munekata, H. *et al.* Diluted Magnetic III-V Semiconductors. *Phys. Rev. Lett.* **63,** 17, 1849–1852 (1989).
106. Ohno, H., Munekata, H., Penney, T., Vonmolnar, S. & Chang, L. L. Magnetotransport Properties of *p*-Type (In,Mn)As Diluted Magnetic III-V Semiconductors. *Phys. Rev. Lett.* **68,** 17, 2664–2667 (1992).
107. Wang, M. *et al.* Three-dimensional Heisenberg critical behavior in the highly disordered dilute ferromagnetic semiconductor (Ga,Mn)As. **93,** 184417, 1–16 (2016).
108. Dietl, T., Haury, A. & Merle dșAubigné, Y. Free carrier-induced ferromagnetism in structures of diluted magnetic semiconductors. *Phys. Rev. B - Condens. Matter Mater. Phys.* **55,** 6, 3347–3350 (1997).
109. Reed, M. L. *et al.* Room temperature ferromagnetic properties of (Ga,Mn)N. *Appl.*

Phys. Lett. **79,** 3473–3475 (2001).
110. Hsieh, D. *et al.* Observation of Time-Reversal-Protected Single-Dirac-Cone Topological-Insulator States in Bi_2Te_3 and Sb_2Te_3. *Phys. Rev. Lett.* **103,** 146401, 2–5 (2009).
111. Wang, G. *et al.* Atomically Smooth Ultrathin Films of Topological Insulator Sb_2Te_3. *Nano Res.* **3,** 12, 874–880 (2010).
112. Kou, X. *et al.* Interplay between different magnetisms in Cr-doped topological insulators. *ACS Nano* **7,** 9205–9212 (2013).
113. Ye, M. *et al.* Carrier-mediated ferromagnetism in the magnetic topological insulator Cr-doped $(Sb,Bi)_2Te_3$. *Nat. Commun.* **6,** 6, 8913, 1–7 (2015).
114. Chang, C. Z. *et al.* Thin Films of Magnetically Doped Topological Insulator with Carrier-Independent Long-Range Ferromagnetic Order. *Adv. Mater.* **25,** 7, 1065–1070 (2013).
115. Feng, X. *et al.* Thickness Dependence of the Quantum Anomalous Hall Effect in Magnetic Topological Insulator Films. *Adv. Mater.* **28,** 6386–6390 (2016).
116. Zhang, Z. *et al.* Electrically tuned magnetic order and magnetoresistance in a topological insulator. *Nat. Commun.* **5,** 4915 (2014).
117. Ni, Y., Zhang, Z., Nlebedim, I. C. & Jiles, D. C. Ultrahigh Sensitivity of Anomalous Hall Effect Sensor Based on Cr-Doped Bi_2Te_3 Topological Insulator Thin Films. **52,** 7, 3–6 (2016).
118. Chang, C. *et al.* Field-effect modulation of anomalous Hall effect in diluted ferromagnetic topological insulator epitaxial films. *Sci. China Physics, Mech. Astron.* **59,** No. 3: 637501 (2016).
119. Gupta, S., Kanai, S., Matsukura, F. & Ohno, H. Magnetic and transport properties of Sb_2Te_3 doped with high concentration of Cr. *Appl. Phys. Express* **10,** 103001 (2017).
120. Zhang, Y. *et al.* Crossover of the three-dimensional topological insulator Bi_2Se_3 to the two-dimensional limit. *Nat. Phys.* **6,** 8, 584–588 (2010).
121. Himpsel, F. J., Ortega, J. E., Mankey, G. J. & Willis, R. F. Magnetic nanostructures. *Adv. Phys.* **47,** 4, 511–597 (1998).
122. Von Molnar, S. & Kasuya, T. Evidence of band conduction and critical scattering in dilute Eu-chalcogenide alloys. *Phys. Rev. Lett.* **21,** 26, 1757–1761 (1968).
123. Kasuya, T. A Theory of Metallic Ferro- and Antiferromagnetism on Zener's Model. *Prog. Theor. Phys.* **16,** 1, 45–57 (1956).
124. Fert, A. Nobel Lecture: Origin, development, and future of spintronics. *Rev. Mod. Phys.* **80,** 4, 1517–1530 (2008).
125. Nguyen, T. *et al.* Topological states and phase transitions in Sb_2Te_3-GeTe multilayers. *Sci. Rep.* **6,** 27716 (2016).
126. Lang, M. *et al.* Competing Weak Localization and Weak Antilocalization in Ultrathin Topological Insulators. *Nano Lett.* **13,** 48–53 (2013).
127. Žutić, I., Fabian, J. & Sarma, S. Das. Spintronics: Fundamentals and applications. *Rev. Mod. Phys.* **76,** 2, 323–410 (2004).
128. Yeats, A. L. *et al.* Local optical control of ferromagnetism and chemical potential in a topological insulator. *PNAS* **114,** 39, 10379–10383 (2017).
129. S. Jacobs & Bean, C. P. Fine Particles, Thin Films and Exchange Anisotropy. *Magn. G. T. Rado H. Suhl, Eds., Acad. New York* **3,** 271–350 (1963).
130. Kaminski, A. & Das Sarma, S. Polaron Percolation in Diluted Magnetic Semiconductors. *Phys. Rev. Lett.* **88,** 247202 (2002).
131. Das Sarma, S., Hwang, E. H. & Kaminski, A. Temperature-dependent magnetization in diluted magnetic semiconductors. *Phys. Rev. B* **67,** 155201 (2003).
132. Kouvel, J. S. & Fisher, M. E. Detailed magnetic behavior of nickel near its curie point.

Phys. Rev. **136,** 6, 1626–1632 (1964).
133. Arrott, A. Criterion for ferromagnetism from observations of magnetic isotherms. *Phys. Rev.* **108,** 6, 1394–1396 (1957).
134. Pelissetto, A. & Vicari, E. Critical phenomena and renormalization-group theory. *Phys. Rep.* **368,** 6, 549–727 (2002).
135. Li, M. *et al.* Experimental Verification of the Van Vleck Nature of Long-Range Ferromagnetic Order in the Vanadium-Doped Three-Dimensional Topological Insulator Sb_2Te_3. *Phys. Rev. Lett.* **114,** 146802 (2015).
136. Cho, J. H. *et al.* Printable ion-gel gate dielectrics for low-voltage polymer thin-film transistors on plastic. *Nat. Mater.* **7,** 11, 900–906 (2008).
137. Yuan, H. *et al.* Liquid-gated ambipolar transport in ultrathin films of a topological insulator Bi_2Te_3. *Nano Lett.* **11,** 7, 2601–2605 (2011).
138. Lee, J. S. *et al.* Ferromagnetism and spin-dependent transport in *n*-type Mn-doped bismuth telluride thin films. *Phys. Rev. B - Condens. Matter Mater. Phys.* **89,** 174425, 1–8 (2014).
139. Chang, C. Z. *et al.* Chemical-Potential-Dependent Gap Opening at the Dirac Surface States of Bi_2Se_3 Induced by Aggregated Substitutional Cr Atoms. *Phys. Rev. Lett.* **112,** 056801, 1–5 (2014).
140. Jungwirth, T. *et al.* Prospects for high temperature ferromagnetism in (Ga,Mn)As semiconductors. *Phys. Rev. B - Condens. Matter Mater. Phys.* **72,** 165204, 1–13 (2005).
141. Haazen, P. P. J. *et al.* Ferromagnetism in thin-film Cr-doped topological insulator Bi_2Se_3. *Appl. Phys. Lett.* **100,** 082404, 3–6 (2012).
142. Liu, W. *et al.* Atomic-Scale Magnetism of Cr-Doped Bi_2Se_3 Thin Film Topological Insulators. *ACS Nano* **9,** 10, 10237–10243 (2015).
143. Benia, H. M., Lin, C., Kern, K. & Ast, C. R. Reactive Chemical Doping of the Bi_2Se_3 Topological Insulator. *Phys. Rev. Lett.* **107,** 177602 (2011).
144. Kamboj, V. S. *et al.* Probing the topological surface state in Bi_2Se_3 thin films using temperature-dependent terahertz spectroscopy. *ACS Photonics* (2017). doi:10.1021/acsphotonics.7b00492
145. Grüner, G. *Millimeter and submillimeter wave spectroscopy of solids*. (Springer, 1998). doi:10.1007/BFb0103417
146. O. Madelung. *Semiconductors: Data Handbook*. (Springer, 2004).
147. Takagaki, Y., Giussani, A., Perumal, K., Calarco, R. & Friedland, K. J. Robust topological surface states in Sb_2Te_3 layers as seen from the weak antilocalization effect. *Phys. Rev. B - Condens. Matter Mater. Phys.* **86,** 125137, 1–7 (2012).
148. Banerjee, K. *et al.* Defect-induced negative magnetoresistance and surface state robustness in the topological insulator $BiSbTeSe_2$. *Phys. Rev. B* **90,** 235427, 1–5 (2014).
149. Li, B. *et al.* Carrier dependent ferromagnetism in chromium doped topological insulator $Cr_y(Bi_xSb_{1-x})_{2-y}Te_3$. *Phys. Lett. A* **377,** 1925–1929 (2013).
150. Park, S. H. *et al.* Reversible Fermi Level Tuning of a Sb_2Te_3 Topological Insulator by Structural Deformation. *Nano Lett.* **15,** 6, 3820–3826 (2015).
151. Park, B. C. *et al.* Terahertz single conductance quantum and topological phase transitions in topological insulator Bi_2Se_3 ultrathin films. *Nat. Commun.* **6,** 6552, 1–8 (2015).
152. Jackson, M. Wherefore Gadolinium? Magnetism of the Rare Earths Visiting Fellows' Reports. *J. Nucl. Mater.* **10,** 3, 1–8 (2000).
153. Meiklejohn, W. H. & Bean, C. P. New Magnetic Anisotropy. *Phys. Rev.* **102,** 5, 1413–1414 (1956).

154. He, Q. L. *et al.* Tailoring exchange couplings in magnetic topological-insulator/antiferromagnet heterostructures. *Nat. Mater.* **16,** 1, 94–100 (2017).
155. Qi, X. & Zhang, S. The quantum spin Hall effect and topological insulators. *Phys. Today* **63,** 1, 33–38 (2010).
156. Hsieh, D. *et al.* A tunable topological insulator in the spin helical Dirac transport regime. *Nature* **460,** 7259, 1101–1105 (2009).
157. Topological, T. *et al.* Experimental Realization of a Three-Dimensional Topological Insulator, Bi_2Te_3. *Science`* **325,** 5937, 178–181 (2009).
158. Ando, Y. Topological insulator materials. *J. Phys. Soc. Japan* **82,** 102001, 1–32 (2013).
159. Hanaguri, T., Igarashi, K., Kawamura, M., Takagi, H. & Sasagawa, T. Momentum-resolved Landau-level spectroscopy of Dirac surface state in Bi_2Se_3. *Phys. Rev. B - Condens. Matter Mater. Phys.* **82,** 081305(R), 1-4 (2010).
160. Cheng, P. *et al.* Landau quantization of topological surface states in Bi_2Se_3. *Phys. Rev. Lett.* **105,** 076801, 2–5 (2010).
161. Butch, N. P. *et al.* Strong surface scattering in ultrahigh-mobility Bi_2Se_3 topological insulator crystals. *Phys. Rev. B - Condens. Matter Mater. Phys.* **81,** 241301, 3–6 (2010).
162. Analytis, J. G. *et al.* Two-dimensional surface state in the quantum limit of a topological insulator. *Nat. Phys.* **6,** 12, 960–964 (2010).
163. Kim, Y. S. *et al.* Thickness-dependent bulk properties and weak antilocalization effect in topological insulator Bi_2Se_3. *Phys. Rev. B - Condens. Matter Mater. Phys.* **84,** 073109, 1–5 (2011).
164. Liu, M. *et al.* Electron interaction-driven insulating ground state in Bi_2Se_3 topological insulators in the two-dimensional limit. *Phys. Rev. B - Condens. Matter Mater. Phys.* **83,** 165440, 1–6 (2011).
165. Chen, J. *et al.* Tunable surface conductivity in Bi_2Se_3 revealed in diffusive electron transport. *Phys. Rev. B* **83,** 241304(R) (2011).
166. Chen, J. *et al.* Gate-voltage control of chemical potential and weak antilocalization in Bi_2Se_3. *Phys. Rev. Lett.* **105,** 176602, 1–4 (2010).
167. Checkelsky, J. G., Hor, Y. S., Cava, R. J. & Ong, N. P. Bulk band gap and surface state conduction observed in voltage-tuned crystals of the topological insulator Bi_2Se_3. *Phys. Rev. Lett.* **106,** 196801, 4–7 (2011).
168. Wang, J. *et al.* Evidence for electron-electron interaction in topological insulator thin films. *Phys. Rev. B - Condens. Matter Mater. Phys.* **83,** 245438, 1–7 (2011).
169. Kim, D., Syers, P., Butch, N. P., Paglione, J. & Fuhrer, M. S. Coherent topological transport on the surface of Bi_2Se_3. *Nat. Commun.* **4,** 2040, 1–5 (2013).
170. Steinberg, H., Laloë, J. B., Fatemi, V., Moodera, J. S. & Jarillo-Herrero, P. Electrically tunable surface-to-bulk coherent coupling in topological insulator thin films. *Phys. Rev. B - Condens. Matter Mater. Phys.* **84,** 233101, 5–8 (2011).
171. Brahlek, M., Koirala, N., Salehi, M., Bansal, N. & Oh, S. Emergence of decoupled surface transport channels in bulk insulating Bi_2Se_3 thin films. *Phys. Rev. Lett.* **113,** 026801, 1–5 (2014).
172. He, L. *et al.* Surface-Dominated Conduction in a 6 nm thick Bi_2Se_3 Thin Film. *Nano Lett.* **12,** 3, 1486–1490 (2012).
173. Gao, L. *et al.* Patterning Bi_2Se_3 single-crystalline thin films on Si(111) substrates using strong oxidizing acids. *RSC Adv.* **7,** 51, 32294–32299 (2017).
174. Se, B., Se, B. I., Augustine, S. & Mathai, E. Growth , morphology , and microindentation analysis of Bi_2Se_3, $Bi_{1.8}In_{0.2}Se_3$, and $Bi_2Se_{2.8}Te_{0.2}$ single crystals. *Mater. Res. Bull.* **36,** 2251–2261 (2001).
175. Goncalves, L. M. *et al.* Fabrication of flexible thermoelectric microcoolers using

planar thin-film technologies. *J. Micromechanics Microengineering* **17,** S168 (2007).
176. Carmo, J. P., Goncalves, L. M. & Correia, J. H. Thermoelectric microconverter for energy harvesting systems. *IEEE Trans. Ind. Electron.* **57,** 3, 861–867 (2010).
177. Goncalves, L. M., Alpuim, P. & Correia, J. H. Fabrication of thermoelectric devices by applying microsystems technology. *J. Electron. Mater.* **39,** 9, 1516–1521 (2010).
178. Carmo, J. P. *et al.* Digitally-controlled array of solid-state microcoolers for use in surgery. *Microsyst. Technol.* **17,** 8, 1283–1291 (2011).
179. Qu, D.-X., Hor, Y. S., Xiong, J., Cava, R. J. & Ong, N. P. Quantum Oscillations and Hall Anomaly of Surface States in the Topological Insulator Bi_2Te_3. *Science`* **329,** 5993, 821–824 (2010).
180. Yan, Y., Wang, L. X., Yu, D. P. & Liao, Z. M. Large magnetoresistance in high mobility topological insulator Bi_2Se_3. *Appl. Phys. Lett.* **103,** 033106 (2013).
181. Gao, B. F., Gehring, P., Burghard, M. & Kern, K. Gate-controlled linear magnetoresistance in thin Bi_2Se_3 sheets. *Appl. Phys. Lett.* **100,** 212402 (2012).
182. Tang, H., Liang, D., Qiu, R. L. J. & Gao, X. P. A. Two-Dimensional Transport-Induced Linear Magneto-Resistance in Topological Insulator Bi_2Se_3 Nanoribbons. *ACS Nano* **5,** 9, 7510–7516 (2011).
183. Xu, R. *et al.* Large magnetoresistance in non-magnetic silver chalcogenides. *Nature* **390,** 6655, 57 (1997).
184. Veldhorst, M. *et al.* Magnetotransport and induced superconductivity in Bi based three-dimensional topological insulators. *Phys. Status Solidi - Rapid Res. Lett.* **7,** 1–2, 26–38 (2013).
185. He, H. T. *et al.* Impurity effect on weak antilocalization in the topological insulator Bi_2Te_3. *Phys. Rev. Lett.* **106,** 166805, 1–4 (2011).
186. Assaf, B. A. *et al.* Linear magnetoresistance in topological insulator thin films: Quantum phase coherence effects at high temperatures. *Appl. Phys. Lett.* **102,** 012102 (2013).
187. Altshuler, B. L., Aronov, A. G. & Khmelnitsky, D. E. Effects of electron-electron collisions with small energy transfers on quantum localisation. *J. Phys. C Solid State Phys.* **15,** 36, 7367–7386 (1982).
188. Harutyunyan, S. R. Thickness-Dependent Magnetoresistance of Sb_2Te_3 Nanoflakes and Weak Antilocalization Effect. *J. Contemp. Phys.* **50,** 3, 282–287 (2015).
189. Jiang, Y. *et al.* Landau quantization and the thickness limit of topological insulator thin films of Sb_2Te_3. *Phys. Rev. Lett.* **108,** 016401, 2–6 (2012).
190. Jiang, Y. *et al.* Fermi-Level Tuning of Epitaxial Sb_2Te_3 Thin Films on Graphene by Regulating Intrinsic Defects and Substrate Transfer Doping. *Phys. Rev. Lett.* **108,** 066809, 1–5 (2012).
191. Young, S. M. *et al.* Dirac Semimetal in Three Dimensions. *Phys. Rev. Lett.* **108,** 140405, 1–5 (2012).
192. Wang, Z., Weng, H., Wu, Q., Dai, X. & Fang, Z. Three-dimensional Dirac semimetal and quantum transport in Cd_3As_2. *Phys. Rev. B - Condens. Matter Mater. Phys.* **88,** 125427, 1–6 (2013).
193. Ali, M. N. *et al.* The Crystal and Electronic Structures of Cd_3As_2, the Three-Dimensional Electronic Analogue of Graphene. *Inorg. Chem.* **53,** 8, 4062–4067 (2014).
194. Hosur, P. & Qi, X. Recent developments in transport phenomena in Weyl semimetals. *Comptes Rendus Phys.* **14,** 9–10, 857–870 (2013).
195. Liu, Z. K. *et al.* Discovery of a Three-Dimensional Topological Dirac Semimetal, Na_3Bi. *Science`* **343,** 6173, 864–867 (2014).
196. Wang, H. *et al.* Observation of superconductivity induced by a point contact on 3D

Dirac semimetal Cd_3As_2 crystals. *Nat. Mater.* **15,** 38–42 (2016).
197. Liu, Z. K. *et al.* A stable three-dimensional topological Dirac semimetal Cd_3As_2. *Nat. Mater.* **13,** 677–681 (2014).
198. Neupane, M. *et al.* Observation of a three-dimensional topological dirac semimetal phase in high-mobility Cd_3As_2. *Nat. Commun.* **5,** 3786, 1–8 (2014).
199. Zhao, Y. *et al.* Anisotropic Fermi Surface and Quantum Limit Transport in High Mobility Three-Dimensional Dirac Semimetal Cd_3As_2. *Phys. Rev. X* **5,** 031037, 1–9 (2015).
200. Liu, Y. *et al.* Gate-tunable quantum oscillations in ambipolar Cd_3As_2 thin films. *NPG Asia Mater.* **7,** 10, e221-8 (2015).
201. Cao, J. *et al.* Landau level splitting in Cd_3As_2 under high magnetic fields. *Nat. Commun.* **6,** 7779 (2015).
202. Zhang, E. *et al.* Magnetotransport Properties of Cd_3As_2 Nanostructures. *ACS Nano* **9,** 9, 8843–8850 (2015).
203. Liang, T. *et al.* Ultrahigh mobility and giant magnetoresistance in the Dirac semimetal Cd_3As_2. *Nat. Mater.* **14,** 3, 280–284 (2014).
204. Narayanan, A. *et al.* Linear Magnetoresistance Caused by Mobility Fluctuations in *n*-Doped Cd_3As_2. *Phys. Rev. Lett.* **114,** 117201, 1–5 (2015).
205. Feng, J. *et al.* Large linear magnetoresistance in Dirac semimetal Cd_3As_2 with Fermi surfaces close to the Dirac points. *Phys. Rev. B - Condens. Matter Mater. Phys.* **92,** 081306(R), 1-5 (2015).
206. Schönherr, P. Growth and characterisation of quantum materials nanostructures (PhD thesis). (Oxford, 2016).
207. D. Shoenberg. *Magnetic Oscillations in Metals*. (Cambridge University Press, 1984).
208. Chang, C.-Z. *et al.* High-precision realization of robust quantum anomalous Hall state in a hard ferromagnetic topological insulator. *Nat. Mater.* **14,** 473 (2015).
209. Li, M. Investigation of Magnetic Interactions in Topological Insulators. PhD thesis (Massachusetts Institute of Technology, 2015).
210. Zatsepin, D. A. & Academy, R. The Shapes of XPS spectra – how to process the background correctly? 1–20 (2014). doi:10.13140/2.1.2961.7606